Valley evolution by meandering rivers

Thesis by

Ajay Brian Sanjay Limaye

In Partial Fulfillment of the Requirements for the

degree of

Doctor of Philosophy

CALIFORNIA INSTITUTE OF TECHNOLOGY

Pasadena, California

2015

(Defended September 8, 2014)

"None show more clearly than the Seine the special features of an invigorated river. The great curves around which it swings fit in nearly all cases close to the bluff on their outer side. It is an able-bodied river, a river of a robust habit of life."

William Morris Davis

ACKNOWLEDGEMENTS

I would like to thank my adviser Mike Lamb for his engagement and creativity, and for his guidance in developing an ethics in science. Mike was incredibly generous with his time, ideas, and enthusiasm in all phases of my time as a student. Several other faculty members have contributed to my growth here. Thanks in particular to Jean-Philippe Avouac for field insights; Andy Ingersoll, for encouraging me to return observations frequently while developing a numerical model; Andrew Thompson, especially for introducing me to sinuous ocean currents; and Bethany Ehlmann, for the opportunity to assist in an exciting new class on planetary surfaces. I thank Oded Aharonson for co-advising me in my first years here, for the opportunity to dive into data from the Mars Reconnaissance Orbiter, and for fostering a group that helped shape my experiences at Caltech. I had the opportunity to learn from many talented students and postdocs, especially Alex Hayes, Kevin Lewis, Paul Hayne, Meg Rosenburg, Antoine Lucas, Edwin Kite, Jeff Prancevic, Joel Scheingross, Mathieu Lapôtre, Luca Malatesta, Vamsi Ganti, Ben Mackey, Ryan Ewing, Roman DiBiase and Dirk Scherler.

Michael Black, Scott Dungan, Ken Ou, Naveed Near-Ansari, and John Lilley put out numerous (figurative!) fires in the realm of computing. Laurie Kovalenko provided great opportunities to meet budding young scientists throughout LA County. Janice Grancich helped me with more practicalities than I am sure I appreciate. Claire Waller Thomas, Kristin Bergmann, Katie Stack Morgan, Mathieu Lapôtre, and Antoine Lucas were great office mates and friends. Thanks to Bill Bing, Nate Light, and Otmaro Ruiz—your dedication and creativity are an inspiration well beyond music. Jennifer Zelaya, Miya

Erickson, and Dr. Edward Helfand offered invaluable perspectives when I needed them most. Thomas Schwei and Jeremy Till have been great friends throughout a decade in California.

Above all, I could not be more fortunate to have a family that has given me limitless inspiration and support. To my parents Ann and Sanjay, my aunt Mary Lou, and my brothers Kiran and Vijay, thank you for making this work possible.

ABSTRACT

Fluvial systems form landscapes and sedimentary deposits with a rich hierarchy of structures that extend from grain- to valley scale. Large-scale pattern formation in fluvial systems is commonly attributed to forcing by external factors, including climate change, tectonic uplift, and sea-level change. Yet over geologic timescales, rivers may also develop large-scale erosional and depositional patterns that do not bear on environmental history. This dissertation uses a combination of numerical modeling and topographic analysis to identify and quantify patterns in river valleys that form as a consequence of river meandering alone, under constant external forcing. Chapter 2 identifies a numerical artifact in existing, grid-based models that represent the co-evolution of river channel migration and bank strength over geologic timescales. A new, vector-based technique for bank-material tracking is shown to improve predictions for the evolution of meander belts, floodplains, sedimentary deposits formed by aggrading channels, and bedrock river valleys, particularly when spatial contrasts in bank strength are strong. Chapters 3 and 4 apply this numerical technique to establishing valley topography formed by a vertically incising, meandering river subject to constant external forcing—which should serve as the null hypothesis for valley evolution. In Chapter 3, this scenario is shown to explain a variety of common bedrock river valley types and smaller-scale features within them—including entrenched channels, long-wavelength, arcuate scars in valley walls, and bedrock-cored river terraces. Chapter 4 describes the age and geometric statistics of river terraces formed by meandering with constant external forcing, and compares them to terraces in natural river valleys. The frequency of intrinsic terrace formation by meandering is shown to reflect a characteristic relief-generation timescale, and terrace length is identified as a key criterion for distinguishing these terraces from terraces formed by externally forced pulses of vertical incision. In a separate study, Chapter 5 utilizes image and topographic data from the Mars Reconnaissance Orbiter to quantitatively identify spatial structures in the polar layered deposits of Mars, and identifies sequences of beds, consistently 1-2 meters thick, that have accumulated hundreds of kilometers apart in the north polar layered deposits.

TABLE OF CONTENTS

LIST OF FIGURES AND TABLES

Chapter 4 *Page*

Chapter 5 *Page*

Chapter 1: Introduction

Meandering is one of nature's most common and captivating patterns. The sinuous arc of a meander loop is cast in many forms, from a water droplet's path down a glass pane [*Nakagawa and Scott*, 1984] to a river canyon cut through bedrock and a sedimentary outcrop on Mars (Fig. 1). Meanders have long inspired scientific interest [e.g., *Thomson*, 1876; *Einstein*, 1926; *Langbein and Leopold*, 1966; *Seminara*, 2006], and, as noted by William Morris Davis, one can recognize a vital spirit in a meandering form. The constant turning path of a meandering river evokes its natural tendency to migrate, and meandering rivers are one of the rare large-scale features of Earth's surface that commonly evolve over a human lifetime. The consequences of meandering river evolution extend over geologic timescales, but in ways that remain poorly understood.

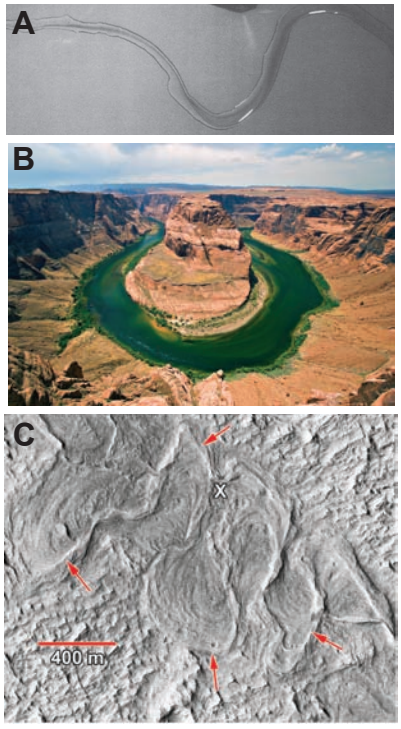

Figure 1. Meanders in different forms. **(A)** Water flowing over a glass pane, from *Nakagawa and Scott* [1984]. **(B)** Meander cut into a bedrock canyon at Horseshoe Bend, Arizona (image: Wikipedia). **(C)** Meandering forms in sedimentary rock, Aeolis Dorsa, Mars, from *Howard* [2009] (MRO/HiRISE image PSP_006683_1740).

Meandering channels shape surrounding landscapes, and are shaped by them—but quantitative predictions of meandering patterns developed over geologic timescales are rare and often schematic. Meandering is perhaps the most common channel form on Earth [*Ikeda and Parker*, 1989], and understanding how meandering rivers generate their own patterns is critical to distinguishing signals from other Earth systems—including climate and tectonics—preserved in landscapes and sedimentary deposits.

The studies that comprise this dissertation take new steps to quantitatively characterize landscape patterns that form as a natural consequence of meandering. Chapter 2 identifies a numerical artifact that hampers numerical model predictions of meandering river evolution over geologic timescales, and presents a new method for tracking the co-evolution of meandering and bank-strength. This method carries the greatest advantages for landscapes with large contrasts in bank-strength, as commonly occurs in bedrock river valleys. Chapter 3 applies this numerical technique to explore generic controls on the evolution of bedrock river valleys, whose form has been suggested to record environmental history. Chapter 4 applies numerical simulations and a new topographic analysis technique to identify controls on the formation and geometry of river terraces, which in many landscapes are considered the primary indicator of landscape response to climate change.

Chapter 5 represents a separate study with the common theme of quantifying patterns in sedimentary deposits and topography—in this case, the polar layered deposits of Mars. Similar to river terraces, the polar layered deposits have long been argued to represent a unique record of recent climate change. Large-amplitude oscillations in solar insolation driven by orbital dynamics have been argued to drive drastic changes in recent

Mars climate [e.g., *Head et al*., 2003; *Laskar et al*., 2004] that likely affected the accumulation and stability of ice at the poles [*Levrard et al*., 2007]. Observational evidence to link polar layered deposit properties to long-term orbital variations, however, has proven elusive—in part because of resolution limitations for remotely sensed image and topographic data. Chapter 5 utilizes new datasets, which likely resolve the finest beds observable from orbit, to characterize stratigraphic structure and periodicity at several locations near the north and south poles and revisit hypotheses for polar layered deposit formation.

Chapter 2: A vector-based method for bank-material tracking in coupled models of meandering and landscape evolution

Originally published in:
Limaye, A. B. S., and Lamb, M. P., 2013, A vector-based approach to bank-material tracking in coupled models of meandering and landscape evolution, Journal of Geophysical Research – Earth Surface 118, doi: 10.1002/2013JF002854.

Abstract

Sinuous channels commonly migrate laterally and interact with banks of different strengths—an interplay that links geomorphology and life, and shapes diverse landscapes from the seafloor to planetary surfaces. To investigate feedbacks between meandering rivers and landscapes over geomorphic timescales, numerical models typically represent bank properties using grids; however, this approach produces results inherently dependent on grid resolution. Herein we assess existing techniques for tracking landscape and bank-strength evolution in numerical models of meandering channels and show that grid-based models implicitly include unintended thresholds for bank migration that can control simulated landscape evolution. Building on stratigraphic modeling techniques, we develop a vector-based method for land surface- and subsurface-material tracking that overcomes the resolution-dependence inherent in grid-based techniques by allowing high-fidelity representation of bank-material properties for curvilinear banks and low channel lateral migration rates. We illustrate four specific applications of the new technique: (1) the effect of resistant mud-rich deposits in abandoned meander cutoff loops on meander belt evolution; (2) the stratigraphic architecture of aggrading, alluvial meandering channels that interact with cohesive-bank and floodplain material; (3) the evolution of an incising, meandering river with mixed bedrock and alluvial banks within a confined bedrock valley;

and (4) the effect of a bank-height dependent lateral-erosion rate for a meandering river in an aggrading floodplain. In all cases the vector-based approach overcomes numerical artifacts with the grid-based model. Because of its geometric flexibility, the vector-based material tracking approach provides new opportunities for exploring the co-evolution of meandering rivers and surrounding landscapes over geologic timescales.

1. Introduction

Meandering channels traverse, erode, and construct landscapes in a wide variety of planetary environments. These include river channels in high-relief mountain landscapes and lowland plains [e.g., *Bridge*, 2003]; tidal channels [e.g., *Fagherazzi et al.*, 1999] and deltas [e.g., *Hudson and Kesel*, 2000]; subglacial [e.g., *Weertman*, 1972] and supraglacial channels [e.g., *Parker*, 1975]; channels formed by lava [e.g., *Greeley et al.*, 1998]; and submarine channels formed by turbidity currents [e.g., *Abreu et al.*, 2003]. In all of these environments, channel lateral migration is influenced by bank strength, and through erosion and deposition there is a rich interplay between channel migration, bank-material strength, and landscape evolution. Bank interaction holds fundamental implications for a number of topics, including flood hydraulics [*Smith*, 1978; *Shiono et al.*, 1999] and the geomorphic expression of climate [*Blum and Tornqvist*, 2000; *Stark et al.*, 2010]. Because vegetation influences bank strength and the stability of sinuous channels [*Braudrick et al.*, 2009], bank strength is also central to the topographic signature of life [*Dietrich and Perron*, 2006] and the development of land plants [*Davies and Gibling*, 2010], as well as stream restoration [*Kondolf*, 2006] and ecology [*Trush et al.*, 2000]. Moreover, an understanding of channel-bank interactions is needed to unravel climatic conditions and material properties for

channel meandering on Mars, Venus, the Moon [*Komatsu and Baker*, 1996], and Titan [*Burr et al*., 2013].

A variety of factors can influence bank strength, including lithology or soil type, vegetation, and susceptibility to weathering from freeze-thaw and wet-dry cycles [*Howard*, 1992; *Montgomery*, 2004]. Differences in bank strength in turn exert first-order controls on channel kinematics in meandering rivers. For example, valley confinement can distort smoothly curving meander bends into sharp bends at valley walls [*Lewin*, 1976; *Lewin and Brindle*, 1977; *Allen*, 1982]. Meandering rivers deposit sediments on the trailing bank and overbank which typically have different strength properties than the preexisting sediment or rock substrate—for example, when erosion-resistant, fine-grained sediment accumulates in abandoned meander loops [*Fisk*, 1947; *Ikeda*, 1989; *Thorne*, 1992].

To model meandering river and landscape evolution, there is a need to accurately couple channel migration with bank-material evolution. Relatively short-timescale models have detailed the influence of stochastic floodplain bank strength on alluvial channel geometry [*Güneralp and Rhoads*, 2011; *Motta et al*., 2012b; *Posner and Duan*, 2012]. Forward models of river meandering over geologic timescales have generated predictions for the planform evolution meander belts [*Howard*, 1996; *Sun et al*., 1996; *Camporeale et al*., 2005; *Karssenberg and Bridge*, 2008], feedbacks between channel migration and floodplain deposition [*Howard*, 1996; *Sun et al*., 1996, 2001], the development of river terraces by incising channels [*Finnegan and Dietrich*, 2011], tectonic uplift influences on channel migration rates [*Lancaster*, 1998], and stratigraphic development in subaerial [*Clevis et al*., 2006; *Karssenberg and Bridge*, 2008] and submarine environments

[*Sylvester et al*., 2011]. Despite this diversity of work, incorporating channel migration in landscape evolution models poses continuing challenges. River banks are commonly steep and mobile, and representing their geometry and erodibility with a grid in numerical models can be problematic [*Tucker and Hancock*, 2010]. While techniques for evolving channel centerlines have been critically assessed [*Crosato*, 2007], to our knowledge no systematic sensitivity tests have been performed for models that represent bank strength in environments influenced by channel migration.

Herein we present a novel framework for tracking the interaction of a migrating channel and its banks in a landscape evolution model. Section 2 establishes the goal of this study: to robustly couple meandering models to a framework for tracking bank-material properties over the temporal and spatial scales of interest for landscape evolution modeling. Section 3 reviews existing approaches to modeling landscape evolution with channel migration and shows that a common, grid-based framework for bank-material tracking can yield results highly sensitive to grid resolution. In Section 4 we present a new, vector-based framework for modeling the co-evolution of a meandering river and its surroundings. We also compare results from grid- and vector-based simulations. In Section 5 we explore the implications of vector-based bank-material tracking for case studies involving subaerial meandering rivers. These examples include the evolution of meander belts with resistant mud-filled abandoned meander cutoffs, the stratigraphic architecture of channel deposits for aggradational meandering rivers with variable bank strength, valley width evolution caused by an incising, meandering river with mixed alluvial and bedrock banks, and bank-height dependent channel migration across an aggrading floodplain. We discuss advantages

and disadvantages of grid- and vector-based approaches to bank-material tracking in Section 6, and present conclusions in Section 7.

2. Modeling goal

Our modeling goal is to develop a numerical framework that can be used to track bank-material properties in a landscape evolution model of a meandering river in the absence of grid-resolution dependencies. In their review of modeling approaches to alluvial river evolution, *Van De Wiel et al*. [2011] identified three principal fronts for progress in modeling meandering rivers and landscape evolution: (1) conceptual: relating to understanding underlying physical processes; (2) structural: relating to algorithms and mathematical formulations within models; and (3) computational resources. Accurate tracking of bank-material properties represents a fundamental structural component of channel migration models because bank strength strongly influences the channel trajectory [*Seminara*, 2006]. In this way, numerical artifacts in tracking bank strength may shape simulated landscapes in subtle but fundamental ways, obscuring the links between physical models and natural process and form [*Dietrich et al*., 2003].

Here we make no contributions to modeling river channel sediment transport and hydrodynamics apart from the interaction between the channel and the evolving landscape. A wide range of channel lateral migration models exist, and they vary considerably in complexity depending on the spatial and temporal scales of the intended application. Some detailed, mathematical models resolve short-term evolution of the left and right bank positions independently and include explicit physical models of sediment transport and bank failure [e.g., *Osman and Thorne*, 1988; *Nagata et al*., 2000; *Darby*, 2002; *Shimizu*,

2002; *Duan and Julien*, 2010; *Parker et al*., 2011; *Motta et al*., 2012a], but are computationally intensive to implement. More commonly, local feedbacks between cut-bank erosion and point-bar growth are approximated as a continuous process [*Seminara*, 2006] and channel width is assumed to be constant [*Parker et al*., 2011a], consistent with field observations [e.g., *Leopold and Wolman*, 1957; *Parker et al*., 2011]. Some channel models explicitly represent hydraulics and bed topography [e.g., *Blondeaux and Seminara*, 1985; *Johannesson and Parker*, 1989], while others employ physically motivated rules [e.g., *Howard and Knutson*, 1984; *Lancaster and Bras*, 2002] to predict local bank migration rates. Computational costs increase with the complexity of the hydraulic and morphodynamic models, so given our interest in landscape evolution over geomorphic timescales herein we employ a relatively simple model (constant channel width, rule-based) that has been shown to produce realistic meandering to represent lateral migration [*Howard and Knutson*, 1984; *Howard and Hemberger*, 1991]. We use this model as the driver of landscape evolution and focus our efforts on properly representing bank-material properties and topography. The landscape-evolution framework we develop is generic, however, so that it can be used in conjunction with a wide range of models for meandering river channels [e.g., *Johannesson and Parker*, 1989; *Zolezzi and Seminara*, 2001].

3. Grid-based approaches to bank-material tracking

We begin this section by reviewing grid-based models for tracking bank-material properties. Second, we introduce a typical setup for grid-based erodibility tracking. Third, we show model results from our own grid-based simulations to illustrate shortcomings with this technique. This leads us to introduce the new vector-based technique in Section 4.

3.1. Review of existing grid-based models

Existing approaches to bank-material tracking over geomorphic timescales all utilize a grid—regularly spaced and fixed, or irregularly spaced and deformable. Two-dimensional grids are used in scenarios with only lateral differences bank-material properties [*Howard*, 1996; *Sun et al*., 1996, 2001; *Lancaster*, 1998; *Finnegan and Dietrich*, 2011] whereas three-dimensional grids are used to additionally track vertical variations in these properties [*Clevis et al*., 2006; *Karssenberg and Bridge*, 2008; *Sylvester et al*., 2011]. In some cases the grid stores elevation or bank-material properties which alter the channel trajectory [*Howard*, 1996; *Sun et al*., 1996; *Lancaster*, 1998; *Güneralp and Rhoads*, 2011; *Motta et al*., 2012b], while in other cases the grid is solely a framework for recording channel-influenced topography [*Finnegan and Dietrich*, 2011] or stratigraphy [*Clevis et al*., 2006; *Karssenberg and Bridge*, 2008; *Sylvester et al*., 2011]. Most commonly, active channel banks are represented using high-resolution vectors tracked independent of the grid (Fig. 1A) [*Howard*, 1992, 1996; *Sun et al*., 1996; *Finnegan and Dietrich*, 2011], which we follow here. Grid-resolution dependencies come into play when areas previously occupied by the channel are recorded in the landscape by mapping the bank vectors onto a discrete grid of comparatively low resolution (Fig. 1B). Consequently, as the banks smoothly migrate, some grid cells are abandoned while others are newly enclosed within the channel, but the process of updating the grid is discontinuous (Fig. 1C). Therefore, past bank positions are incompletely recorded in the grid, and the maximum resolution for differentiating successive bank positions is the grid cell size.

Lancaster [1998] adopted a distinct approach that recorded bank-material evolution

using an adaptive irregular grid within the Channel-Hillslope Integrated Landscape Development model [*Tucker et al*., 2001]. In this framework, the channel centerline is explicitly tracked using nodes, but bank migration is incorporated by adding nodes in the point bar region and removing nodes in the cutbank region after the channel migrates more than a threshold distance. The finest horizontal resolution attainable by this scheme is the wetted channel width [*Lancaster*, 1998], and reducing the re-meshing threshold can be computationally expensive [*Udaykumar et al*., 1999; *Clevis et al*., 2006; *Liu*, 2010]. Thus, as with fixed regular grids, bank positions are discontinuously recorded.

3.2. Demonstration of resolution dependence in grid-based models

3.2.1. Meandering model implementation

To illustrate spatial resolution controls on bank interactions in grid-based models, we use a bank-material tracking model similar to *Howard* [1996] and *Sun et al*. [1996, 2001], which is briefly reviewed here. In this implementation a channel with a rectangular cross-section scours the land surface to the bed elevation as it migrates laterally. The channel is forced to maintain a fixed width by balancing cutbank erosion with point bar deposition. As in *Howard* [1996], *Sun et al*. [1996, 2001], *Lancaster* [1998] and *Finnegan and Dietrich* [2011], fluxes of sediment are not tracked explicitly; thus all eroded sediment is assumed to contribute to point bar deposition or leave the system. Bank migration rates are driven by local and upstream-weighted channel curvature [*Howard and Knutson*, 1984]. The channel centerline and banks are represented using discrete nodes connected by straight segments, a geometry common to many meandering models [*Crosato*, 2007]. The relative centerline migration rate (R_l) is calculated as

$$R_1(s) = \Omega R_o(s) + \frac{\Gamma \int_0^{\xi_{max}} R_o(s-\xi)G(\xi)d\xi}{\int_0^{\xi_{max}} G(\xi)d\xi}, \quad (1)$$

where s is the node index, the dimensionless channel curvature is $R_o = (r/w)^{-1}$, r is the local centerline radius of curvature and w is channel width. The dimensionless weighting parameters Γ and Ω are set to 1 and -2.5, respectively, after *Ikeda et al*. [1981]. ξ is the upstream distance, and G is an exponential weighting function

$$G(\xi) = e^{-(\frac{2kC_f}{h})\xi}. \quad (2)$$

Here k is a dimensionless scaling parameter equal to 1 [*Ikeda et al*., 1981], C_f is a friction coefficient (set as 0.01 after *Stølum* [1996]), and h is the channel depth. The curvature integration proceeds upstream to the distance ξ_{max}, where the normalized value of the weighting function G falls below 1%. The local lateral erosion rate ($E_L(s)$) is then computed for the sinuosity (μ) and the bank erodibility coefficient (k_e) as

$$E_L(s) = k_e R_1(s)\mu^{\varepsilon}, \quad (3)$$

where ε =-2/3 [*Howard and Knutson*, 1984]. The bank erodibility coefficient k_e is set to yield the user-defined, space-averaged lateral migration rate.

We track different classes of material in the river valley; for example, point bar sediments that are deposited along the inner bank by the river may have different strength properties than pre-existing sediment or bedrock, sediment fill in abandoned cutoff loops, or floodplain deposits. In the course of each simulation, two-dimensional grids of land-surface topography and material properties are updated with the movement of the channel; thus only lateral differences in bank-material properties are considered. A bank-

material erodibility coefficient (k_e) is assigned to each intersected grid cell, and is a linear function of the fraction of the bank comprised by each material of differing erodibility

$$k_e = \sum k_i f_i , \qquad (4a)$$

where f_i is the fraction of the bank (from the channel bed to the bank-full elevation) that has an erodibility k_i. For example, in the common case of differences in bank strength between bedrock and sediment, Eq. 4a becomes

$$k_e = k_s (1 - f_b) + k_b f_b, \qquad (4b)$$

where f_b is the fraction of the bank (from the channel bed to the bank-full elevation) that is bedrock and k_s and k_b are the erodibilities of sediment and bedrock, respectively. The linear dependence of bank strength is similar to the parameterization of bank height influences on channel migration rates used by *Lancaster* [1998].

The bank bedrock fraction is recalculated for each cell intersected by a test vector extended from the cutbank node in the direction of bank migration. The test vector length (d_{max}) is calculated for each node as

$$d_{max}(s) = k_{e,max} R_l(\mathrm{s}) \mu \Delta t, \qquad (5)$$

where $k_{e,max}$ is a fixed constant that represents the maximum erodibility amongst all bank materials present in the simulation, and Δt is the time step. This formulation ensures that the bank-material properties are inspected over a length-scale long enough to account for the maximum possible bank migration distance but no further. The test vector length varies in response to the local relative migration rate at each node (R_l(s)), and so varies from node

to node and through time. Thus the length of the test vector is set before any information about the local bank composition has been ascertained.

The erodibility can vary with distance from the channel banks in a given time step, so channel migration would proceed too far or not far enough if erodibility were only considered right at the banks. Therefore to determine the appropriate bank migration distance, we define a "cost" for each increment of bank migration through material of constant erodibility. The cost represents the time required to migrate through that area relative to the time required to migrate through an area with the highest erodibility. For example, areas with relatively low erodibility take longer for the channel to migrate through and incur relatively high cost. The cost of bank migration through each cell intersected by the test vector is recorded, and is equal to the ratio of the distance traveled within the cell (d_n) to the length of the test vector (d_{max}), divided by of the erodibility for that grid cell ($k_{e,n}$). The channel bank node is moved incrementally until the cost function sums to 1, i.e.,

$$\sum_{n=1}^{N} \frac{d_n}{k_{e,n} d_{\max}} = 1 \quad , \tag{6}$$

where N is the number of cells traversed by the test vector. This formulation ensures that the actual bank migration distance properly accounts for the erodibility of all materials encountered in that time step. For example, the actual bank migration distance only equals the maximum possible bank migration distance (d_{max}) when all of the material encountered by the search vector has the highest erodibility found in the model domain.

The initial separation distance between channel centerline nodes (l) is equal to the channel width. In plan view, nodes move perpendicular to the channel centerline in the

direction specified by the sign of $E_L(s)$ (positive to the left, looking downstream). Node-to-node distances along the centerline change as meander bends evolve; consequently, nodes are added and removed following rules similar to *Howard* [1984]. When two consecutive nodes (*A* and *B*) become separated by $2l$, an intervening node is added. When a node *B* is less than $0.5l$ from its upstream neighbor *A* but greater than $0.5l$ from its downstream neighbor *C*, *B* is shifted to a point equidistant from *A* and *C*. When any three consecutive nodes (*A*, *B*, and *C*) are oriented such that the distances from *A* to *B* and *B* to *C* are both less than $0.5l$, *B* is removed.

New node locations are calculated using a local spline interpolation of the channel centerline. This local interpolation method bounds the node-to-node distances to the range $0.5l$ to $2l$, or $0.5w$ to $2w$ when $l = w$, where *w* represents the channel width. *Crosato* [2007] recommended $l > 0.3w$ to reduce numerical artifacts in centerline evolution, and $l < w$ to limit the visual effect of the centerline discretization. Maintaining the node spacing within this narrower range requires globally re-interpolating the channel centerline. While such an approach is desirable for the constant bank strength cases such as those presented by *Crosato* [2007], our preliminary tests showed that re-interpolating the entire centerline in cases with variable bank strength suppresses channel migration in areas of slow channel migration. This occurs because reaches that migrate quickly through weak bank materials set the frequency of centerline interpolation. As a result, areas that migrate slowly through strong bank materials are re-interpolated too frequently, which locally straightens the centerline and inhibits meander bend growth. To our knowledge, this numerical artifact has not been identified in previous studies. Although

the local interpolation approach adopted here places looser constraints on the centerline node-to-node distance than would a global interpolation approach, it allows for slowly migrating reaches to undergo centerline interpolation less frequently than quickly migrating reaches, and thus does not inhibit meander bend growth.

A periodic boundary condition is employed in three respects. First, the channel planform is periodic along the valley axis, such that meander bends that migrate across the downstream edge of the model domain reappear on the upstream side, and vice versa. No channel centerline nodes are fixed, so the channel axis can drift freely. The extent of the model domain parallel to the valley axis scales with the average meander wavelength, and is long enough that the channel curvature integration never spans the entire channel centerline. Second, the channel curvatures are computed in a periodic fashion, in accordance with the periodicity of the channel planform. Third, longitudinal profile elevations are periodic. Just as the channel centerline repeats with a lateral offset equal to the valley-parallel centerline distance range within the domain, the vertical component of the longitudinal profile repeats with a vertical offset equal to the vertical range of the long profile within the model domain. This ensures that reaches that enter the model domain on the upstream side are no lower than reaches downstream, and vice versa.

Neck cutoffs occur whenever one of the channel banks intersects itself; chute cutoffs are not modeled. Because there is no sub-grid parameterization for determining the bank position, a criterion must be established for whether or not a cell is considered within the channel. In this regard, *Howard* [1996] mentioned two end-member cases: (1) a conservative case, in which a cell must be fully contained by the banks to be considered

within the channel, and (2) a liberal case, in which any cell partially contained by the banks is also considered within the channel. Both cases are illustrated in Figure 2; the conservative case is adopted here to illustrate the resulting strong grid-resolution dependence of landscape evolution. The liberal case could also be adopted; it would consistently over-predict the area affected by channel migration because even partial bank migration across a cell boundary would result in alteration of bank-material properties for the entire cell.

3.2.2. Grid-based model application and results

For the simulations presented in this subsection we model the evolution of a river channel incising into bedrock, and with mixed alluvial and bedrock banks that evolve in composition throughout the simulation. Specifically, the channel migrates 20 times faster in areas it has already visited (where it erodes through previously deposited sediment, i.e., $k_s = 1$) than it does when eroding against unvisited areas (which are entirely bedrock, i.e., $k_b = 0.05$). We track grids of land-surface topography and bedrock topography, the difference between the two being the sediment depth. Initially the grid elevations are equal in elevation because the landscape is entirely bedrock. As the channel migrates laterally, the depth to bedrock is reset to the channel bed elevation. Cells abandoned by the channel are assigned a new elevation equal to the bedrock elevation plus the channel depth, which enacts sediment deposition along the trailing bank. The channel begins in a high-sinuosity state at the beginning of the simulations. The initial channel planform morphology is set by evolving the centerline in an identical simulation, except in the absence of bank-strength variations, from an initial straight centerline seeded with meter-

scale noise. Channel bed elevation is set to be constant for simplicity and there is neither aggradation nor vertical incision.

Three simulations were performed where the only difference between simulations was the grid resolution (Fig. 3). A number of phenomena are common to all three simulations. The channel migrates, and the bank-material tracking grid records areas visited by the channel. Meander bends elongate, and several experience neck cutoffs. The bank material evolves in time as the channel erodes bedrock and deposits sediment, commonly on the inside of growing meander bends. The evolving bank materials also influence channel planform development: straightened reaches form because bedrock banks slow bend growth in reaches that have experienced neck cutoffs. In places the channels turn sharply where they transition from primarily sediment to primarily bedrock cutbank materials.

Despite these similarities, the simulations also show that the small-scale representation of bank composition dramatically influences channel and bank-material evolution. The area visited by the channel (Fig. 3A-C) declines precipitously as the grid-cell width increases. As compared to the simulation shown in Fig. 3A, which has a finer grid resolution, the simulation in Fig. 3B shows slightly less area has been visited, and also that the final channel position is different. In Fig. 3C, the cell width is larger still; and though the cell width is less than the channel width, old meander loops are discontinuously recorded in the grid. Consequently, the visited area recorded in the grid is far less than in Fig. 3A and Fig. 3B, and the final channel planform is again different from both cases. The pattern of grid cells crossed by the final channel extent (Fig. 3D-F)

shows that finer grid resolutions result in more area recorded as visited by the channel.

Despite starting with the same channel planform, the channel trajectory differs for all three simulations because the different grid resolutions cause different spatial distributions of bank strength to evolve. These differing bank-material properties cause reaches with similar geometries to migrate at different rates, which quickly causes the channel planform shapes to diverge. This implies that in general, model predictions for short-term channel trajectory and large-scale landscape evolution depend strongly on the grid resolution. Depending on the model outcome considered, the resolution artifact may greatly distort the influence of bank-material properties.

One solution to remove the dependency of landscape evolution on grid resolution is to decrease the grid cell size so that it is much smaller than any incremental change in the river channel location. To illustrate this point, the cell width (Δx) can be non-dimensionalized ($\Delta x'$) using the migration length scale

$$\Delta x' = \frac{\Delta x}{E_L \Delta t}, \tag{7}$$

where E_L is the mean lateral erosion rate; a solution that is independent of grid resolution would require $\Delta x' \leq 1$. In practice, however, such a resolution is difficult to achieve given memory constraints, especially for model cases run over geomorphic timescales where E_L and Δt are small. As an example, bankfull river floods often occur at approximately annual timescales (Δt = 1 yr) and bedrock erosion rates are typically on the order of E_L = 1 mm/yr, which implies a minimum memory footprint of 1 TB per square kilometer of model domain using a uniformly spaced rectangular grid, a memory requirement that can only be met by supercomputers. Due to these memory limitations, coarser grid resolutions are

exclusively used in practice. For example, the cell width in the *Howard* [1992, 1996] and *Sun et al*. [1996, 2001] models and the threshold distance for node addition in *Lancaster* [1998] are approximately one channel width. Alluvial meandering rivers typically migrate at less than one tenth of a channel width per year [e.g., *Nanson and Hickin*, 1983; *Hudson and Kesel*, 2000]. Taking this as an upper bound for the bank migration rates and assuming an annual time step yields approximate values of $\Delta x' = 10$ (for extremely rapid migration at 0.10 widths per year) to 100 (for a more typical migration rate of 0.01 widths per year) for the aforementioned studies.

Because lateral erosion rates vary spatially for meandering channels [*Nanson and Hickin*, 1983; *Hudson and Kesel*, 2000], bends that migrate relatively slowly may be affected by grid resolution even if other bends are not. Consequently, existing frameworks for landscape evolution in meandering environments with bank strength differences generally yield grid-resolution dependent results except for cases with very large lateral migration rates. The grid-resolution issue is especially significant for rivers with bedrock banks, which have lateral migration rates of millimeters to centimeters per year even in relatively weak rock [*Hancock and Anderson*, 2002; *Montgomery*, 2004; *Fuller et al*., 2009a; *Finnegan and Dietrich*, 2011].

4. A new vector-based method for modeling meandering-landscape interactions

In light of the resolution dependence of bank-material properties and channel trajectories in grid-based approaches to modeling meandering-landscape interactions, we propose a new framework for tracking bank-material geometry. The framework builds off the stratigraphic visualization approaches of *Pyrcz and Deutsch* [2005] and *Pyrcz et al*.

[2009], which use a channel's extent and longitudinal profile as reference objects for identifying simultaneously formed fluvial deposits. In these studies, modeled stratigraphy is formed by assembling channel extents from different points in its trajectory. We extend this approach by including interactions between the channel trajectory and the properties of the bank material. In contrast to the method of recording bank-material properties with grids, in our new approach topography and bank-material properties are recorded using initial valley geometry and the full history of channel positions, which are stored as vector data. As the channel migrates and encounters areas it has previously visited, the new algorithm queries a database of previous channel positions to reconstruct these bank-material properties instead of querying a bank-material grid. The database of channel positions is used to define polygonal regions of bank material formed during the simulation where the node spacing along the polygon boundaries is set by the channel boundaries themselves. Therefore there is no data degradation with respect to the geometry produced by the underlying meandering model, as occurs in mapping the channel boundaries onto a grid.

To illustrate the new vector-based approach for tracking bank-material properties we use the same model to drive channel migration [*Howard and Knutson*, 1984] as in Section 3.2.1. At each time step, the channel translates laterally by the local lateral erosion rate times the time step ($E_L \Delta t$), and vertically by vertical erosion or aggradation rate times the time step ($E_V \Delta t$) (Fig. 4A). The channel is forced to maintain a constant width, and point bar sediment (with thickness $\Delta z_{point\ bar}$) is assumed to accumulate on the trailing bank to the height of the flow depth. To calculate the vertical erosion or aggradation rate, an evolution equation such as the stream power equation [*Howard and Kerby*, 1983] can be

applied to the longitudinal profile. To introduce the bank interaction algorithm, we discuss a case with only lateral differences in bank-material properties. The general principles used for bank-material tracking also extend to cases with vertically stratified bank materials, however, and we present one such example in Section 5.3.

The bank interaction algorithm proceeds as follows. A meandering model is used to compute a preliminary, bank strength-independent lateral migration rate for each centerline node. The channel banks are tracked as separate vectors, and each left and right bank node is associated with a centerline node. The local channel migration direction determines which bank node represents the trailing bank and which represents the cutbank. At each time step the bank vectors are used to construct the planform extent of the channel. The local elevation of the channel bed within this extent is calculated by interpolating along the channel longitudinal profile (Fig. 4B), and can be refined using vector-based cross-section data that is also stored. The channel bed elevation represents the elevation to which the channel bed scoured the land surface (z_{scour}) at the time the channel extent occupied that location. Thus, whereas the grid-based method would look up z_{scour} from a grid of elevation values that spans the model domain, the vector-based method determines z_{scour} using only the past positions of the channel. The channel planform extents from different time steps collectively characterize the areas of a valley scoured by channel migration (Fig. 4C).

Because channel geometric information is saved at every time step, reconstructing bank-material properties becomes more computationally intensive as the simulation proceeds. Part of this operation is to determine which of the saved previous channel locations are needed to reconstruct the local elevation and composition of bank material.

Rather than search the entire channel geometry database, we use an indexing system that associates each channel extent with an approximate time interval and spatial location. We query this database to find the most recent time of channel occupation in order to determine local bank-material properties. The most recent time is used because when the channel migrates across an area, it updates the landscape properties set during earlier instances of channel occupation. The spatial and temporal indexing increments are user-defined, can vary during the simulation, and do not affect the model results; they only affect the efficiency of the bank-material look-up operations.

To account for variable strength material in the calculation of local lateral migration distance, we use the test vector approach as described in Section 3.2.1 (Eq. 5; Fig. 4D). Bank-material properties are reconstructed at points along this test vector separated by an interval distance of $E_L \Delta t$. Parts of the model domain beyond the channel-visited area are represented by a valley-bounding polygon which is user-defined and can represent an arbitrary topography and bank-material composition. In the example in Figure 4D, the test vector encounters sediment and bedrock, and therefore the local migration distance is adjusted according to these different erodibilities (Eq. 6).

Once the original channel scour depth is determined, it is used to calculate the land surface elevation (z)

$$z = z_{scour} + \Delta z_{point\ bar} + \Delta z_{overbank}, \qquad (8)$$

where $\Delta z_{point\ bar}$ represents the thickness of point bar deposits and $\Delta z_{overbank}$ is the elevation contribution from overbank deposition. The locations of meander cutoff loops are tracked independently, so that areas abandoned by the channel through cutoffs are not assigned a

mantle of point bar deposits. Equation 8 applies only outside of the channel; within the channel, the elevation is equal to z_{scour}. Overbank deposition can be incorporated using different models. Here we choose the model of *Howard* [1996]

$$\frac{dz_{overbank}}{dt} = \eta + D_s e^{-d_c/\lambda}, \tag{9}$$

where $dz_{overbank}/dt$ is the rate of elevation change within the floodplain; η is a constant deposition term; and the second term is a spatially dependent overbank deposition rate, where D_s is the deposition rate of overbank sediment at the channel banks, d_c is the minimum distance to the active channel, and λ is a decay length scale. Within the vector-based framework, the local sediment cover due to overbank deposition is determined by calculating the overbank sediment contribution from the channel at each time step after the channel abandoned the point

$$\Delta z_{overbank} = \sum_{t=t_a+\Delta t}^{t_f} (\eta + D_s e^{-d_c(t)/\lambda}), \tag{10}$$

where t is time, t_f is the current model time, t_a is the time the channel abandoned the point, and $d_c(t)$ is the minimum distance from the point to the channel at time t. A gridding procedure, used to visualize the final topography, can be performed at arbitrary resolution. This is because the elevation at any particular point is not stored explicitly, but rather is calculated as needed to determine bank-material height. To do this, the algorithm uses the channel polygon that contains the point of interest, retrieves the time step associated with the channel polygon from the database of previous channel positions, and projects the point onto the longitudinal profile associated with that time step to reconstruct the original channel scour depth. Adding contributions from point bar and overbank sedimentation

yields the exact elevation.

The channel scour and land surface elevations are bank-material properties that can be used to define an effective bank erodibility, which is a user-defined function (e.g., of bank elevation and composition) and can vary with the application as in Section 3.2.1 (Eq. 4a). A unique erodibility value is calculated for each interval between checkpoints along the test vector. The final lateral migration distance for each centerline node is calculated using the erodibility in each interval until the cost condition (Eq. 6) is met. Once the final migration distance is calculated for each centerline node, the nodes are moved perpendicular to the local centerline azimuth by this distance, and the bank nodes track along with them.

The memory required by the vector-based approach depends on the channel trajectory, which determines the size of the channel geometry indexing data structure. In trial simulations of bedrock river valley evolution, we noted a memory savings of at least two orders of magnitude over a grid-based model of equivalent resolution, because in the vector-based approach, areas with similar bank-material properties can be stored using their boundary coordinates instead of a grid of contiguous pixels. This is analogous to the efficiency offered by boundary element models as compared to finite element models used widely in engineering [*Katsikadelis*, 2002; *Li and Liu*, 2002; *Liu*, 2010].

5. Case studies

The vector-based framework for bank-material tracking can be applied to a broad array of systems with interactions between channels and bank material. In this section we focus on four particularly common and diverse scenarios for rivers. First we model

floodplain evolution for a scenario in which a channel bed neither aggrades nor degrades, and material that accumulates in oxbows (abandoned meander cutoffs) has a different strength than point bar sediments that accumulate by channel lateral migration. Second, we extend the floodplain development scenario to a case with channel aggradation and floodplain deposition to analyze the resulting stratigraphy. Third, we model topographic evolution by a meandering river incising a bedrock valley with mixed alluvial and bedrock banks that evolve in the simulation. Fourth, we model a case of overbank deposition by an alluvial river in which bank height rather than bank material determines erodibility. We begin by discussing aspects of the initial conditions and the model domain common to all four case studies.

Grid- and vector-based tests within each case study use the same initial conditions, and the underlying meandering model is identical to that described in Section 3.2.1. The channel bed is initially inset by one channel depth into a planar landscape with constant slope. The initial channel centerline is straight, with random perturbations of order 0.01 channel widths to seed meander development. The initial channel slope matches the landscape slope.

5.1. Bank strength effects on floodplain evolution

The tendency for meandering channels to confine themselves within a narrow channel belt is a subject of ongoing debate. Cutoffs inherently limit channel sinuosity and meander-belt width [*Howard*, 1996; *Camporeale et al*., 2005], but fine-grained, oxbow-filling sediments have been argued to further enhance meander-belt confinement because they tend to be more resistant to erosion than other floodplain materials [*Fisk*, 1947; *Allen*,

1982; *Ikeda*, 1989]. For example, *Hudson and Kesel* [2000] argued that fine-grained sediments in oxbows account for large spatial variability in bank migration rates along the Mississippi River, USA. This mechanism implies a feedback between meander growth, cutoff, and overbank sedimentation, and was simulated in *Howard* [1996] and *Sun et al*. [1996]. Both studies suggested that oxbow sediments could steer the trajectory of subsequent meanders and potentially facilitate self-confinement of meander belts. However, given the relatively coarse grids used in these studies, the grid resolution itself could have caused greater meander belt confinement. Thus, determining the relative importance of these confinement mechanisms requires accurate modeling of bank-material properties.

The vector-based framework presented here can contribute to a better understanding of the temporal and spatial scales associated with the co-evolution of meandering rivers and floodplain material properties, and can quantify grid-resolution effects inherent in the models of *Howard* [1996] and *Sun et al*. [1996]. To demonstrate this, we reproduce the style of clay plug resistance modeled by *Howard* [1996]: abandoned meander loops are set to instantly fill with sediment more resistant than the rest of the floodplain, and the overbank sedimentation outside of oxbows is set to zero. The relative erodibility of cutoff-fill compared to point bar sediment (k_{ec}) is varied between 0.01 and 1, spanning a range explored in *Howard* [1996] and *Sun et al*. [1996]. The portions of cutoff loops within three channel widths of the closest channel bank at the time step following cutoff are set to in-fill with material equivalent in erodibility to point bar sediments [*Howard*, 1996]. *Sun et al*. [1996] additionally modeled cases with time-dependent bank-

material strength due to progressive infilling of oxbows with relatively resistant sediments. Though not implemented for this case study, such scenarios could similarly be modeled using vector-based bank-material tracking because surface or deposit age is saved along with bank-material polygon geometry.

Figure 5 compares the resulting topography for simulations using grid-based and vector-based bank-material tracking. In Figure 5A-C, $k_{ec} = 1$, so there are no bank strength contrasts. Consequently, these three panels show identical final planform geometries because only bank strength differences that arise during these simulations can cause the geometries to diverge. Except for the coarse grid case (Fig. 5A), all simulations show an active record of meander bend growth and cutoff, and that the channel axis drifts. Abandoned meander cutoffs are numerous and distributed across the area and commonly intersect one another, similar to Johnson Creek, Yukon Territory, Canada [*Camporeale et al*., 2005], for example. In cases with resistant oxbow-filling sediments ($k_{ec} = 0.1$; Fig. 5D-E), the portion of the meander belt that was recently visited by the channel is confined to the center of the valley where oxbow remnants are relatively rare. In the cases with no bank strength differences ($k_{ec} = 1$; Fig. 5B-C), the recently visited area tends to the top half of the model domain, and the numerous oxbows in this area have no influence on the channel migration.

When the grid resolution is relatively coarse and equal to the channel width (Fig. 5A), little of the channel migration is recorded in the topography because it is rare for the channel banks to instantaneously enclose full cells. With a finer grid resolution of $0.4w$ (Fig. 5B), where w is the channel width, the visited area more closely resembles that for the

vector-based case (Fig. 5C) and the final channel planform extents coincide. Cutoff loops are thinner in the grid-based cases (Fig. 5B and 5D) than in the vector-based cases (Fig. 5C and 5E) because the channel width spans some cells incompletely in the grid-based case, and the bank-material in these cells is not recorded as cutoff loop-filling sediments. The floodplains are expected to be the same in these two cases because the channel migration does not interact with evolving bank-material properties.

Topography differs in subtle but potentially important ways between the fine grid- and vector-based simulations when k_{ec} = 0.1 (Fig. 5D-E) and spatially variable bank materials are allowed to evolve. Most importantly, despite beginning with the same channel planform extent, the two cases differ in the final channel planform extent and the geometry of the active meander belt. This occurs because the finite resolution at which the grid-based case stores bank-material composition leads to divergent bank-material properties and channel trajectories.

Calculation of the mean active width of the meander belts in these simulations allows for more quantitative comparisons (Fig. 5F). We define the mean active meander-belt width as the area modified by the channel in the last 10% of simulation time divided by the left-to-right length of the model domain. The coarse grid resolution simulations ($\Delta x = w$) record only fragments of the channel migration regardless of the relative erodibility of oxbow sediments, which results in a minimal active meander belt width. When the grid resolution is higher ($\Delta x = 0.4w$), the mean active width increases as a function of k_{ec}. The vector-based approach shows the same relationship, and the grid-based and vector-based approaches give equivalent results when $k_{ec} = 1$ because bank strength is uniform. When k_{ec}

< 1, the vector-based method yields a larger mean active meander-belt width than the grid-based case ($\Delta x = 0.4w$), and this discrepancy increases as the erodibility contrast between oxbow and other sediments increases. The meander belt in the grid-based case is about 40% narrower than for the vector-based case when $k_{ec} = 0.01$. Mean active meander-belt width decreases with decreasing k_{ec} because the channel migrates more slowly through oxbow sediments and thus becomes confined to a narrower area. The vector-based case shows less narrowing than the grid-based case ($\Delta x = 0.4w$), however, because in the grid-based case the channel must sweep entirely across a cell in order to reset its bank strength. This makes channel-confining oxbow sediments more persistent than in the vector-based case, for which there is no such threshold for updating bank strength. As a result, the channel can reset bank strength more easily in the vector-based case and can maintain a wider mean active meander-belt width.

Vector-based simulation results demonstrate that oxbow sediments that are less erodible than other floodplain sediments can indeed confine the active width of meandering. Thus, while cutoffs play a role in confining the meander belt [*Camporeale et al*., 2005], bank strength differences established by channel migration should result in narrower meander belts than would be predicted based on cutoff-driven confinement alone (i.e., when $k_{ec} = 1$). A significant proportion of the meander-belt narrowing predicted using grid-based models is due, however, to a numerical artifact.

5.2. Bank strength effects on channel body geometry

Meander-belt evolution in aggrading rivers is a prime determinant of the stratigraphic architecture of the resulting fluvial deposits, with important implications for

reservoir analysis including the connectivity of porous and permeable sand bodies [*Henriquez et al*., 1990; *Hirst et al*., 1993]. To illustrate the potential for differential bank strength to influence deposit geometry, we model a scenario equivalent to the floodplain evolution case in Section 5.2, but here we force the river to aggrade at a constant rate. *Sylvester et al*. [2011] presented a similar model scenario, but without variable bank strength. As in the previous case study, oxbows are set to instantly fill with sediment whose erodibility is a fraction (k_{ec}) of the erodibility of point bar sediment. Outside of oxbows, overbank sediments must accumulate in order to maintain channel confinement. For consistency with *Howard* [1996] and *Sun et al*. [1996], which for the relevant simulations did not track overbank sediments that accumulated outside of oxbows, such overbank sediments are assumed to have no effect on bank strength (i.e., only fine sediments that accumulate in oxbows alter bank strength). While this is a highly idealized model for floodplain sedimentation, it allows isolating the kinematic role of oxbow-filling sediments in aggrading environments. We extend the two-dimensional approach to bank-material tracking used in previous examples to three dimensions by tracking the lateral and vertical extent of resistant sediments, in order to account for multiple layers of channel deposits.

We compare cross-sections perpendicular to the valley axis for scenarios with and without bank strength contrasts, for two different aggradation rates; all cases utilize vector-based bank-material tracking (Fig. 6). For both high (0.001 channel depths/yr) and low (0.0002 channel depths/yr) channel aggradation rates, the total deposit width is approximately 50% larger in cases with no bank strength contrast (k_{ec} = 1; Fig. 6A and 6C) than for cases with a bank strength contrast (k_{ec} = 0.01; Fig. 6B and 6D). While under rapid

aggradation with no bank strength contrast, channel bodies record channel axis drift (Fig. 6A), which leads to spatial clustering of channel bodies similar to that commonly observed at larger scale in alluvial basins [e.g., *Hajek et al*., 2010]. The case with aggradation and a strong bank strength contrast results in a deposit with more tightly constrained lateral excursions (Fig 6B). This occurs because when deposits that accumulate in oxbows have a low relative erodibility, they impede channel lateral migration and hence overall deposit width. Taken together, these simulations indicate that vector-based bank-material tracking may be useful for constructing reservoir models when there are bank strength differences between sedimentary units, e.g., due to grain size differences [e.g., *Sylvester et al*., 2011].

5.3. Bedrock valley widening

Bank strength in upland rivers varies strongly between sediment and bedrock and in these environments the vector-based method is well suited to represent the relatively slow erosion rates in bedrock. Extensive research has focused on quantifying rates and controls on river vertical incision in bedrock (see *Whipple* [2004] and references therein) and more recently bedrock channel width [*Finnegan et al*., 2005; *Wobus et al*., 2006b; *Turowski et al*., 2008; *Yanites and Tucker*, 2010]. Processes that cause channel widening also contribute to bedrock valley widening, and thus are important for understanding the large-scale evolution of mountain landscapes [*Montgomery*, 2004; *Whipple*, 2004]. To compare grid- and vector-based frameworks for recording bank-material composition for channels with mixed bedrock and alluvial banks, we construct a numerical experiment in which a channel migrates laterally and erodes vertically within an established valley. Similar to *Howard* [1996], the bedrock valley walls are prescribed higher bank strength than bank material

within the valley. Here we model a 100-fold bank strength contrast between bedrock and sediment, as is likely common in bedrock-walled valleys where valley widening rates of 1 cm/yr or less predominate [*Montgomery*, 2004].

The longitudinal profile node farthest downstream in the model domain is lowered at a constant rate to drive relative base-level fall and vertical incision. The vertical erosion rate (E_V) is set to be proportional to the local bed shear stress [*Howard and Kerby*, 1983]

$$E_V = k_v \rho g h S. \qquad (11)$$

The rate constant k_V is set to 0.003 to achieve an average incision rate of 1 mm/yr; ρ is the density of water; g is gravitational acceleration; h is the channel depth; and S is the local bed slope, calculated as a first-order, forward finite-difference. In order for a channel reach to remain confined during downstream translation, its rate of vertical incision must match or exceed the rate of elevation loss due to translation if the landscape slopes downstream, i.e., $E_V \geq E_L S_s$, where S_s is the mean slope of the surface over which the node migrates. Consequently, we limit our analysis to a case where $E_V \geq E_L S_s$ to avoid cases where the channel loses confinement through lateral migration on a tilted landscape.

We model the evolution of the valley-bound channel using both grid-based and vector-based approaches to bank-material tracking for comparison. In both cases, the channel bends grow from an initial state of low sinuosity. Before bends can become highly sinuous and reach neck cutoff, however, the valley walls inhibit their motion. This results in angular channel planform extents where the channel deforms against the valley walls (Fig. 7), similar to the Beaver River, Alberta, Canada [*Parker et al.*, 1983; *Nicoll and Hickin*, 2010], for example. Because the bank material in valleys has lower strength than at

the valley walls, meander bends preferentially drift down-valley rather than across-valley. This causes frequent planation of the entire valley floor, which lowers the sediment-bedrock interface and permits the channel to remain mobile and unentrenched within the valley. At the valley margins where there is a large contrast in bank strength between sediment and bedrock, the grid- and vector-based bank-material tracking schemes yield divergent behaviors.

When bank material is modeled with a grid of 2 m (0.08*w*) resolution (Fig. 7A), the channel is fully restricted to the initial valley width and meander bends only propagate down-valley. This occurs because the channel must advance a full cell width beyond the initial valley wall before updating the bank-material grid. Any bank advance less than a cell width is not recorded, so that these minor advances leave no record of erosion and subsequent channel migration always encounters a fully intact valley wall unless the bank cumulatively advances through an entire cell.

With the vector-based approach the valley more than doubles in width as compared to the grid-based approach (Fig. 7B and 7C). Lateral erosion, which is suppressed by the implicit erosion threshold in the grid-based case, occurs steadily in the vector-based case. The channel widens both sides of the valley, but erodes more material from the top side of the model domain because channel axis drift—an inherent behavior in the underlying meandering model—can cause asymmetric erosion patterns.

The ability of vector-based bank-material tracking to represent the kinematics of channel migration in an environment with large bank strength contrasts, and without imparting inadvertent lateral erosion thresholds, opens a number of opportunities for

understanding the evolution of bedrock landscapes. Vector-based material tracking could enable the incorporation of physical models of channel width and meandering dynamics into larger-scale landscape evolution models. Consequently, the long-term behavior of different channel evolution models could be directly evaluated without the confounding effects introduced by grid-based bank-material representation. At a larger scale, the influence of channel migration on bedrock valley width and the formation of strath terraces [e.g., *Finnegan and Dietrich*, 2011] can be more accurately ascertained with vector-based bank-material tracking. Finally, links between external drivers—including climate, tectonics, and base-level—and large-scale channel characteristics such as sinuosity [*Stark et al*., 2010] and entrenchment [*Harden*, 1990] can be more rigorously evaluated.

5.4. Floodplain evolution with a bank height-dependent channel lateral migration rate

In the preceding case studies, erodibility differences result from differences in bank material composition. Here we assess a scenario in which bank materials are uniform, but bank height sets the local erodibility [e.g., *Lancaster*, 1998; *Parker et al*., 2011]. Figure 8 shows topography formed by a channel that migrates laterally and deposits overbank sediment over 1000 years, with a maximum lateral erosion rate of 1 m/yr, a constant deposition rate (η) of 10 mm/yr, and a spatially varying deposition rate of 3 mm/yr at the channel bank (D_s) with a decay length scale (λ) equal to 4 channel widths. For simplicity, meander cutoff loops are assumed to instantaneously fill completely with sediment. We consider a case in which lateral channel migration is independent of bank height (Fig. 8A) and, similar to *Lancaster* [1998], a case in which lateral channel migration rates vary inversely with bank height scaled to channel depth (Fig. 8B) as

$$E_L^{'} = E_L\left(\frac{z - z_{channel}}{h}\right)^{-1}, \quad (12)$$

where $z_{channel}$ is the local elevation of the channel bed. Equation 12 is applied so that bank height can only reduce lateral erosion rate (i.e., cases with $(z - z_{channel})/h < 1$ do not cause lateral erosion rate to increase). The channel bed is set to aggrade at a constant rate equivalent to the aggradation rate at a distance of 4 channel widths from the channel (i.e., the *e*-folding distance for distance-dependent overbank deposition) (Eq. 9). Consequently, the levee tops aggrade faster than the channel bed. Levee growth is paced by the competition between overbank deposition that builds the levees and lateral channel migration that causes the channel to erode existing levees and shift the locus of deposition. This causes spatial differences in bank height that modulate channel lateral migration rates.

Both cases show a highly sinuous channel that has undergone meander bend growth and cutoff, and cutoff loops are preserved in the floodplain topography, similar for example to the Sacramento River, California, USA [*Constantine and Dunne*, 2008]. Although both cases start with the same planform channel geometry, the modulation of lateral channel migration rate by bank height in Figure 8B causes the channel trajectories to diverge. Because topographic evolution is governed by channel scour and overbank deposition, these different channel lateral migration patterns result in differing topography. In both cases, topographic profiles (Fig. 8C) show higher elevations near the active channel and abandoned channel segments in cutoff loops because overbank sedimentation declines with distance from the channel (Eq. 9).

These simulations demonstrate that while the vector-based method emphasizes tracking the planform extent of the channel, it is also flexible to reconstruct floodplain

topography due to overbank deposition—even though floodplain elevations are not explicitly stored in memory during the simulation (see Section 4). Moreover, unlike a grid-based formulation for tracking topography, which applies the same overbank deposition rate across the area of an entire grid cell, the vector-based approach allows calculation of the exact local elevation during the simulation and hence more precise topographic tracking. Such precise tracking is needed when, for example, local differences in bank height alter channel lateral migration rates (Eq. 12) or the quantity of sediment entrained from the eroding bank [e.g., *Parker et al*., 2011].

6. Discussion

Model results using the grid- and vector-based bank-material tracking schemes should converge in the limit of high grid resolution (Eq. 7), because when the grid cells are small enough to record all bank migration there is no threshold for updating bank-material properties. To assess the degree to which grid-based model predictions approach a vector-based prediction as grid resolution increases, we analyze the landscape area altered by bank migration in each time step using the channel trajectory from Figure 5A-C. Figure 9 shows the mean bank area updated in each time step using grids of different resolutions, normalized by the value for the vector-based approach. These simulations demonstrate that the mean area updated using the grid-based approach asymptotes to the value for the vector-based approach when small non-dimensional grid resolutions are computationally feasible.

The case studies presented herein demonstrate that a framework that couples meandering to bank-material evolution is free of resolution dependence when the active

channel bank and the topography itself are represented in vector form. Given memory constraints which limit the practical resolution of grid-based methods, the vector-based framework is advantageous in landscapes with high variability in bank strength, which may occur in depositional environments with variable grain sizes and in net-erosional landscapes with mixed bedrock and sediment banks. Simulations show the new framework to be flexible to track meander belt topographic (Fig. 5 and 8) and stratigraphic evolution (Fig. 6), and channel incision (Fig. 7). Phenomena not discussed here—such as asymmetric channel cross-sections and overbank deposition with different grain sizes—could also be incorporated using vector-based techniques.

Bank migration simulations involving grids are more likely to be resolution-independent for cases of constant bank resistance, and for cases where the characteristic bank migration distance in one time step is larger than the cell width. In the vector-based scheme presented here, bank-material properties are determined by computations based on stored data (e.g., interpolation of past channel longitudinal profiles to determine elevation). In contrast, when the memory cost is feasible, grid-based frameworks eliminate some computation time because bank-material properties are directly accessed. Therefore in cases, computation time may be an important subsidiary consideration in selecting a method for bank-material tracking, particularly when algorithms for reconstructing erodibility are complex.

The traditional grid-based approach remains efficient for sediment routing approaches to modeling fluvial systems [*Coulthard and Van De Wiel*, 2006; *Karssenberg and Bridge*, 2008], particularly those dominated by braiding [*Murray and Paola*, 1994],

in which channel banks are ephemeral. Consequently, connecting vector-based and grid-based frameworks for topographic representation may represent an important next step in advancing landscape evolution modeling for meandering channels. In such a framework, grid elements could continue to represent hillslopes as in current landscape evolution models [e.g., *Tucker et al.,* 2001], and to route sediment within active channels. Vector elements would be used to track sharp discontinuities in elevation or bank-material composition related to channel migration, as presented here, as well as drainage divides because their precise locations are often between grid nodes [*Castelltort et al.*, 2012]. The cut-cell method [*Beyer and LeVeque*, 1992], which temporarily slices cells crossed by a boundary, could also be used with an Eulerian grid to represent hillslopes. In this way, an extended time series of bank advance could be used to create a complex valley boundary shape within a rectangular grid [*Udaykumar and Shyy*, 1995; *Udaykumar et al.*, 1996, 1999]. As with using an adaptive mesh to track moving boundaries, however, using the cut-cell technique could be computationally intensive [*Udaykumar et al.*, 1999]—in this case because sediment fluxes would have to be tracked across cells with complicated geometries.

Although the examples explored here only involve river channels, the vector-based framework for bank-material tracking could be applied to any environment in which bank-material properties interact with a channel. Potential applications include channels formed by sediment in tidal, deltaic, and submarine environments, as well as and channels in which thermodynamic processes are important. For example, channels formed by lava and supraglacial channels evolve largely based on heat fluxes, which determine the spatial

distribution of freezing and melting [*Parker*, 1975; *Kerr*, 2001; *Karlstrom et al*., 2013]. As these channels migrate, they may reset the local temperature field, just as river channels alter topography as they migrate, which implies interaction between channel migration and bank-material properties. Vector-based channel extent tracking could be useful for recording the kinematics of these channels.

The similarities between subaerial rivers and submarine channels formed by turbidity currents suggest more direct applications of the present framework. In deposits formed by submarine channels, the spatial distribution of grain size is determined by channel migration and aggradation [*Sylvester et al*., 2011]. Cohesive fine-grained sediments [*Panagiotopoulos et al*., 1997] may inhibit channel migration, as suggested for clay plugs in subaerial oxbows [*Fisk*, 1947; *Allen*, 1982; *Ikeda*, 1989]. While grid-based methods exist for tracking stratigraphy formed by meandering channels [e.g., *Clevis et al*., 2006], such methods would be susceptible to grid resolution-scale erosion thresholds. Therefore the vector-based approach could advance modeling of channel-bank interactions for stratigraphic development.

7. Conclusions

Grid-based models are commonly applied to representing the evolution of bank-material properties in environments shaped by channel migration. However, simulation results are highly resolution-dependent when there are large differences in bank strength, and when the characteristic bank migration distance is less than one grid cell width. We have developed a new, vector-based framework for representing bank-material properties that extends existing vector-based approaches and does not have the problem of resolution-

dependence found in grid-based techniques. For areas the channel has migrated across, bank-material properties are reconstructed using vector-based channel geometric data. This approach can treat sloping longitudinal profiles, overbank deposition, and stratigraphic development, and may be adapted to a variety of environments in which channel migration interacts with topography or stratigraphy. This enables more accurate modeling of the co-evolution of channels and bank-material properties, particularly where there are large contrasts in bank strength.

Case studies show that erodibility differences due to bank-material properties or bank height can strongly influence the co-evolution of channels and the surrounding topography and stratigraphy. Oxbow-filling sediments that are less erodible than other floodplain sediments can narrow the width of meander belts and stacked channel deposits; grid-based methods may artificially enhance this narrowing effect if the grid resolution is coarse. A simulation of meandering river evolution in a bedrock valley indicates that meandering kinematics and patterns of valley widening respond strongly to bank strength differences between bedrock and sediment; grid-based methods can artificially restrict valley widening by implicitly imposing a threshold to update bank properties. Finally, simulations suggest that elevation differences due to spatial variations in overbank deposition across a floodplain strongly influence channel trajectory and floodplain topography when the channel lateral migration rate responds to bank height.

Acknowledgments

This work was supported by the Department of Defense through the National Defense Science and Engineering Graduate Fellowship (NDSEG) Program and NSF grant

EAR-1147381 to MPL. We thank Noah Finnegan, Antoine Lucas, Edwin Kite, and Vamsi Ganti for helpful discussions, and Nicole Gasparini and three anonymous reviewers for their valuable comments.

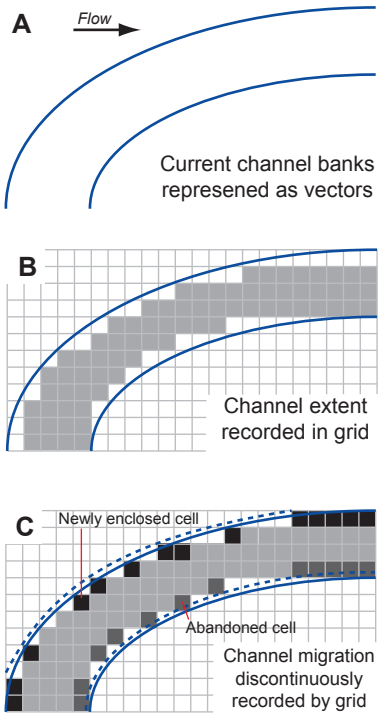

Figure 1. A commonly used technique for representing bank-material properties in models of landscape evolution with a migrating channel. **(A)** The channel boundary is represented explicitly by vectors. Arrow indicates general flow direction for all panels. **(B)** The plan view channel extent is recorded by mapping the bank locations onto a grid, which may represent topography or material composition and is altered during channel migration. Cells fully contained within the channel extent are shaded light gray. **(C)** When the channel banks shift (dashed lines), some cells are abandoned (medium gray) while other cells become enclosed by the channel (black). The process of updating the grid is spatially discontinuous, such that bank migration is not fully recorded with the grid.

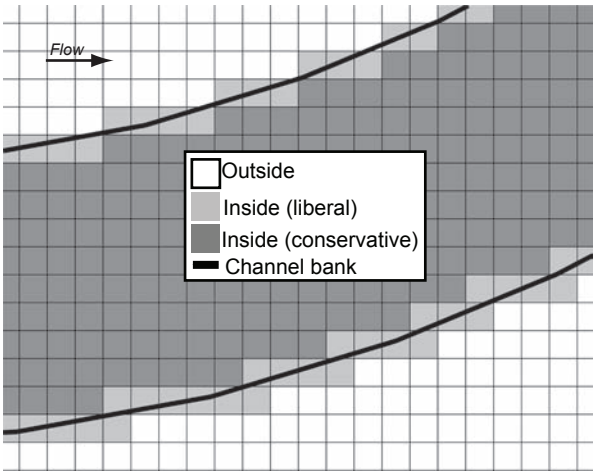

Figure 2. Comparison of rules for determining which grid cells are considered inside the channel banks, after *Howard* [1996]. Dark shaded cells are completely within the channel, meeting the conservative in-channel definition. Light shaded cells meet the conservative and liberal definitions, for which any cell partially traversed by the bank is also considered within the channel. Arrow indicates general flow direction.

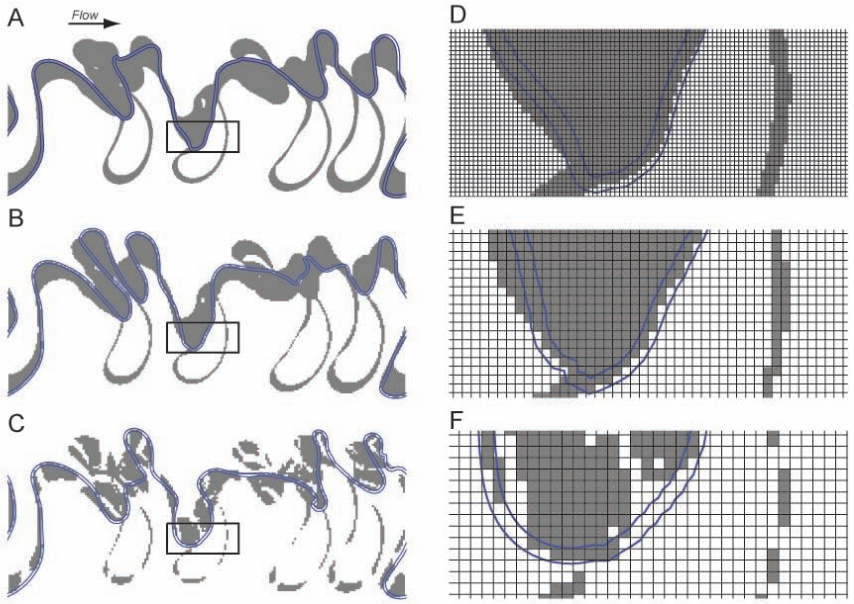

Figure 3. Simulations of a meandering river using grid-based bank-material tracking. Channel banks are indicated in blue; areas that have been visited by the channel, as recorded by the grid, are mantled with sediment and shaded gray. Bedrock is 20 times more resistant to erosion than sediment. Arrow in (A) indicates general flow direction for all panels. Boxes in **A-C** indicate respective extents of **D-F**. Topography and bank composition are recorded using rectangular grids with cell widths of (**A**) 7 meters, **(B)** 14 meters, and (**C**) 18 meters. Channel width is 25 meters. The area visited by the channel changes dramatically as a function of grid resolution, with all other parameters held constant. Panels **D-F** show the detailed relationship between the final channel bank vectors and the grids.

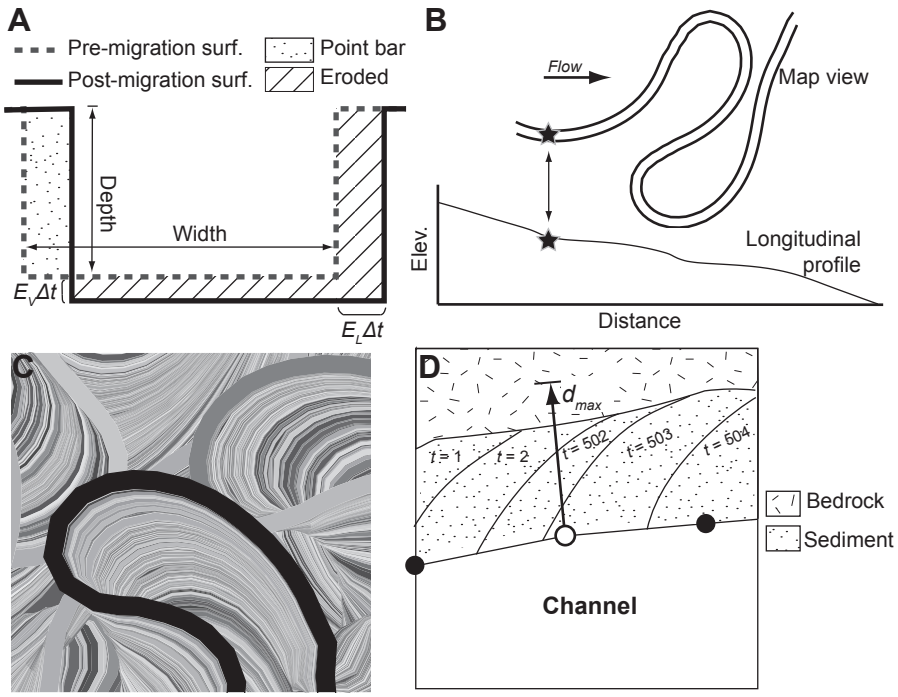

Figure 4. The new, vector-based method for erodibility and topography tracking. **(A)** Lateral channel migration and vertical incision of a rectangular channel during one time step is viewed in cross-section. Dashed line indicates the pre-migration surface. During each time step, the channel cross-section is shifted laterally and vertically to form the post-migration surface (thick black line) and erode material from the bed and cutbank (hatched area). In order to maintain constant channel width, point bar sediment (dotted area) is deposited over the abandoned surface with a thickness equal to the channel depth. **(B)** The channel map view extent and longitudinal profile from each time step are used to reconstruct bank-material properties. **(C)** After subsequent iterations, the pattern of channel scour is recorded by the current channel extent (black polygon) and the collection of abandoned channel-extent polygon remnants preserved from earlier in the simulation, with channel extents shaded to highlight their different formation times. **(D)** Map view of the bank-material inspection procedure. A meandering model is used to calculate the maximum centerline migration distance (d_{max}) assuming the most erodible bank material. A test vector with length equal to d_{max} is extended perpendicular to the cutbank node and is used to identify regions with different bank-material properties and adjust the actual migration distance accordingly. In this example, the test vector encounters sediment-mantled surfaces from different time steps (t = 503, 502, and 2, in order) followed by a bedrock valley wall.

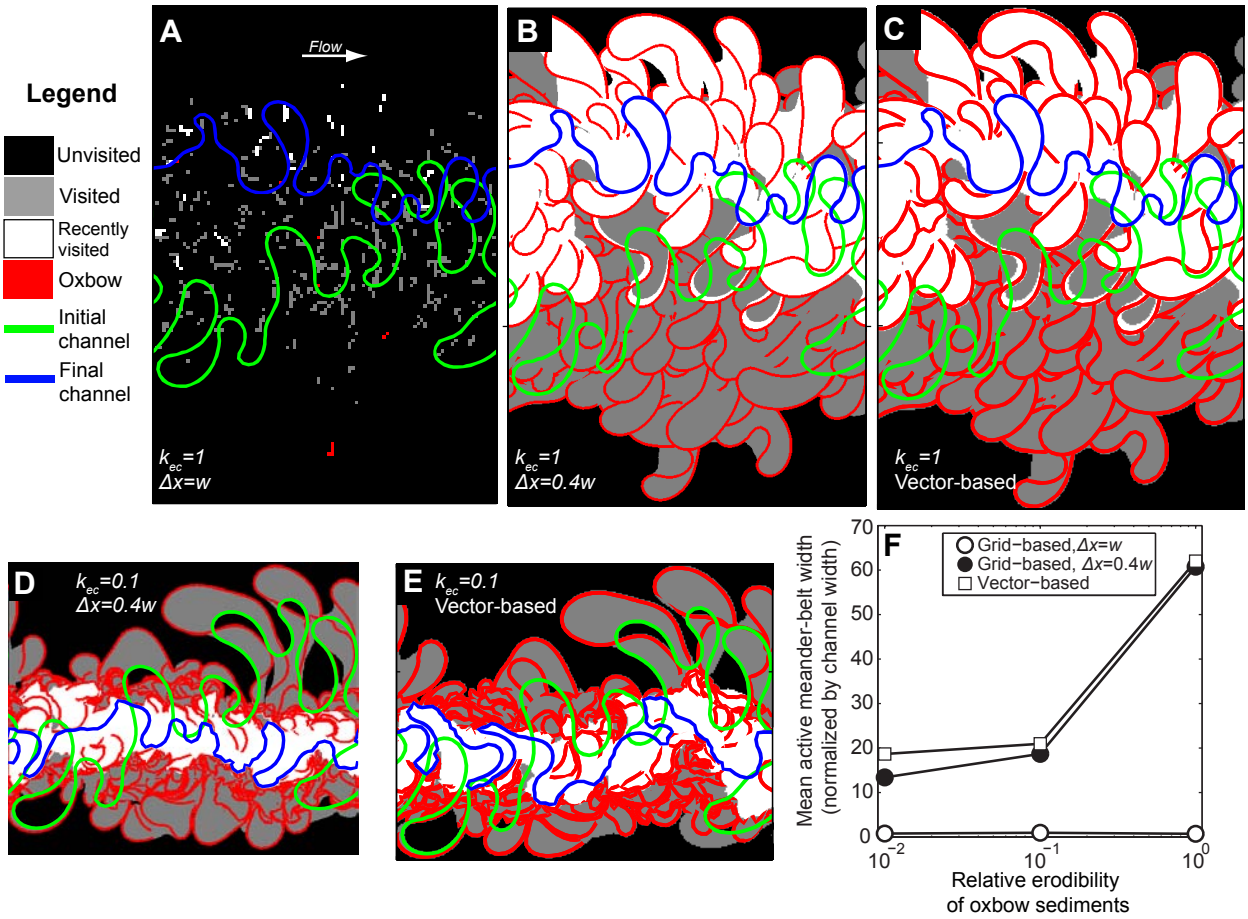

Figure 5. Meander-belt evolution with variable erosion susceptibility for meander cutoff loops (k_{ec}) relative to point bar sediment. Panels A-E are at the same scale; their width is 100w. In all simulations, Δt = 2 yr, simulation time is 1000 yr, w = 25 m, and h = 1 m. Areas recorded as visited by the channel are shaded gray (first 90% of simulation time) and white for recently visited areas (last 10% of simulation time). Unvisited areas, as recorded in the grid- or vector-based tracking schemes, are black. Initial (green) and final (blue) channel extents are indicated, as are remnants of oxbow sediments (red). Panels **(A-C)** represent the case of k_{ec} = 1, i.e., constant bank composition. **(A)** The coarse grid resolution ($\Delta x = w$) results in small area recorded as visited. Arrow indicates general flow direction for all panels. **(B)** With a finer grid resolution ($\Delta x = 0.4w$), the visited area more closely resembles that using vector-based tracking **(C)**. Panels **(D-E)** represent k_{ec} = 0.1, i.e., erosion resistant material stored in cutoff loops. **(D)** Grid-based case, with $\Delta x = 0.4w$. **(E)** Vector-based case. **(F)** Mean active meander-belt width (normalized by channel width, w), versus the relative erodibility of oxbow sediments (k_{ec}) for grid- and vector-based schemes.

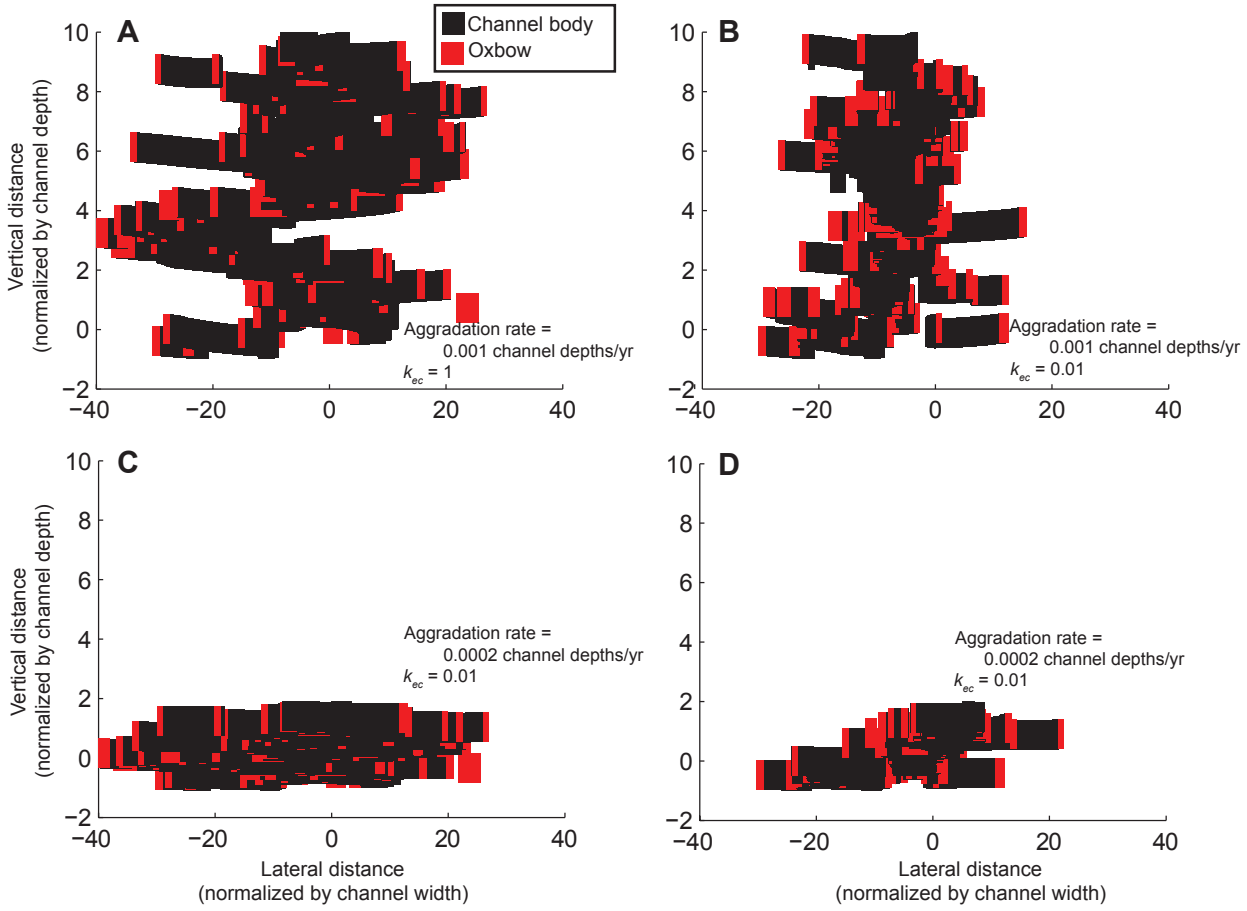

Figure 6. Cross-valley cross-sections of stratigraphy formed by an aggrading, meandering channel. As the channel migrates it deposits channel body material (black) and distinct sediments in oxbows (red). Other overbank deposits, not shown, accumulate at a rate sufficient for the channel to remain confined, and have a material strength equal to that of channel body material. For all simulations, w = 25 m; h = 1; the maximum lateral migration rate is 1 m/yr for erosion of channel body deposits; Δt = 2 yr; and simulation time is 10 kyr. Vertical axes are scaled to channel depth and horizontal axes are scaled to channel width. k_{ec} is the relative erodibility of oxbow sediments. **(A)** Fast aggradation (0.001 channel depths/yr), k_{ec} = 1. **(B)** Fast aggradation, k_{ec} = 0.01. **(C)** Slow aggradation (0.0002 channel depths/yr), k_{ec} = 1. **(D)** Slow aggradation, k_{ec} = 0.01.

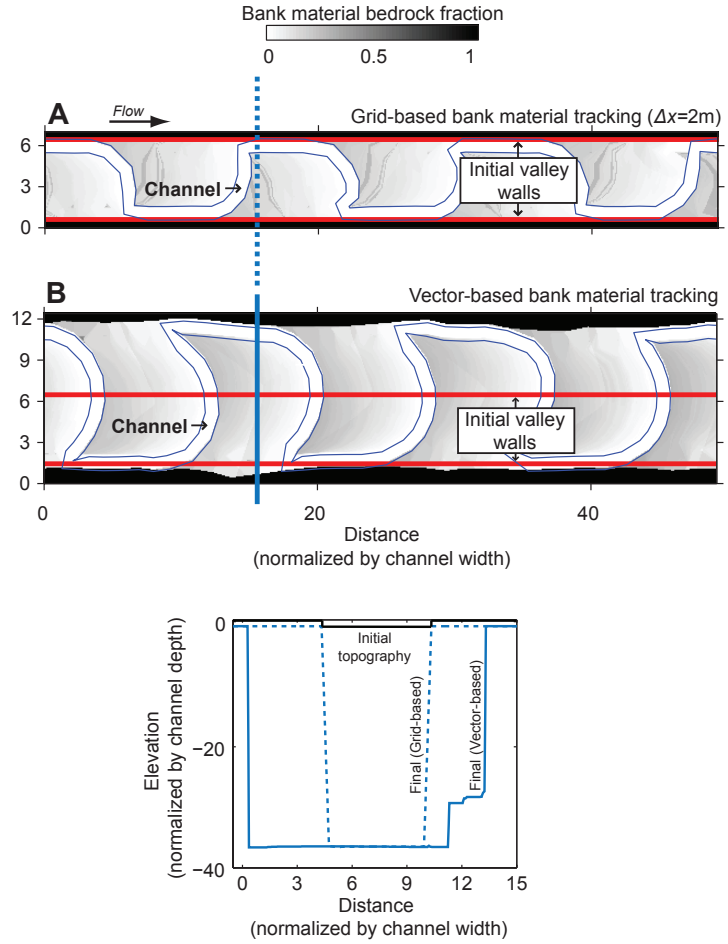

Figure 7. Valley widening in a bedrock landscape using grid-based and vector-based bank-material tracking. Active channel banks in (A) and (B) are shown with thin blue lines. In both cases, Δt = 2 yr, simulation time is 40 kyr, the maximum lateral erosion rate in bedrock is 1 cm/yr, the maximum lateral erosion rate in sediment is 1 m/yr, E_v = 1 mm/yr at the outlet, w = 25 m, h = 1 m, and the initial valley width is approximately 5w. Initially the bank material within the valley floor is entirely sediment above the local elevation of the channel bed, and entirely bedrock below this elevation, such that the channel banks are all sediment. The channel bed begins entrenched one channel depth below the land surface. The valley walls are composed entirely of bedrock and initially have the same surface elevation as the valley floor. The fraction of bedrock in bank material, as sensed locally by the channel, is calculated by comparing the bedrock elevation to the bed elevation of the nearest point on the channel. Distance is normalized by the channel width, and elevation by the channel depth. **(A)** The simulated landscape using grid-based bank composition tracking, with Δx = 2 m, shows no valley widening. Arrow indicates general flow direction for both panels. **(B)** Simulated topography using vector-based approach. Valley width more than doubles during the simulation because all bank advances beyond the initial valley wall extent are recorded. **(C)** Cross-sections of the initial topography of both simulations (black line) and the final topography for the grid-based (dashed blue line) and vector-based (solid blue line) simulations.

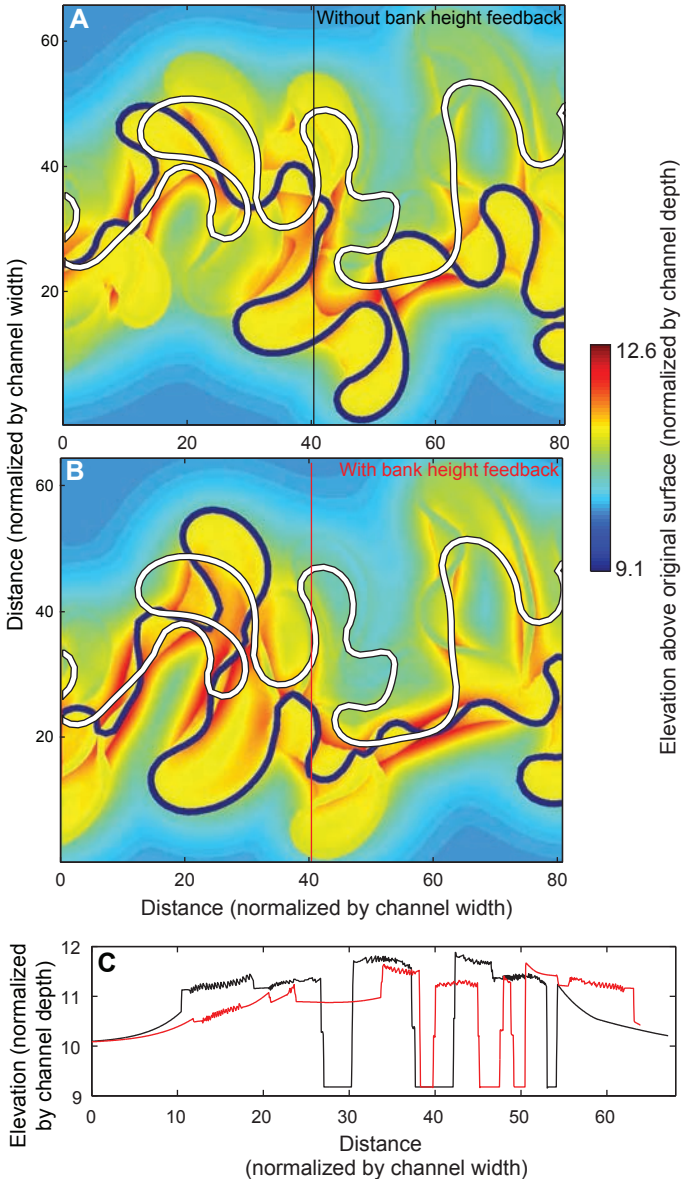

Figure 8. Simulated landscapes formed by channel migration and floodplain deposition. Elevation above the original surface is normalized by channel depth; distance is normalized to channel width. Sediment accumulates by overbank deposition, with constant and exponential decay terms (Eq. 10). Simulation parameters are a maximum lateral erosion rate of 1 m/yr, η =10 mm/yr, D_s = 3 mm/yr, and $\lambda = 4w$. Arrow indicates general flow direction. The white trace indicates initial channel planform geometry; the active channel is in dark blue. Topographic profiles run from top to bottom in panels (A) and (B). **(A)** Topography when channel lateral migration rate is insensitive to bank height. **(B)** Topography when channel lateral migration rate varies inversely with bank height. **(C)** Topographic profiles for the case without the bank height feedback (black) and with the feedback (red).

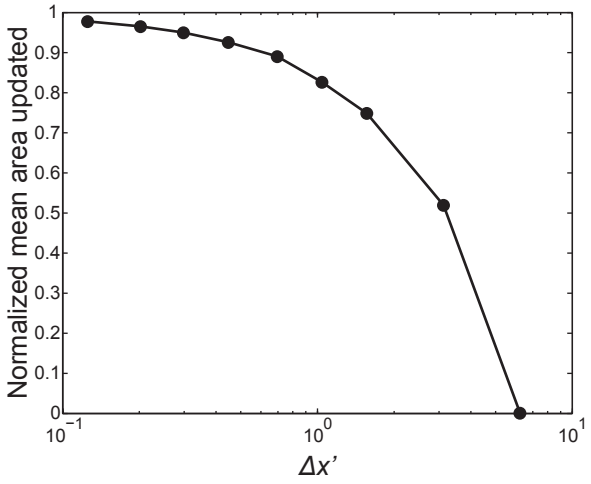

Figure 9. Bank area updated for the same channel trajectory as in Fig. 5A-C, but with variable grid resolution. The mean area updated by the channel banks in a single time step, normalized by the value for vector-based bank material tracking, is plotted for a range of non-dimensional grid cell widths ($\Delta x' = \Delta x/(E_L \Delta t)$). The finest resolution corresponds to a dimensional cell width of 0.5 meters. The area updated asymptotes to the value obtained using vector-based bank-material tracking.

Chapter 3: Numerical simulations of bedrock valley evolution by meandering rivers with variable bank material

Originally published in:
Limaye, A. B. S., and Lamb, M. P., 2014, Numerical simulations of bedrock valley evolution by meandering rivers with variable bank material, Journal of Geophysical Research – Earth Surface 119, doi:10.1002/2013JF002997.

Abstract

Bedrock river valleys are fundamental components of many landscapes, and their morphologies—from slot canyons with incised meanders to wide valleys with strath terraces—may record environmental history. Several formation mechanisms for particular valley types have been proposed that involve changes in climatic and tectonic forcing, but the uniqueness of valley evolution pathways and the long-term stability of valley morphology under constant forcing are unknown, and are not predicted in existing numerical models for vertically incising rivers. Because rivers often migrate more rapidly through alluvium than through bedrock, we explore the hypothesis that the distribution of bank materials strongly influences river meandering kinematics and can explain the diversity of bedrock river valley morphology. Simulations using a numerical model of river meandering with vector-based bank-material tracking indicate that channel lateral erosion rate in sediment and bedrock, vertical erosion rate, and initial alluvial-belt width explain first-order differences in bedrock valley type; that bedrock-bound channels can evolve under steady forcing from alluvial states; and that weak bedrock and low vertical incision rates favor wide, shallow valleys, while resistant bedrock and high vertical incision rates favor narrow, deep valleys. During vertical incision, sustained planation of the valley floor is favored when bedrock boundaries restrict channel migration to a zone of thin sediment

fill. The inherent unsteadiness of river meandering in space and time is enhanced by evolving spatial contrasts in bank strength between sediment and bedrock and can account for several valley features—including strath terraces and underfit valleys—commonly ascribed to external drivers.

1. Introduction

The morphology of bedrock-floored river valleys is diverse. For example, deep slot canyons host highly sinuous channels (Fig. 1A); wider mountain valleys include floodplains and stepped strath terraces (Fig. 1B); confining valleys with relatively small width variations contain rivers that bend sharply at the valley walls (Fig. 1C); and wide, low-sloping valleys can resemble alluvial river valleys (Fig. 1D). The origin of such different valley types is a longstanding question in Earth surface science, and valley topography is commonly used to reconstruct channel kinematics [*Shyu et al*., 2006; *Cook et al*., 2009; *Finnegan and Dietrich*, 2011; *Finnegan and Balco*, 2013] and to infer drivers of landscape evolution including climate [*Molnar et al*., 1994; *Hancock and Anderson*, 2002; *Pan et al*., 2003], tectonics [*Lavé and Avouac*, 2000], and sea level [*Merritts et al*., 1994; *Blum and Tornqvist*, 2000]. Understanding channel-valley interactions is an important consideration for stream restoration [*Wohl et al*., 2005], especially in mountainous environments. Beyond Earth, valleys and valley networks are the most widespread indicators of fluid flow on the surfaces of Mars [*Baker*, 2001] and Titan [*Burr et al*., 2013], and thus represent rare constraints on past and present climate. Linking valley type to channel hydrology and geomorphology, however, remains a significant challenge.

Although bedrock river valleys are key to landscape evolution, the diversity of

valley types has not been explained quantitatively. Pulses of channel vertical incision have been argued to generate specific valley types, including deep and sinuous canyons (e.g., Fig. 1A) [*Davis*, 1893] and broader valleys with flights of strath terraces [e.g., *Gilbert*, 1877; *Hancock and Anderson*, 2002; *Pan et al*., 2003; *Finnegan and Dietrich*, 2011]. Other studies suggest rock strength as an important control on valley width [*Harden*, 1990; *Montgomery*, 2004; *Shyu et al*., 2006; *Barbour*, 2008; *Finnegan and Dietrich*, 2011].

Despite these important studies, there are several major unknowns in how different valley types evolve. First, it is unclear whether changes in vertical incision rate are necessary to form particular valley types, or whether similar valleys can form under steady vertical incision rates. More generally, it is unknown whether multiple forcing mechanisms can lead to a particular bedrock valley type. Second, while previous work has suggested that vertical incision rate, lateral erosion rate, and bank strength may control valley topography, the relative importance of these independent variables has not been quantified. Third, it is unknown whether the different valley types observed in nature are stable, even under steady forcing, or whether they are transient. This distinction is vital for interpreting valley types for the history of river vertical incision—and by extension, the influences of tectonics, climate, and base-level on landscape evolution.

Bedrock river valleys evolve over millennial timescales, making it difficult to measure their dynamics directly [*Hancock and Anderson*, 2002; *Montgomery*, 2004]. Consequently, numerical experiments offer important means for testing controls on valley evolution. Numerous landscape evolution models have been used to explore river valley evolution, and have reproduced valley features including strath terraces [*Hancock and*

Anderson, 2002; *Finnegan and Dietrich*, 2011], meander bends that deform against valley walls [*Howard and Knutson*, 1984; *Howard*, 1992, 1996; *Sun et al*., 1996], and meandering rivers with banks of different heights in uplifting mountain landscapes [*Lancaster*, 1998]. No model, however, reproduces the full diversity of bedrock river valley forms from incised meanders to wide valleys with terraces (Fig. 1). Moreover, many larger-scale landscape evolution models represent valleys at scales too coarse to include valley evolution by lateral channel migration [*Howard et al*., 1994; *Braun and Sambridge*, 1997].

Previous work on alluvial river floodplain development has shown that variable bank strength that evolves in response to channel migration can strongly control channel kinematics and meander-belt width [*Howard*, 1996; *Sun et al*., 1996]. Based on this insight, we hypothesize that bank strength that evolves dynamically in concert with river meandering is the key ingredient to explain the diversity of bedrock river valleys. For example, in narrow valleys with resistant bedrock walls (e.g., the San Juan River valley, Utah; Fig. 1A), and wide valleys with weak bedrock walls (e.g., the Colorado River valley, Texas; Fig. 1D), the consistency of channel bank materials results in meandering forms seemingly insensitive to valley geometry; rather, the bank materials control channel and valley evolution rates. In contrast, in intermediate-width valleys with large contrasts in bank strength between valley floor sediments and valley walls, channel migration is strongly influenced by bank strength, and meanders bend sharply at valley walls due to differential migration rates between the valley interior and margins (e.g., the Beaver River valley, Alberta, Canada; Fig. 1C).

We aim to test the dynamic bank-strength hypothesis as follows. In Section 2, we

describe our specific modeling objectives and identify potential controls on valley evolution. In Section 3, we describe the numerical framework used to model meandering channels and track bank-material properties. In Section 4, we explore valley-type transitions under constant forcing. In Section 5, we explore examples of valley-type transitions by pulses of vertical incision, which represents the kinematics of vertical incision driven for example by changes in sediment supply [e.g., *Hancock and Anderson*, 2002]. In Section 6, we assess the ability of the numerical model to reproduce the observed bedrock river valley types, and discuss implications for inferring valley evolution in Section 7.

2. Modeling goals and hypotheses

Our modeling goal is to test the null hypothesis that the diversity of bedrock valley types can be explained without changes in external forcing that modulate channel vertical incision rate, but rather through the co-evolution of channel lateral migration and bank strength under a constant vertical incision rate, as would correspond to a steady-state longitudinal profile undergoing tectonic uplift [e.g., *Merritts et al*., 1994]. Although climate and tectonics likely force pulses in vertical incision rates in nature [e.g., *Molnar et al*., 1994; *Whipple and Tucker*, 1999; *Hancock and Anderson*, 2002; *Yanites et al*., 2010], it is important to understand the potential diversity of valley forms that can arise from intrinsic meandering dynamics as a baseline. Intrinsic dynamics may occur because as a channel migrates laterally, it can erode bedrock along the cutbank and channel bed, and deposit sediment along the trailing bank, thus converting bedrock to sediment. Since channel migration rates are commonly faster in alluvium than in bedrock, this process should

enhance lateral migration rates, relative to those in intact bedrock, in areas where the channel has previously visited. Bank materials are also affected by vertical incision rates because vertical incision lowers the channel bed with respect to the sediment-bedrock interface, and thus favors bedrock exposure in the banks. Hence we hypothesize that the competition of river lateral and vertical erosion determines the alluvial-belt width within a valley and the first-order valley topography.

In order to test this hypothesis, we construct the simplest possible model that can incorporate channel lateral migration and vertical incision, while tracking the spatial distribution of bedrock and sediment. In our model, the proportion of bedrock and sediment in the channel banks modulates channel lateral migration rates. We seek to balance the complexity inherent in river valley evolution—including meandering dynamics and evolving bank-material properties—with model simplicity in order to make predictions over 10^4-year timescales. We also seek to explain first-order differences in valley type in a generic way with as few controlling parameters as possible, which include time, bank strength, channel vertical incision rate, and the initial valley topography. A variety of other factors can influence channel geometry and evolution within valleys, including sediment supply [e.g., *Sklar and Dietrich*, 2001], channel slope [e.g., *Stark*, 2006; *Finnegan and Dietrich*, 2011], uplift rate [e.g., *Lavé and Avouac*, 2001; *Finnegan et al*., 2005; *Amos and Burbank*, 2007; *Yanites and Tucker*, 2010], discharge variability [e.g., *Turowski et al*., 2008; *Stark et al*., 2010], and channel substrate [e.g., *Ferguson*, 1973; *Finnegan et al*., 2005]. For example, a rapid decrease in channel width due to changes in uplift rate would transform the abandoned portions of the channel bed into strath terraces [*Lavé and Avouac*,

2001]. Here we exclude these diverse factors in order to isolate the how meandering with evolving bank strength alone influences valley evolution.

A variety of channel meandering and bank evolution models exist, and their computational costs correspond to their complexity in representing factors including bed topography, hydraulics, and bank strength. Because significant computational costs are required for tracking bank-material properties over geologic timescales [*Limaye and Lamb*, 2013a], we employ a relatively simple and often-utilized meandering model [*Howard and Knutson*, 1984] that imposes a fixed channel width and assumes erosion driven by channel curvature while still reproducing fundamental meandering kinematics [*Howard and Hemberger*, 1991]. Numerical models of river meandering are largely untested over geologic timescales [*Seminara*, 2006], but models with different degrees of complexity converge statistically for evolution beyond the stage of initial bend cutoff [*Camporeale et al*., 2005].

Although knickpoints can be important drivers of channel vertical incision [e.g., *Wobus et al*., 2006a; *Finnegan and Dietrich*, 2011], here we focus on constant and spatially uniform channel vertical incision, which will be shown to produce a wide range of valley types. The main difference between our work and most previous work is that we focus on the emergent, unsteady patterns of lateral migration for vertically incising rivers with evolving bank strength. Our approach is new because numerical experiments that account for differing channel migration rates within valleys and at their boundaries have been limited to cases with imposed geometries [*Tucker et al*., 2001], or without meandering [*Hancock and Anderson*, 2002] or channel vertical incision [*Howard and Knutson*, 1984;

Howard, 1992, 1996; *Sun et al*., 1996]. Models that link meandering and vertical incision [*Lancaster*, 1998; *Finnegan and Dietrich*, 2011] have not incorporated evolving, mixed bedrock and alluvial bank materials.

We define the channel as the zone of active sediment transport (of width w_c and depth h_c) that migrates laterally within a valley. We have identified seven characteristic parameters that we hypothesize control the geometry and kinematics common to mixed bedrock-alluvial, meandering channels and their valleys, irrespective of the detailed mechanics of erosion and deposition. These are the lateral erosion rate in bedrock (E_{Lb}) and sediment (E_{Ls}), the vertical incision rate into a bedrock bed (E_v), channel width (w_c), initial alluvial-belt width (w_{ab}), channel depth (h_c), and the total simulation time (t) (Table 1). Using dimensional analysis, these seven parameters can be recast as five key dimensionless parameters: the dimensionless simulation time

$$t^* = \frac{tE_{Ls}}{w_c} \tag{1a}$$

is the total simulation time normalized by the time to erode laterally one channel width in sediment; the dimensionless vertical incision rate with sediment banks

$$E_{Vs}^* = \frac{E_V w_c}{E_{Ls} h_c} \tag{1b}$$

is the characteristic time to erode one channel width in sediment normalized by the characteristic time to erode one channel depth; the corresponding dimensionless vertical incision rate with bedrock banks is

$$E_{Vb}^* = \frac{E_V w_c}{E_{Lb} h_c} . \tag{1c}$$

We select these two non-dimensional vertical incision rate parameters to explore distinct regimes of channel migration in the simulations. E_{Vs}* reflects the competition between lateral channel mobility in sediment banks that actively bevels the bedrock-sediment interface, and vertical incision that drives the channel toward entrenchment in bedrock. In comparison, E_{Vb}* reflects the competition of lateral and vertical erosion in bedrock that should determine the evolution of valley topography if the channel has primarily bedrock banks. The channel width-to-depth ratio is

$$w_c^* = \frac{w_c}{h_c}, \tag{1d}$$

and is fixed at 25 in our simulations. This value is representative of alluvial meandering channels for moderate valley slopes [e.g., *Parker*, 1976] and within the observed range for bedrock-alluvial rivers [*Yanites and Tucker*, 2010].

All simulations begin with a simple initial landscape condition: the channel is inset one depth in a level plane. All topography develops during the simulations as the channel simultaneously incises vertically and migrates laterally. The initial bank strength is locally set to represent either bedrock or sediment banks. To do this, we establish an initial zone of sediment fill one channel depth in thickness, such that the channel banks are composed entirely of sediment within this zone (Fig. 2D), but the area's lateral margins and the channel bed are entirely bedrock. In cross-section, the channel bed rests on a bedrock surface that extends across the valley and is mantled with sediment. Subsequent channel migration planes off the bedrock surface to the channel bed elevation and emplaces sediment through point-bar accretion. To explore the influence of initial channel confinement on valley evolution, we vary the width of the initially sediment-

mantled zone, which we call the initial alluvial-belt width (w_{ab}). We define a non-dimensional initial alluvial-belt width (w_{ab}*)

$$w_{ab}^{*} = \frac{w_{ab}}{w_{uab}}, \quad (2)$$

where w_{uab} is a representative unconfined alluvial-belt width, defined as the maximum lateral distance (perpendicular to valley direction) between channel segments when the channel evolves without confinement by bedrock (Fig. 2B). When $w_{ab}^{*} = 0$ there is no initial alluvial belt, so the channel begins fully entrenched in bedrock. When $w_{ab}^{*} = \infty$, the initial alluvial belt is infinitely wide and the channel banks are composed entirely of sediment. We explore these cases as well as cases with $0 < w_{ab}^{*} < 1$, where there is a pre-established alluvial belt whose width is less than the unconfined width (Fig. 2D).

We track the evolution of valley topography by calculating the valley aspect ratio

$$w_{v}^{*} = \frac{w_{v} - w_{c}}{h_{v}}, \quad (3)$$

where h_v is the median depth of the valley and w_v is the median valley width measured at the top of the valley. All areas lower than the elevation of the initial planar surface belong to the valley. In simulations that begin with low initial alluvial-belt confinement, the channel may initially sweep across a wide area before the influences of vertical incision rate and bedrock erodibility are expressed. In order to better characterize the typical valley width maintained during the simulation, we only consider topography that forms after the first channel depth of vertical incision (when the total incision exceeds one depth). Numerical experiments are designed to systematically vary the five controlling dimensionless parameters (Eq. 1, 2) and to track valley morphology and aspect ratio (Eq.

3).

3. Model formulation

In this section we describe methods for simulating meandering channel evolution, with bank strength feedbacks and vertical incision, over geologic timescales. We then detail procedures for setting the initial channel and alluvial-belt configurations.

3.1. Meandering model implementation

In the single-thread meandering channel model of *Howard and Knutson* [1984], the channel centerline migration rate responds to local and upstream-integrated curvature

$$R_1(s) = \Omega R_o(s) + \frac{\Gamma \int_0^{\xi_{max}} R_o(s-\xi) G(\xi) d\xi}{\int_0^{\xi_{max}} G(\xi) d\xi}, \quad (4)$$

where R_1 is the dimensionless local migration rate, s is the centerline node index, ξ is the upstream distance, and $R_o = (r/w_c)^{-1}$, where r is the local centerline radius of curvature and w_c is channel width. Ω and Γ are fixed dimensionless parameters set to -1 and 2.5, respectively, and control the relative influence of local (Ω) and upstream (Γ) curvature [*Ikeda et al.*, 1981]. The numerator in equation 4 is a convolution integral of curvature with a weighting function

$$G(\xi) = e^{-(\frac{2kC_f}{h_c})\xi}, \quad (5)$$

where k =1 [*Ikeda et al.*, 1981], h_c is the channel depth, and C_f is a dimensionless friction coefficient set to 0.01 after *Stølum* [1996]. Although channel hydraulics are not explicitly modeled, the friction coefficient reflects the downstream decay of velocity perturbations induced by local channel geometry. The dimensionless lateral migration rate is scaled

according to the local lateral erosion rate constant (k_e, with dimensions LT^{-1}) and domain-averaged channel sinuosity (μ) to yield the dimensional lateral erosion rate

$$E_L = k_e R_1 \mu^{\varepsilon} \quad (6)$$

where $\varepsilon = -2/3$ [*Howard and Knutson*, 1984]. Therefore lateral channel erosion rates, which are increased by high planform curvature of mature meander bends, are moderated as channel sinuosity increases.

The channel is assigned a rectangular cross-section with fixed dimensions; the width and depth represent bankfull values. Consequently, the time step is fixed at two years to represent a typical recurrence interval of the bankfull discharge for an alluvial river [*Leopold and Wolman*, 1960]. While floods with longer recurrence intervals may play a more important role in setting channel width in bedrock landscapes with large thresholds for sediment entrainment [*Baker*, 1977; *Hartshorn et al*., 2002; *Turowski et al*., 2008], there is considerable uncertainty in the appropriate adjustment timescale for bedrock rivers [*Tinkler and Wohl*, 1998] and the channel bed and banks may evolve on different timescales due to bed sediment cover effects [*Lague*, 2010]. In rivers with mixed bedrock and alluvial banks the adjustment timescale may be closer to that for alluvial rivers, therefore we fix the time step irrespective of the degree of channel entrenchment in bedrock.

We seek to vary the channel vertical incision rate as an independent parameter, which is commonly on the order of 0.1-1 mm/yr in tectonically active environments [*Montgomery*, 2004]. Slope breaks in meandering channel longitudinal profiles are a natural consequence, however, of bend growth and cutoff, and have been hypothesized to

influence vertical incision rates [e.g., *Stark*, 2006; *Finnegan and Dietrich*, 2011]. To control the vertical incision rate for a sloping channel would then require static knickpoints [*Seidl and Dietrich*, 1992] that would increasingly dominate the channel longitudinal profile with each cutoff. Therefore we set the channel slope to zero, which prevents knickpoint formation. Likewise, slope across the model domain is initially set to zero so that model landscape elevations can be measured with respect to the uniform channel elevation. The zero-slope assumption implies that model results for valley evolution should approach those for low-sloping rivers, except for modulation of vertical incision rates by slope reduction and knickpoint formation.

Neck cutoffs occur when the channel banks impinge upon themselves, and chute cutoffs are omitted in the model [e.g., *Sun et al*., 1996; *Lancaster*, 1998; *Finnegan and Dietrich*, 2011]. Overbank deposition is also omitted, except to fill in meander loops abandoned by cutoff [e.g., *Sun et al*., 1996; *Finnegan and Dietrich,* 2011], which is assumed to occur instantaneously. A periodic boundary condition is employed so that portions of the channel that drift outside the downstream edge of the model domain enter the upstream edge, and vice-versa. Consequently, the channel axis is free to wander about the model domain and the curvature integration (Eq. 4) is not affected by the domain boundaries.

3.2. Bank-material tracking

We track two classes of material: channel/floodplain sediments and bedrock. The local lateral erosion rate constant in Eq. 6 takes on distinct values in cases where the bank materials are entirely sediment ($k_e = k_s$) or entirely bedrock ($k_e = k_b$); these values represent

the effects of sediment and bedrock strength on bank migration. Channel lateral migration rates for alluvial rivers often exceed several meters per year, with large variations between reaches [e.g., *Nanson and Hickin*, 1986; *Hudson and Kesel*, 2000]. For lateral migration in bedrock banks, rates rarely exceed a few cm/yr even for weak sedimentary rocks [*Montgomery*, 2004]. Although channel-widening processes in mixed bedrock-alluvial channels are a topic of active research [*Montgomery*, 2004; *Finnegan et al*., 2005; *Stark*, 2006; *Wobus et al*., 2006b; *Yanites and Tucker*, 2010], the influence of stratified sediment and bedrock on lateral erosion rates is relatively unconstrained [*Howard*, 1992]. In the simulations we track the depth of sediment cover, and for simplicity the local bank erodibility is scaled according to the local fraction of bedrock (f_b) in the bank material, measured from the channel bed to the bankfull elevation

$$k_e = k_s (1 - f_b) + k_b f_b. \quad (7)$$

This fraction represents the amount of bedrock that would be exposed by the channel banks if the channel were to migrate to that portion of the landscape without further vertical incision. The bank-material bedrock fraction is useful for visualizing the width of the alluvial belt that is conducive to relatively rapid channel lateral migration.

Most existing approaches to modeling the co-evolution of meandering channels, floodplains, and valleys use grids to represent factors that may influence bank migration rates, such as topography [*Lancaster*, 1998] and bank-material susceptibility to erosion [*Howard*, 1996; *Sun et al*., 1996]. Grid-based bank-material tracking, however, can implicitly impart thresholds for channel migration when bank strength varies spatially; this inadvertently suppresses lateral erosion as a result of numerical artifacts [*Limaye and*

Lamb, 2013a]. Consequently, we employ a new, vector-based method for bank-material tracking that more faithfully captures the kinematics of channel migration driven by an underlying meandering model without the resolution effects of grid-based approaches [*Limaye and Lamb*, 2013a]. This method uses the time history of channel planform and longitudinal profile geometry to reconstruct bank-material properties and topography in areas influenced by channel migration, and thus avoids losses in geometric information commonly incurred from mapping the channel banks onto a relatively coarse grid. The vector-based method is particularly advantageous in scenarios with large differences in bank strength, as is commonly the case when comparing bedrock and sediment bank materials.

Depending on the process of bank erosion, increasing bank height could inhibit lateral migration by requiring removal and transport of more sediment [*Hickin and Nanson*, 1975; *Lancaster*, 1998; *Seminara*, 2006; *Parker et al*., 2011b], which can be incorporated into our model framework [*Limaye and Lamb*, 2013a]. However, here we make the lateral erosion rate independent of bank height to focus on the effect of bank strength.

3.3. Initialization of alluvial-belt width and channel planform geometry

We wish to explore a range of initial alluvial belt widths, from $w_{ab}^* = 0$ to ∞, to which the channel is initially confined. As a result, the same sinuous channel centerline cannot be used to begin all simulations because in some cases the channel would extend beyond the initial alluvial belt. Therefore we develop an initialization procedure that produces a channel that is sinuous but confined to an initial alluvial belt of arbitrary width. As a preliminary step, we empirically determined a representative unconfined alluvial-belt

width from a set of 50 simulations. In each, the channel had sediment banks and grew from an initially straight channel centerline seeded with meter-scale random noise (Fig. 2A) for a fixed non-dimensional simulation time ($t^* = 500$, equivalent to $t = 25$ kyr for $w_c = 50$ m and $E_L = 2$ m/yr for example) to allow the channel to mature through several cycles of meander bend growth and cutoff. The mean unconfined alluvial-belt width ($w_{uab} = 2538$ m), measured perpendicular to the mean flow direction (Fig. 2B), was used in subsequent simulations.

The model initialization phase establishes a realistic geometry for the channel where it meets confining bedrock walls by first evolving the channel within the alluvial belt bounded by non-erodible walls, and without vertical incision (Fig. 2C). When $0 < w_{ab}^* < \infty$, the meander bends can deform against the non-erodible walls but do not advance beyond them. At the end of the initialization phase ($t^* = 500$), the channel planform geometry is recorded and used to begin the main simulation. The model time starts at $t^* = 0$, and the non-erodible walls are replaced with erodible bedrock walls (Fig. 2D).

Meandering channel planform evolution is highly sensitive to initial geometry [e.g., *Frascati and Lanzoni*, 2010], and we have found this behavior is reinforced by strong feedbacks between meandering and bank strength. The channel trajectory in turn determines the pattern of erosion within the valley. Therefore, we assess the sensitivity of final valley aspect ratio to initial conditions by running the simulations for each unique set of parameter values in triplicate, each time with a different initial, sinuous planform geometry reflecting different noise in the channel centerline used during the simulation initialization phase.

4. Controls on bedrock valley type under constant forcing

We begin this section by exploring independently the influence of non-dimensional simulation time (t^*), initial alluvial-belt width (w_{ab}^*), and vertical erosion rate with sediment banks (E_{Ls}^*) and bedrock banks (E_{Vb}^*) on the evolution of meandering rivers in bedrock valleys. The channel dimensions are fixed at w_c = 50 m and h_c = 2 m. In Section 4.5, we introduce a method for objectively classifying valley type and summarize results for a suite of simulations that span a wide parameter space in the non-dimensional variables.

4.1. Temporal evolution

In this section, we analyze the evolution of a meandering river and its bedrock valley for a baseline simulation to which we will compare results from other simulations. The chosen parameters fall in the mid-range of parameters explored in this study (E_{Vb}^* = 0.5; E_{Vs}^* = 0.005, w_{ab}^* = 0.5), which correspond to a river with moderate bedrock erodibilty, vertical incision rate, and initial alluvial-belt confinement. In subsequent sections we perturb this base case by fixing the non-dimensional simulation time ($t^* = tE_{Ls}/w_c$; Eq. 1a) and varying one of the other non-dimensional parameters in order to isolate its influence on model results. Figure 3 shows the shaded relief of the land surface for the base case at different times, where the coloration indicates the local fraction of bedrock versus alluvium in the bank materials. We vary t^* from 0 to 1000 (Movie 1 in Supplementary Material), which corresponds to timescales up to tens of kyr for alluvial rivers with widths of 10-100 meters.

At the beginning of the simulation ($t^* = 0$; Fig. 3A), the river is sinuous and laterally mobile, and bends at sharp angles where it meets bedrock walls. Sediment with thickness equal to the channel depth is distributed across the uniform-width alluvial belt. As time advances, this simulation shows major reductions in short-wavelength ($\leq 15w_c$) channel sinuosity and average alluvial-belt width. We observe the following sequence involving the interplay of lateral channel migration and vertical incision, which leads to channel autogenic entrenchment in bedrock. Channel bends tend to sweep in the downstream direction, as is commonly observed in nature in the absence of bank strength differences [*Howard*, 1992]. Despite its initial mobility, the channel sweeps laterally across the valley in an uneven manner because of the spatial variability in local channel curvature and lateral erosion rates. With ongoing vertical incision, this unsteady channel lateral migration results in spatial variations in the fraction of bedrock in bank materials (Fig. 3B). The downstream limb of a meander bend tends to plane off the bedrock-sediment interface in advance of the arrival of the upstream limb, so that the cutbank of the upstream limb commonly encounters bank materials with low bedrock fractions. Conversely, the cutbank on the downstream limb encounters areas with heterogeneous bank strength due to irregular channel sweeping (Fig. 3B), though no bank materials within the initial alluvial belt are all bedrock (i.e., $f_b < 1$). Because the upstream bend limb encounters uniformly weak bank materials along the cutbank, but the downstream limb encounters bank materials with a range of strengths along the cutbank, the downstream limb eventually propagates more slowly than the upstream limb. The upstream limb catches up with the downstream limb, causing a neck cutoff (Fig. 3C).

Thus, the frequency and locations of cutoffs evolve with the changing fraction of bedrock in bank material.

This cutoff mechanism does not occur at the same time for all bends, and so the channel is straighter in some reaches than others. As the channel continues to incise, bends encounter local bedrock constrictions (i.e., f_b =1) (Fig. 3D). These constrictions strongly inhibit the downstream movement of downstream bend limbs, resulting in more cutoffs (Fig. 3E). Eventually, cutoffs remove so much low-wavelength sinuosity ($\leq 15w_c$) that the diminished curvature causes channel lateral migration to stall, even while the banks are largely sediment in some locations (Fig. 3F). In the absence of continued channel lateral migration, the sediment-bedrock interface is no longer lowered across a broad alluvial belt, so continued vertical incision causes the low-sinuosity channel to become more entrenched locally in bedrock (Fig. 3G). These results suggest a pathway for channel entrenchment that can occur without a pulse of vertical incision—but that instead emerges through the interplay of channel meandering and vertical incision in a mixed bedrock-alluvial valley.

This baseline simulation also indicates that the valley type observed for a set of model parameters depends on the time of observation. Valley types that are seemingly stable, such as those with partially confined alluvial belts (Fig. 3A-C), can abruptly change in planform morphology due to the interaction of irregular lateral migration with vertical incision, resulting in a change in channel entrenchment state (Fig. 3G). Given this inherent instability in valley type, in subsequent model comparisons we fix the time of observation to t^* = 1000. This is sufficient time for the fastest-migrating bends to migrate laterally against sediment banks a total distance of approximately 1000 channel widths. For w_c = 50

m and E_{Ls} = 2 m/yr, for example, this is equivalent to t = 25 kyr.

4.2. Non-dimensional initial alluvial-belt width (w_{ab}*)

In this section we isolate the influence of non-dimensional initial alluvial-belt width (w_{ab}* = w_{ab}/w_{uab}; Eq. 2) on valley type by exploring the full range of possible initial alluvial-belt widths while holding other model parameters fixed at the values for the baseline case (t* = 1000; E_{Vb}* = 0.5; E_{Vs}* = 0.005). As defined in Figure 2, the alluvial belt is a region of uniform-width sediment fill, with thickness equal to the channel depth, and represents the zone in which the channel can initially migrate against entirely sediment banks. Figure 4 shows simulation results for initial alluvial-belt widths of w_{ab}* = 0 (a bedrock plain with a channel inset by one depth), 0.75 (a region of alluvium one channel deep, with a finite width), and ∞ (a broad blanket of alluvium one channel deep across the entire domain).

For w_{ab}* = 0 (Fig. 4A), the sinuous channel is initially surrounded by fully bedrock banks. As a result, meander bends largely migrate into bedrock for the entire simulation, leaving sediment-mantled slip-off surfaces behind them. In the time allowed, three bends migrate to the point of reaching cutoff. The valley cross-section shows that much of the valley remains entirely bedrock, similar to the valley cross-section topography of the San Juan River (Fig. 1A), for example, except for a greater prevalence of slip-off surfaces and cutoff loops in the model case.

For w_{ab}* = 0.75, the sinuous channel is initially partially confined and deforms against the valley walls. As the system evolves, channel migration becomes confined to an ever-narrower portion of the valley (Fig. 4B; Movie 2 in Supplementary Material) because the channel does not sweep laterally frequently enough to bevel the bedrock-sediment

interface to the level of the incising channel bed. Consequently, the channel encounters a significant fraction of bedrock in the banks except in areas recently visited by the channel. The alluvial-belt width at $t^* = 1000$ varies across the model domain (Fig. 4B). Within the valley, the channel is sinuous in places but deforms strongly against areas with all-bedrock banks. If the channel were to frequently sweep across the entire alluvial belt, it would bevel the valley floor to a consistent elevation and would not leave any terraces, but incomplete sweeping of the alluvial belt during vertical incision causes the abandonment of sediment-mantled bedrock surfaces as strath terraces. After 5 depths of vertical incision, the channel occupies a narrow valley floor ($< 10w_c$) filled with alluvium.

For $w_{ab}^* = \infty$ (Fig. 4C; Movie 3 in Supplementary Material) the full model domain is mantled with sediment to one channel depth. The channel initially wanders across a large area, but lateral migration slows dramatically because the channel does not sweep across the same portion of the model domain frequently enough to plane off the bedrock-sediment interface across the broad initial alluvial belt. Areas of low bank bedrock fraction are largely restricted to slip-off surfaces, and like the case with $w_{ab}^* = 0.75$ (Fig. 4B), there are widespread terraces. The channel planform retains sinuosity at long wavelengths ($> 15w_c$) but has low sinuosity at shorter wavelengths, which reduces lateral erosion rates. The valley cross-section shows the extent of the initial sediment cover preserved at the edges of the model domain, but interestingly the channel ends the simulation largely bound in bedrock, similar to the case with $w_{ab}^* = 0$. As a more straightforward consequence of initial alluvial-belt dimensions, the valley aspect ratio shows that wider valleys form when w_{ab}^* is

larger (Fig. 4D) because the initial sediment banks enable widespread channel migration (Fig. 4C).

The most surprising result from comparing simulations that vary the initial alluvial-belt width is that channels that begin with partially confined alluvial belts ($w_{ab}^* = 0.75$; Fig. 4B) are able to maintain mobility in sediment banks more than channels that begin with either no alluvial belt ($w_{ab}^* = 0$; Fig. 4A) or one of infinite width ($w_{ab}^* = \infty$; Fig. 4C). A partially confined alluvial belt steers the channel to frequently plane off the bedrock-sediment interface over a narrow zone, which ensures that the bank materials there are largely sediment. The alluvial-belt boundaries are eroded into arcs with wavelengths that are longer than that of a free meander bend (Fig. 4B), reflecting bend deformation and translation parallel to the boundaries. If there is no initial alluvial belt, the bank-material properties initially exert no control on the spatial pattern of erosion, only the rate of planform evolution. Consequently, the channel laterally migrates over significant distances before it re-occupies an area where it has planed off the bedrock and emplaced sediment. The bank bedrock fraction therefore remains high throughout the simulation. On the other hand, a channel that begins with an infinite-width alluvial belt can initially migrate freely over a wide swath of the model domain, with no steering of channel migration by alluvial-belt boundaries. The channel cannot plane off this entire area frequently enough to stave off an increase in entrenchment due to ongoing vertical incision, and the channel eventually reaches a less mobile, bedrock-bound state resembling that in the $w_{ab}^* = 0$ case.

In subsequent sections we fix the non-dimensional initial alluvial-belt width to an intermediate value ($w_{ab}^* = 0.5$), which produces a partially confined state. Simulations with

partially confined initial alluvial belts generally allow greater variety in valley state after $t^* = 1000$ than simulations with either non-existent or infinitely wide initial alluvial belts.

4.3. Non-dimensional vertical incision rate with sediment banks (E_{Vs}*)

In the next set of simulations, we vary the non-dimensional vertical incision rate with sediment banks ($E_{Vs}^* = (E_V w_c)/(E_{Ls} h_c)$; Eq. 1b) while fixing other model parameters to their baseline values ($t^* = 1000$; $E_{Vb}^* = 0.5$; $w_{ab}^* = 0.5$). The initial channel and alluvial belt geometries are similar to those at $t^* = 0$ for the baseline case (Fig. 3A). We vary E_{Vs}^* from 0.001 to 0.01, reflecting a range in dimensional vertical incision rates from a low of 0.08 mm/yr (i.e., a slowly uplifting continental interior environment) to a high of 0.8 mm/yr (i.e., an active orogen) for our scaled river example (i.e., $w_c = 50$ m, $h_c = 2$ m). E_{Vs}^* should control the tendency of the channel to plane laterally and maintain an alluvial belt versus incise vertically and entrench in bedrock, and so is relevant when channels encounter a large fraction of sediment in the banks. E_{Vb}^* is explored in the next section and should dictate valley topography for largely bedrock-bound channels.

Figures 5A-C show map views of topography and local bank-material bedrock fraction for increasing values of E_{Vs}^*. Overall, as E_{Vs}^* increases, channel sinuosity, alluvial-belt width, and valley width decline, and meander bends more commonly encounter valley walls. For a relatively small value of E_{Vs}^* (0.001; Fig. 5A; Movie 4 in Supplementary Material), the channel is able to maintain a consistently wide alluvial belt compared to the baseline case (Fig. 3G) because the channel incises minimally during lateral migration and a low bank bedrock fraction is maintained across the valley. Meander bends curve smoothly in sediment-filled areas, but turn sharply where the channel meets resistant

bedrock walls near the top edge of the model domain. The valley cross-section shows only slight variation in the depth to bedrock. For a moderate value of E_{Vs}* (0.005; Fig. 5B), meander bend amplitude at short wavelengths ($\leq 15w_c$) is reduced, and the valley width indicated by the topographic contours varies considerably. The valley cross-section shows that the total depth of incision is larger than in Figure 5A because of the higher vertical incision rate. For large values of E_{Vs}* (0.01; Fig. 5C), the amplitude of long-wavelength bends ($> 15w_c$) is also reduced. The valley cross-section shows a stranded surface from the initial alluvial belt, and the deeply bedrock-bound channel. The valley aspect ratio (Fig. 5D) declines sharply as E_{Vs}* increases because of increased channel entrenchment in bedrock, which limits valley widening during vertical incision.

4.4. Non-dimensional vertical incision rate with bedrock banks (E_{Vb}*)

Figure 6 shows results of simulations in which the vertical incision rate with bedrock banks ($E_{Vb}^* = (E_{Vb}w_c)/(E_{Ls}h_c)$; Eq. 1c) is varied while fixing other parameters to their baseline values ($t^* = 1000$; $E_{Vs}^* = 0.005$; $w_{ab}^* = 0.5$). The initial channel and alluvial-belt geometry is similar to that at $t^* = 0$ for the baseline case (Fig. 3A). We vary E_{Vb}* from 0.05 to 5 by using a range of dimensional bedrock lateral erosion rates from 2 mm/yr (i.e., highly resistant lithologies) to 20 cm/yr (poorly consolidated valley fill sediments).

For $E_{Vb}^* = 0.05$ (Fig. 6A), a broad valley forms and the channel maintains its short-wavelength sinuosity ($\leq 15w_c$) because the channel can substantially erode bedrock valley walls even in a bedrock-entrenched state. The topographic cross-section highlights the breadth of the alluviated zone as well as unpaired terraces of variable widths. For $E_{Vb}^* = 5$ (Fig. 6B), the alluvial-belt width varies widely. As was the case for previous simulations,

local suppression of channel migration by bedrock banks led to further reduction in channel sinuosity and increased entrenchment in bedrock. The valley aspect ratio (Fig. 6C) declines as E_{Vb}* increases because higher E_{Vb}* favors channel vertical incision over lateral channel migration in bedrock. More scatter exists in the valley aspect ratio than for w_{ab}* and E_{Vs}* because in the present simulations the valley widened during both the transient period in the beginning of the simulation when the channel had alluvial banks (as occurred in previous cases, including Fig. 3A-3C) and during the bedrock-entrenched phase when the bedrock was relatively weak (Fig. 6A). Thus, E_{Vb}* explains the most variance in valley aspect ratio when the channel consistently has largely bedrock banks.

The bank strength contrast, which we define as the ratio of bedrock lateral erosion rate to sediment lateral erosion rate (equivalent to k_s/k_b in Eq. 7), co-varies with both the dimensionless vertical incision rate with sediment banks (E_{Vs}*) and the corresponding rate with bedrock banks (E_{Vb}*). The primary effect of the bank strength contrast is that for a valley with an alluvial belt of significant width, low bank strength contrast causes smoothly curved meander bends (Fig. 6A, k_s/k_b = 10), whereas high bank strength contrast causes meander bends to deform strongly at the margins of the alluvial belt (Fig. 5B, k_s/k_b = 100).

4.5. Summary of model predictions for valley type

Here we analyze simulations that span a phase space in the variables t*, w_{ab}*, E_{Vs}*, and E_{Vb}*, in order to systemmatically assess controls on bedrock river valley type. In all cases, the parameters that are not systematically varied are set to values employed in the baseline simulation.

The morphology of bedrock river valleys spans the examples shown in Figure 1.

These include deep, narrow canyons (e.g., San Juan River valley; Fig. 1A) and valleys with local floodplain and strath terrace development and channel confinement (e.g., Mattole River valley; Fig. 1B); valleys with relatively uniform floodplain widths and pronounced bend deformation against valley walls (e.g., Beaver River valley; Fig. 1C); and broad, low-relief valleys with relatively little meander bend deformation (e.g., Colorado River valley; Fig. 1D). We find that quantitatively, these four valley types also fall into different ranges of the valley aspect ratio ($w_v^* = (w_v - w_c)/h_c$; Eq. 3). Type 1 valleys are distinguished by their narrow width relative to depth ($w_v^* < 50$). Type 2 valleys are slightly wider for the same depth ($50 \leq w_v^* < 100$). Type 3 valleys ($100 \leq w_v^* < 150$) have a greater median depth than type 2 valleys of the same width. Finally, type 4 valleys ($w_v^* > 150$) are widest with respect to their depth. We select quantitative bounds for these ranges based on visual inspection. The bounds separating these valley types are arbitrary, and some simulations yield topography consistent with two valley types—but the classification technique is consistent, quantitative, and reveals the major trends in valley type.

Figure 7A shows results for a phase space of simulations in E_{Vs}^* and E_{Vb}^*. The majority of each set of three simulations with the same parameters but different initial channel planform geometries yields a consistent valley type, but in some cases different valley types develop because strong feedbacks between meandering and bank strength strongly shift the distribution of erosion across the valley. Where valley types differ within a simulation set, only two valley types occur and they fall in neighboring classification ranges of w_v^*. Differences in valley type are most strongly controlled by E_{Vb}^*. At low values of E_{Vb}^* (< 0.16), only the most expansive (type 3 and 4) valleys form, because

lateral channel migration in bedrock is rapid relative to the rate of vertical incision so valley widening can keep pace with channel vertical incision even when the banks are largely bedrock. At higher values of E_{Vb}* (> 0.16), only narrower, deeper (type 1 and 2) valleys form, because lateral channel migration in bedrock is slower relative to the rate of vertical incision. The trend of decreasing valley aspect ratio for increasing E_{Vb}* holds for all values of E_{Vs}*, which indicates that the ratio of channel lateral erosion in bedrock to vertical erosion is more important than the corresponding ratio for channel lateral erosion in sediment. E_{Vb}* dictates valley aspect ratio because, although the channel begins each simulation with sediment banks within the initial alluvial belt, the channel transitions to a state with a majority of all-bedrock banks except for low values of E_{Vs}*. When E_{Vs}* is low (0.005-0.01), channel entrenchment in bedrock is less likely and on average the channel can more broadly plane off the bedrock-sediment interface (e.g., Fig. 5A). As a result, for fixed E_{Vb}* wider valleys (higher w_v*) form at the lowest values of E_{Vs}*. In contrast, when E_{Vs}* is high (> 0.01), the channel bed lowers much faster than the average bedrock-sediment interface and channel evolution occurs largely with all-bedrock banks. In this case, the valley dimensions are more strongly influenced by the lower lateral erosion rate in bedrock and narrower valleys (lower w_v*) form.

Figure 7B shows results for simulations that span a phase space in E_{Vs}* and w_{ab}*. In general, low values of E_{Vs}* (≤ 0.0025) favor type 3 and 4 valleys because the rate of channel downcutting is slow with respect to lowering of the bedrock-sediment interface. For all values of vertical incision rate, valleys with larger w_v* are favored as the degree of initial alluvial-belt confinement decreases (increasing w_{ab}*) because the channel starts with

a higher degree of mobility in sediment banks that allows it to sweep a wider valley (Fig. 4). For all values of w_{ab}*, type 1 and 2 valleys are favored as E_{Vs}* increases because the channel cuts down faster with respect to the bedrock-sediment interface. The channel banks consequently include more bedrock, which slows valley widening. Only type 1 valleys form when there is no initial alluvial belt (w_{ab}* = 0) with moderate to high vertical incision rates (E_{Vs}* ≥ 0.0025), because the channel begins with entirely bedrock banks and cannot erode laterally fast enough to widen the valley significantly during downcutting.

Finally, Figure 7C shows the time evolution of simulations for different values of E_{Vs}*. In all cases the valley evolves to a new type, and transitions to narrower, deeper valley types occur more quickly as E_{Vs}* increases. Within each set of three simulations the valley type at the conclusion of the simulation (t* = 1000) is the same. The similarity in outcomes indicates that while the bedrock valley type observed can depend on the time, for the spin-up procedure utilized (Fig. 2) the detailed sinuous channel planform geometry does not exert a strong influence on the type of valley observed at a particular time. Rather, the channel vertical incision and lateral migration rates and initial alluvial-belt width are more important in determining the valley type at t* = 1000. The channel evolves from its initial state, and henceforth the evolution of the valley type depends on the relative rates of lateral and vertical erosion and on the spatial pattern of lateral erosion guided by the alluvial-belt geometry.

5. Valley-type transitions by pulses of vertical incision

While scenarios considered to this point have focused exclusively on cases of constant river vertical incision, a number of studies identify pulses of vertical incision as

important drivers of valley-type transitions. For example, rapid vertical incision relative to lateral channel migration is the key mechanism hypothesized by *Davis* [1893] for transforming a highly sinuous alluvial channel into a bedrock-bound channel with inherited sinuosity. Pulses of vertical incision may be driven by a host of external factors, including changes in the balance of water discharge and sediment supply due climate change [e.g., *Hancock and Anderson*, 2002], sea level fall [e.g., *Fisk*, 1944], tectonic uplift [e.g., *Yanites et al*., 2010], and potentially knickpoint propagation following meander cutoff [*Finnegan and Dietrich*, 2011]. Here, we relax the assumption of constant vertical incision employed in the simulations in Section 4 by comparison to example cases with pulses of vertical incision.

We first consider the effect of a vertical incision pulse less than the channel depth. We initialize a simulation with a partially confined meander-belt equivalent to the baseline case (w_{ab}* = 0.5), i.e., the channel is inset in alluvium with depth equal to the channel depth, with bedrock below and on the lateral margins of this sediment cover, and other model parameters (E_{Vb}* = 0.5 and t* = 1000) are equal to those in the baseline case. In this case, however, the channel also undergoes a spatially uniform pulse of vertical incision of $0.5h_c$ at the start of the simulation, which establishes a bank bedrock fraction of 0.5 throughout the model domain (Fig. 8A). At t* = 88 (Fig. 8B), the channel maintains high sinousity in a zone of low bank bedrock fraction within the boundaries of the initial alluvial belt, similar to the the corresponding time step for the baseline case with no vertical incision pulse (Fig. 3C). At t* = 1000 (Fig. 8C), in most places the channel has extremely low sinuosity at short wavelengths ($\leq 15\ w_c$) because it lost sinuosity in a manner similar to

the baseline case (Fig. 3G), and similarly the channel is entrenched in all-bedrock banks. These similarities with the baseline case suggest that pulses of vertical incision–-and by extension, changes in external forcing—must exceed a threshold in order to affect valley type.

In Figure 9, we simulate the response of a valley following an incision pulse equal to the channel depth for cases with relatively rapid (E_{Vb}* = 0.5; Fig. 9A) and relatively slow subsequent vertical channel incision (E_{Vb}* = 0.05; Fig. 9B). Other model parameters (t* = 1000; w_{ab}* = 0.5) are equal to those in Figure 8 and the baseline case, except E_{Vs}* which covaries with E_{Vb}* in this case. The simulations show that following the vertical incision pulse, the persistence of the sinuous channel's bedrock-bound state depends on the vertical incision rate. When the vertical incision rate is high, after the initial incision pulse the channel forms slip-off surfaces along the inside of meander bends (Fig. 9A), but the cutbanks along growing bends are entirely bedrock. In contrast, in the baseline case with no incision pulse (Fig. 3) terraces near the channel level illustrate that the valley took longer to reach a bedrock-entrenched state. Under a low vertical incision rate following the incision pulse, channel lateral migration is able to widen the valley quickly enough to form a continuous zone of largely sediment fill in which the channel is more mobile (Fig. 9B). The final alluvial-belt width is wider than in the baseline case (Fig. 3G). The different states of the two valleys that have undergone pulses of vertical incision show that while the bedrock-entrenched channel state at the start of the simulation is genetically related to the vertical incision pulse, the preservation of this geomorphic signal depends on the subsequent evolution of the channel under steady forcing.

6. Comparison to natural river valleys

To relate the model results to natural bedrock river valleys, we compare the valleys introduced in Figure 1 to summary model predictions for constant vertical incision cases. Because of the difficulty of reconstructing the initial alluvial-belt width of the channel, we focus the comparison on model predictions that fix the non-dimensional alluvial belt width but vary the vertical erosion rate and the lateral erosion rates in bedrock and sediment (Fig. 7A). We begin this section by briefly introducing the key attributes of four field sites that correspond to model inputs (Table 2). While all field sites may have undergone changes in climate and base-level that could influence their present valley type, here as in Section 4 we restrict our analysis to a constant-forcing framework that serves as a null hypothesis to more complex scenarios. Each river valley may have developed over longer timescales, but we compare each valley to model data with a dimensional simulation time of t = 25 kyr in order to test whether the constant-input model can reproduce the general valley types represented by each field case. Lateral migration rates for meandering rivers vary in space [*Hickin and Nanson*, 1975; *Hudson and Kesel*, 2000], and the meandering model employed yields a maximum migration rate approximately three times faster than the mean. Therefore where constraints for lateral erosion rate are available, they are assumed to be mean rates and are converted to maximum rates (E_{Lb}, E_{Ls}) by multiplying by a factor of three.

The San Juan River (southern Utah) is one of many sinuous channels incised in bedrock in the Colorado Plateau [*Harden*, 1990]. Geochronology data indicates a vertical incision rate of 0.11-0.21 mm/yr in the region averaged over the last several hundred thousand years [*Pederson et al*., 2002; *Wolkowinsky and Granger*, 2004; *Hanks and Finkel*,

2005]. Lateral erosion rate measurements are unavailable for the San Juan River, and are generally scarce for similar bedrock-bound rivers, but we estimate that the bedrock lateral erosion rate is an order of magnitude slower than rates of ~1 cm/yr estimated for rivers eroding weaker sedimentary rock [e.g., *Montgomery*, 2004; *Fuller et al*., 2009; *Finnegan and Dietrich*, 2011]. Taking 1 mm/yr as a mean lateral erosion rate in bedrock, this yields E_{Lb} = 3 mm/yr. From the average of 10 spot measurements in air photos, we estimate w_c = 53 m (bankfull) near Mexican Hat, Utah, and h_c = 2.1 m (assuming w_c/h_c = 25).

The Mattole River traverses a tectonically active region in coastal northern California. Dated strath terraces constrain the river vertical incision rate to 0.7-1.8 mm/yr over the last 12 kyr near Honeydew, CA [*Merritts et al*., 1994]. *Merritts et al*. [1994] argued that the Mattole's strath terraces—subparallel, closely spaced in elevation, unpaired, and with similar gradients to adjacent channel reaches—were formed by channel wandering with constant vertical incision. The lateral erosion rate in bedrock has been estimated at 13 mm/yr for the Eel River, California [*Fuller et al*., 2009b] and 6 mm/yr along the Smith River, Oregon [*Finnegan and Dietrich*, 2011], which also incise predominantly weak, fine-grained sedimentary rocks in similar climatic and tectonic settings. Based on these constraints we estimate a mean lateral erosion rate in bedrock of 10 mm/yr (E_{Lb} = 30 mm/yr) and E_V = 1 mm/yr. We estimate w_c = 102 m (bankfull) based on 10 spot measurements in air photos near Honeydew, CA, and h_c = 4.1 m (assuming w_c/h_c = 25).

The Beaver River crosses the plains east of the Canadian Rockies and regularly meets its valley walls at large angles [*Carson and Lapointe*, 1983; *Nicoll and Hickin*,

2010]. The long wavelength of the valley walls compared to the active meanders has been inferred to reflect a decrease in discharge following deglaciation [*Dury*, 1964]. *Nicoll and Hickin* [2010] reported a 3.5 m/yr maximum lateral erosion rate over a 48-yr interval based on air photo analysis. The regularity of meander geometry suggests that down-valley bend translation occurs much faster than valley widening [*Parker et al*., 1983], which we estimate as two orders of magnitude less than the maximum lateral erosion rate (3.5 cm/yr). Because the valley walls are alluvium rather than consolidated bedrock, the valley widening rate substitutes for E_{Lb} in the model framework. The channel width (h_c) is 44 m [*Nicoll and Hickin*, 2010] and we estimate h_c = 1.8 m (assuming w_c/h_c = 25). Based on the continental interior setting and lack of prominent terraces we estimate E_V = 0.1 mm/yr.

The Colorado River (Texas) flows through a low-relief valley composed of weak sedimentary bedrock, with a mixed bedrock-alluvial bed, between Austin and Columbus [*Baker*, 1977; *Baker and Penteado-Orellana*, 1977; *Blum and Aslan*, 2006]. Meandering rivers in the region have abandoned a series of strath terraces that extend inland ~250 km from the coast [*Baker and Penteado-Orellana*, 1977; *Blum and Valastro*, 1994]. Meanders throughout the Texas outer coastal plain evolve significantly on an annual timescale, with channel migration rates of several meters per year [e.g., *Wellmeyer et al*., 2005], but channel migration likely proceeds more slowly for inner coastal plain meanders incised in bedrock [*Stricklin*, 1961]. Based on stratigraphic data [*Baker and Penteado-Orellana*, 1977; *Blum and Valastro*, 1994], we estimate E_{Lb} = 5 cm/yr and E_V = 0.25 mm/yr over the last 20 kyr. Cross-section data from Austin indicate w_c = 275 m and h_c = 8 m for a 2-year flood before damming [*Blum*, 1992], which are taken as the bankfull dimensions.

Among the chosen field sites, only the Beaver River actively migrates in sediment banks, so we estimate E_{Vb}* for each river (Table 2) and compare these values to model predictions for valley type in Figure 7A. The estimated values of E_{Vb}* are relatively low for the Colorado River and Beaver River, and this portion of the model phase space uniformly predicts the formation of relatively broad and shallow (type 3 and 4) valleys. Similarly, the estimated values of E_{Vb}* are relatively high for the Mattole and San Juan Rivers, and correspond to a portion of phase space dominated by narrow and deep (largely type 1) valleys. These results suggest that the constant vertical erosion framework can reproduce the general trends in valley aspect ratio for the field sites, even without knowledge of the lateral erosion rate each river would exhibit in sediment banks. This result is consistent with E_{Vb}* operating as a key driver of valley type (Fig. 7A). Importantly, pulses of vertical incision are not required to explain the trend in valley aspect ratio for the field sites, implying that valley aspect ratio may not be a diagnostic indicator of vertical incision history.

7. Discussion

The modest number of independent variables explored here—channel lateral migration rates in sediment and bedrock, vertical erosion rate, and initial alluvial-belt width—can account for a wide range of observed bedrock valley types (Fig. 7) that cannot be reproduced without accounting for bank strength differences. In particular, without bank strength differences, the model can produce bedrock-bound meanders [e.g., *Finnegan and Dietrich*, 2011] and broad alluvial plains [e.g., *Howard*, 1996] like the San Juan and Colorado River valleys, respectively, but it cannot produce meander bends that deform

against valley walls nor confined alluvial belts, as occur in the Beaver and Mattole River valleys. Such bend deformation only occurs when a factor external to the channel locally slows channel migration with respect to neighboring reaches. Simulations confirm the central hypothesis that the co-evolution of channel lateral migration and bank strength under a constant vertical incision rate can determine the first-order geometry of bedrock river valleys.

Simulation results that span a range of channel lateral migration rates in sediment and bedrock, vertical incision rates, and initial alluvial widths (Fig. 7) allow reassessment of the hypotheses for bedrock river valley evolution posed in Section 1. We revisit whether valley type can be used to differentiate river vertical-incision scenarios, and whether valley types can be formed without abrupt pulses of vertical incision. In contrast, an alternate view is that particular bedrock valley types, and in particular deep, narrow valleys with sinuous channels or those with strath terraces, require pulses of vertical incision to form [e.g., *Gilbert*, 1877; *Davis*, 1893; *Hancock and Anderson*, 2002; *Pan et al*., 2003; *Finnegan and Dietrich*, 2011]. Simulations presented here suggest that a range of river vertical incision rates can result in an initially alluvial-banked channel becoming entrenched into bedrock (Fig. 7). Moreover, simulations indicate that channel entrenchment may arise not solely through high rates of vertical incision and low rates of channel lateral migration in bedrock, but also by interplay between channel lateral migration in sediment and vertical incision that determines the ability of the channel to maintain a zone of sediment fill within the valley.

Counterintuitively, the channel is most effective at maintaining an alluvial channel

belt when bedrock boundaries constrain the range of lateral channel migration (Fig. 4B). On one hand, channels can move rapidly in alluvium and develop high sinuosity, which reinforces high lateral erosion rates, including for local zones of bedrock banks. On the other hand, the bedrock constraints focus planation of the sediment-bedrock interface to a relatively narrow zone, which forces valley floor lowering to keep pace with channel vertical incision. Without a bedrock constraint at the margins of the alluvial belt (Fig. 4C), lateral channel migration is spread over a relatively broad zone, which causes the sediment-bedrock interface to lower more slowly than the vertically incising channel and leads to channel entrenchment in bedrock. This behavior suggests that even when alluvium only mantles a bedrock river valley, it plays an important role in valley evolution because it determines the width of the valley floor that the channel can actively migrate across and plane off the sediment-bedrock interface (e.g., Fig. 5).

The existence of a laterally constrained alluvial belt also influences the planform sinuosity of the valley boundaries. Our simulations show that for a fixed channel geometry and wavelength of unconfined meandering, channel migration in a confined alluvial belt results in erosional arcuate scars in the valley walls that have a range of wavelengths. Large contrasts in bedrock versus sediment bank strength favor scars with wavelengths longer than the typical channel wavelength for unconfined meandering (> 15 w_c; Fig. 6), a pattern widely observed in natural, "underfit" river valleys [*Dury*, 1964]. In the simulations, the long-wavelength valley scars form by meander bend deformation at the alluvial-belt boundaries [*Lewin and Brindle*, 1977], but also through progressive sculpting by wall-parallel channel migration (Fig. 4B and Supplementary Movie 2). Meander wavelength is

well established to scale with channel width and discharge in alluvial rivers [e.g., *Leopold and Wolman*, 1960; *Williams*, 1986], and so meander scars in valley walls have been interpreted as evidence of higher paleodischarge [e.g., *Dury*, 1964, 1985; *Baker and Penteado-Orellana*, 1977; *Alford and Holmes*, 1985]. Our results instead suggest that eroded forms in valley walls do not directly record paleochannel dimensions because meander bend deformation and migration parallel to the valley walls generates scars with wavelengths longer than the typical channel wavelength for free meandering. Therefore paleochannel deposits [e.g., *Leigh and Feeney*, 1995] may be more reliable indicators of channel dimensions.

The result that bedrock-bound channels can evolve under steady forcing from alluvial states leads to the broader question of whether, in general, multiple kinematic paths can lead to a particular bedrock river valley type. Simulations indicate that several bedrock valley types can arise from one of the other bedrock valley types (Fig. 7). Of particular interest is the emergent development of valleys in which meander bends deform at the alluvial-belt boundaries (Fig. 1C; Fig. 4B and Supplementary Movie 2), as suggested by earlier studies that did not include channel vertical incision [*Howard*, 1996; *Sun et al*., 1996]. The broader significance of this finding is that the evolution of bank strength accounted for in the present model and suggested in previous work [*Howard*, 1996; *Sun et al*., 1996] allows for valley states to arise naturally from other states without being directly imposed by initial conditions. Using the non-dimensional variables E_{Vb}*, E_{Vs}*, and w_{ab}*, there are zones of phase space in which particular valley types are likely to emerge, and other zones that may yield multiple valley types (Fig. 7).

While channel lateral migration rate, vertical incision rate, and bank strength have been suggested as important controls on valley type [e.g., *Harden*, 1990; *Merritts et al*., 1994; *Hancock and Anderson*, 2002; *Montgomery*, 2004], their combined influences have not been tested quantitatively in previous models. Results here suggest that (1) channel lateral migration rates in bedrock and sediment, (2) vertical incision rate, and (3) the width of the initial alluvial belt with respect to the potential width of the unconfined alluvial belt can each strongly influence valley evolution; no single factor overwhelms the others. As suggested by *Montgomery* [2004], bedrock erodibility can explain differences in bedrock valley type, with weaker bedrock favoring formation of relatively wide valleys across a range of river vertical incision rates. Low channel lateral migration rates and high vertical incision rates generally favor narrow valleys, while high lateral migration rates and low vertical incision rates favor wide valleys. While past valley topography and alluvial-belt width are difficult to constrain, particularly over landscape evolution timescales of $\geq 10^5$ yr, forward modeling can explore the implications of different hypotheses for former valley chacteristics.

The simulation results can also address whether the different valley types observed in nature are stable under steady forcing, or whether aspects of their geometry may be transient. We find that some portions of the explored parameter space are likely stable: for example, narrow and deep valleys, and broad and shallow valleys can remain stable because channel vertical incision rates are either high enough to keep channels persistently entrenched in bedrock or low enough to allow channel lateral migration to widely bevel the bedrock-sediment interface and maintain alluvial banks (Fig. 7A and 7B). There are,

however, ranges of lateral migration and vertical incision rates and initial alluvial-belt widths that permit evolution through transient valley types (Fig. 7C). In the intermediate ranges of E_{Vb}*, E_{Vs}*, and w_{ab}*, transitions between different valley types can be driven by the inherent unsteadyness of lateral channel migration, which can cause different valley topography despite similar process rates (Fig. 7). Therefore, the statistical behavior of a set of simulations may be needed to identify links between environmental drivers and valley evolution, and to characterize uncertainty in simulation results [e.g., *Griffiths*, 1982; *Nicholas and Quine*, 2010; *Perron and Fagherazzi*, 2012]. While constant vertical incision can drive transitions between valley type, we also find that valley type may be unaffected by pulses of vertical incision as large as 0.5 channel depths (Figure 9). This suggests a threshold on the magnitude of climate and base-level signals that can be preserved in bedrock valley topography.

Changes in base-level, sediment supply, and water discharge are widely implicated as drivers of time-varying river vertical incision rates, which are the commonly argued prerequisite to strath terrace formation [e.g., *Gilbert*, 1877; *Hancock and Anderson*, 2002; *Wegmann and Pazzaglia*, 2002; *Pan et al*., 2003; *Fuller et al*., 2009]. The numerical model of *Hancock and Anderson* [2002] illustrates this concept, but importantly utilizes a one-dimensional framework with a consistent direction of valley widening that cannot generate terraces by changes in channel migration direction under constant vertical incision rates. The simulations presented here, which incorporate two-dimensional channel meandering, show that the intrinsic unsteadiness of meander migration in space and time, coupled with a constant vertical incision rate, can generate strath terraces without pulses of incision. These

terraces are commonly unpaired (Fig. 6), which has been argued to indicate formation by intrinsic processes [e.g., *Merritts et al*., 1994]. Yet paired terraces also form (Fig. 5B), and this geometry is commonly suggested to implicate external drivers of channel evolution [e.g., *Wegmann and Pazzaglia*, 2002], which is not the case in our simulations.

Our simulations suggest more broadly that constant-forcing scenarios that account for unsteady channel lateral channel migration represent an important null hypothesis for valley evolution. Since a variety of bedrock valley types can be explained without pulses of vertical incision, valley aspect ratio may not diagnostically identify valleys that have undergone externally forced pulses of vertical incision. Other morphologic evidence may distinguish constant from pulsed vertical-incision histories—for example, in the simulations bedrock-bound channels that evolve from initial states with sediment banks (Fig. 3G) exhibit low sinuosity at short wavelengths ($\leq 15\ w_c$) compared to bedrock-bound channels that do not lose sinuosity during a transient alluvial phase (Fig. 9A). Alternatively, geochronology can offer more direct constraints on vertical incision history, however even here inferring the degree to which river incision is unsteady is not straightforward [*Finnegan et al*., 2014].

8. Conclusions

We present a model, based on interactions between channel lateral migration and vertical incision, that can reproduce a wide spectrum of bedrock valleys with single-thread meandering channels. We identify the channel vertical incision rate, lateral migration rates in sediment and bedrock, and initial alluvial-belt width as key controls on valley type. Despite these first-order trends, model results indicate that valley types can be unstable

under steady forcing and that different valley types can arise from multiple evolutionary pathways. Bedrock-bound channels, strath terraces, and valley scars with wavelengths longer than the free meander wavelength all arise under constant forcing, further suggesting that unsteady lateral channel migration due to meandering should be considered as a null hypothesis for valley evolution. Bank strength differences between sediment and bedrock reinforce irregularity in meandering in space and time, and sustained planation of the valley floor is enhanced when lateral bedrock boundaries focus the zone of lateral channel migration in sediment banks. Finally, the persistence of channel entrenchment in bedrock following a rapid pulse of vertical incision depends on subsequent rates of channel lateral migration and vertical incision, suggesting that bedrock river valley topography is a useful but potentially transient marker of environmental and tectonic signals.

Acknowledgments

This work was supported by the Department of Defense through the National Defense Science and Engineering Graduate Fellowship (NDSEG) Program and NSF grant EAR-1147381 to MPL. Acknowledgment is also made to the Donors of the American Chemical Society Petroleum Research Fund for partial support of this research. We thank Jean-Philippe Avouac, Noah Finnegan, Alan Howard, Bob Anderson, Brian Yanites, and Associate Editor Dimitri Lague for helpful comments.

Symbol	Description
Dimensional variables	
w_c	Channel width
h_c	Channel depth
w_v	Valley width
h_v	Valley depth
w_{ab}	Initial alluvial belt-width
w_{uab}	Initial alluvial belt-width (unconfined)
C_f	Friction coefficient
E_V	Vertical incision rate
E_{Ls}	Lateral erosion rate in sediment
E_{Lb}	Lateral erosion rate in bedrock
k_e	Lateral erosion rate constant
k_s	Lateral erosion rate constant (sediment)
k_b	Lateral erosion rate constant (bedrock)
f_b	Fraction of bedrock in bank materials
Δt	Time step
t	Simulation time
Γ, Ω	Channel migration rate weighting coefficients
ξ	Distance along channel centerline
μ	Channel sinuosity
Non-dimensional variables	
$t^* = \frac{tE_{Ls}}{w_c}$	Non-dimensional time
$E_{Vb}^* = \frac{E_V w_c}{E_{Lb} h_c}$	Non-dimensional vertical incision rate with bedrock banks
$E_{Vs}^* = \frac{E_V w_c}{E_{Ls} h_c}$	Non-dimensional vertical incision rate with sediment banks
$w_{ab}^* = \frac{w_{ab}}{w_{uab}}$	Non-dimensional initial alluvial-belt width
$w_v^* = \frac{w_v - w_c}{h_v}$	Non-dimensional valley width

Table 1. Model variables.

Valley name	w_c **(m)**	h_c **(m)**	E_{Lb} **(m/yr)**	E_V **(mm/yr)**	E_{Vb}*
San Juan	53	2.1	0.003	0.15	1.26
Mattole	102	4	0.03	1	0.86
Beaver	44	1.8	0.035	0.1	0.07
Colorado	275	8	0.15	0.25	0.06

Table 2. Estimated parameters for field sites shown in Figures 1 and 7.

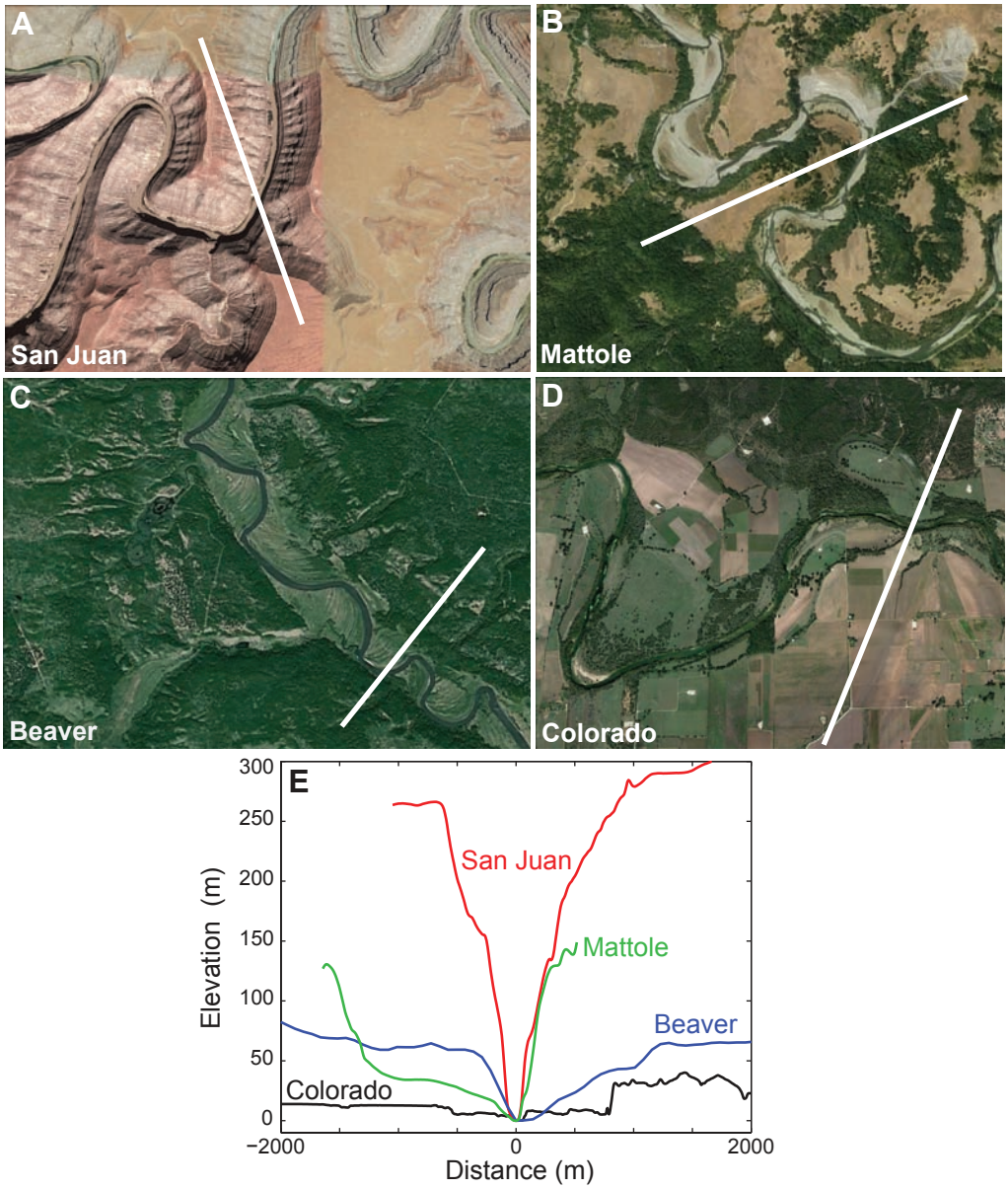

Figure 1. Bedrock river valleys with diverse morphologies. White lines denote topographic transects, all oriented from the lower portion of each image to the upper portion. **(A)** The San Juan River, Utah (37.2°N, 109.9°W). **(B)** The Mattole River, California (40.2°N, 124.2 °W). **(C)** The Beaver River, Alberta, Canada (54.4°N, 110.4°W). **(D)** The Colorado River valley, Texas (30.2°N, 97.5°W). **(E)** Valley cross-section elevation profiles for valleys in (A-D). Images: Google Earth/ USDA Farm Service Agency / CNES Spot Image.

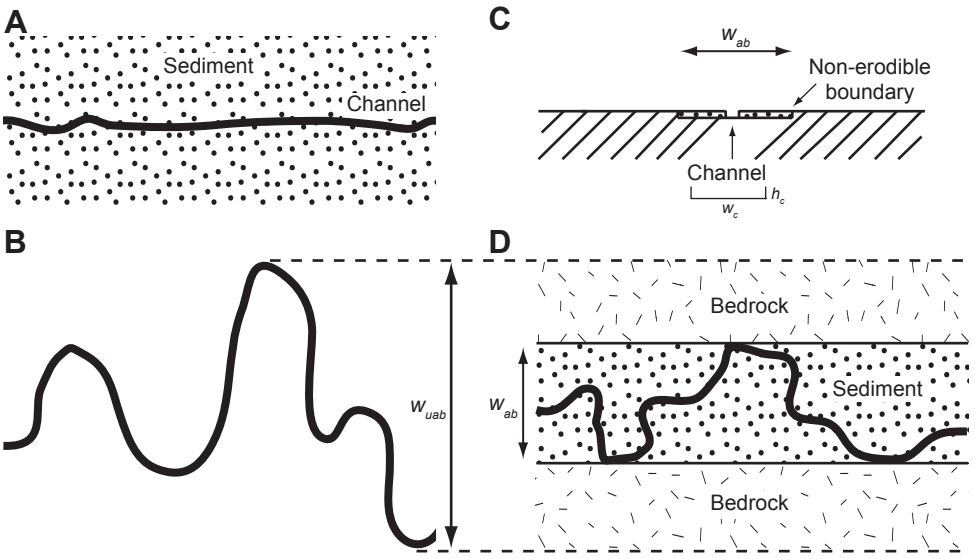

Figure 2. Model procedure for setting initial alluvial-belt width and channel planform geometry. The mean flow direction is from left to right. **(A)** A preliminary set of simulations is run to determine the maximum unconfined alluvial-belt width. The channel (black line) begins from a low-sinuosity state, and has entirely sediment banks. **(B)** Each simulation is run until a fixed non-dimensional time (t^*), at which the maximum range of the channel perpendicular to the mean flow direction is recorded as the unconfined alluvial-belt width (w_{uab}). **(C)** The channel is again evolved from a low-sinuosity state, but this time within a valley with impenetrable walls. The initial alluvial-belt width (w_{ab}) is a fraction w_{ab}^* of the unconfined alluvial-belt width (w_{uab}). In this panel, $w_{ab}^* = 0.5$. This phase proceeds for a fixed non-dimensional simulation time (t^*), and the channel may deform against the impenetrable walls. **(D)** For the start of the full simulation, the impenetrable valley walls are replaced with erodible bedrock walls. The banks are entirely sediment within the alluvial belt, and the depth of sediment is equal to the channel depth. Outside of the alluvial belt, and within the alluvial belt below the elevation of the channel bed, the landscape is entirely bedrock.

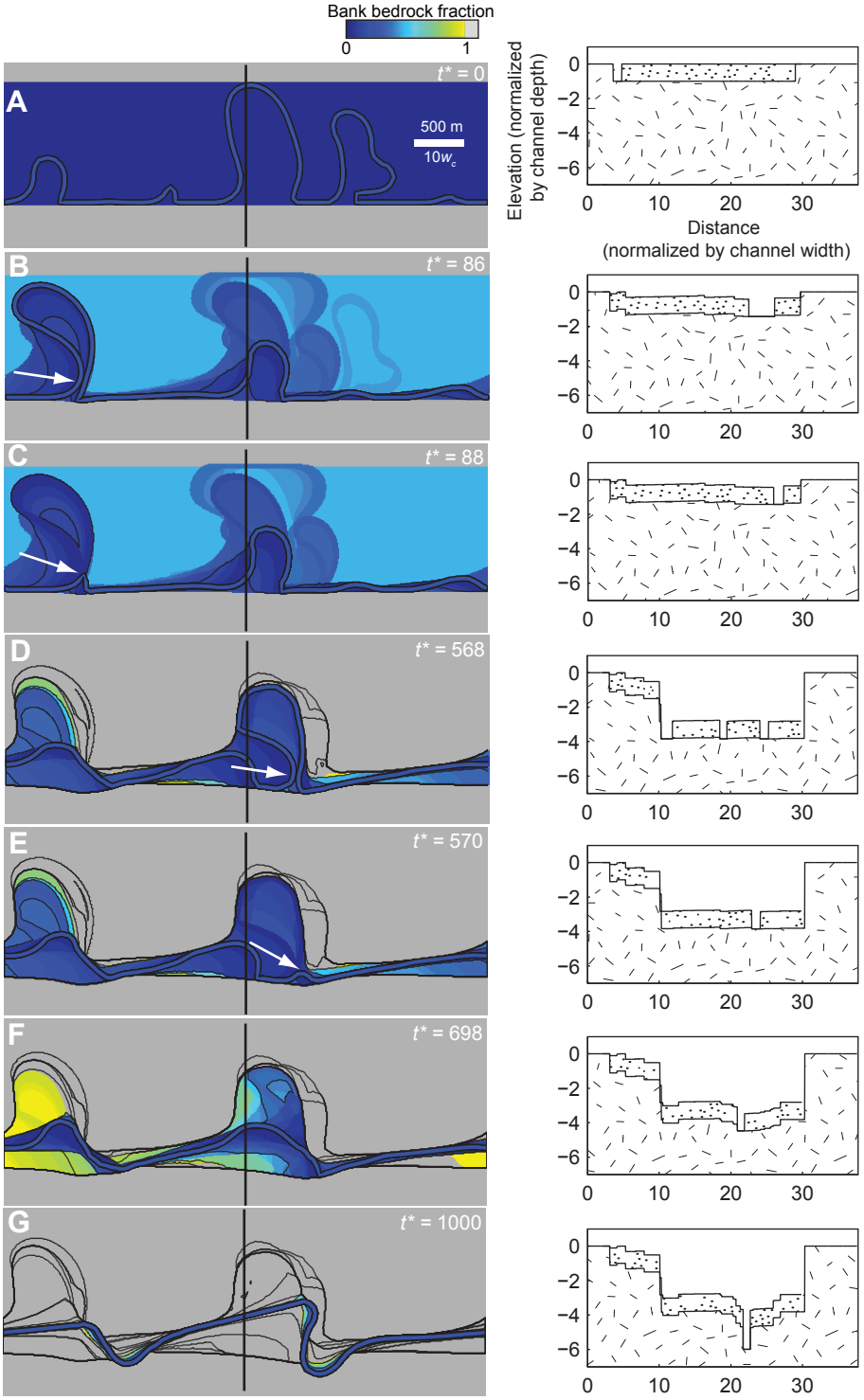

Figure 3 (caption next page)

Figure 3. Snapshots of channel and valley evolution under constant vertical incision. The mean flow direction is from left to right. The left side of each panel shows the shaded relief topography, with a fixed contour interval of 0.5 channel depths (equal to 1 meter here and in all simulations). The width of the model domain is 100 channel widths, and the scale is consistent for all map-view panels. The coloration represents the fraction of bedrock (f_b) in bank materials that the channel would encounter if it migrated laterally into that portion of the landscape with no change in its vertical position. For areas in gray $f_b = 1$, indicating that if the channel were to migrate to those areas it would encounter entirely bedrock in the bank up to the bankfull depth. Also shown are the channel planform extent (blue), top-to-bottom topographic profile locations (black), and the non-dimensional simulation time (t^*). The right side of the figure shows valley cross-sections, including bedrock (hatched areas) and sediment (stippled areas). Model parameters are $t^*_{max} = 1000$, $E_{Vs}^* = 0.005$, $E_{Vb}^* = 0.5$, and $w_{ab}^* = 0.5$, which represent the base case parameters. Where white arrows appear, they indicate the locations of neck cutoffs. **(A-G)** Valley and channel state at times from $t^* = 0$ to 1000. The end state in (G) is also shown in Figure 5B.

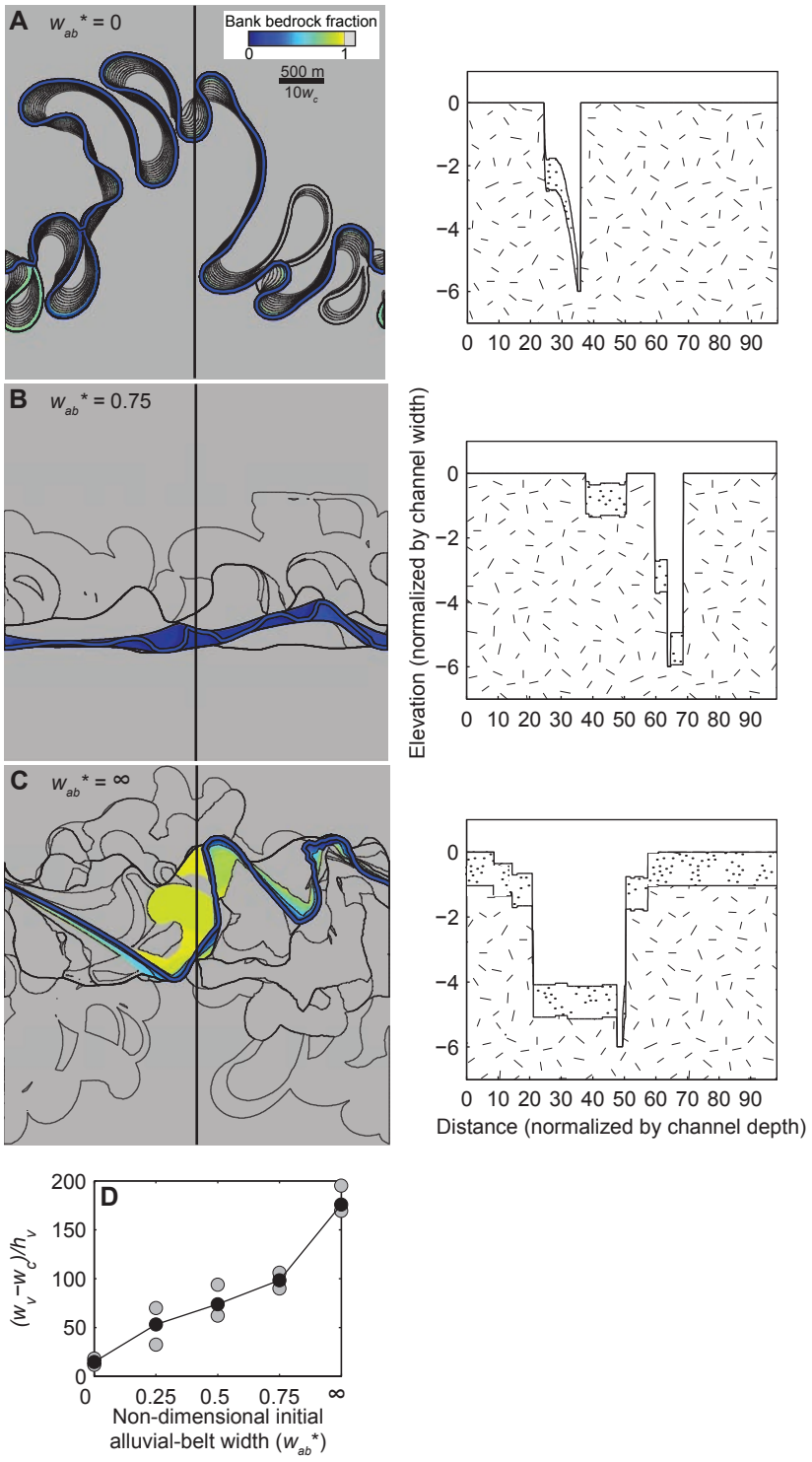

Figure 4 (caption next page)

Figure 4. Valley topography formed for different initial alluvial-belt widths, where w_{ab}* represents the ratio of the initial alluvial-belt width to the unconfined alluvial-belt width. Symbols and coloration are the same as in Figure 3; the scale is identical in all map-view panels and the mean flow direction is from left to right. All simulations use the base case parameters other than w_{ab}* (t* = 1000, E_{Vs}* = 0.005, and E_{Vb}* = 0.5). Map views are shown for **(A)** a valley with no initial alluvial belt (w_{ab}* = 0), **(B)** a valley with a partially confined initial alluvial belt (w_{ab}* = 0.75), and **(C)** a valley with a fully unconfined initial alluvial belt (w_{ab}* = ∞). **(D)** Valley aspect ratio versus w_{ab}* for five simulations run in triplicate with different initial channel planform geometries. The median valley aspect ratio for each value of w_{ab}* is shown in black.

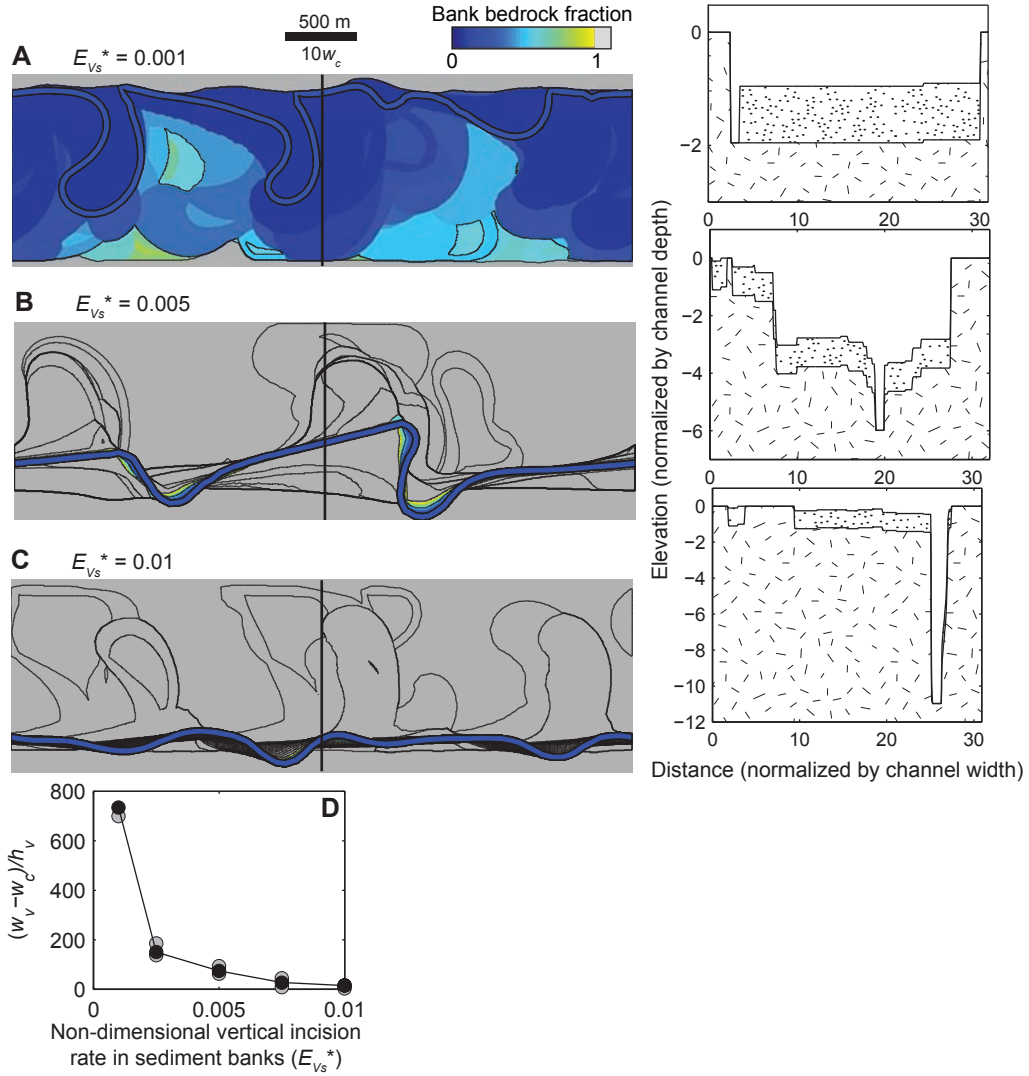

Figure 5. Topography of valleys formed by initially high-sinuosity channels for different values of non-dimensional vertical incision rate with sediment banks (E_{Vs}*). All simulations use the base case parameters other than E_{Vs}* (w_{ab}* = 0.50, t* = 1000, and E_{Vb}* = 0.5). Symbols and coloration are the same as in Figure 3; the scale is identical in all map-view panels and the mean flow direction is from left to right. Map views are shown for **(A)** E_{Vs}*=0.001, **(B)** E_{Vs}*=0.005, and **(C)** E_{Vs}*=0.01. **(D)** Valley aspect ratio versus E_{Vs}* for five simulations run in triplicate with different initial channel planform geometries. The median valley aspect ratio for each value of E_{Vs}* is shown in black. Panel (B) corresponds to the final time of the baseline case (Fig. 3G).

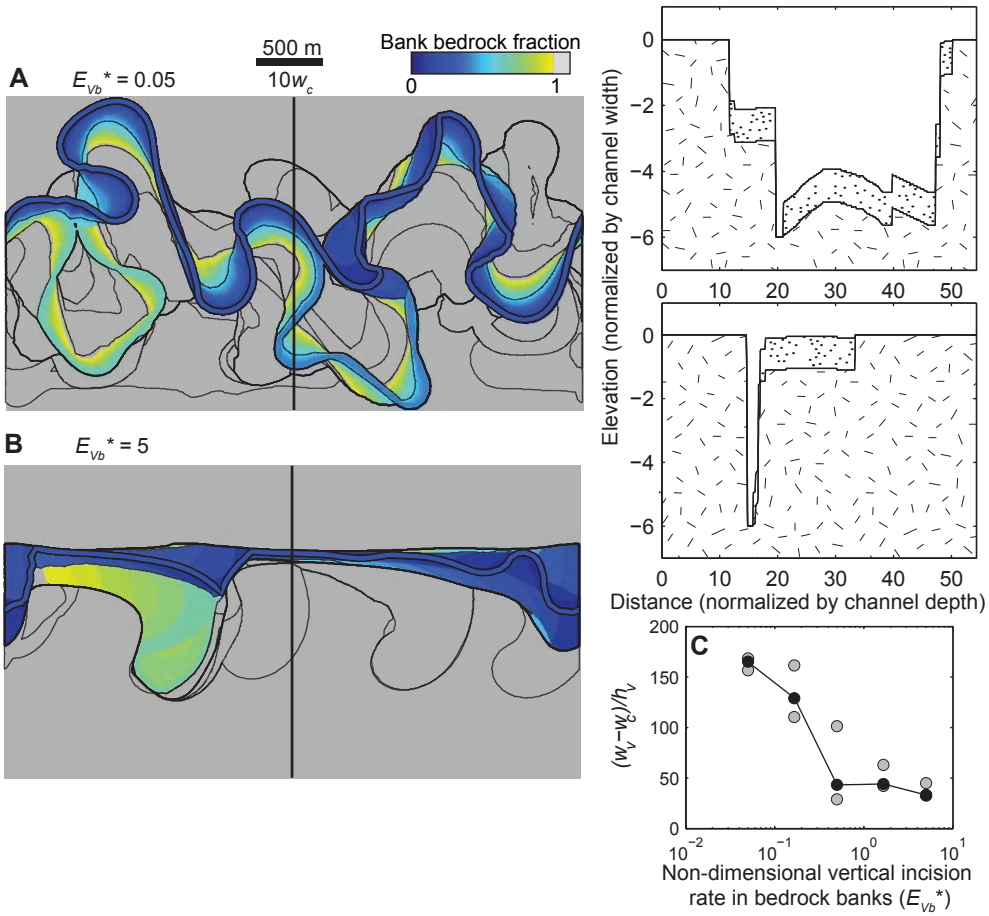

Figure 6. Valley topography formed for different values of non-dimensional channel vertical erosion rate with bedrock banks, E_{Vb}*. Symbols and coloration are the same as in Figure 3; the scale is identical in all map-view panels. All simulations use the base case parameters other than E_{Vb}* (t* = 1000, w_{ab}* = 0.5, and E_{Vs}* = 0.005). The mean flow direction is from left to right. Map views are shown for **(A)** E_{Vb}* **=** 0.05 and **(B)** E_{Vb}* = 5. **(C)** Valley aspect ratio versus E_{Vb}* for five simulations run in triplicate with different initial channel planform geometries. The median valley aspect ratio for each value of E_{Vb}* is shown in black.

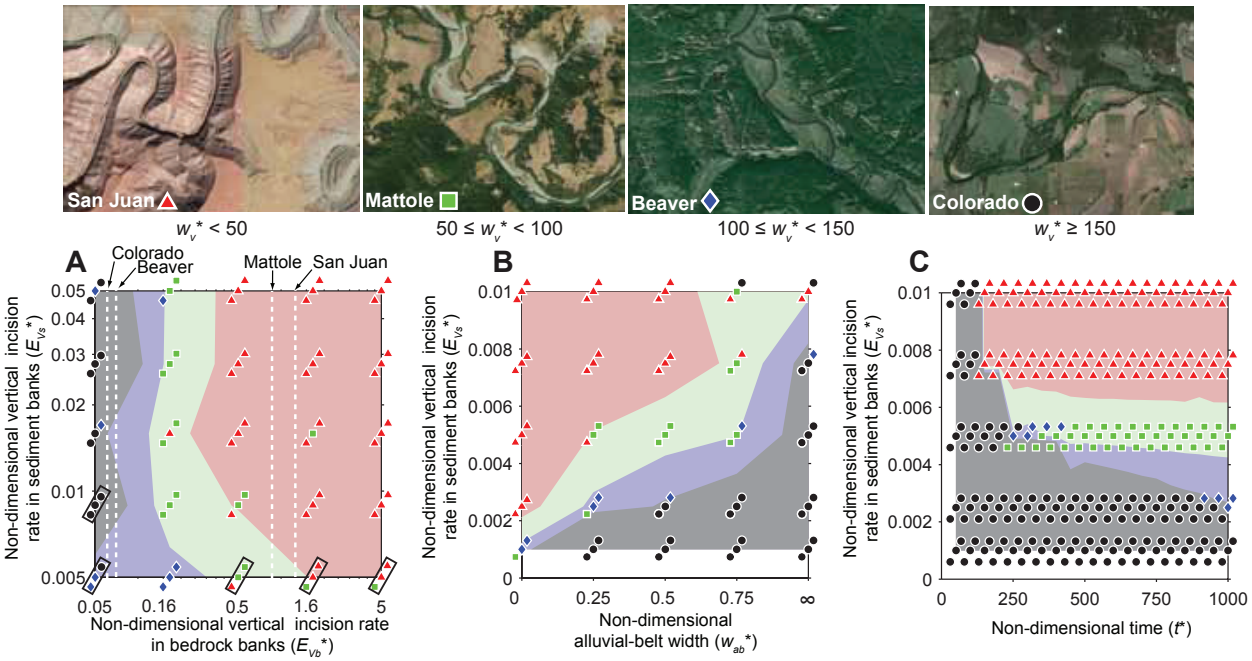

Figure 7. Model predictions for bedrock valley type, classified using valley aspect ratio (w_v^*). Each unique set of parameter values is used in three distinct simulations with different initial channel planform geometries. Each trial is plotted slightly offset from the others for legibility. For example, (A) shows a 5 x 5 matrix of simulations in the phase space of E_{Vs}^* and E_{Vb}^*, where each unique set of parameters is plotted for three separate simulations. Valley classifications based on w_v^* are plotted for individual trials; w_v^* is averaged for each set of unique parameter values, and contoured. Filled color contours indicate the classified valley types (1-4) and correspond to the representative field sites at the top of the figure. **(A)** Phase space of E_{Vs}^* and E_{Vb}^*. Dashed lines indicate estimated values of E_{Vb}^* for each field site. Boxes indicate simulation sets for which the majority of the channel banks are entirely bedrock. **(B)** Phase space of E_{Vs}^* and w_{ab}^*. **(C)** Phase space of E_{Vs}^* and t^*.

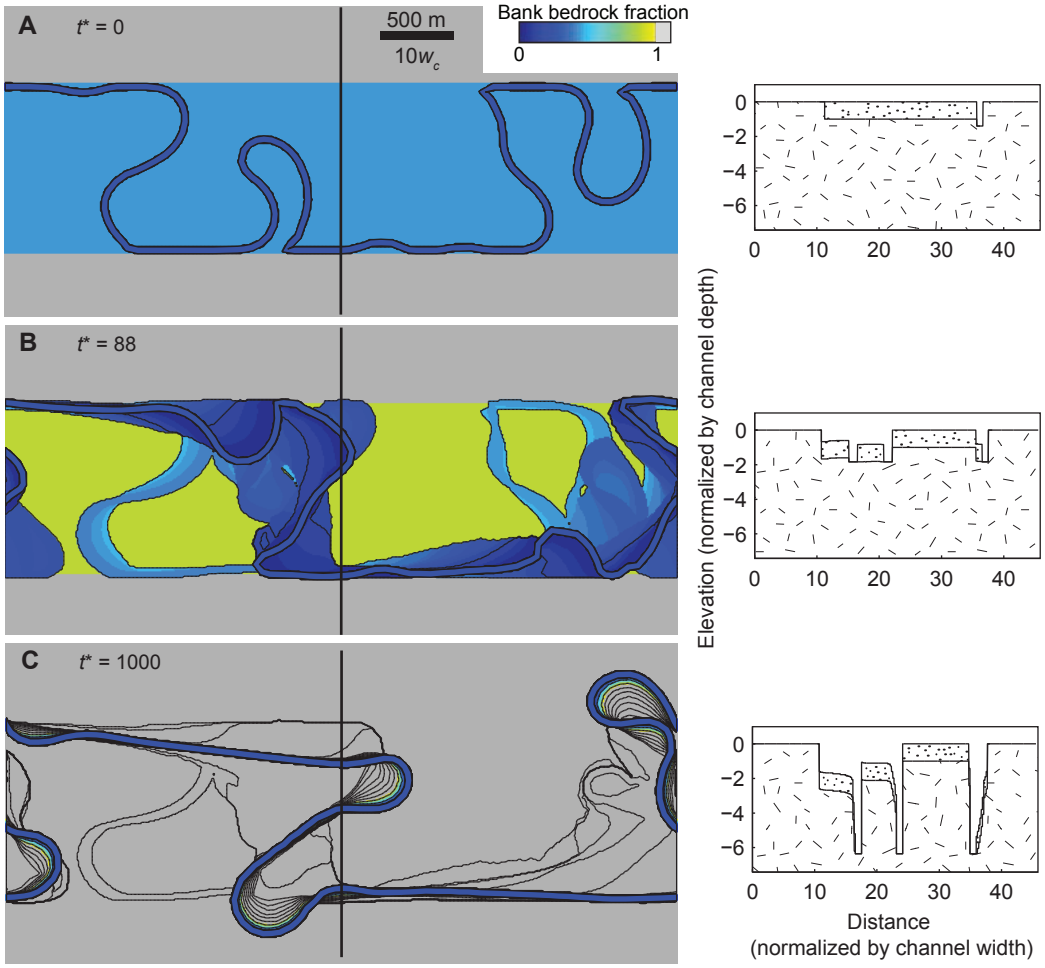

Figure 8. Valley topography during evolution from an alluvial state following a pulse of vertical incision of $0.5h_c$ and constant subsequent vertical incision with $E_{Vs}^* = 0.005$. Other model parameters are set to the baseline case values ($t^* = 1000$ at the conclusion of the simulation; $E_{Vb}^* = 0.5$; and $w_{ab}^* = 0.5$). Symbols and coloration are the same as in Figure 3; the scale is identical in all map-view panels and the mean flow direction is from left to right. **(A)** $t^* = 0$; **(B)** $t^* = 88$ (as in panel 3C of the baseline case); **(C)** $t^* = 1000$ (as in panel 3G of the baseline case).

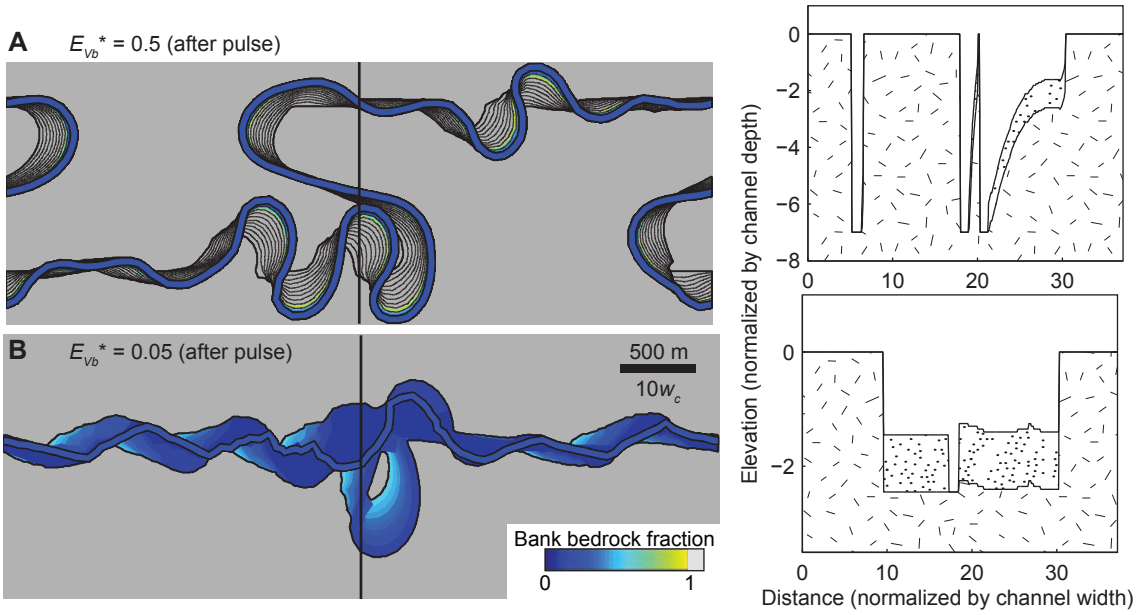

Figure 9. Valley topography during evolution from an alluvial state following a pulse of vertical incision of h_c, larger than the pulse in Figure 9. Other model parameters are set to the baseline case values (t^* = 1000; and w_{ab}^* = 0.5). Symbols and coloration are the same as in Figure 3; the scale is identical in both map-view panels and the mean flow direction is from left to right. **(A)** Pulse of vertical incision is followed by constant, relatively rapid vertical incision with E_{Vs}^* = 0.005. **(B)** Pulse of vertical incision is followed by constant, relatively slow vertical incision with E_{Vs}^* = 0.0005.

Chapter 4: Numerical model predictions of intrinsically generated fluvial terraces and comparison to climate-change expectations

Submitted as:
Limaye, A. B. S., and Lamb, M. P., Numerical model predictions of intrinsically generated fluvial terraces and comparison to climate-change expectations, Journal of Geophysical Research – Earth Surface.

Abstract

Terraces eroded into sediment (cut-fill) and bedrock (strath) preserve a geomorphic record of river activity. River terraces are often thought to form when a river switches from a period of low vertical incision rates and valley widening to high vertical incision rates and terrace abandonment. Consequently, terraces are frequently interpreted to reflect landscape response to changing external drivers, including tectonics, sea-level, and most commonly, climate. In contrast, unsteady lateral migration in meandering rivers may generate river terraces even under constant vertical incision rates and without changes in external forcing. To explore this latter mechanism, we use a numerical model and an automated terrace detection algorithm to simulate landscape evolution by a vertically incising, meandering river and isolate the age and geometric fingerprints of intrinsically generated river terraces. Simulations indicate that terraces form for a wide range of lateral and vertical incision rates. Terraces form after a characteristic timescale for relief generation, and once this is surpassed the time interval between terraces increases in time due to re-working of previously visited areas. Surprisingly, intrinsically generated terraces are commonly paired and longitudinally extensive. Evolving, spatial differences in bank strength between bedrock and sediment reduce terrace formation frequency and length,

favor pairing, and can explain sub-linear terrace margins at valley boundaries. Modeled terrace timing and geometries for intrinsically generated terraces are consistent with several natural landscapes previously interpreted to be formed from climate change. We suggest a new phase space that may allow separation of intrinsically formed terraces from other formation mechanisms.

1. Introduction

River terraces are low-relief surfaces formed by deposition and erosion of valley-fill sediments (i.e., fill and fill-cut terraces) or erosion of bedrock (i.e., strath terraces) [*Bucher*, 1932; *Bull*, 1991; *Pazzaglia*, 2013]. The geometry and number of terraces differs widely. For example, terraces may be contiguous and occupy several topographic levels (e.g., Clearwater River valley; Fig. 1A), or may be separated and less numerous (e.g., Mattole River valley; Fig. 1B). In some locations terraces are particularly wide and long (e.g., Wind River valley; Fig. 1E), and Colorado River valley, Texas; Fig. 1D), with boundaries that are loosely (Fig. 1E) or closely (Fig. 1D) associated with the neighboring river channel. Terraces are globally distributed [*Montgomery*, 2004; *Bridgland and Westaway*, 2008] and span a range of physiographic environments, including coastal mountain ranges (e.g., Fig. 1A and 1B), continental interiors (e.g., Fig. 1C and 1E), and broad coastal plains (e.g., Fig. 1D).

Terraces are stranded above the active floodplain, and thus preserve a unique geomorphic and sedimentologic record of channel evolution over timescales up to hundreds of thousands of years [e.g., *Hancock et al*., 1999; *Pan et al*., 2003]. Consequently, river terraces are the principal geomorphic features for reconstructing channel aggradation

and incision, and constraining long-term sediment fluxes from landscapes [*Bull*, 1991; *Fuller et al*., 2009b] to marine depositional basins [e.g., *Blum and Aslan*, 2006; *Phillips and Slattery*, 2006]. Tectonic studies also frequently utilize terraces as passive markers of deformation [e.g., *Rockwell et al*., 1984; *Lavé and Avouac*, 2000] and rock uplift [e.g., *Personius*, 1995; *Pazzaglia et al*., 1998; *Lavé and Avouac*, 2000]. Although terrace abandonment has been directly observed in rare cases [*Born and Ritter*, 1970; *Yanites and Tucker*, 2010], strath terraces likely evolve over millennial timescales [*Hancock and Anderson*, 2002; *Montgomery*, 2004].

Terrace formation requires valley widening to bevel terrace treads and vertical incision to abandon these surfaces above the channel [e.g., *Hancock and Anderson*, 2002; *Montgomery*, 2004; *Bridgland and Westaway*, 2008]. A change in the ratio of vertical to lateral erosion rate is commonly cited as a requirement for terrace formation [e.g., *Hancock and Anderson*, 2002; *Fuller et al*., 2009; *Finnegan and Dietrich*, 2011], and is usually attributed to changes in vertical incision rate driven by external factors, including tectonics [e.g., *DiBiase et al*., in press; *Bull*, 1991; *Tyráček et al*., 2004; *Peters and van Balen*, 2007; *Claessens et al*., 2009; *Demir et al*., 2009; *Yanites and Tucker*, 2010], base-level change [e.g., *Fisk*, 1944; *Pazzaglia and Gardner*, 1993; *Merritts et al*., 1994; *Blum and Tornqvist*, 2000; *Matoshko et al*., 2009; *Finnegan and Balco*, 2013], and most frequently, changes in water and sediment fluxes due to climate change [*Bull*, 1991; *Pazzaglia and Gardner*, 1993; *Blum and Valastro*, 1994; *Molnar et al*., 1994; *Meyer et al*., 1995; *Tucker and Slingerland*, 1997; *Hancock and Anderson*, 2002; *Hartshorn et al*., 2002; *Wegmann and Pazzaglia*, 2002b, 2009; *Bogaart et al*., 2003, 2003; *Pan et al*., 2003; *Vandenberghe*, 2003;

Bridgland and Westaway, 2008; *Picotti and Pazzaglia*, 2008; *Fuller et al*., 2009b; *Westaway et al*., 2009; *Doğan*, 2011; *Pazzaglia*, 2013]. Thus, terraces are commonly interpreted as the enduring landscape marker of river response to external perturbations of regional or global significance [*Merritts et al*., 1994].

Evidence for climate change-driven terrace formation primarily relates to terrace age and geometry. Terrace age is commonly compared to paleoclimate proxies [e.g., *van den Berg and van Hoof*, 2001; *Hancock and Anderson*, 2002; *Pan et al*., 2003; *Bridgland and Westaway*, 2008; *Picotti and Pazzaglia*, 2008; *Fuller et al*., 2009] some of which record quasi-periodic variations such as Milankovich cycles [*Hays et al*., 1976]. Despite these important studies, relationships between terrace age and paleoclimate records are complicated by dating precision limits [e.g., *Wegmann and Pazzaglia*, 2002] and in the case of strath terraces uncertainty in the elapsed time between strath beveling and deposition of overlying alluvium [e.g., *Merritts et al*., 1994]. Terrace geometries attributed to climate change include terrace occurrence at similar elevation on opposites sides of a channel (i.e., pairing) [e.g., *Wegmann and Pazzaglia*, 2002] and along-valley continuity [*Pazzaglia et al*., 1998], in accordance with conceptual models that predict long periods of river longitudinal stability and strath beveling that are punctuated by channel incision and terrace abandonment [e.g., *Hancock and Anderson*, 2002].

Although external forcing can affect rivers, climatic and tectonic signals pass through a potentially complex geomorphic filter [*Schumm*, 1977; *Bull*, 1991; *Jerolmack and Paola*, 2010; *Ganti et al*., 2014] that may both generate [*Davis*, 1909; *Merritts et al*., 1994; *Finnegan and Dietrich*, 2011] and destroy [*Lewin and Macklin*, 2003] terraces. For

example, *Finnegan and Dietrich* [2011] showed that if vertical erosion rate is proportional to channel slope, then meander bend growth and cutoff should cause abrupt changes in channel slope (i.e., knickpoints) that propagate upstream resulting in a pulse of vertical incision that creates terraces. For meandering streams, lateral erosion rates inherently vary in space and time. For example, meander bends can migrate along the valley axis and abruptly change migration direction by cutoffs, and the channel axis can drift [e.g., *Brice*, 1974; *Howard and Knutson*, 1984; *Seminara*, 2006]. *Davis* [1909] hypothesized that a vertically incising, laterally migrating channel (Fig. 2A) can abandon terraces when it migrates in one direction (Fig. 2B), then switches direction and migrates back toward its starting point (Fig. 2C). Because the channel is incising vertically, the terrace riser is formed by lateral erosion of the cutbank (Fig. 2C) and the terrace is fully abandoned once the channel changes direction once more (Fig. 2D). This mechanism has been observed to drive terrace formation in experimental alluvial fans [*Mizutani*, 1998] and in field settings where engineered base-level fall has induced rapid vertical incision [*Born and Ritter*, 1970; *Ben Moshe et al*., 2008]. Although switching channel-migration direction is rarely considered as a mechanism for forming fill-cut or strath terraces [*Challinor*, 1932; *Hack*, 1955; *Stricklin*, 1961; *Merritts et al*., 1994; *Erkens et al*., 2009], numerical model results indicate that meandering can generate strath terraces even under constant rates of vertical incision [*Limaye and Lamb*, 2014].

A limited conceptual framework exists to predict the frequency and geometry of terraces formed by unsteady channel lateral migration. Such terraces have been suggested to be discontinuous along-valley [*Pazzaglia et al*., 1998; *Pazzaglia*, 2013], unpaired

[*Merritts et al*., 1994; *Pazzaglia et al*., 1998; *Wegmann and Pazzaglia*, 2002], and to dip inward toward the center of the valley with a slope equal to the long-term average ratio of vertical to lateral incision [*Merritts et al*., 1994]. In a rare test of these hypotheses, experimental alluvial fans with migrating, vertically incising channels have been observed to form inward-sloping terraces [*Mizutani*, 1998]. Models have been developed for terrace formation by pulses of vertical incision [*Veldkamp*, 2000; *Hancock and Anderson*, 2002; *Finnegan and Dietrich*, 2011], but not for terrace formation driven by irregular lateral channel migration—a process that should represent a null hypothesis for terrace formation by meandering rivers. Thus, there is a need to identify what components of the terrace record are significant for interpreting external drivers, and to distinguish them from patterns of terrace formation that would result from intrinsic unsteadiness of channel migration alone.

We seek to test the null hypothesis that river terraces commonly form in the absence of pulses of vertical incision driven by changes in external forcing, but rather through the combination of variable lateral channel migration intrinsic to meandering rivers and constant vertical incision, as would occur for a river at topographic steady state undergoing steady tectonic uplift [e.g., *Merritts et al*., 1994]. Our approach to modeling terrace formation is new because existing models do not include meandering [*Veldkamp and van Dijke*, 2000; *Hancock and Anderson*, 2002] or do not represent spatial bank-strength differences [*Veldkamp*, 2000; *Hancock and Anderson*, 2002; *Finnegan and Dietrich*, 2011]. Existing valley evolution modeling studies that include meandering have not systematically analyzed the age and geometric properties of simulated terraces

[*Lancaster*, 1998; *Finnegan and Dietrich*, 2011; *Limaye and Lamb*, 2014].

We aim to isolate the expected age distribution and geometry of terraces formed where unsteady lateral erosion due to meandering, rather than unsteady vertical erosion due to external forcing, drives changes in the ratio of vertical to lateral incision rate. In Section 2, we describe our specific numerical modeling and terrace analysis objectives, and identify potential controls on terrace age distribution and geometry. In Section 3, we describe methods used for modeling channel migration and identifying simulated terraces automatically. Section 4 presents the simulation results, including the variety of surface morphologies formed by the meandering model. We analyze terrace age and geometry across a broad range of channel lateral and vertical erosion rates, and also consider cases in which variable bank-material strength (Section 5) and pulses of vertical incision (Section 6) influence terrace formation. In Section 7 we compare simulation results to natural terraces. We discuss implications for inferring terrace origin in Section 8.

2. Hypotheses and non-dimensionalization

Meander bends possess characteristic lengthscales [*Leopold and Wolman*, 1960; *Williams*, 1986] and migration patterns [*Brice*, 1974; *Howard and Knutson*, 1984; *Camporeale et al*., 2005; *Bradley and Tucker*, 2013]. Consequently, we hypothesize that terraces generated by meandering with constant vertical incision have characteristic geometric properties and age distributions that may set them apart from vertical incision pulse-driven terraces. Because differences in bank strength between bedrock and sediment can also steer channel migration and influence valley topography [*Limaye and Lamb*,

2014], we also hypothesize that evolving bank-strength differences alter the age and geometry of terraces generated by meandering with constant vertical incision.

We seek to determine the characteristics of terraces—including the time between formation of unique terrace levels ($\Delta t_{terrace}$), and maximum terrace length ($L_{terrace,max}$), slope (θ), dip direction (ϕ), and pairing fraction (f_{paired})—formed by meandering with constant vertical incision in a general way for both fill-cut and strath terraces. Seven parameters can describe the kinematics of valley evolution by a mixed bedrock-alluvial meandering channel: lateral erosion rate in bedrock (E_{Lb}) and sediment (E_{Ls}), the vertical incision rate into a bedrock bed (E_v), channel width (w_c), initial alluvial-belt width (w_{ab}) and unconfined alluvial-belt width (w_{uab}), channel depth (h_c), and the total simulation time (t) (Table 1).

Several factors may influence vertical incision rates, lateral erosion rates, and terrace formation, including sediment supply [e.g., *Sklar and Dietrich*, 2001] channel slope [e.g., *Stark*, 2006; *Finnegan and Dietrich*, 2011], uplift rate [e.g., *Lavé and Avouac*, 2001; *Finnegan et al*., 2005; *Amos and Burbank*, 2007; *Yanites and Tucker*, 2010], discharge variability [e.g., *Turowski et al*., 2008; *Stark et al*., 2010] and channel substrate [e.g., *Ferguson*, 1973; *Finnegan et al*., 2005]. In addition, valley widening may be carried out by braided rather than meandering channels [*Finnegan and Balco*, 2013]. We omit these factors as independent variables, so that the vertical incision and lateral erosion rates can themselves be varied as independent variables.

Using dimensional analysis these seven parameters can be recast as five independent non-dimensional parameters, including the dimensionless simulation time

$$t^* = \frac{E_L t}{w_c} ; \tag{1a}$$

the dimensionless vertical incision rate

$$E_V^* = \frac{E_V h}{E_L h} ; \tag{1b}$$

the channel width-to-depth ratio

$$w_c^* = \frac{w_c}{h_c} ; \tag{1d}$$

and the dimensionless initial alluvial-belt width (w_{ab}*)

$$w_{ab}^* = \frac{w_{ab}}{w_{uab}} , \tag{1e}$$

which describes the initial width of a sediment-filled zone, one channel depth thick, with respect to the estimated meander-belt width an unconfined case [*Limaye and Lamb*, 2014]. In Eq. 1a and 1b, E_L represents the lateral erosion rate for uniformly erodible bank material.

We quantify the age distribution of terraces by measuring the time between formation of unique terrace levels ($\Delta t_{terrace}$), defined as the difference in mean surface age between surfaces with mean elevations separated by a distance Δz. For simulations in which one or fewer terraces forms, $\Delta t_{terrace}$ is undefined. The timescale for vertical incision to generate relief sufficient to define a unique terrace level is

$$t_{vert} = \frac{\Delta z}{E_V} , \tag{2}$$

and reflects a minimum timescale for terrace formation. Terraces may not form in this timescale if lateral erosion during vertical incision occurs too slowly to generate a terrace. In the analysis that follows, the median time between unique terrace levels ($\Delta t_{terrace,50}$) is

normalized by the vertical incision timescale for terrace formation (t_{vert}), where $\Delta t_{terrace,50}$ / t_{vert} = 1 corresponds to the highest frequency of terrace generation allowed by the model setup.

In addition to terrace age, a variety of terrace geometric properties are commonly considered in order to interpret terrace origin or infer channel kinematics. These properties include terrace slope [e.g., *Merritts et al*., 1994; *Fuller et al*., 2009; *Finnegan and Dietrich*, 2011], terrace pairing [e.g., *Merritts et al*., 1994; *Wegmann and Pazzaglia*, 2002; *Pazzaglia*, 2013], terrace width [e.g., *Lavé and Avouac*, 2001], and terrace length [e.g., *Wegmann and Pazzaglia*, 2002]. Several characteristics have been attributed to terraces generated by unsteady channel migration, including a slope equal to the ratio of channel vertical incision to lateral erosion [*Merritts et al*., 1994; *Fuller et al*., 2009; *Finnegan and Dietrich*, 2011]; a dip direction oriented towards the center of the valley [*Davis*, 1909; *Merritts et al*., 1994]; and limited length [e.g., *Pazzaglia et al*., 1998]. To our knowledge, however, none of these terrace properties has been verified through direct field observations, numerical model modeling, or laboratory experiments, except for the experiments of *Mizutani* [1998]. We non-dimensionalize terrace length and width by channel width. To quantify the influence of the non-dimensional variables on terrace geometry, we identify terrace surfaces in simulated topography at the end of each simulation.

Because vertical and lateral erosion are needed to form terraces, we hypothesize that the non-dimensional vertical incision rate (E_V*) exerts the primary control on terrace frequency and geometry. We also hypothesize that non-dimensional simulation time (t*)

influences the number and geometry of preserved terraces because more extensive lateral channel migration erodes existing landforms and deposits as it creates new ones. Field data sufficient to test this hypothesis are rare, but *Lewin and Macklin* [2003] identified fill terrace deposits consistent with selective preservation, and numerical modeling results suggest that the distribution of floodplain sediment ages generated by meandering reflects preferential preservation of older sediments [*Bradley and Tucker*, 2013]. Thus, to test these specific hypotheses, we hold w_c^* constant and separately vary t^* and E_V^* for cases. w_{ab}^* is irrelevant for these cases with uniform bank materials because channel lateral migration rates are equal in bedrock and sediment.

For cases with contrasts in bank strength between bedrock and sediment, we hypothesize that the different lateral erosion rates in bedrock compared to sediment alter spatial patterns of channel migration and consequently influence terrace formation and geometry. Thus, to test this hypothesis, we hold w_c^*, t^*, and w_{ab}^* constant and systematically explore terrace formation timescale ($\Delta t_{terrace,50}/t_{vert}$) and geometry as a function of dimensionless vertical incision rate.

3. Model formulation

We follow an approach to simulating river valley evolution similar to *Limaye and Lamb* [2014]. We use the simplest possible numerical model that incorporates river meandering and vertical incision, and tracks bank-strength differences between bedrock and sediment. To limit the computational intensity of the simulations and permit simulation of terrace evolution over timescales of 100,000 years, we employ a relatively simple and commonly used model of river meandering [*Howard and Knutson*, 1984], in which channel

width is fixed and channel curvature drives bend migration. This model reproduces key meandering kinematics and geometries [*Howard and Hemberger*, 1991].

3.1. Meandering and landscape evolution

We model meandering channel and bank-strength evolution using methods identical to *Limaye and Lamb* [2014]. In summary, we adapt the centerline evolution model of *Howard and Knutson* [1984], in which local lateral erosion rate is a function of local and upstream-integrated curvature

$$R_1(s) = \Omega R_o(s) + \frac{\Gamma \int_0^{\xi_{max}} R_o(s-\xi) G(\xi) d\xi}{\int_0^{\xi_{max}} G(\xi) d\xi} \quad (3)$$

where R_1 is the dimensionless lateral erosion rate, s is the centerline node index, ξ is the distance upstream and $R_o = (r/w_c)^{-1}$, where r is the radius of curvature of the centerline at node s. Ω and Γ are dimensionless parameters set to -1 and 2.5, respectively, and determine the relative weight of local (Ω) and upstream (Γ) curvature [Ikeda et al., 1981]. $G(\xi)$ is a weighting function

$$G(\xi) = e^{-(\frac{2kC_f}{h_c})\xi} \quad (4)$$

with k =1 (Ikeda et al., 1981). C_f is a dimensionless friction coefficient set to 0.01, as in *Stølum* [1996].

The dimensional lateral migration rate is

$$E_L = k_e R_1 \mu^{\varepsilon} \quad (5)$$

where k_e is the local lateral erosion rate constant that responds to bank erodibility, μ is the domain-averaged channel sinuosity, and ε is a dimensionless parameter set to -2/3 [*Howard*

and Knutson, 1984].

We seek to explore terrace formation for a range of constant vertical incision rates. Yet channel slope evolves in natural meandering channels as meander bends grow and suddenly shorten through cutoffs [e.g., *Knighton*, 1998; *Finnegan and Dietrich*, 2011], and slope has been hypothesized to influence vertical incision rates [e.g., *Howard and Kerby*, 1983; *Stark*, 2006; *Finnegan and Dietrich*, 2011]. If vertical incision rates were fixed, then knickpoints formed by meander cutoff could neither propagate nor diffuse [*Seidl and Dietrich*, 1992] and would comprise an increasing proportion of the channel longitudinal profile. Therefore, we set channel slope to zero to prevent slope evolution, and vertical incision rate is varied as an independent parameter. Thus, model results should most closely approximate natural streams with low slopes.

The channel cross-section is fixed and rectangular, where the channel width and depth are the bankfull values. A two-year time step is used and represents the recurrence interval of the bankfull discharge for an alluvial river [e.g., *Leopold et al*. 1960]. Given uncertainties in the formative discharge for bedrock streams [*Tinkler and Wohl*, 1998; *Whipple*, 2004], the two-year time step is used for all simulations. Neck cutoffs are identified when channel banks connect with themselves; chute cutoffs are not modeled [e.g., *Sun et al*., 1996; *Lancaster*, 1998; *Finnegan and Dietrich*, 2011]; and overbank deposition is implicitly assumed to fill meander loops immediately following cutoff [e.g., *Sun et al*., 1996; *Finnegan and Dietrich,* 2011]. The model domain is arbitrarily large in the cross-valley direction and periodic in the along-valley direction, which permits the channel axis to wander freely. The along-valley length of the model domain is set to 120 channel

widths, or approximately ten meander wavelengths [*Leopold et al*., 1960]. The initial topography is a flat plane, with the channel inset one channel depth.

Although several existing studies model valley widening by channel migration [*Howard*, 1996; *Lancaster*, 1998; *Finnegan and Dietrich*, 2011], models with spatial variations in bank strength yield predictions for meandering channel trajectory that are generally sensitive to grid resolution except in cases of large channel migration rates [*Limaye and Lamb,* 2013]. Therefore, we couple the centerline evolution model to the vector-based method of *Limaye and Lamb* [2013] for bank-material tracking, which does not use grids and hence overcomes the grid resolution limitation. We track two classes of material in the valley, which can be assigned distinct erodibilities: bedrock and sediment. The local channel migration rate is scaled according to the fraction of bank material that is bedrock, as measured from the channel bed to the bank-full depth

$$k_e = k_s (1 - f_b) + k_b f_b. \quad (6)$$

Fluxes of water and sediment are not explicitly tracked; instead the modeling goal is to predict channel evolution given that different channel migration rates will occur in areas with primarily sediment versus primarily bedrock banks.

3.2. Automated terrace detection

For each simulation, surface age, land-surface topography, bedrock topography and sediment thickness are saved for quantitative statistical comparison of resultant terrace attributes. In order to track the influence of channel evolution on the landscape we employ a new, automated algorithm to detect terraces in the simulated topography, similar to *Stout and Belmont* [2013]. The algorithm identifies terraces as areas with low local relief,

characterized by the standard deviation of elevation over a fixed 30 x 30 meter window. The threshold local relief is set at 1 m, a scale that approximates the minimum difference in elevation commonly used to differentiate terrace riser elevations (i.e., Δz) [e.g., *Personius*, 1995; *Berg*, 1996; *Wegmann and Pazzaglia*, 2002; *Gran et al*., 2013], considering the disguising effects of vegetation, hillslope processes, and inherent irregularity of the terrace tread. Qualitatively, the same relief threshold identifies most terraces in digital elevation models of natural landscapes. The relief threshold is important for determining the spatial extent of terrace and the number of terrace levels, as will be discussed in Section 4.

Any landscape element that is less than one meter above the channel is classified as belonging to the channel/floodplain, and is removed from consideration as a terrace. A threshold area of 100 m^2 is applied to reduce spurious terrace detections [e.g., *Fuller et al*., 2009]. Additionally, abandoned channel beds in meander cutoff loops are automatically identified using their large perimeter to area ratio and excluded from consideration as terraces. Each group of contiguous pixels that meets the local relief and elevation criteria is identified as a terrace object, which permits measurement of individual terrace attributes including mean surface elevation and age, slope, dip direction, area, length, and width. We define length and width as the maximum distance spanned by the terrace parallel and perpendicular to the mean valley direction, respectively. For natural terraces, individual terrace surfaces may be diachronous because of longitudinal differences in abandonment time, for example due to spatially variable sediment evacuation [*Weldon*, 1986] or knickpoint propagation [*Seidl and Dietrich*, 1992; *Zaprowski et al*., 2001; *Finnegan*, 2013]. These factors are not included in the simulations, and in general the simulated topography

does not exhibit systematic streamwise trends in surface age.

We identify paired terraces automatically and objectively. A rectangular bounding box is fit to each individual terrace, and a search window with a width approximately equal to the width of the terrace is constructed by extending the bounding box in the valley-perpendicular direction. The local valley azimuth is determined by smoothing the local channel planform trace. If the search window overlaps another terrace on the other side of the active channel and the mean terrace elevation with respect to the local channel elevation differs by less than a threshold value then the terraces are flagged as paired. Considering the threshold local relief for terrace riser definition (1 meter over a 30 meter baseline) and the range of terrace widths (commonly tens to hundreds of meters), a single terrace tread can span several meters in elevation. Therefore, we identify terraces with mean elevations within 2 meters of each other as paired. This pairing criterion is relatively conservative because terraces with overlapping elevation ranges are classified as unpaired if the difference in mean terrace elevation exceeds 2 meters, or if terraces are separated along the valley.

Commonly terrace surfaces in a given catchment are grouped into unique levels according to their elevation with respect to the channel [e.g., *Baker and Penteado-Orellana*, 1977; *Wegmann and Pazzaglia*, 2002; *Fuller et al*., 2009], which along with sedimentologic characteristics and ages [e.g., *Baker and Penteado-Orellana*, 1977; *Blum and Valastro*, 1994; *Bridgland and Westaway*, 2008; *Wegmann and Pazzaglia*, 2009] are used to identify surfaces formed at similar times and by similar processes. In order to identify the number of unique terrace levels consistently across different simulations, we

classify terraces with mean elevations that fall within the same elevation bin as belonging to the same level. The elevation bin height (Δz) is set at 1 meter, consistent with reported variations of strath elevation and minimum differences in terrace elevation [e.g., *Personius*, 1995; *van den Berg*, 1996; *Wegmann and Pazzaglia*, 2002; *Gran et al*., 2013]. The time intervals between unique terrace levels ($\Delta t_{terrace}$) is calculated by sorting the unique terrace levels by age, then differencing these ages. Unless otherwise noted, we analyze the median value ($\Delta t_{terrace,50}$) of this distribution of time intervals.

3.3. Modeled parameter space

We conducted two sets of simulations: one with constant bank-strength, and the other with variable bank-strength (Table 2). In both cases, the channel width-to-depth ratio (w_c*) is fixed at 20 in our simulations—a value within the range of mixed bedrock-alluvial channels [*Yanites and Tucker*, 2010] and alluvial meandering channels for moderate valley slopes [e.g., *Parker*, 1976]. Though some strath terraces date to before 100 ka [e.g., *Hancock et al*., 1999; *Pan et al*., 2003], terraces are commonly dated to several or tens of thousands of years old [e.g., *Blum and Valastro*, 1994; *Merritts et al*., 1994; *Fuller et al*., 2009; *Gran et al*., 2013]. Consequently, in our simulations we employ a maximum dimensional simulation time (t) of 100,000 years.

In the constant bank-strength simulations, we separately vary the non-dimensional vertical incision rate (E_V*) and the non-dimensional simulation time (t*) while holding the other parameters constant. We vary E_V* from 0.002 to 200, representing a range of maximum lateral erosion rates from 1 mm/yr (i.e., highly resistant bedrock) to 1 m/yr (i.e., highly erodible floodplain sediments), and a range of dimensional vertical incision rates

from 0.1 mm/yr (i.e., a slowly uplifting continental interior environment) to a high of 10 mm/yr (i.e., an active orogen) [*Montgomery*, 2004]. We vary t^* from 1 to 5000 (i.e., the time for the channel to migrate laterally 1 to 5000 channel widths in sediment bank-materials).

The variable bank-strength simulations involve tracking the evolving spatial distribution of bedrock and sediment, and thus are more computationally intensive [*Limaye and Lamb*, 2013].

Therefore, instead of an exhaustive exploration of model parameters for cases with variable bank strength, we focus our analysis on the effect of changing bedrock bank-strength. Because erodibilities are assigned to bedrock and sediment in this subset of simulations, we modify Eq. 1b to define separate non-dimensional vertical incision rates for lateral erosion in bedrock

$$E_{Vb}^* = \frac{E_V w_c}{E_{Lb} h_c} \tag{7a}$$

and in sediment

$$E_{Vs}^* = \frac{E_V w_c}{E_{Ls} h_c}, \tag{7a}$$

where E_{Lb} and E_{Ls} are the maximum lateral erosion rates in bedrock and sediment, respectively. E_{Vb}^* is varied from 0.004 to 4. To isolate the influence of this variable, we fix the non-dimensional vertical incision rate for sediment banks ($E_{Vs}^* = 0.002$) and the non-dimensional simulation time ($t^* = 5000$) for these cases. The variable bank-strength cases involve an additional parameter, the non-dimensional initial alluvial-belt width (w_{ab}^*), due to erodibility differences between sediment and bedrock. In order to characterize the first-

order influence of a finite-width initial alluvial-belt, we set $w_{ab}^* = 0.1$ (i.e., the channel is initially confined within a zone of sediment fill one channel depth in thickness, with bedrock at the lateral boundaries and at the channel bed (Fig. 5A)). See *Limaye and Lamb* [2014] for simulation results that vary w_{ab}^*.

The initial channel sinuosity is established by evolving an initially straight channel seeded with random, meter-scale noise for a fixed dimensionless simulation time $t^* = 500$ [*Limaye and Lamb*, 2014]. The kinematic evolution of simulated meandering channels is highly sensitive to initial planform geometry [e.g., *Frascati and Lanzoni*, 2010], which causes different patterns of erosion and terrace development for the same model parameters. Consequently, we run each simulation with constant bank-strength and a unique set of parameters ten times, each with a different initial, sinuous channel planform geometry. Terrace statistical distributions, including the time between terrace levels ($\Delta t_{terrace}$), and maximum terrace length, slope, dip direction, and pairing fraction, are computed separately for each simulation, and then considered collectively for each set of parameters. We set $\Delta t_{terrace}$ as undefined when it is undefined for more than half of the simulations with the same parameters but different initial channel geometry. Because simulations that track bank-strength differences are more computationally intensive, individual simulations are conducted for each unique set of parameters in these cases.

4. Results for intrinsically generated terraces

In this section we present simulation results for terrace formation. We begin by describing the types of landscapes and terraces formed for meandering with constant vertical incision and constant bank-strength. Next, we separately analyze the distribution of

terrace ages and controls on terrace geometry—including terrace slope, dip direction, length, and pairing—for cases with constant bank-strength. In Section 5 we then consider the effects of variable bank-strength on terrace formation and geometry. Finally, in Section 6 we compare examples of terrace formation by pulsed and constant vertical incision rates.

4.1. Types of terraces formed by the numerical model for constant bank-strength

We first consider how t^*, which reflects the amount of lateral channel migration, and E_V^*, which describes the competition of river vertical incision and lateral erosion, influence terrace formation for cases where topography forms due to meandering and vertical incision. Spatial variations in bank strength that would otherwise steer channel migration [*Limaye and Lamb*, 2014] are omitted in this section, and all other non-dimensional numbers are fixed to baseline values ($w_c^* = 20$).

Qualitatively, the simulations generate three types of landscapes, and Figure 3 shows examples of terraces formed in these different regimes. In the absence of vertical incision, the meander bends grow to the point of neck cutoff, which causes them to straighten before growing anew. Adjacent meander bends can grow at different rates and times, leading to a spatially complex pattern of erosion. The elevation set in the area swept by the channel is determined by the vertical incision rate, with higher vertical incision rates generating higher surface slopes and greater vertical relief. Thus, the ratio of vertical to lateral erosion influences the valley aspect ratio [*Limaye and Lamb*, 2014] and smaller-scale terrace attributes.

For $t^* = 5000$ and $E_V^* = 0.003$ (Fig. 3A), channel lateral migration is extensive and vertical incision is slow compared to lateral erosion, so the channel erodes broad surfaces

that are continuous along-valley, similar to the Colorado River terraces (Fig. 1D). All eroded surfaces that are above the channel/floodplain elevation window are classified as terraces. The curves in the terrace margins and in the shaded relief indicate that the surfaces formed by the growth of numerous meander bends that each eroded a separate swath. Because of the relatively low vertical incision rate, the channel incised vertically only minimally between successive cycles of meander loop growth and cutoff. As a result, the surfaces eroded by the channel have similar elevations, and thus contribute to forming the same terrace surface.

For $t^* = 108$ and $E_V^* = 0.7$ (Fig. 3B), channel lateral migration is also extensive, but the higher relative vertical incision rate impacts terrace properties in two ways. First, less area near the channel falls beneath the minimum elevation threshold for classification as a terrace, so terraces occur closer to the channel. Second, the terraces are smaller, more numerous, and bounded by individual meander cutoff loops, similar to the Clearwater River terraces (Fig. 1A). This terrace geometry develops because under the relatively high vertical incision rate, the channel incises vertically a substantial amount between successive cycles of meander bend growth and cutoff. As a result, when the channel reoccupies a portion of the landscape, it commonly does so at a lower elevation and cuts a terrace riser (Fig. 2C). For $t^* = 5$ and $E_V^* = 200$ (Fig. 3C), channel lateral migration is limited and vertical incision greatly outpaces lateral erosion, and all topography takes the form of slip-off surfaces and occasional meander cutoff loops, as is common for meanders deeply entrenched in bedrock [e.g., *Harden*, 1990]. No terraces form because the surface slope, and thus local relief, is too high along the channel-eroded surfaces.

These examples illustrate that t^* and E_V^* strongly influence the number and geometry of river terraces formed by meandering with constant vertical incision. Low t^* results in minimal valley widening and terrace formation, whereas high t^* causes substantial valley widening and favors terrace formation. Low E_V^* favors low-relief valleys with few terrace levels, while high E_V^* forms slip-off surfaces rather than terraces. In subsections 4.2-4.6 we analyze the age distribution and geometry of terraces formed across a similarly broad range of t^* and E_V^*.

4.2. Terrace age distributions

In this subsection we separately vary the non-dimensional simulation time (t^*) and the non-dimensional vertical incision rate (E_V^*) in order to isolate their influences on terrace age. Figure 4A shows time between unique terrace levels ($\Delta t_{terrace,50}/t_{vert}$) as a function of t^* for several fixed values of E_V^*. In general, terraces do not form at the margins of parameter space where different terrace definition thresholds are encountered. Terraces do not form for three reasons. First, relatively low non-dimensional vertical incision rates do not generate sufficient relief for terrace formation (e.g., $E_V^* < 0.02$ for $t^* < 1000$; Fig. 4A). Second, for relatively low non-dimensional simulation times lateral channel migration is insufficient to bevel a terrace surface (e.g., $t^* < 40$; Fig. 4A). Third, for relatively high non-dimensional vertical incision rates ($E_V^* > 1$; Fig. 4B) surface slopes formed by the laterally migrating and vertically incising channel exceed the threshold for local relief to be classified as terrace treads, and slip-off surfaces form instead (Fig. 3C). Subsequent plots highlight regimes where terraces do not form for one of these three reasons. For increasing E_V^*, $\Delta t_{terrace,50}/t_{vert}$ is defined over a broader range of t^* because the

channel generates more vertical relief, and potentially more terraces, for the same dimensionless simulation time.

By definition, no data falls below $\Delta t_{terrace,50}/t_{vert} = 1$ because t_{vert} represents the minimum timescale of terrace formation. For all values of E_V* with defined $\Delta t_{terrace,50}/t_{vert}$, $\Delta t_{terrace,50}/t_{vert}$ is near unity for relatively low t*, which corresponds to limited lateral channel migration. Because re-working of existing surfaces is limited in these cases, the time between formation of unique terrace levels is set only by the timescale for sufficient relief generation, and so $\Delta t_{terrace,50} \approx t_{vert}$. As t* increases, $\Delta t_{terrace,50}/t_{vert}$ increases approximately logarithmically because continued channel migration re-works areas previously visited by the channel. Frequent re-working of surfaces near the channel can prevent abandonment of these areas as terraces (e.g., Fig. 3A), or alternatively destroy existing terraces; both processes result in longer time intervals between unique terrace levels. The logarithmic increase in $\Delta t_{terrace,50}/t_{vert}$ with dimensionless simulation time is consistent with the finding that meander-belt width increases logarithmically with simulation time [*Howard*, 1996]. The margins of the meander belt are less likely to be visited by the migrating channel than areas close to the channel [*Bradley and Tucker*, 2013], so areas near the channel are preferentially re-worked and terraces are less likely to be preserved there. Similarly, as the meander belt widens, the likelihood of the channel eroding past the margins of the alluvial-belt decreases and the rate of meander-belt widening decreases. The rate of increase of $\Delta t_{terrace,50}/t_{vert}$ with increasing t* is generally more pronounced for relatively low E_V*, because for low E_V* the channel is more likely to re-work previously visited areas before they can be abandoned as terraces.

Figure 4B shows the time between unique terrace levels ($\Delta t_{terrace,50}/t_{vert}$) as a function of E_V* for seve increases sharply as E_V* approaches unity until $\Delta t_{terrace,50}/t_{vert}$ is undefined. This behavior occurs because the relatively high rate of vertical incision relative to lateral erosion causes high surface slopes in areas eroded by the channel and results in a greater proportion of slip-off slopes relative to terraces because of the relief threshold imposed in the definition of a terrace (Fig. 3C). As the number of terraces decreases, $\Delta t_{terrace,50} / t_{vert}$ increases until there are so few terraces that $\Delta t_{terrace,50} / t_{vert}$ is undefined. The transition from forming terraces to forming slip-off surfaces is sharpest near E_V* = 1, where the vertical incision rate typically exceeds the maximum lateral erosion rate. For t* = 5000, $\Delta t_{terrace,50} / t_{vert}$ varies widely with E_V* and is greater than for other values of t* because of increased re-working of previously visited areas.

Figure 4C shows the distribution in terrace formation time, expressed as the ratio of the 90th and 50th percentiles of the time between unique terrace levels, as a function of t* and for several fixed values of E_V*. For all values of E_V* > 0.002, where $\Delta t_{terrace,90} / \Delta t_{terrace,50}$ is defined it is relatively small (i.e., < 3) for low values of t* and typically increases with t*. This increase in the variety of time intervals between unique terrace levels indicates that terraces are destroyed by increased lateral channel migration. The rate of increase of $\Delta t_{terrace,90} / \Delta t_{terrace,50}$ with t* is similar for different values of E_V* for t* < 1000, but as in Figure 4A each curve is offset because simulations with lower E_V* require larger t* to generate terraces and for $\Delta t_{terrace}$ to be defined.

Figure 4D shows the variety in $\Delta t_{terrace,90} / \Delta t_{terrace,50}$ as a function of E_V* and for several unique values of t*. The trends in $\Delta t_{terrace,90} / \Delta t_{terrace,50}$ are very similar to those in

$\Delta t_{terrace,50}/\Delta t_{vert}$ (Fig. 4B). Except for the simulations with $t^* = 5000$, for which terrace destruction causes large variations in the terrace age distribution, $\Delta t_{terrace,90} / \Delta t_{terrace,50}$ is relatively consistent and low until it approaches $E_V^* = 1$. Terrace formation is rarer for $E_V^* = 1$, and preferentially occurs on the insides of relatively rapidly migrating meander bends; elsewhere, slip-off surfaces form. In this case, the lower terrace formation frequency and the terrace association with exceptionally active meander bends may contribute to greater variety in $\Delta t_{terrace,90} / \Delta t_{terrace,50}$.

4.3. Terrace slope

Terrace tread slope has been proposed to reflect the ratio of channel vertical incision to lateral erosion [e.g., *Merritts et al.*, 1994]. Long-term channel vertical incision rates are most commonly estimated by dating terrace sediments and measuring the elevation difference between the terrace and the active channel [e.g., *Repka et al.*, 1997; *Hancock et al.*, 1999; *Wegmann and Pazzaglia*, 2002; *Wolkowinsky and Granger*, 2004; *Finnegan et al.*, 2014]. Constraints on long-term channel lateral erosion rates in bedrock can be difficult to establish in this manner because the lateral migration direction may change in time and the erodibility of past bank materials is difficult to reconstruct. If the slope of the strath surface is directly set by channel vertical incision and lateral erosion [*Merritts et al.*, 1994], then the lateral erosion rate during terrace tread formation can be back-calculated from the other two variables [e.g., *Finnegan and Dietrich*, 2011].

Figure 5A shows model results for median terrace slope as a function of t^* for several fixed values of E_V^*. Terrace slope is generally insensitive to t^*, except for increases in terrace slope for $t^* > 1000$ and $E_V^* < 0.02$. This increase in terrace slope for relatively

long dimensionless simulation times and low dimensionless vertical incision rates occurs because the terraces formed under those conditions are broad, compound surfaces formed by the sweeping of many meander bends (Fig. 3A). Consequently, terrace surface slopes are set not only by instantaneous bend migration and vertical incision, but also by wandering of the channel axis that causes the channel to return to the same area at a lower elevation. For relatively high vertical incision rates, this wandering would leave a terrace (i.e., Fig. 2D); but for relatively low vertical incision rates, the scarp formed at the channel cutbank is short and is not identified as a terrace riser due to the elevation threshold for terrace identification (Section 3.3).

Figure 5B shows median terrace slope as a function of E_V^* for several fixed values of t^*. For cases in which terraces form, there is a linear relationship between median terrace slope and E_V^* for $t^* \leq 100$. Slightly higher than expected terrace slopes occur for $t^* > 100$ and $E_V^* < 0.1$ due to surface planation by channel wandering. These results suggest that despite the kinematic complexity of meandering, terrace slope is a reliable indicator of channel lateral migration and vertical incision rates in cases with constant bank-strength. The relationship between channel kinematics and terrace slope is analogous to the smaller-scale shaping of bounding surfaces by aggrading, laterally migrating bedforms [*Ganti et al.*, 2013]. Accounting for the influences of channel dimensions (w_c and h_c), the fit for $t^* \leq 100$ implies a scaling coefficient between terrace slope and the ratio of vertical incision to lateral erosion rates slightly greater than unity. Because in all simulations the channel slope is set to zero, these results are most applicable where terrace slope is significantly greater than longitudinal channel slope.

4.4. Terrace dip direction

Terraces formed by a channel that switches its direction of migration while incising vertically have been hypothesized to slope toward the center of the valley, as has been observed for an experimental alluvial fan [*Mizutani*, 1998]. Figure 6A shows an example of the distribution of terrace dip directions, measured with respect to the mean, downstream-oriented valley axis, for a set of simulations with fixed parameters but different initial channel planform geometries. Terraces with $\phi = 0^\circ$ dip parallel to the local valley orientation defined by the smoothed channel planform trace; similarly, $\phi = \pm 180^\circ$ corresponds to terrace dip in the up-valley direction. In this example, terrace dips are preferentially oriented in the valley-perpendicular direction (i.e., ±90°). As with terrace slope, terrace dip direction may be set by either instantaneous bend growth or by wandering of the channel axis during vertical incision. Thus, the terrace dip direction can develop either through the migration of a single bend (Fig. 3B), or reflect the overall orientation of a composite surface formed by the migration of different meander bends (Fig. 3A).

Figure 6B shows the most common dip direction as a function of t^* for fixed values of E_V^*. For all values of E_V^*, terraces dip in approximately the valley-parallel directions (0° and ±180°) for $t^* < 100$ and then approach valley-perpendicular dip directions for $t^* \geq 1000$ (except for $E_V^* = 0.2$, $t^* = 5000$). Figure 6C shows the strength of the preferred terrace dip direction, expressed as the ratio of the probability for the most probable dip direction divided by the median probability (P_{max} / P_{median}). The strength of the preferred terrace dip direction is highest for $t^* \leq 100$ and $t^* \geq 1000$; between these values of t^*, P_{max} / P_{median} is near unity and terraces do not show a preferred dip direction. Figure 6D shows the most

common dip direction (ϕ) as a function of E_V* for fixed values of t*. Dip direction does not respond systematically to E_V*, but is most strongly oriented in the valley-perpendicular direction for $t^* \geq 1000$. The strength of the preferred terrace dip direction does not show a consistent relationship with E_V* (Fig. 6E). The association of valley-perpendicular terrace dip direction with large values of t* (i.e., $\geq$ 1000) indicates that these surfaces form as a consequence of channel wandering rather than meander-bend growth.

4.5. Terrace length

Along-valley terrace continuity has been proposed to indicate terrace formation by external drivers rather than irregular lateral migration with vertical incision, which has been suggested to generate terraces of limited length [*Merritts et al.*, 1994; *Pazzaglia et al.*, 1998; *Wegmann and Pazzaglia*, 2002]. Figure 7 shows maximum terrace length normalized by channel width as a function of t* for several fixed values of E_V*. Maximum terrace length does not exhibit a consistent relationship with t* for cases in which terraces form; the maximum terrace length is set by the domain length and is reached for $0.006 < E_V^* < 0.2$ and $t^* > 100$. Simulations which vary E_V* for several fixed values of t* (Fig. 7B) indicate that for sufficiently long simulations, maximum terrace length plateaus at the domain length for $E_V^* < 10^{-1}$. These long terraces form because lateral erosion is rapid relative to vertical incision, and multiple generations of meander bends at different locations along the river erode a composite surface (Fig. 3A) of roughly consistent elevation. There is a sharp decrease in maximum terrace length for $0.1 < E_V^* < 1$ because the relatively higher vertical incision rates cause successive generations of meander bends

to erode surfaces as distinct elevations, so these surfaces are classified as separate and increasingly smaller terraces (Fig. 3B).

4.6. Terrace pairing

Paired terraces have been proposed to indicate an extended period of channel longitudinal profile stability and valley widening that is punctuated by increased vertical incision that simultaneously abandons terraces on either side of the channel [e.g., *Hancock and Anderson*, 2002]. In contrast, terraces formed by unsteady lateral channel migration have been proposed to be more commonly unpaired [e.g., *Merritts et al*., 1994; *Wegmann and Pazzaglia*, 2002] and numerical model results with knickpoints generated by meandering generally produce unpaired terraces [*Finnegan and Dietrich*, 2011]. In contrast, paired terraces commonly occur in our simulations through two distinct mechanisms. First, for high rates of lateral channel migration relative to vertical incision, the channel wanders extensively while generating little relief (Fig. 3A). Terrace treads with similar elevations form on either side of the channel, and in cases their differences in mean elevation are less than the threshold for classification as paired (i.e., 2 meters). Although these surfaces form at different times, their measured age differences may be within the uncertainties of dating techniques (i.e., 10^2-10^4 yr , depending on terrace age [*Hancock et al*., 1999; *Wegmann and Pazzaglia*, 2002b]). In the second mechanism for forming paired terraces, higher vertical incision rates cause terraces form roughly simultaneously at similar elevations along adjacent meander bends (Fig. 3B). We calculate the fraction of paired terraces (f_{paired}) that form in our simulations with constant vertical incision rates by

automatically determining whether each terrace is paired and then weighting the results by terrace area.

Figure 8A shows f_{paired} as a function of t^* for several fixed values of E_V^*. In all cases where terraces form, f_{paired} exceeds 0.8 and declines toward 0 as t^* increases. This rapid decline in terrace pairing occurs because of destruction of existing terraces. In only one case, for $E_V^* = 0.006$, f_{paired} increases again after its initial decrease. This result indicates that paired terraces, whether formed intrinsically or by pulses of vertical incision, may subsequently become unpaired. For simulations that vary E_V^* for several fixed values of t^* (Fig. 8B), f_{paired} initially increases with increasing E_V^* for $10 < t^* \leq 1000$, then decreases as E_V^* approaches 1 because relatively high vertical incision rates cause high surface slopes and inhibit terrace formation (Fig. 3C). Terraces that do form are more likely to be offset in elevation.

4.7. Summary of constant bank-strength simulations

For all other factors equal, simulations with low vertical incision rates relative to lateral erosion rates tend to produce larger, unpaired terraces formed by the compound sweeping of several meander bends. These terraces dip toward the valley center with slopes higher than the ratio of vertical incision rate to lateral erosion rate, and have terrace recurrence ages that are relatively large. In contrast, simulations with high vertical incision rates relative to lateral erosion rates tend to produce terraces that are smaller, paired, and bounded by meander cutoff loops. These terraces have no particular slope orientation, their gradient is directly proportional to the ratio of vertical incision rate to lateral erosion rate, and they form frequently with a recurrence timescale that is set by the time needed to

generate the relief of one terrace. In time lateral erosion destroys terraces, which in general results in less pairing and larger time gaps between terraces. Terraces may not form for short simulation times due to insufficient vertical or lateral erosion, and due not form at very high vertical incision rates. In the next section, we fix the extent of channel migration (i.e., the dimensionless simulation time t^*) and examine the effect of spatial differences in bank strength between bedrock and sediment on model predictions for terrace age and geometry.

5. Effects of variable bank-strength on simulations

Spatial differences in bank resistance—for example, due to lithology [e.g., *Montgomery*, 2004], or sediment grain size [e.g., *Fisk*, 1947; *Sun et al*., 1996]—can alter patterns of channel migration. Simulations suggests that in bedrock river valleys, differences in bank strength between alluvial sediments and bedrock can explain a variety of valley morphologies and promote unsteady lateral channel migration and terrace formation [*Limaye and Lamb*, 2014]. In this section we consider factors that control strath terrace formation and geometry for cases in which the channel encounters mixed bedrock and alluvial bank-materials. For this subset of simulations, we set the dimensionless initial alluvial-belt width (w_{ab}^*) to 0.10, which corresponds to a zone of sediment fill one channel depth in thickness and one-tenth the width of the unconfined meander-belt [*Camporeale et al*., 2005] (Fig. 9A). Because of the differences in bank strength between bedrock and sediment, the non-dimensional vertical incision rate takes two different forms for these simulations (Eq. 7). Here we vary the non-dimensional vertical incision rate in bedrock banks (E_{Vb}^*) from 0.004-4 and hold the non-dimensional vertical incision rate in sediment

banks (E_{Vs}* = 0.002). Because E_{Vs}* is fixed, the relative bank erodibility of bedrock versus sediment decreases as E_{Vb}* increases. Non-dimensional simulation time is fixed to the maximum value explored in the constant bank-strength cases (t* = 5000).

Figure 9 shows examples of terrace formation for three cases with t* equal to that in Figure 3A and E_{Vb}* between the values of E_V* in Figures 3A and 3B. Initially, the channel develops sinuosity within the sediment-filled zone but turns at sharp angles where it meets the confining bedrock walls at the alluvial-belt margin (Fig. 9A). From this initial condition, three different regimes of channel lateral migration and terrace evolution can occur depending on the values of E_{Vs}* and E_{Vb}* [*Limaye and Lamb* 2014]. Here, we fix E_{Vs}* to isolate the influence of bedrock bank strength through E_{Vb}*.

In the first regime, the channel actively erodes the bedrock boundaries at the edge of the alluvial belt, and strath terraces form (Fig. 9B; E_{Vb}* = 0.02) beyond the margin of the initial alluvial-belt regardless of whether the channel entrenches in bedrock. In the second regime, the channel initially migrates through the sediment-filled zone and bevels the sediment-bedrock interface at the channel bed, but eventually entrenches in bedrock because the channel incises vertically into bedrock at a rate faster than the lowering of the sediment-bedrock interface [*Limaye and Lamb*, 2014]. The entrenched channel abandons terraces, which are usually paired (Fig. 9C; E_{Vb}* = 0.07). In the third regime, the channel remains mobile within the alluvial belt but is impeded by relatively resistant bedrock at the alluvial-belt boundaries. Consequently, the channel consistently erodes the same portions of the alluvial belt while incising vertically, and terraces are rarely abandoned (Fig. 9D; E_{Vb}* = 0.71). To identify simulations in which the channel entrenches in bedrock, we track

the fraction of bedrock at the cutbank measured from the channel bed up to the bankfull height. The channel is classified as entrenched in bedrock if > 90% of the channel length has an all-bedrock cutbank. Subsequent plots differentiate cases where the channel is entrenched or unentrenched, and those that do not generate terraces. In the following paragraphs, terrace ages and geometries for the cases with variable bank-strength are compared to the results for the constant bank-strength simulations collectively, as well as a single constant bank-strength case with a dimensionless vertical incision rate ($E_V^* = 0.002$) equal to the dimensionless vertical incision rate for sediment banks ($E_{Vs}^* = 0.002$). The latter case is indicated with a star and referred to as the constant bank-strength control case.

Figure 10A shows the dimensionless time interval between unique terrace levels ($\Delta t_{terrace,50} / t_{vert}$) as a function of E_{Vb}^*. For simulations in which terraces form, $\Delta t_{terrace,50} / t_{vert}$ varies between 1 and 3 for all but one simulation—a similar timescale range as for the ensemble of constant bank-strength cases (Fig. 4A-B) but with a greater proportion of short time intervals between terraces. $\Delta t_{terrace,50} / t_{vert}$ is also lower than for the constant bank-strength control case. Terraces do not form for three simulations near $E_{Vb}^* = 1$ due to highly resistant bedrock boundaries that preferentially steer meander bends to migrate down-valley and consistently sweep the alluvial belt, thus preventing terrace formation (e.g., Fig. 9C). For cases in which terraces form, there are no systematic trends between $\Delta t_{terrace,50} / t_{vert}$ and E_{Vb}^*.

Median terrace slope (Fig. 10B) generally increases with E_{Vb}^* for $E_{Vb}^* < 0.1$, similar to the trend for constant bank-strength cases (Fig. 5B) but with additional scatter owing to the more complex patterns of channel migration, which occurs at different rates in

bedrock and sediment. The constant bank-strength control case yields a slightly lower terrace slope than predicted for the variable bank-strength cases. For $E_{Vb}^* > 0.1$, terrace slopes no longer increase. Thus, terrace slope is a less reliable indicator of the ratio of vertical incision rate to lateral erosion rate in bedrock for cases where bank strength varies spatially.

The preferred terrace dip direction (Fig. 10C) does not vary systematically with E_{Vb}^*, and includes several cases in which terraces preferentially dip valley perpendicular (i.e., ± 90°). In comparison, a valley-perpendicular terrace dip direction occurs for a large range of dimensionless vertical incision rate for constant bank-strength cases with $t^* \geq 1000$ (Fig. 5B), including the constant bank-strength control case. The greater variety in dip direction for the variable bank-strength cases is consistent with steering of channel migration and erosion in different directions due to evolving, spatial differences in bank strength. Maximum terrace length (Fig. 10D) approaches the domain length for $E_{Vb}^* < 10^{-2}$, similar to constant bank-strength cases (Fig. 7); maximum terrace length generally declines as E_{Vb}^* increases. The lower erodibility of bedrock relative to sediment limits valley widening to be local in extent, and so terraces are shorter in length compared to the constant bank-strength control case.

Paired terraces in the variable bank-strength cases form through two mechanisms. In cases with relatively erodible bedrock and low vertical incision rates (i.e., $E_{Vb}^* \leq 0.003$; Fig. 9D), paired terraces form by channel wandering with low relief generation, similar to constant bank-strength cases. For the range E_{Vb}^* explored in the simulations, terraces do not occur simultaneously along adjacent, growing meander bends, as occurs in cases for

constant bank-strength simulations. Instead, channel entrenchment in bedrock can abandon extensive paired terraces in the former alluvial belt (Fig. 9C). The fraction of paired terraces (Fig. 10D) does not vary systematically with E_{Vb}*, but the highest values of f_{paired} occur for E_{Vb}* < 0.1 except for cases in which the channel entrenches. Paired terraces are relatively rare for E_{Vb}* > 0.1. The constant bank-strength control case does not generate paired terraces.

In summary, model results suggest that spatial differences in bank strength between bedrock and sediment cause distinct patterns of channel migration and entrenchment in bedrock that can alter patterns of terrace formation and geometry compared to cases with constant bank-strength. For these simulations, increasing E_{Vb}* is equivalent to increasing the strength of bedrock banks, because E_{Vs}* is held constant. In comparison to constant bank-strength cases, for variable bank-strength cases with E_{Vb}* > 0.002 there are smaller age differences between terraces, indicating that terraces form more frequently or are preserved for longer periods; terraces are smaller, because bedrock banks suppress the formation compound surfaces by multiple meander sweeps; and terraces are more commonly paired. These differences are consistent with reduced lateral migration due to the presence of resistant bedrock. Relationships between terrace slope and dip direction and E_{Vb}* are more scattered than for constant bank-strength cases, likely due to the relatively irregular lateral migration caused by spatial differences in bank strength. We note that the quantitative trends in terrace formation and geometry for variable bank-strength cases may to vary for different values of E_{Vs}*, t*, and w_{ab}*. Qualitatively, simulations with E_{Vb}* > 0.002 result in terrace geometries that more strongly resemble natural river terraces, in that

terrace boundaries are sub-linear at valley margins (e.g., Figure 1A and 1B). In comparison to cases with constant bank-strength, in which terrace shapes are generated by the imprint of one or more smoothly curved meander loops (Fig. 3), for the variable bank-strength cases terraces can form with shapes that do not directly mirror individual meander loops (e.g. Fig. 9B) because meander bends straighten at boundaries between sediment and bedrock bank materials.

6. Effects of pulses of vertical incision on simulation results

Simulations in the preceding sections have all involved constant rates of vertical incision, but pulsed vertical incision has been suggested to drive terrace formation in many settings. Potential mechanisms for pulsed vertical incision include changes in sea-level [e.g., *Fisk*, 1944], tectonic displacement [e.g., *Yanites et al*., 2010], and climate change [e.g., *Hancock and Anderson*, 2002]. In all of these cases, vertical incision rates may be quasi-periodic; for example, 100-kiloyear Milankovich cycles [*Hays et al*., 1976] have been suggested to drive terrace formation [*Hancock and Anderson*, 2002; *Bridgland and Westaway*, 2008]. But as shown in Section 4, intrinsically generated terraces from meandering can also form quasi-periodically ($t_{terrace} \sim t_{vert}$). In this subsection we compare examples of terraces formed under pulsed and constant vertical incision rates.

Figure 11 shows topography formed by a meandering river over 100,000 years for three scenarios: the first with pulsed vertical incision on a repeating 25,000 year timescale, the second for a constant vertical incision rate (similar to simulations in Section 4), and the third with pulses vertical incision with greater amplitude but shorter duration. The total vertical incision is the same in all cases, bank strength is constant, and the maximum lateral

erosion rate (1 m/yr) corresponds to sediment bank materials. Thus, over the course of the simulations the average non-dimensional vertical incision rate is the same in all three cases (E_V* = 0.004, slightly greater than in Figure 3A). The non-dimensional simulation time (t* = 5000) is equal to that in Figures 3A and 9B-D, and the channel width-to-depth ratio is also fixed to its baseline value (w_c* = 20). The different vertical incision histories (Fig. 11A-C) cause differences in topography, but the lateral extent of channel migration is the same in all three cases (Fig. 11D-F). Mean terrace elevations are binned at 1 meter (i.e., Δz).

The first case with pulsed vertical incision includes four full cycles of vertical incision (Fig. 11A), but several more unique terraces levels form (Fig. 11J) because the pulses are not instantaneous, and irregular lateral channel migration during a period of relatively high vertical incision rate can create more than one terrace level. In comparison, the case with a constant vertical incision rate yields a planview terrace extent very similar to that for the first case with cyclic vertical incision (Fig. 11E), and several distinct terrace levels form (Fig. 11K). From Section 4, the timescale for terrace formation ($\Delta t_{terrace,50}$) for a constant vertical incision rate is approximately 1-4 times the timescale for vertical incision to generate a unique terrace level (t_{vert}; Eq. 2); for the simulation in Figure 11E, this corresponds to $\Delta t_{terrace,50} \approx$ 5000 to 20,000 yr, which approaches the 25,000 period of vertical incision pulses. Thus, in this example the intrinsic frequency of terrace generation by meandering is similar to the frequency of terrace formation driven by external forcing. The simulation with relatively brief, high-amplitude pulses of vertical incision (Fig. 11C) also has a similar planview terrace extent (Fig. 11F) compared to the other two cases. Moreover,

the topographic cross-section (Fig. 11I) is nearly identical to the corresponding cross-section for the constant vertical incision-rate case (Fig. 11H). The distribution of mean terrace elevations (Fig. 11L) in the case with sharp vertical incision pulses forms terraces at more distinct elevation groupings than in the first pulsed-incision case, because in the case of the sharper pulses the river transitions more quickly between different elevations and thus erodes the valley to more discrete elevations. However even in this case, the terraces abandoned by the first vertical incision pulse were eroded.

These examples suggest that terraces formed in environments with low ratios of vertical to lateral erosion rate should be interpreted with caution, particularly with respect to changes in external forcing. In these environments, lateral channel migration rather than vertical incision exerts the dominant control on erosion patterns and can generate quasi-periodic terrace sequences due to meandering. In addition, the duration and amplitude of vertical incision pulses affects their expression in the terrace record: brief, high-amplitude vertical incision pulses are more sharply preserved in the distribution of terrace levels.

7. Comparison to natural river valleys

To relate model results for terrace formation frequency and geometry to natural river valleys, we measure terrace attributes at the field sites introduced in Figure 1 and compare their attributes to those in the simulations. Comparison between simulated and natural topography raises two methodological considerations. First, topography develops in the simulations entirely through fluvial erosion and deposition, and so all automatically mapped surfaces are fluvial in origin and can be identified from topography alone. In practice, automated feature detection for natural topography yields spurious terrace

detections [e.g., *Routt and Belmont*, 2013], and natural terraces are identified using sedimentologic observations in addition to topography [e.g., *Merritts et al*., 1994; *Bridgland and Westaway*, 2008; *Pazzaglia and Wegmann*, 2009]. Therefore, for natural landscapes we use existing maps to identify terrace extent. Second, in the simulations a uniform sediment thickness equal to the channel depth is deposited on all strath surfaces, so except for absolute elevation the geometry of terrace straths and treads is the same. For natural strath terraces, the tread geometry can deviate from the strath geometry [e.g., *Fuller et al*., 2009] because the tread represents the top of the sedimentary deposit that caps the strath [*Pazzaglia and Wegmann*, 2009]. This distinction in form between the terrace tread and strath is important because the strath is more directly linked to patterns of lateral and vertical bedrock erosion by the channel. In general, however, the three-dimensional strath geometry is difficult to independently constrain. Therefore to facilitate comparison between simulated and natural terraces, we utilize the terrace tread (surface) topography and assume that its geometry mirrors that of the underlying strath. Terrace tread extents were extracted from geologic maps, which are partially shown in Figure 1, except for the Le Sueur River where terraces were mapped automatically using the methods in Section 3.3.

Other effects may complicate relationships between the simulated topography and natural river terraces. For example, terrace dip direction and slope magnitude may be altered by hillslope processes, including colluvium accumulation near terrace margins [e.g., *Niviere and Marquis*, 2000]. Terrace slope is also influenced by the instantaneous channel longitudinal profile [e.g., *Merritts et al*., 1994] and may respond to knickpoint propagation [*Frankel et al*., 2007; *Finnegan*, 2013]. Moreover, fluvial dissection may alter terrace

treads [e.g., *Wegmann and Pazzaglia*, 2009] and separate laterally extensive terrace surfaces into several smaller features, which would cause measurements of terrace length to decrease with time. We acknowledge these complications, and herein focus on identifying terrace geometric characteristics set by meandering with constant vertical incision alone.

We consider terraces that have been suggested to form in diverse ways. The Clearwater River (Washington), the Wind River (Wyoming), and the Colorado River (Texas) have all been suggested to have developed terraces by unsteady vertical incision driven by climate change [*Blum and Valastro*, 1994; *Hancock and Anderson*, 2002; *Wegmann and Pazzaglia*, 2002b]. The Le Sueur River (Minnesota) has abandoned many terraces as a result of knickpoint propagation following the rapid drainage of a glacial lake [*Gran et al*., 2013], and strath terraces along the Mattole River (California) have been argued to form by steady vertical incision and unsteady lateral erosion [*Merritts et al*., 1994]. In the following subsections we analyze the geometry of terraces within these valleys and discuss how terrace geometry relates to vertical incision history. To compare model predictions for terrace geometry to the natural cases, for each valley we utilize the modern channel width and depth, and estimate the mean vertical incision rate and lateral erosion rate during the time of terrace formation (Table 3). For all of these valleys, we compare terrace properties to simulation results for a constant bank-strength regime (for a fixed value of dimensionless simulation time, $t^* = 5000$) where model predictions are clearer.

7.1. Terrace formation frequency

For most river valleys, dates are too sparse to sufficiently constrain a characteristic time interval between terrace levels. However, the estimated non-dimensional vertical incision rate (E_V*; Table 3) is within the range of intrinsic terrace formation (approximately E_V* < 1; Fig. 4B) for all of the valleys in Figure 1. This suggests that under conditions of constant vertical incision, river terraces would be expected to form in these valleys. We note that for the Le Sueur River, background rates of vertical incision between the passage of knickpoints may be too slow to generate terraces. The San Juan River, which generally lacks terraces, also has an estimated E_V* = 1.26, which is higher than for the other rivers and in the portion of model parameter space where slip-off surfaces form instead of terraces.

Another criterion related to terrace formation frequency is the separation of terrace elevations. For the intrinsically generated terraces, terraces form on a timescale similar to the timescale for relief generation (t_{vert}; Fig. 4). This terrace formation interval implies that groups of intrinsically generated terraces should be separated vertically by a multiple of 1-4 times the threshold relief for identification as a unique terrace level (1 meter) unless re-working of previously visited areas is extensive. To test whether natural river terraces are consistent with terrace formation with constant vertical incision rates, we extract the mean elevation of terraces mapped for the valleys in Figure 1, and calculate the median elevation difference between unique terrace levels in the same manner used for the simulated terraces. The terrace elevations are translated to a median time difference between terrace levels ($\Delta t_{terrace,50}$) using the vertical incision rate at each site (Table 3) and

$$\Delta t_{terrace} = \frac{\Delta z_{50}}{E_V}, \quad (8)$$

where Δz_{50} is the median elevation between unique terrace levels. Similarly, the minimum timescale for relief generation sufficient to abandon a terrace (t_{vert}) is estimated for each valley following Eq. 2. These calculations assume a constant vertical incision rate; unsteady vertical incision rates would yield different values of $\Delta t_{terrace,50}$ and t_{vert}.

Figure 12 shows the estimated, median time between terrace levels versus the minimum terrace formation time for each valley. The estimated time between terrace levels for the Clearwater River and the Colorado River is consistent with the terrace formation times predicted by the simulations with constant vertical incision rates. Compared to the simulations with constant vertical incision rates, the estimated time between terrace levels is slightly longer for the Mattole River and the Wind River, and slightly shorter for the Le Sueur River.

7.2. Terrace slope

Figure 13 shows terrace slope for the natural river valleys versus the estimated non-dimensional vertical incision rate. The natural terrace slopes are similar to the simulated terrace slopes except for the Colorado River terraces, which have substantially higher slopes than predicted with the simulations. We speculate that either dissection of terrace treads or errors in mapping (i.e., inclusion of relatively steep areas at terrace margins) may contribute to these relatively high slopes.

7.3. Terrace dip direction

Figure 14 shows the distribution of terrace dip directions (ϕ) for each of the field sites, measured with respect to the local valley axis orientation. The Mattole River (Fig.

14A) possesses the fewest number of terraces; while each dips in a distinct direction, none dip parallel to the valley, which is consistent with the conceptual model in *Merritts et al*. [1994] of terraces formed by lateral erosion and constant and vertical incision that dip toward the valley center. Terraces for the Colorado (Fig. 14B), Le Sueur (Fig. 14D), and Clearwater Rivers (Fig. 14E) all show a variety of orientations, and preferred orientations in directions oblique or nearly perpendicular to the valley axis. Finally, the Wind River terraces show the greatest preference for down-valley dips, although all terraces show at least a 30˚ deviation from the valley-parallel direction. The dominant terrace dip direction for each valley plotted against E_V* shows that terraces oriented perpendicular to the valley trace occur at a variety of values of E_V*. In contrast, in the constant bank-strength simulations, terraces dip perpendicular to the valley trend more commonly for moderate values of E_V* (Fig. 14F).

7.4. Terrace length

Figure 15A shows maximum terrace length, normalized by channel width, for each of the field sites. In contrast to the constant bank-strength simulations, for which the longest terraces occur for low values of E_V* and decline systematically as E_V* approaches 1, for the natural terraces there is not a systematic trend in terrace length. Notably, the Colorado, Le Sueur, and Mattole River terraces all have similar $L_{terrace,\,max}/w_c$, across a range of channel dimensions and E_V* (Table 3). The exceptionally large $L_{terrace,\,max}/w_c$ for the Wind River greatly exceeds the modeled maximum terrace length for the same value of E_V* (for which model domain length is greater than maximum terrace length), which suggests that at least some of the Wind River terraces formed through means other than meandering with

constant vertical incision. Terraces for the Colorado River show substantially lower lengths than predicted by the simulations. Notably, the simulations do not include tributaries, which bound some terraces in the Colorado River valley and thus limit their length.

7.5. Terrace pairing

Figure 15B shows the fraction of paired terraces, weighted by terrace area, for each of the field sites. Only the Colorado River, Le Sueur River and Clearwater River terraces meet the pairing criteria of (1) adjacency across the river, and (2) mean terrace elevation within a threshold range (2 meters). The pairing results are qualitatively consistent with the model prediction for constant bank-strength cases that the pairing fraction peaks at intermediate values of E_V*. The fraction of paired terraces along the Le Sueur River is exceptionally high, and consistent with models that predict a large fraction of paired terraces for cases with pulsed vertical incision.

8. Discussion

Terrace formation is commonly argued to require periods of channel longitudinal profile stability and valley widening that are punctuated by pulses of vertical incision [e.g., *Hancock and* Anderson, 2002; *Pazzaglia*, 2013]. In cases, unsteady lateral channel migration has been suggested to influence the river terrace record even with constant vertical incision rates [*Davis*, 1909; Merritts *et al*. 1994; *Pazzaglia et al*., 1998], but this hypothesis has not been explored quantitatively. The numerical model that couples unsteady lateral channel migration by meandering with constant vertical incision suggests that across a broad range of river lateral and vertical incision rates, river terraces form after

the river generates sufficient relief to abandon a terrace (i.e., $t_{terrace}/t_{vert} \sim$ 1-4; Fig. 4). Simulations by *Finnegan and Dietrich* [2011] also involved terrace formation linked to meandering, wherein meander growth and cutoff generated knickpoints that caused unsteady vertical incision rates. In comparison, the present simulations indicate that a broader suite of meandering rivers—including low-sloping rivers without knickpoints—can generate terraces under steady external forcing.

Climate change has undoubtedly driven dramatic changes in water discharge and sediment supply, particularly near the headwaters of glaciated catchments [e.g., *Hallet et al*., 1996; *Hancock and Anderson*, 2002]. The magnitude of water and sediment supply variations in these catchments, however, is likely much larger than in many other locations. Nonetheless, a similar model of terrace formation driven by climate change has been adopted for many catchments that likely experience smaller changes in water and sediment supply, including the coast ranges of Oregon [*Personius et al*., 1993] and California [*Fuller et al*., 2009] and the coastal plain of Texas [*Blum and Valastro*, 1994]. While in some landscapes dramatic climate change is also indicated by moraines and other glacial features [e.g., *Hancock et al*., 1999], in settings far from the glacial headwaters terraces are the primary geomorphic markers used to infer climate change [e.g., *Bull*, 1991; *Personius et al*., 1993; *Blum and Valastro*, 1994; *Fuller et al*., 2009]. However, the simulation results presented herein suggest that the intrinsic unsteadiness of lateral erosion should be considered as a null hypothesis for terrace formation in many landscapes, and the frequency of terrace formation by intrinsic processes and external forcing may overlap in cases (Fig. 11).

Using the elevation difference between terrace levels as a proxy for time, the estimated time between unique terrace levels is consistent with terrace formation under constant vertical incision rates for several natural river valleys (Fig. 12). A constant rate of river vertical incision implies that regardless of its elevation above the channel, each terrace would yield the same estimated vertical incision rate. Strath terrace ages and elevations compiled by *Finnegan et al*. [2014], however, demonstrate that for many bedrock river valleys the estimated vertical incision rate declines as the measurement timescale increases, which can be explained by hiatuses in vertical incision. Thus, for bedrock rivers the model results presented here represent an end-member vertical incision scenario that in nature is likely overprinted by vertical incision hiatuses. In a new finding, model results indicate that in environments with low dimensionless vertical incision rates (i.e., $E_V^* < 0.1$; Fig. 4), the channel commonly re-works areas it has visited previously and thus biases preserved terraces toward older ages. This terrace preservation bias should enhance the terrace age-vertical incision rate relationship identified by *Finnegan et al*. [2014], whether vertical incision rates are constant (this study), cyclic [*Hancock and Anderson*, 2002] or stochastic [*Finnegan et al*., 2014]. We also note that an analogous database of terrace ages and elevations does not exist for fill-cut terraces, and therefore it is uncertain whether constant vertical rates may have been more prevalent for river valleys with fill-cut terraces.

Re-working of previously visited areas implies that as the valley widens, there is less contact between the channel and the valley walls, which is consistent with the parameterization of valley widening employed by *Hancock and Anderson* [2002]. Notably,

however, terraces were not destroyed in their model because meandering dynamics were not included and the valley was forced to widen in a consistent direction.

The geometry of internally generated terraces has not been investigated quantitatively, but these terraces have been proposed to be unpaired and limited in length. For cases with constant bank-strength, simulations indicate that terraces formed by meandering with constant vertical incision rates have some attributes more commonly associated with terraces formed by pulses of vertical incision. The internally generated terraces are commonly paired (Fig. 8), and can extend downstream over distances significantly longer than a typical meander wavelength (i.e., 10-15 channel widths [*Williams*, 1986]; Fig. 7). Notably, paired terraces did not form in the *Finnegan and Dietrich* [2011] simulations, but occur in our simulations because of longer dimensionless simulation times (i.e., more extensive lateral channel migration) and the use of a periodic boundary condition that allows free motion of the channel axis.

Simulations also indicate that lateral channel migration alters existing terraces. The time interval between unique terrace levels increases approximately logarithmically with dimensionless simulation time (Fig. 4A), and the fraction of paired terraces decreases with dimensionless simulation time (Fig. 8A) because existing terraces are destroyed. In areas argued to show a strong relationship between climate transitions and terrace formation, rivers often have greater or fewer fill [e.g., *Bridgland and Westaway*, 2008] or strath [e.g., *Pan et al*., 2003] terraces than can be matched to a particular climate cycle. Terrace formation with meandering during vertical incision may explain this discordance because

irregular channel migration causes more terrace levels to form than vertical incision pulses (Fig. 11), causes terraces to form without incision pulses, and destroys existing terraces.

Terraces generated by meandering with constant vertical incision rates have also been hypothesized to dip toward the valley center with a slope equal to the ratio of channel vertical to lateral incision rates. Model results for constant bank-strength cases partially support both hypotheses. Terrace dips toward the valley center are most common for composite terrace surfaces formed by the migration of several meander bends, but are less common as E_V^* increases and terraces are increasingly associated with individual meander bends (Fig. 3A-B and 6). Simulated terrace slopes increase linearly with the ratio of channel vertical incision rate to maximum lateral erosion rate (Fig. 5B). Given the variety in lateral erosion rates around a meander bend [e.g., *Nanson and Hickin*, 1983], the common correspondence between terrace slope and the ratio of channel vertical and lateral incision rates is non-trivial. Steeper-than-predicted terrace slopes occur for $t^* > 1000$ and $E_V^* < 0.01$ because terraces formed under those conditions are compound surfaces formed by the action of multiple meander bends.

In light of these geometric characteristics of terraces formed by meandering with constant vertical incision rates, we consider which are potentially diagnostic. Terrace dip direction perpendicular to the valley axis is distinguishing only for cases with extensive channel wandering (i.e., $t^* > 300$) (Fig. 6B), and natural terraces formed by pulsed vertical incision driven by knickpoints are also observed to dip perpendicular to the valley in cases (i.e., Le Sueur River terraces, Figure 14D). The magnitude of the terrace slope shows a

strong relationship with channel vertical and lateral erosion rates (Fig. 5B), and the slope of terraces formed by pulsed vertical incision would be expected to be lower because of low vertical incision rates during the time of strath beveling [e.g., Hancock and Anderson, 2002]. Yet terrace slope is unlikely to be useful as a distinguishing characteristic unless the lateral erosion rate during terrace formation can be independently constrained (e.g., from dating laterally separated terrace surfaces [*Wegmann and Pazzaglia*, 2002; *Fuller et al*., 2009]).

Paired terraces commonly form in the simulations with both constant bank strength (Fig. 8) and variable bank strength (Fig. 10D), and in cases are as common as for the Le Sueur River (Fig. 15B) where vertical incision is largely accomplished by knickpoints. Furthermore, given the potential for pairing to decrease in time due to terrace destruction (Fig. 8A), pairing does not appear to be a reliable indicator of terrace formation process in valleys where channel migration is extensive. Notably, terraces commonly mapped as paired in the Colorado and Wind River valleys are sufficiently offset in mean elevation that the objective algorithm utilized here classifies them as unpaired. Thus, the threshold elevation difference used to classify terraces as paired or unpaired may weigh heavily in their interpretation.

Terrace length appears to be a more robust indicator of formation process, as especially long terraces only form by meandering with constant vertical incision for $E_V^* < 0.1$ (Fig. 7B). Thus, the existence of long terraces (i.e., $L_{terrace}/w_c > 100$) combined with $E_V^* > 0.1$ rules out terrace formation by meandering with constant vertical incision, as for the longest Wind River terraces (Fig. 15A). For valleys with $E_V^* < 0.1$ (e.g., the Colorado

River valley), however, terraces with $L_{terrace}/w_c > 100$ could be expected to form for constant external forcing. In these cases, longitudinally extensive terraces would not necessarily suggest formation during periods of suppressed vertical incision.

Natural river terraces commonly exhibit relatively straight margins where they meet adjoining hillslopes (Fig. 1A-B). Simulations with meandering and constant bank strength cannot reproduce this morphology (Fig. 3). Simulations with spatial differences in bank-strength between bedrock and valley-floor alluvium can generate terraces with relatively straight margins (Fig. 9) because meander bends can deform and straighten at valley margins [e.g., *Lewin and Brindle*, 1977; *Limaye and Lamb*, 2014]. The complexity of meander migration with mixed bedrock and alluvial bank-materials, including transitions between conditions of high mobility in sediment banks and low mobility in bedrock banks, renders relationships between terrace geometry and channel vertical and lateral erosion rates more complicated for constant bank-strength cases. Spatial variations in bank strength between bedrock and sediment tend to reduce the time interval between unique terrace levels (Fig. 10A) and terrace length (Fig. 10D), while increasing pairing (Fig. 10E) and favoring the formation sub-linear terrace margins.

Longitudinally extensive and paired terraces have been proposed as key indicators of terrace formation by external factors [e.g., *Merritts et al*., 1994; *Pazzaglia et al*., 1998; *Pazzaglia*, 2013]. Model results suggest that a range of constant vertical incision rates and lateral erosion rates can generate terraces that are both long (Fig. 7) and paired (Fig. 8). These results are presented for dimensional erosion rates in Figure 16, and indicate that for a constant vertical incision rate, valleys may develop no terraces; short (i.e., $L_{terrace}/w_c <$

100), unpaired (i.e., $f_{paired} < 0.25$) terraces; or long (i.e., $L_{terrace}/w_c > 100$) and paired (i.e., $f_{paired} > 0.25$) terraces. The lack of significant terrace development in the San Juan River valley is consistent with the model prediction that any eroded surfaces are likely to be slip-off surfaces rather than terraces due to the slow pace of lateral erosion relative to vertical incision. If long, paired terraces are the signature of climate change, then this signature is unlikely to be confounded by intrinsic terrace formation by meandering in rivers with maximum lateral erosion rates less than 3 cm/yr. Moreover, bedrock rivers with high vertical incision rates (i.e., > 1 mm/yr) are unlikely to generate long, paired terraces because that would require unreasonably high lateral erosion rates (i.e., > 20 cm/yr). These results indicate that terrace geometries thought to indicate formation by climate change are more likely to develop intrinsically for some river valleys than for others. For example, the Wind River valley represents a more advantageous location for identifying signatures of climate change in terrace geometry than the Colorado River valley, which would be expected to develop long, paired terraces due its high rate of lateral erosion relative to vertical incision.

The terrace recurrence timescale offers another criterion for distinguishing terrace formation mechanisms. Figure 16 also indicates the minimum timescale for vertical incision sufficient to abandon a terrace (t_{vert}), which has an inverse relationship with the vertical incision rate (Eq. 2) and is typically 1-4 times shorter than the typical terrace recurrence time (Fig. 4A). Model results indicate that short, unpaired terraces are expected to have recurrence times of less than 1000 yr for vertical incision rates greater than 1 mm/yr and lateral erosion rates greater than 1 cm/yr, and recurrence times of greater than

1000 yr for lower vertical incision rates and lateral erosion rates. Intrinsically generated terraces that are long, paired, and occur at common timescales for climate change (e.g., 10 kiloyears) only form for vertical incision rates less than 1 mm/yr and lateral erosion rates grater than 2 cm/yr. If a group of terraces has a typical formation interval at a timescale for climate change, and long-term vertical incision rates and lateral erosion rates are predicted to form intrinsic terraces at much shorter or much longer timescales, then a climatic interpretation is more strongly supported. Thus, in order to identify terraces that record climate change, the best environments are those with terraces whose ages and geometries differ strongly from those predicted for intrinsically generated terraces. In one extreme, long, paired terraces with large time gaps (i.e., > 1000 yr) between terraces in a setting with very high vertical incision rates (~ 1 cm/yr) are not predicted to form by meandering if lateral erosion rates are moderate (< 1 m/yr). At the other extreme, short, unpaired terraces with relatively short recurrence times (i.e., < 1000 yr) and in a setting with very low vertical incision rates (< 10^{-4} m/yr) are unlikely to form by meandering with constant vertical incision rates, as the model predicts that this regime should be dominated by long, paired terraces with larger time gaps between terraces.

9. Conclusions

We utilize a numerical model of river meandering with vertical incision to identify controls on the formation frequency and geometry of river terraces that form with constant external forcing. Model results indicate that for a variety of constant vertical incision rates and lateral erosion rates, rivers can generate terraces due to the intrinsically unsteady patterns of lateral erosion by meandering. The ratio of channel vertical to lateral erosion

rate and the simulation time exert the strongest controls on terrace age and geometry. The minimum time interval between unique terrace levels scales with the timescale of vertical incision required to generate sufficient relief to generate a new terrace, and this time interval between terrace levels increases with simulation time due to re-working of previously visited areas. Terrace formation ceases for high ratios of channel vertical incision to lateral erosion because eroded surfaces possess high surface slopes and are classified as slip-off surfaces. Simulations suggest that the intrinsically generated terraces possess several consistent properties, including (1) surface slopes that are commonly proportional to the ratio of vertical to lateral erosion rates during terrace formation; (2) dip directions oriented perpendicular to the valley orientation for low ratios of vertical to lateral erosion rate and long channel evolution times; (3) greater along-valley extents for low ratios of vertical to lateral erosion rate; and (4) a maximum in paired terrace formation for intermediate ratios of vertical to lateral erosion rate. Spatial variations in bank strength between bedrock and sediment cause terrace ages to be separated by shorter time intervals. These terraces are also smaller and more frequently paired than terraces formed in constant bank-strength cases, and also possess sub-linear terrace margins, similar to many natural river terraces.

Natural river terraces show an increase in terrace slope with the estimated vertical to lateral erosion rate ratio, but no consistent relationship between terrace dip direction and dimensionless vertical incision rate. Maximum terrace length is the most reliable geometric indicator of terrace formation by episodic vertical incision; for moderate to high values of dimensionless vertical incision rate, terraces formed by meandering with constant vertical

incision have relative limited lengths because successive generations of meander bends erode surfaces at different elevations. For landscapes without independent indicators of climate change, river terrace formation by intrinsic meandering processes should be considered as the null hypothesis. Long, paired terraces with millennial-scale intervals between terrace levels, which have been suggested to indicate formation driven by external factors, are likely to develop intrinsically in landscapes with relatively high lateral erosion rates and low vertical incision rates. Thus, efforts to identify terraces that record climate signals are best focused on environments where terrace ages and geometries are far different than would be predicted by a constant vertical incision model.

Acknowledgments

This work was supported by the Department of Defense through the National Defense Science and Engineering Graduate Fellowship (NDSEG) Program and NSF grant EAR-1147381 to MPL. Acknowledgment is also made to the Donors of the American Chemical Society Petroleum Research Fund for partial support of this research. Simulation data from this manuscript is available upon request. We thank Bob Anderson, Jean-Philippe Avouac, Patrick Belmont, Noah Finnegan, Dirk Scherler and Andrew Thompson for insightful discussions.

Tables

Symbol	Description
Model dimensional variables	
w_c	Channel width
h_c	Channel depth
w_{ab}	Initial alluvial belt-width
w_{uab}	Initial alluvial belt-width (unconfined)
C_f	Friction coefficient
E_V	Vertical incision rate
E_L	Lateral erosion rate
E_{Ls}	Lateral erosion rate in sediment
E_{Lb}	Lateral erosion rate in bedrock
k_e	Lateral erosion rate constant
k_s	Lateral erosion rate constant (sediment)
k_b	Lateral erosion rate constant (bedrock)
f_b	Fraction of bedrock in bank materials
Δt	Time step
t	Simulation time
Γ, Ω	Channel migration rate weighting coefficients
ξ	Distance along channel centerline
μ	Channel sinuosity
Model non-dimensional variables	
$t^* = \frac{tE_{Ls}}{w_c}$	Non-dimensional simulation time
$E_V{}^* = \frac{E_V w_c}{E_L h_c}$	Non-dimensional vertical incision rate
$E_{Vb}{}^* = \frac{E_V w_c}{E_{Lb} h_c}$	Non-dimensional vertical incision rate with bedrock banks
$E_{Vs}{}^* = \frac{E_V w_c}{E_{Ls} h_c}$	Non-dimensional vertical incision rate with sediment banks
$w_c{}^* = \frac{w_c}{h_c}$	Channel width-to-depth ratio
$w_{ab}{}^* = \frac{w_{ab}}{w_{uab}}$	Non-dimensional initial alluvial-belt width
Terrace age statistics	
Δz	Size of elevation bin for distinguishing unique terrace levels

$\Delta t_{terrace}$	Distribution of time intervals between unique terrace levels (i.e., separated vertically by $\Delta z \geq 1$)
$\Delta t_{terrace,90}$	90th percentile of time interval between unique terrace levels
$\Delta t_{terrace,50}$	50th percentile of time interval between unique terrace levels
Terrace geometry statistics	
ϕ	Terrace dip direction (degrees), measured relative the to the mean azimuth of the valley centerline.
θ	Terrace slope (percent)
$L_{terrace,max}$	Maximum terrace length in the valley-parallel direction
f_{paired}	Fraction of paired terraces (i.e., terraces adjacent, on opposite sides of the channel, and with mean elevation less than 2 meters apart) in the model domain, weighted by terrace area

Table 1. Model variables and statistics for terrace age and geometry.

Simulation set	t^*	E_V^*	E_{Vs}^*	E_{Vb}^*	w_{ab}^*	Number of simulations
Constant bank-strength	1-5000	0.002-200	N/A	N/A	N/A	190[a]
Variable bank-strength	5000	N/A	0.002	0.004-4	0.1	21

[a]Each simulation with a unique set of parameters was run ten times, each with a different initial, sinuous channel planform geometry.

Table 2. Simulation parameters.

Valley name	w_c (m)	h_c (m)	E_L (m/yr)	E_V (mm/yr)	E_V*	$t_{vert} = \Delta z/E_V$ (yr)
San Juan	53[f]	2.1[d]	0.003[m]	0.15[l]	1.26	6700
Mattole	102[f]	4.1[d]	0.03[k]	1[j]	0.86	1000
Colorado	275[g]	8[g]	0.15[h]	0.25[h]	0.06	4000
Wind	41.7[i]	1.8[i]	0.01[a]	0.15[a]	0.36	6700
Le Sueur	47.5[e]	1.9[d]	0.3[e]	2[e]	0.17	500
Clearwater	49.1[f]	2.0[d]	0.125[b]	1.5[b]	0.30	670

[a]Estimated from *Hancock and Anderson* [2002].
[b]Estimated from *Wegmann and Pazzaglia* [2002].
[c]Mean vertical incision rate estimated from *Gran et al*. [2013] for the mainstem Le Sueur River.
[d]Estimated assuming $w_c/h_c = 25$.
[e]Estimated from *Gran et al*. [2011].
[f]Estimated from aerial photographs.
[g]*Blum* [1992].
[h]Estimated from stratigraphic data in *Blum and Valastro* [1994].
[i]*Smalley et al*. [1994].
[j]Estimated from *Merritts et al*. [1994].
[k]Estimated from bedrock lateral erosion rates in similar geologic environments in *Fuller et al*. [2009] and *Finnegan and Dietrich* [2011].
[l]Estimated from *Wolkowinsky and Granger* [2004].
[m]Estimated for a mean lateral erosion rate in bedrock of 1 mm/yr, approximately one order-of-magnitude slower than in more erodible sedimentary rock [*Montgomery*, 2004].

Table 3. Estimated parameters for rivers shown in Figure 1 and the San Juan River.

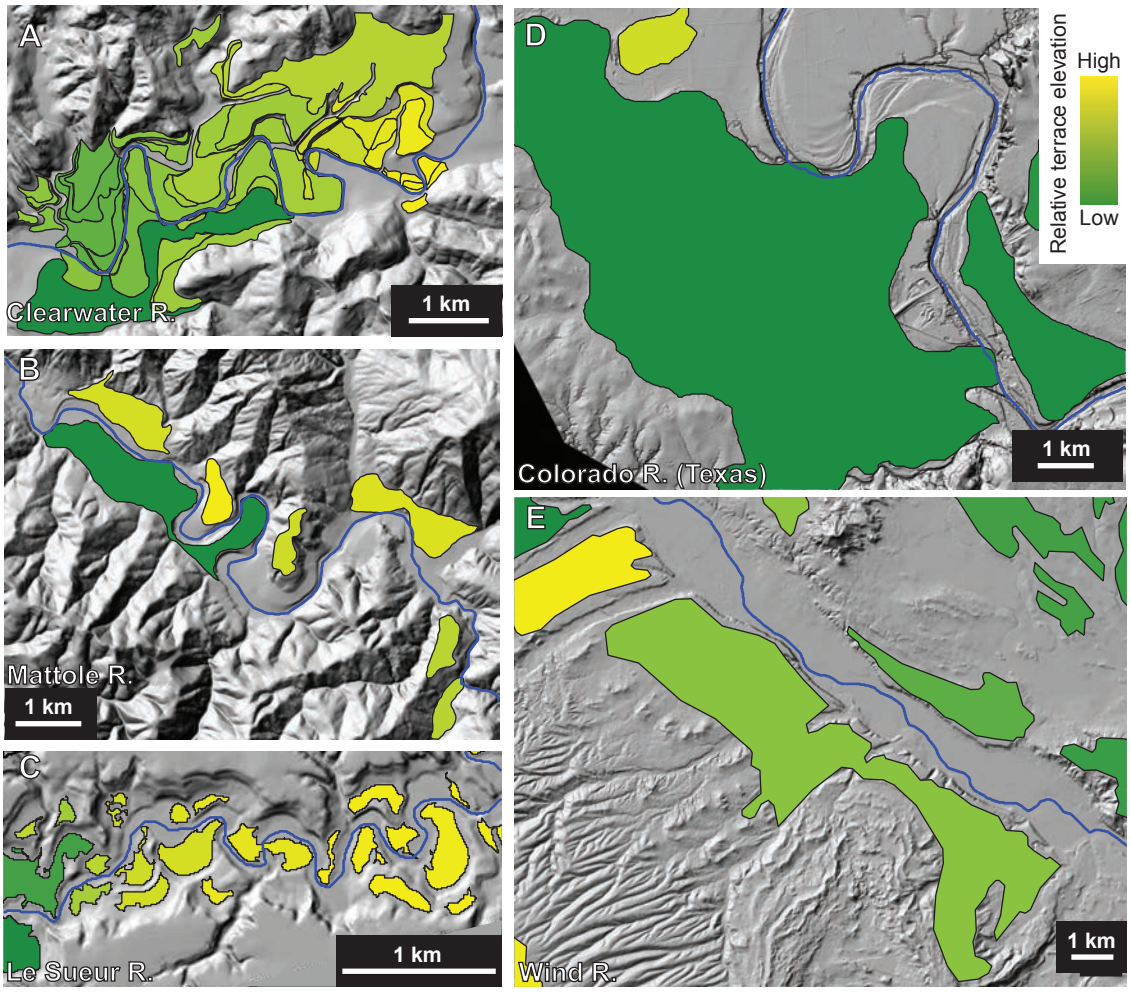

Figure 1. A variety of river terrace morphologies. Shaded relief topography is overlain by terrace extents that have been previously mapped unless otherwise noted. Terraces are colored according to their mean elevation (green-yellow), and the range of mean terrace elevations is noted below. **(A)** The Clearwater River, Washington (47.6°N, 124.2°W; mapped by *Wegmann and Pazzaglia* [2002]; range in mean terrace elevation is 41 m). **(B)** The Mattole River, California (40.2°N, 124.2°W; mapped by *Dibblee and Minch* [2008]; range in mean terrace elevation is 48 m). **(C)** The Le Sueur River, Minnesota (44.0°N, 94.0°W; mapped automatically using methods described in Section 2; range in mean terrace elevation is 27 m). **(D)** The Colorado River, Texas (30.2°N, 97.5°W; mapped by *Barnes et al*., [1974a] and *Barnes et al*. [1974b]; range in mean terrace elevation is 31 m). **(E)** The Wind River, Wyoming (42.3°N, 109.1°W; mapped by *Case et al*. [1998]; range in mean terrace elevation is 119 m). Topography data is from the National Elevation Dataset digital elevation model (DEM; ~10 meter-resolution), except for the Colorado River valley, which uses a 5-meter resolution DEM based on LiDAR point cloud data from the Texas Water Development Board.

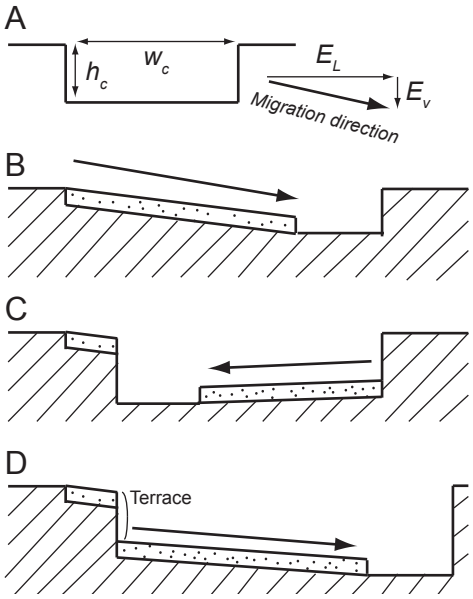

Figure 2. Schematic of river terrace formation by vertical erosion and unsteady lateral erosion, after Merritts et al. [1994]. **(A)** The cross-section of a channel with width w_c and depth h_c. The channel migrates with a constant mean lateral erosion rate and constant vertical erosion rate, resulting in a sub-horizontal channel migration direction. **(B)** As the channel erodes laterally and vertically, it planes off a bedrock (hatched area) surface. Here, constant channel width is maintained by emplacing sediment (dotted area) on the trailing bank up to the flow depth. The arrow indicates the mean channel migration direction. **(C)** The direction of net lateral channel migration switches. **(D)** The direction of net lateral channel migration reverts to its initial direction. A strath terrace is preserved because the channel does not sweep a consistent distance across the valley.

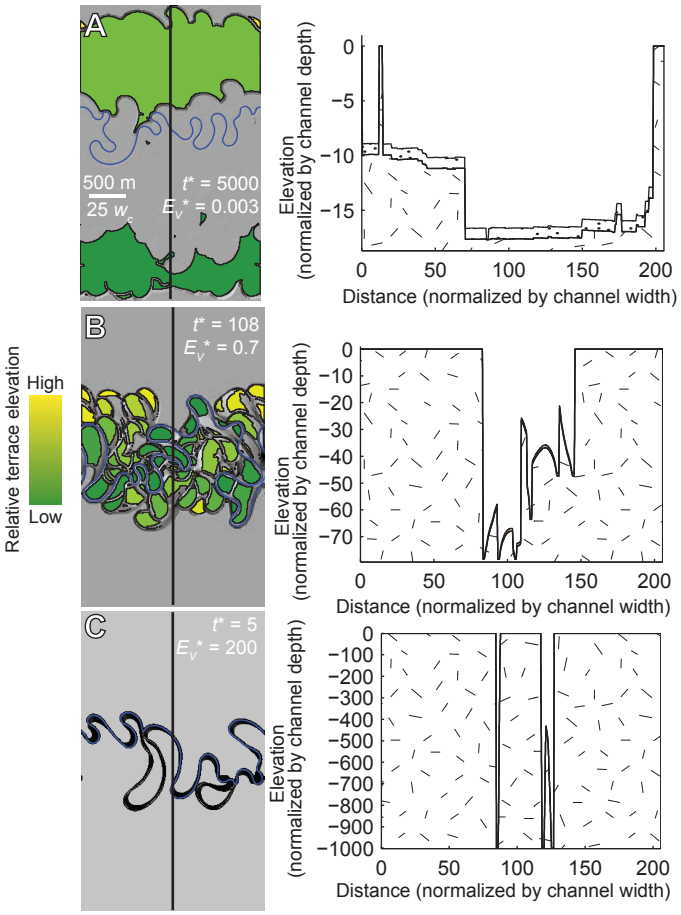

Figure 3. The surface morphologies produced by the model for constant bank-strength, as a function of dimensionless simulation time (t^*) and dimensionless vertical incision rate (E_V^*). In each planview panel, flow is from left to right, the channel is indicated in blue, the background is the shaded relief of topography, and terraces are colored according to their mean elevation (green-yellow). The range of mean terrace elevations is noted below. The domain width is $120w_c$ and all mapview panels have the same scale. **(A)** For $t^* = 5000$ and $E_V^* = 0.003$, wide and long terraces form, and represent the amalgamation of numerous meander bends. Terrace elevation range is 15.3 m. **(B)** For $t^* = 108$ and $E_V^* = 0.7$, numerous terraces form and are generally bounded by abandoned meander cutoff loops. Terrace elevation range is 75 m. **(C)** For $t^* = 5$ and $E_V^* = 200$, no terraces form because surfaces eroded by lateral channel erosion are exceedingly steep. The topography consists entirely of slip-off surfaces and abandoned meander cutoff loops.

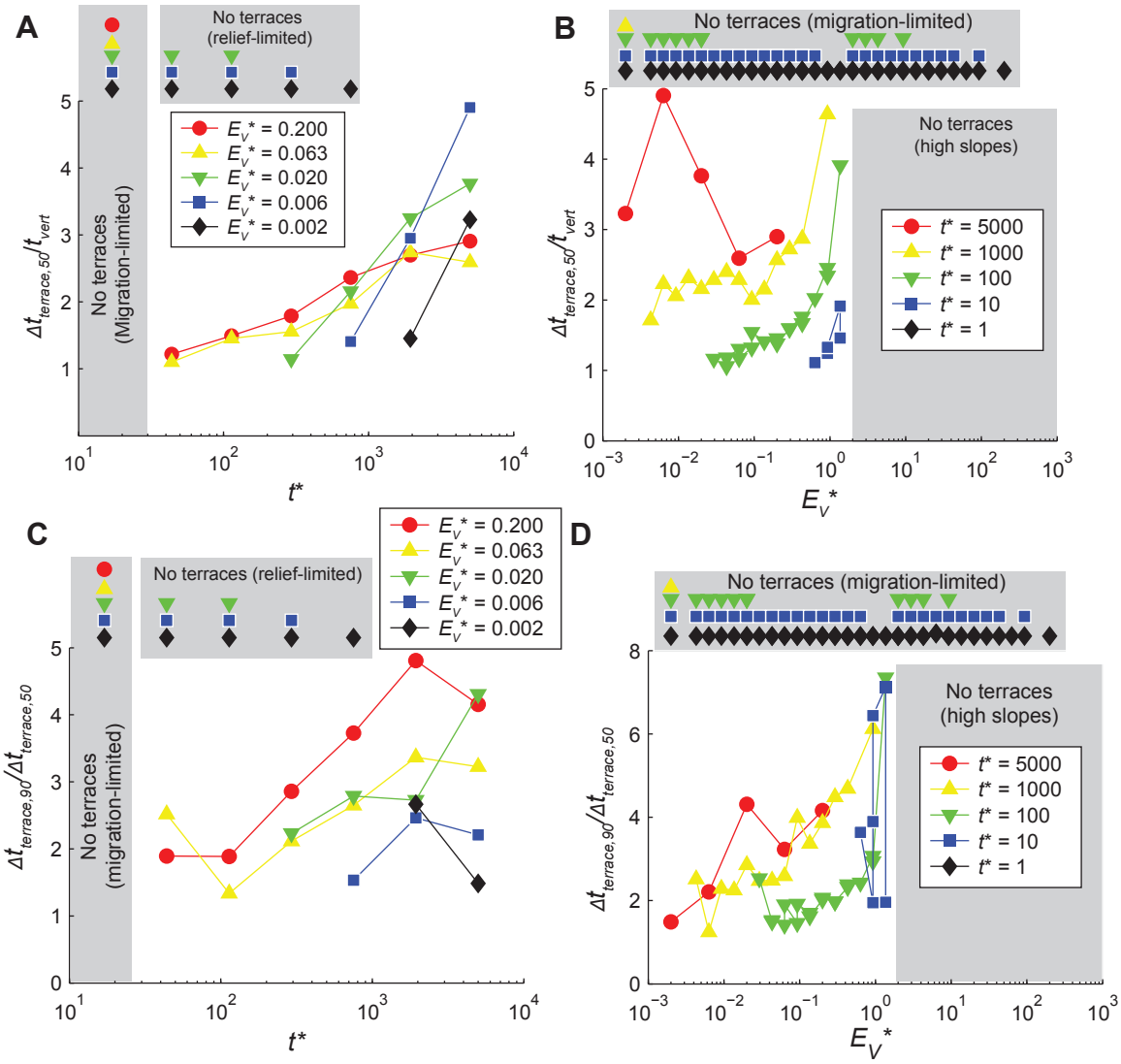

Figure 4. Dimensionless time interval between formation of unique terrace levels ($\Delta t_{terrace,50}/ t_{vert}$) for constant bank-strength cases, as a function of dimensionless simulation time (t^*) and dimensionless vertical incision rate (E_V^*). For simulation sets in which one or fewer terraces typically form, $\Delta t_{terrace}$ is undefined and these cases are labeled "No terraces." Terraces do not form either due to insufficient lateral channel migration (migration-limited) or insufficient vertical incision to generate relief for forming terraces (relief-limited), or because surface slopes formed by channel migration are too high for classification as terrace treads (high slopes). **(A)** $\Delta t_{terrace,50}/ t_{vert}$ vs. t^* for the subset of simulations for fixed values of E_V^*. **(B)** $\Delta t_{terrace,50}/ t_{vert}$ vs. E_V^* for fixed values of t^*. **(C)** Ratio of the 90th and 50th percentiles of $\Delta t_{terrace}$ vs. **(C)** t^*, for fixed values of E_V^*; and **(D)** E_V^*, for fixed values of t^*.

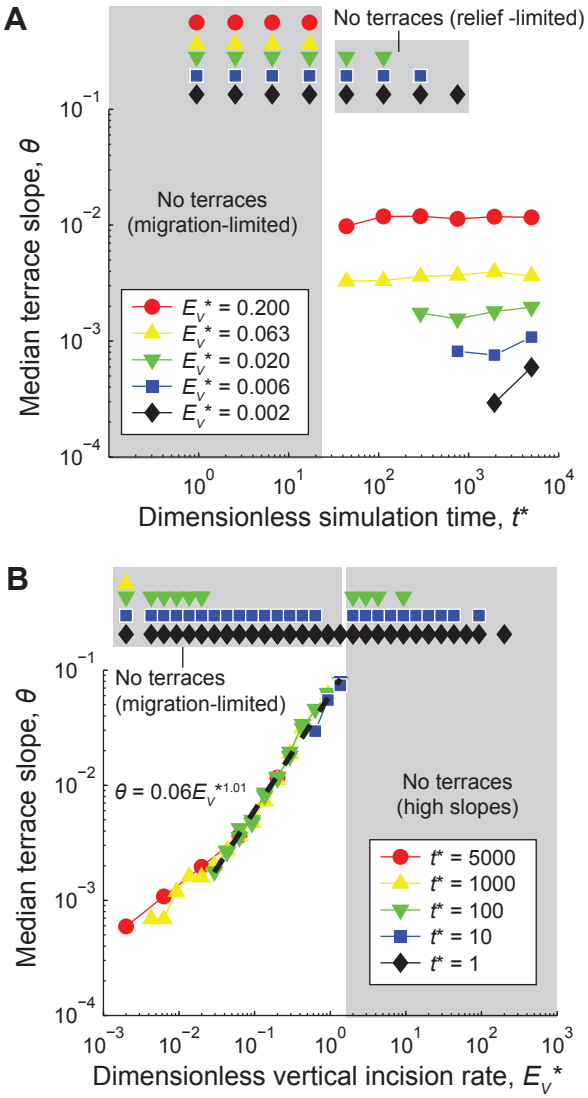

Figure 5. Median terrace slope vs. **(A)** t^*, for fixed values of E_V^*; and **(B)** E_V^*, for fixed values of t^*.

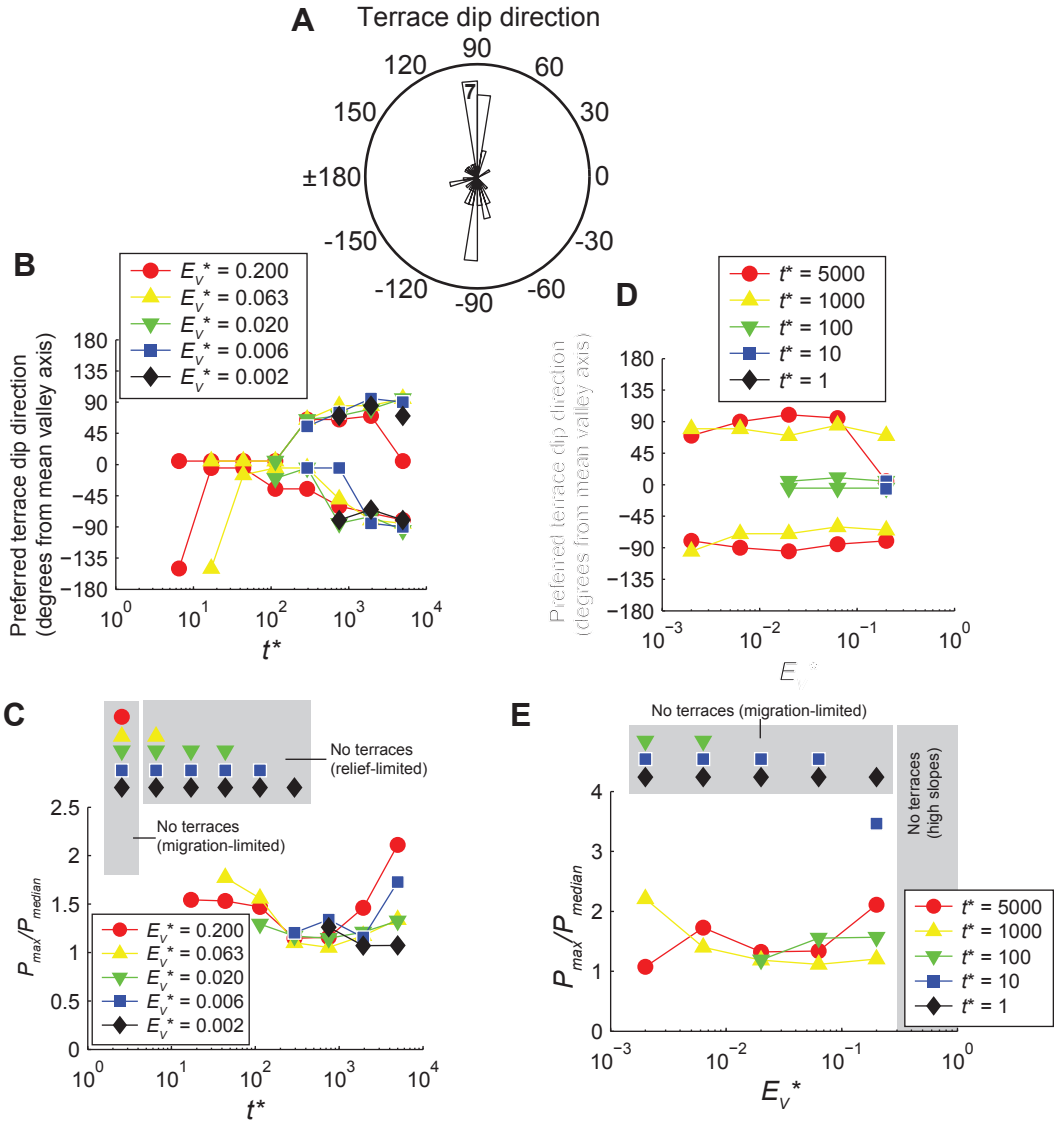

Figure 6. Terrace dip direction in simulations (ϕ; measured in degrees from of the downstream-directed, mean valley axis), as a function of dimensionless simulation time (t^*) and dimensionless vertical incision rate (E_V^*). **(A)** Rose diagram of ϕ for $E_V^* = 0.002$ and $t^* = 5000$, combining results from ten simulations with different initial channel planform geometries. Most probable terrace dip direction is plotted vs. **(B)** t^*, for fixed values of E_V^*; and **(C)** E_V^*, for fixed values of t^*. In (B) and (D), positive and negative values of ϕ indicate dip direction toward different sides of the valley axis, and are plotted separately. The strength of the preferred terrace dip direction, expressed as the ratio of the probability for the most probable dip direction divided by the median probability (P_{max}/P_{median}), is plotted vs. **(D)** t^*, for fixed values of E_V^*; and **(E)** E_V^*, for fixed values of t^*.

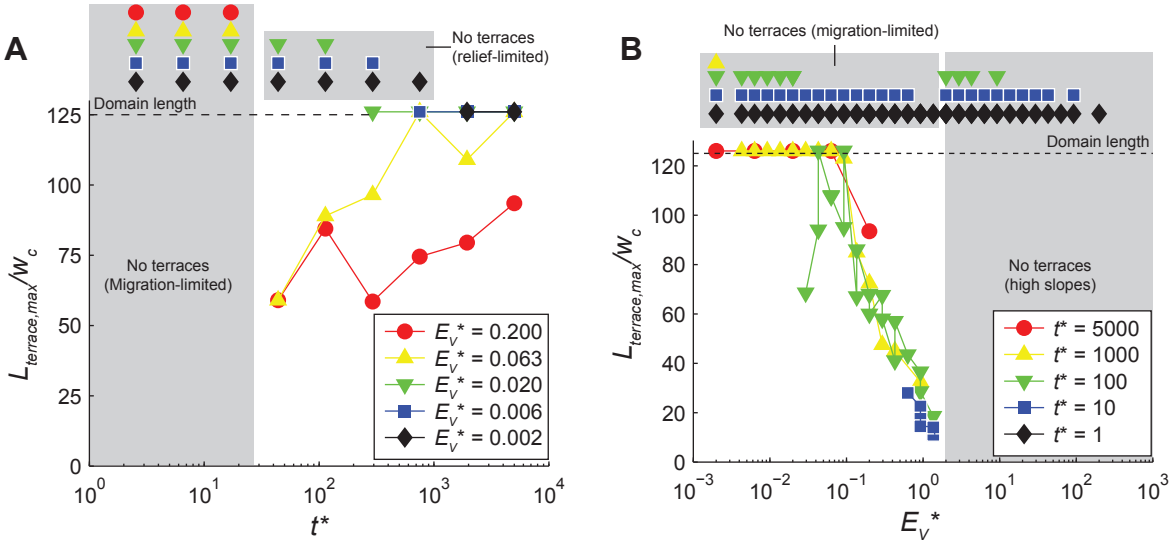

Figure 7. Maximum terrace length (normalized by channel width) vs. **(A)** dimensionless simulation time (t^*) for fixed values of dimensionless vertical incision rate (E_V^*); and **(B)** E_V^*, for fixed values of t^*.

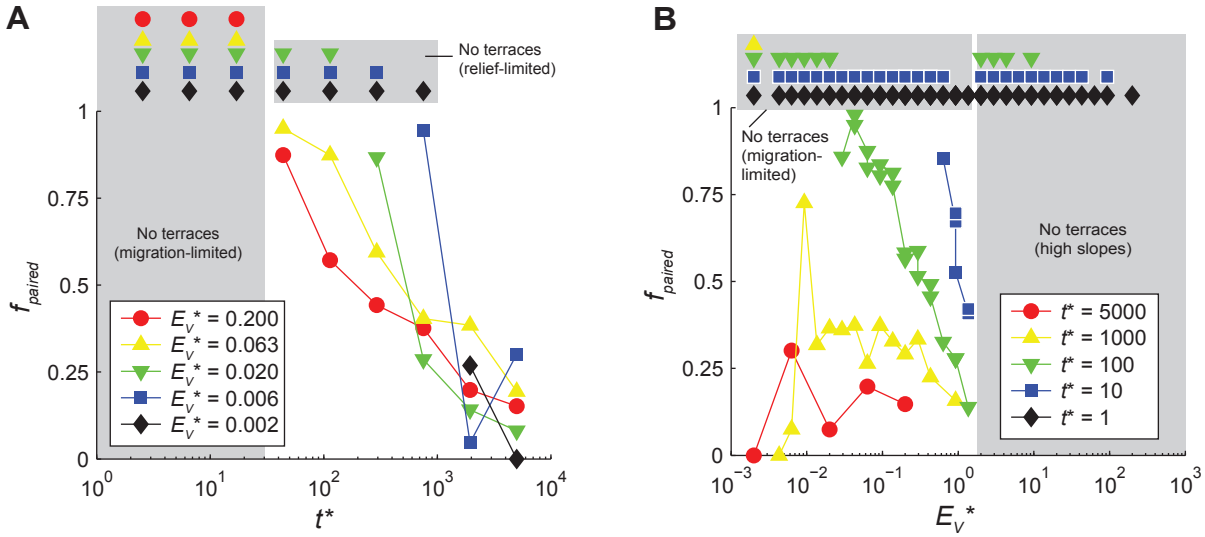

Figure 8. Fraction of paired terraces in the model domain, weighted by area (f_{paired}), vs. **(A)** vs. dimensionless simulation time (t*), for fixed values of dimensionless vertical incision rate (E_V*); and **(B)** E_V*, for fixed values of t*.

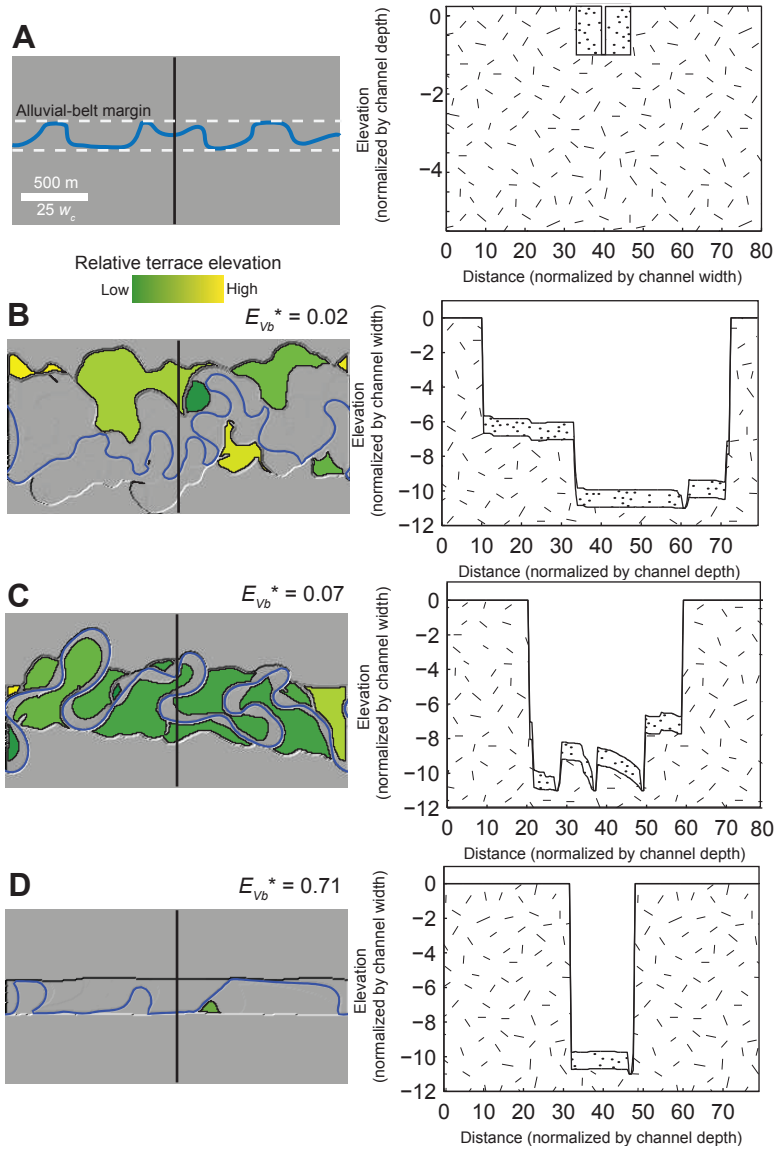

Figure 9. Types of terraces produced by the model for variable bank-strength cases. The mean flow direction in all panels is from left to right and the channel is blue. Terraces are colored according to their mean elevation (green-yellow), and the range of mean terrace elevations is noted below. **(A)** The initial cross-section and planview geometry of the channel and alluvial belt, in schematic form. Because w_{ab}* < 1 in this case, the the initial alluvial-belt width (w_{ab}) is less than unconfined alluvial-belt width (w_{uab}), and initially the channel is constrained to the alluvial-belt boundaries. Within the initial alluvial-belt the banks are entirely sediment and the sediment depth equals the channel depth. Areas beyond the alluvial belt and below the elevation of the channel bed are all bedrock. **(B)** A simulation in which the channel erodes beyond the initial alluvial-belt and creates extensive terraces (E_{Vb}* = 0.02). The terrace elevation range is 6.8 m. **(C)** A simulation in which the channel entrenches in bedrock and paired terraces are abandoned, largely within the initial alluvial-belt (E_{Vb}* = 0.07). The terrace elevation range is 4.3 m. **(D)** A simulation in the

channel erodes vertically while largely confined to the initial alluvial-belt, resulting in minimal terrace formation (E_{Vb}* = 0.71). The lone terrace has a mean elevation of -8.9 m.

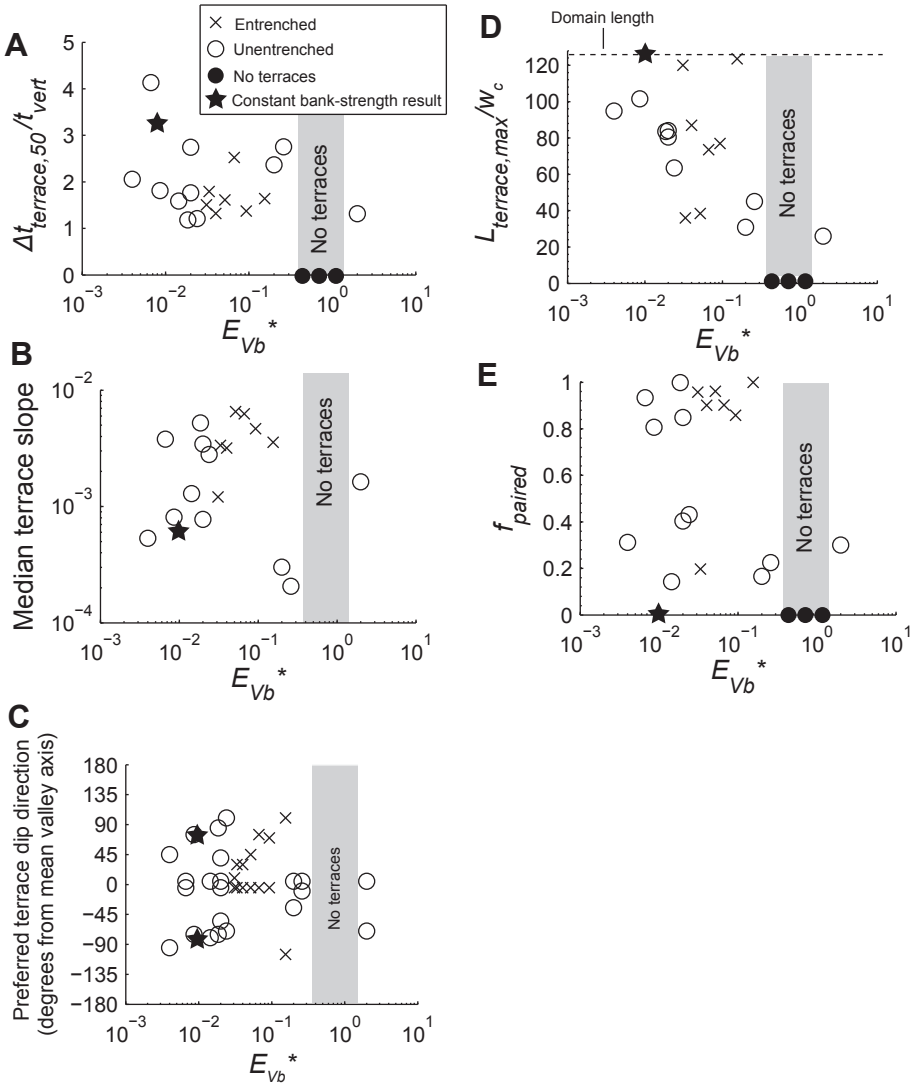

Figure 10. Terrace formation frequency and geometry for variable bank-strength cases, as a function of non-dimensional vertical incision rate for bedrock banks (E_{Vb}*). For these simulations, the dimensionless simulation time (t* = 5000) and dimensionless vertical incision rate for sediment banks (E_{Vs}* = 0.002) are fixed, so increasing E_{Vb}* is equivalent to increasing bedrock bank strength. Model results for constant bank-strength control cases (with t* = 5000 and E_V* = 0.002) are indicated with black stars. **(A)** Terrace formation frequency ($\Delta t_{terrace,50}/ t_{vert}$) vs. E_{Vb}*. **(B)** Median terrace slope vs. E_{Vb}*. Simulations that did not produce terraces are not plotted. **(C)** Preferred terrace dip direction, measured in degrees from the valley axis, vs. E_{Vb}*. Simulations that did not produce terraces are not plotted. **(D)** Maximum terrace length (normalized by channel width) vs. E_{Vb}*. **(E)** Fraction of paired terraces in the model domain, weighted by area (f_{paired}), vs. E_{Vb}*.

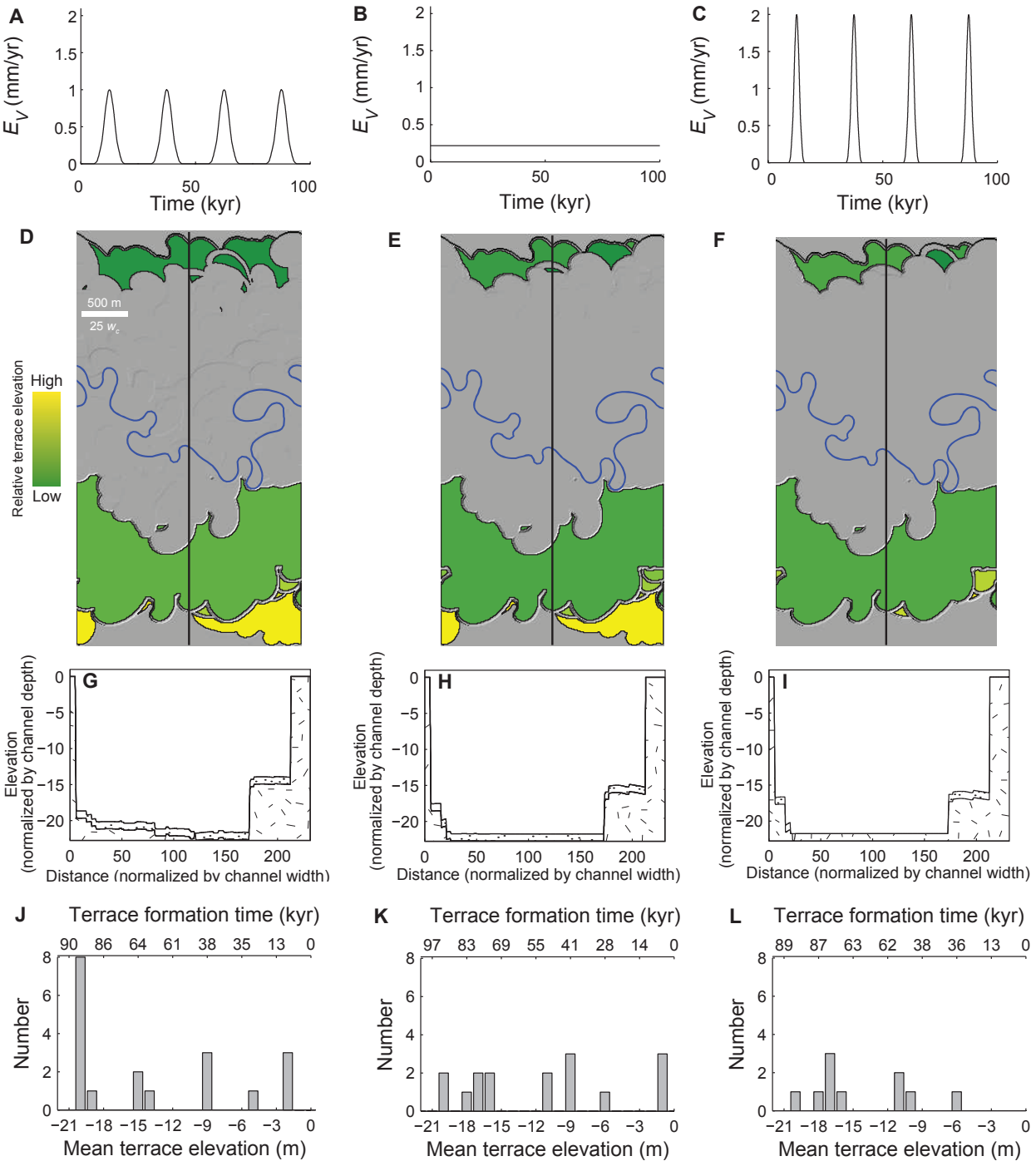

Figure 11. Examples of terrace formation by pulses of vertical incision (left and right panels) and constant vertical incision (center panels). (**A-C**) Vertical incision rate versus time. (**D-F**) Shaded relief topography and automatically detected terraces are highlighted in yellow. The channel is shown in blue and black line indicates the cross-section location, oriented from top-to-bottom across the model domain. Mean flow is from left to right. Total vertical incision is the same in both cases. Terraces are colored according to their

mean elevation (green-yellow); elevation distributions are given in panels J-L. (**G-I**) Topographic cross-sections indicating bedrock (hatched) and sediment (stippled). (**J-L**) Histograms of mean terrace elevation, binned at 1 m intervals. The time that corresponds to the center of each elevation bin is indicated in the top axis for each panel. Time axes in (J) and (L) are nonlinear due to the variable vertical incision rate for those cases.

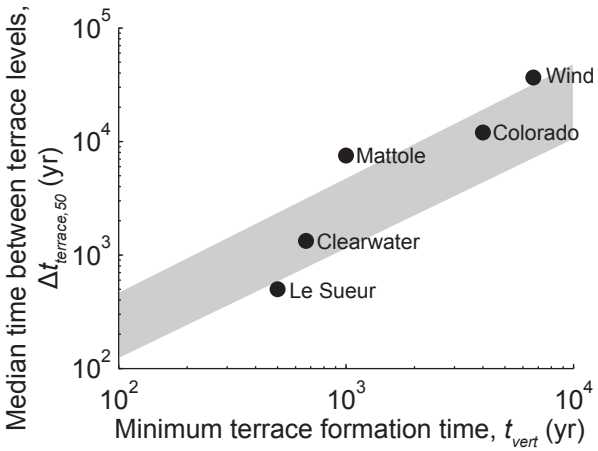

Figure 12. The estimated median time between terrace levels ($\Delta t_{terrace,50}$) versus the minimum terrace formation time (t_{vert}), both assuming a constant vertical incision rate at each site. The shaded area indicates the range of terrace formation times in the simulations with constant vertical incision rates.

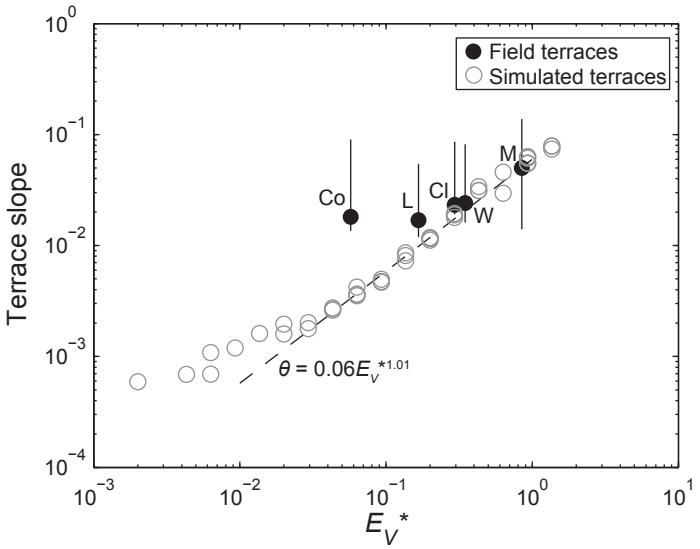

Figure 13. Terrace slope for natural river valleys vs. estimated dimensionless vertical incision rate (E_V*). Labels indicate terraces for the Colorado River (Co), Le Sueur River (L), Clearwater River (Cl), Wind River (W) and Mattole River (M). Error bars indicate the 90th and 10th percentiles of slope for different terraces in each river valley.

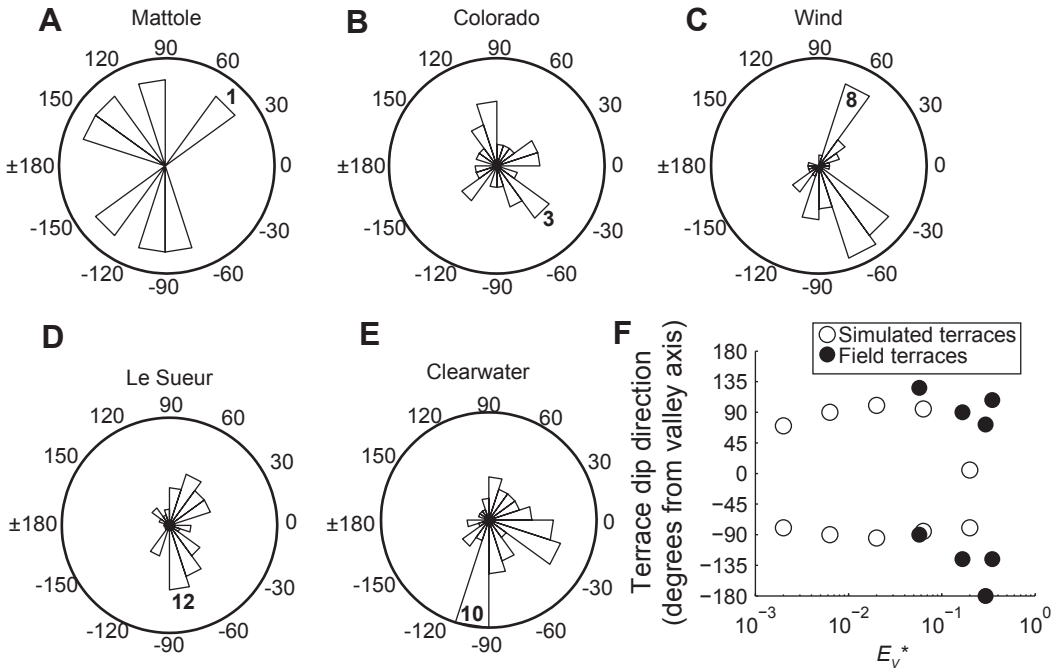

Figure 14. (A-E) Rose diagrams of terrace dip direction relative to valley orientation for natural valleys. A dip direction of 0º is oriented down-valley. **(F)** Preferred terrace dip direction vs. dimensionless vertical incision rate (E_V*). Positive and negative values, indicating dip direction toward different sides of the valley axis, are plotted in gray (positive) and black (negative). The Mattole River is not included in (F) due to the small number of terraces (seven).

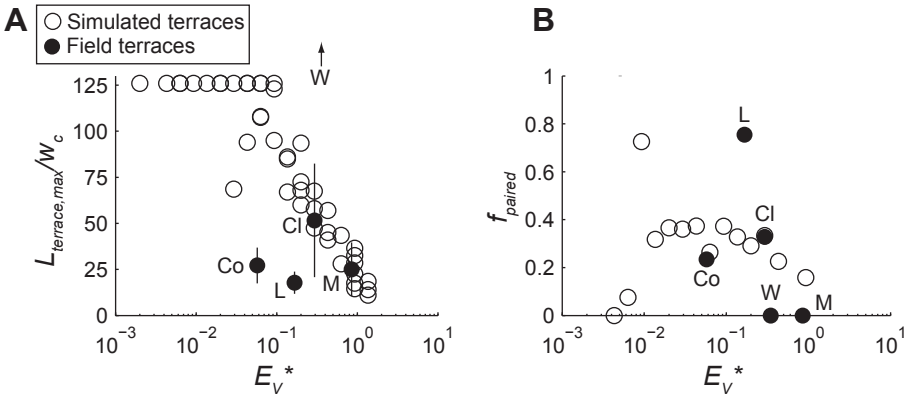

Figure 15. (A) Maximum terrace length (normalized by channel width) vs. estimated dimensionless vertical incision rate (E_V*) for natural river valleys. Terraces with $L_{terrace}/w_c$ = 125 are as long as the model domain. Error bars indicate the upper and lower bounds on terrace length; filled symbols are plotted using the mean of these bounds. The arrow indicates that the Wind River terraces have a range $L_{terrace,max}/w_c$ that is off-scale (150-450). Labels correspond to those in Figure 13. **(B)** Fraction of paired terraces, weighted by terrace area, vs. estimated E_V* for natural river valleys.

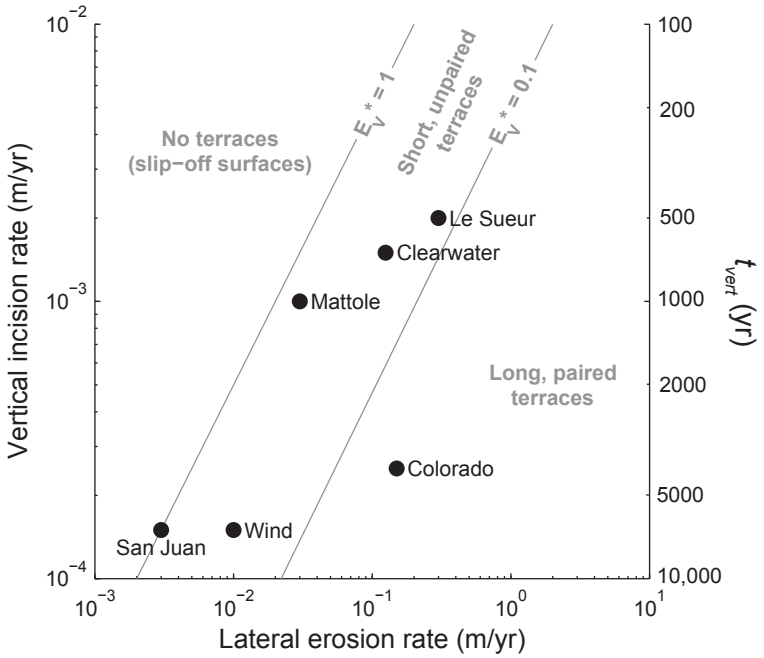

Figure 16. Summary of model predictions for terrace occurrence, pairing and length (gray) as a function of vertical incision rate and lateral erosion rate. Markers indicate estimated erosion rates for natural river valleys. The timescale for vertical incision sufficient to abandon a unique terrace level (t_{vert}) is indicated on the right. The time in between terrace levels can shift from t_{vert} for relatively long simulation times and low dimensionless vertical incision rates (see Figure 4).

Chapter 5: Detailed stratigraphy and bed thickness of the Mars north and south polar layered deposits

Originally published in:
Limaye, A. B. S., Aharonson, O., and Perron, J. T., 2012, Detailed stratigraphy and bed thickness of the Mars north and south polar layered deposits, Journal of Geophysical Research – Planets 117, doi:10.1029/2011JE003961.

Abstract

The Mars polar layered deposits (PLD) likely hold an extensive record of recent climate during a period of high-amplitude orbit and obliquity cycles. Previous work has detected limited evidence for orbital signatures within PLD stratigraphy, but data from the High Resolution Imaging Science Experiment (HiRISE) permit renewed analysis of PLD stratigraphy at sub-meter scale. Topography derived from HiRISE images using stereogrammetry resolves beds previously detectable only as alternating light and dark bands in visible images. We utilize these data to measure the thickness of individual beds within the PLD, corrected for non-horizontal bed orientation. Stratigraphic columns and bed thickness profiles are presented for two sites within the NPLD, and show several sets of finely bedded units 1-2 m thick; isolated marker beds 3-4 m thick; and undifferentiated sections. Bed thickness measurements for three sites within the SPLD exhibit only one bed type based on albedo and morphology, and bed thicknesses have a larger mean and variance compared to measurements for the NPLD. Power spectra of brightness and slope derived along the measured stratigraphic sections confirm the regularity of NPLD fine bed thickness, and the lack of a dominant SPLD bed thickness. The regularity of fine bed

thickness of the NPLD is consistent with quasi-periodic bed formation, albeit with unknown temporal period; the SPLD thickness measurements show no such regularity.

1. Introduction

Atmospheric pressure on Mars fluctuates annually by thirty percent, causing significant interaction between the atmosphere and near-surface ice [*Hess et al*., 1980]. On $>10^4$ yr timescales, Mars' high-amplitude, quasi-periodic orbital (i.e., orbit and obliquity) variations cause insolation cycles [*Laskar et al*., 2004] that may profoundly impact atmospheric circulation and water ice stability. Models predict ice redistribution from the poles to lower latitudes at higher obliquity [*Forget et al*., 2006; *Schorghofer*, 2007], and surface features—including mid-latitude mantling deposits [*Head et al*., 2003] and deposits reminiscent of terrestrial rock glaciers [*Head et al*., 2005]—may reflect such orbital states. Numerous authors have proposed that the polar layered deposits (PLD) respond to orbital cycles [*Murray et al*., 1973; *Ward*, 1973; *Toon et al*., 1980; *Cutts and Lewis*, 1982; *Thomas et al*., 1992], analogous to terrestrial Milankovitch periods driving glacial cycles [*Hays et al*., 1976]. *Perron and Huybers* [2009] noted that the apparent simplicity of Mars' climate does not, however, guarantee translation of an orbital signal into a discernable bed sequence. Although the confidence attributed to detection of an orbital signal may depend strongly on the continuity of the stratigraphic record [*Cutts and Lewis*, 1982; *Sori et al*., 2011], repeating patterns of bed thickness and organization would lend support to the hypothesis of orbital control.

This study seeks such patterns in PLD stratigraphy with datasets that capture bed properties at the finest scale attainable from remotely sensed visible images. We address

three principal questions. First, are the bed thickness characteristics of the previously measured NPLD stratigraphic column [*Fishbaugh et al*., 2010b] found elsewhere in the NPLD? Second, what range of bed thickness exists in the south polar layered deposits (SPLD)? Third, how do spectral characteristics of the PLD relate to direct measurements of bed thickness and organization, using refined topographic data? Section 2 reviews general characteristics of the polar domes and previous work on PLD stratigraphy. Section 3 details methods used for topographic extraction and data analysis. Section 4 presents results of stratigraphic analyses at several sites within the PLD, which are compared to spectral estimates of PLD organization in Section 5. We discuss the measurements with respect to the orbital-control hypothesis in Section 6, and distill conclusions in Section 7.

2. Stratigraphy of the polar layered deposits

Both PLD are dissected by spiral troughs, which dominate the large-scale topography of the NPLD. The SPLD extend as far equatorward as ~70° S, and form a broad plateau from 70-82° S and 130-230° W (Fig. 1) [*Kolb and Tanaka*, 2001]. Several lines of evidence indicate that water ice comprises most of the PLD [*Mellon*, 1996; *Nye et al*., 2000; *Bibring et al*., 2004; *Langevin*, 2005; *Zuber et al*., 2007; *Piqueux et al*., 2008; *Wieczorek*, 2008]. Radar data suggest a <2% and <10% dust component by mass of within the NPLD and SPLD, respectively, and also reveal that the PLD are commonly 1-2 km thick [*Picardi et al*., 2005; *Plaut et al*., 2007; *Phillips et al*., 2008]. The SPLD likely harbors a buried CO_2 deposit comparable to the mass of CO_2 in the atmosphere [*Phillips et al*., 2011]. A collection of several beds discernable in visible images may produce a single reflection in the radar data; thus detailed stratigraphic study requires visible images of PLD

outcrops [*Milkovich et al*., 2009]. Unconformities pervade both PLD [*Howard et al*., 1982; *Tanaka and Kolb*, 2005], while faulting is rare [*Byrne*, 2009]. These parallels suggest that the NPLD and SPLD share a similar composition and origin. The two units differ, however, in stratigraphic context and age.

The NPLD unconformably overlie the Planum Boreum Cavi, which outcrops on the NPLD periphery and consists of beds of ice and locally cross-bedded sand [*Herkenhoff et al*., 2007]. A meter-thick, water ice residual cap unconformably overlies the NPLD and is seasonally draped by CO_2 and water frost [*Tanaka et al*., 2008; *Byrne*, 2009]. Few craters mark either PLD surface, particularly for the NPLD, whose surface age has been estimated at ~10^5 yr old or less [*Herkenhoff and Plaut*, 2000; *Tanaka and Kolb*, 2005; *Banks et al*., 2010]. In contrast, the population of relatively small craters implies a 10-100 Myr SPLD surface age [*Herkenhoff and Plaut*, 2000; *Koutnik*, 2002]. *Pathare et al*. [2005] suggested an age of several hundred Myr to >1 Gyr due to the removal of large craters by viscous relaxation The SPLD base is roughly 6 km higher than that of the NPLD, and overlies Hesperian and Noachian surfaces, including the Dorsa Argentea Formation [*Tanaka and Scott*, 1987]. The SPLD are covered in places by an annually persistent CO_2 ice cap of a few meters thickness, and seasonal frosts of CO_2 and occasionally water [*Byrne, 2009*].

Several studies have used image analysis to construct conceptual models of large-scale SPLD accumulation. *Byrne and Ivanov* [2004] used the orientation of a widespread and prominent topographic bench to infer a domical structure. *Milkovich and Plaut* [2008] interpreted the SPLD to consist of three distinct units with different areal extents, which include (from stratigraphically highest to lowest) the Bench-Forming Layer sequence, a

distinct layered sequence termed the Promethei Lingula Layer sequence, and a buried unit inferred from radar observations [*Plaut et al*., 2007].

A number of theoretical studies have investigated connections between Mars' climate and the growth of PLD stratigraphy. *Toon et al*. [1980], *Cutts and Lewis* [1982], and *Jakosky et al*. [1993, 1995] approached polar deposit evolution through one-dimensional energy balance models. More recently, *Levrard et al*. [2007] simulated PLD growth with meridional water vapor exchange calculated from a global circulation model, and parameterized dust activity; discrete beds formed with the aid of a sublimation dust lag effect. Models that involve dust can generally produce PLD beds in response to insolation variations, but have not been designed to reproduce the number, thickness, and albedo characteristics of beds at a particular location. Distinct beds could form in several ways, including through changes in the ice to dust ratio, variations in ice or dust grain size, or depositional hiatuses [*Cutts and Lewis*, 1982; *Levrard et al*., 2007]. Quasi-periodic forcing of ice deposition could result in ordering or clustering of bed thickness values. Noachian bedrock outcrops in Arabia Terra exhibit such periodicity: several outcrops possess narrowly distributed bed thicknesses, including a location in Becquerel crater where beds are topographically grouped in bundles [*Lewis et al*., 2008]. In addition to recording orbital forcing, trends in PLD bed thickness with depth could hold information on water or dust supply in different climate states and the influences of compaction and flow. For example, compaction should cause beds to thin with depth in a stratigraphic column due to increasing overburden.

Several previous studies have sought to identify an orbital signature in PLD stratigraphy, and image data acquired in the last decade has revealed the polar landscape in increasing detail. *Fenton and Herkenhoff* [2000] used photoclinometry and point-measurements of elevation from stereogrammetry using *Viking* images, as well as Mars Orbiter Laser Altimeter (MOLA) data, to identify beds between 10 and 100 m thickness in a single NPLD trough. Several investigators analyzed brightness profiles of the upper few hundred meters of the NPLD using higher-resolution Mars Observer Camera (MOC) images and MOLA topography, with the aim of capturing periodicity in the stratigraphic record. The interior troughs of Planum Boreum only expose this upper section of the NPLD, while larger sections are exposed closer to the perimeter [*Byrne*, 2009]. *Laskar et al*. [2002] found a spectral peak at ~26 m in a MOC image, and tuned the time represented by the image brightness profile to the modeled insolation history in order to estimate ice accumulation rates. *Milkovich and Head* [2005], *Milkovich et al*. [2008], and *Perron and Huybers* [2009] assessed periodicity using the same datasets, but for a much larger suite of sites. Power spectra of NPLD brightness derived by *Milkovich and Head* [2005] and *Milkovich et al*. [2008] show peaks from 23-35 m wavelength in several images, but *Perron and Huybers* [2009] found that only a ~1.6 m wavelength signal consistently exceeds the red noise background common to PLD brightness spectra.

Correlation studies have also benefitted from increased image and topography resolution. *Fishbaugh and Hvidberg* [2006] used MOC images and MOLA topography to correlate two bed sequences within the upper 500 m of NPLD stratigraphy, and inferred that relative net ice accumulation rates varied by as much as a factor of two within each

sequence. *Kolb and Tanaka* [2001], *Malin and Edgett* [2001], and *Milkovich and Head* [2005] also report NPLD bed correlations across large distances. *Kolb and Tanaka* [2006] identified beds that were continuous over >150 km along canyon walls in Australe Sulci, while *Milkovich and Plaut* [2008] discontinuously correlated individual beds and bed sequences across the entire SPLD and found that individual sequence thicknesses varied by up to a factor of four over several hundred kilometers.

Relating the various unconformities with the SPLD to each other and the surrounding stratigraphy represents a prominent need for establishing stratigraphic relationships. SPLD unconformities range in elevation from 1500 to 3200 m, but have resisted correlation due to limited bed exposure stratigraphically above and below *Milkovich and Plaut* [2008]. In their study of the Promethei Lingula region, *Kolb and Tanaka* [2006] used mapping of bed orientations and unconformities to also infer three primary PLD accumulation periods separated by major hiatuses. Although at least one regional stratigraphic mapping study *Kolb and Tanaka* [2006] has established a framework for relating unconformities near one of our study sites (SP3), the intervening distance is too large to confidently correlate unconformities without extensive image analysis and is beyond the scope of this study.

Where High Resolution Imaging Science Experiment (HiRISE) [*McEwen et al*., 2007] image pairs and MOLA altimetry data are available (below 87° latitude), stereogrammetry-derived digital elevation models (DEMs) have superseded the MOLA elevation dataset central to many of the aforementioned studies, and permit direct bed thickness measurements. A 400 m section of the upper NPLD [*Fishbaugh et al*., 2010b]

shows undifferentiated sections, groups of fine beds (thicknesses 1-2 m) and dark, topographically prominent marker beds, so-named because similar beds have been observed to correlate over large distances [*Malin and Edgett*, 2001; *Fishbaugh et al*., 2010a]. Where appropriate we adopt the same bed classification, with the caveat that we do not evaluate whether the marker beds discussed herein are expressed elsewhere in the NPLD stratigraphy.

Beds within the SPLD are more uniform in albedo; the majority of the exposed stratigraphy has been mapped as a single layered unit, termed the Planum Australe 1 unit [*Tanaka and Kolb*, 2005]. The main correlated sequence [*Milkovich and Plaut*, 2008], the Promethei Lingula Layer sequence (after its type locality), also belongs to this unit. A relatively thin, overlying horizon has been distinguished by its pitted and knobby texture as the Planum Australe 2 unit [*Tanaka and Kolb*, 2005] and as the Bench-Forming Layer sequence [*Milkovich and Plaut*, 2008], after the horizon identified by *Byrne and Ivanov* [2004]. The work presented herein is focused on the Planum Australe 1 unit. Because beds within this unit lack textural or albedo differences with which to distinguish bed types, no facies-based stratigraphic columns are generated for the SPLD sites described herein. In contrast, the variability between the marker beds and fine bed sets in the NPLD enables mapping boundaries between these bed types. As noted by *Byrne* [2009], SPLD beds commonly form topographic benches, while in profile NPLD beds protrude less distinctly from trough slopes. As in the NPLD, some SPLD bed boundaries are gradational due to a combination of erosive and depositional processes (see *Fishbaugh et al*. [2010a]).

SPLD bed thickness and stratigraphic periodicity has garnered limited attention in previous work. *Herkenhoff and Kirk* [2001] derived bed thicknesses of ~10 m within the SPLD using MOC image photoclinometry, and suggested the presence of thinner beds. *Byrne and Ivanov* [2004] measured beds in Australe Mensa at several meters thick, while *Milkovich and Plaut* [2008] estimated bed thicknesses ranging from ~5-40 meters on the basis of ~17 m/pixel Thermal Emission Imaging System (THEMIS) images and MOLA topography. *Milkovich et al*. [2008] found a principal wavelength of 35 m in MOC image brightness at one SPLD location. Mars' chaotic obliquity evolution limits inference of insolation prior to 10-20 Ma [*Laskar et al*., 2004], which likely precludes direct comparison of modeled insolation to SPLD stratigraphic columns. A periodic component to SPLD stratigraphy nonetheless remains possible.

This work presents stratigraphic columns and bed thickness distributions at two sites within the NPLD, as well as the first three bed thickness distributions within the SPLD at the scale of HiRISE image data. Because of the presence of undifferentiated sections limits the continuity of direct bed thickness measurements, and for comparison to previous analyses, we also perform spectral analysis of slope and image brightness to characterize the dominant spatial scales of bed organization.

3. Bed thickness measurement methods

3.1. Bed identification

With existing datasets, beds are definable using image brightness, meter-scale topography, or a combination of the two. Though previous studies of NPLD bed thickness have mostly utilized image brightness, this property has been demonstrated to vary with

lighting conditions, surface roughness, and the presence of frost or dust veneers [*Fishbaugh et al*., 2010a]. As an alternative method of bed delineation, high-resolution DEMs allow bed definition by breaks in slope in shaded relief maps, but the topographic irregularity from mantling deposits and erosive processes (including eolian modification, slumping, and sublimation pitting) is similar in magnitude to the stratigraphic thickness of the finest visible beds in the NPLD [*Fishbaugh et al*., 2010a]. Thus the topography does not consistently reveal distinct bed surfaces. In practice, light and dark bands observed in images are laterally continuous and commonly do coincide with slope transitions in the co-registered DEM. Consequently, in this study, where beds are apparent from image brightness but indistinct in shaded relief, we determine the brightness corresponding to the ledge (sub-horizontal surface) and slope of each bed as long as a locally high slope (in the DEM) occurs between the bright and dark bands (in the orthophoto). Where the beds are distinct in shaded relief, the shaded relief map is used to delineate bed ledges. The difference of successive ledges is taken as the apparent bed thickness (Fig. 2). We assume similar controls on image brightness of SPLD surfaces [*Milkovich and Plaut*, 2008] as has been investigated in the NPLD [*Fishbaugh et al*., 2010a], and that the topographic criteria used to identify bed ledges and slopes are equally applicable to beds in both PLD.

3.2. Image processing and DEM extraction

DEMs are generated with methods similar to previous studies [*Kirk et al*., 2008; *Lewis et al*., 2008; *Fishbaugh et al*., 2010a]. HiRISE image resolution is typically 25 cm/pixel. Each pair of images undergoes radiometric calibration, correction for detector orientation and optical distortions, and mosaicking using the US Geological Survey's

Integrated Software for Imagers and Spectrometers 3. Topography is derived from the images using BAE Systems' SOCET SET following methods similar to *Kirk et al*. [2008] and *Lewis et al*. [2008]. The elevations of surface points common to each image are controlled using individual MOLA retrievals and gridded data. All DEMs possess residuals—the discrepancy between feature locations and their predicted locations based on the sensor model—with a maximum root-mean-square of 0.70 pixel. Initial DEM quality control entails plotting contours of the extracted topography over the source images to check alignment with the surface. Finally, one HiRISE image is ortho-rectified with respect to the DEM to correct the image for optical distortion. High-frequency vibrations unresolved by spacecraft orientation kernels cause decimeter-scale elevation discontinuities at CCD boundaries, and failure of the pixel correlation algorithm also contributes artifacts in limited regions, which are clearly visible in the shaded relief and avoided for analysis.

3.3. Correction for non-horizontal bed orientation

For each site, the orthophoto, DEM, and shaded relief map are examined concurrently (Fig. 2). An equidistant cylindrical projection centered on the latitude of the image is used at all sites. We measure bed orientation by fitting a plane to the bed ledge. Using the orthophoto and shaded relief map, the orientation of each discernable bed is measured by tracing a profile along the bed ledge, interpolating the DEM for elevation along the profile, and determining the best-fit plane using multiple linear regression. We fit the equation of a plane:

$$z = ax + by + c. \quad (1)$$

The dip azimuth (θ) and magnitude (ϕ) are determined from the regression coefficients using:

$$\tan(\theta + \pi) = b/a \quad (2a)$$

$$\tan \phi = (a^2 + b^2)^{1/2}. \quad (2b)$$

A bed ledge must have appreciable planform curvature or width to allow a well-constrained plane fit, so some beds do not permit meaningful orientation measurements. Therefore in moving up-section, we assume that a group of adjacent beds possesses a consistent orientation until a measurement higher in the stratigraphic section suggests a change in orientation. Any regression solutions for which the uncertainty in the fitted plane's pole orientation exceeds 1° are disregarded. Orientation information enables projecting the elevation of each bed ledge to a common stratigraphic reference frame. A dip correction yields the stratigraphic distance between bed ledges (i.e., derived true bed thickness).

Shallow topographic slopes enhance bed exposure; thus the effective stratigraphic resolution is generally finer than the typical 1 m horizontal resolution of the DEM and orthophoto. Consequently, any beds that escape detection would have to be much finer than a few decimeters in thickness [*Herkenhoff et al*., 2007; *Lewis et al*., 2008]. Topography has been modeled at five sites (Fig. 1 and S1-S5), based on the availability of HiRISE observations suitable for stereogrammetry, and the quality of bed exposure. Site-specific bed thicknesses and orientations are shown in Table 1. Stratigraphic sections are oriented to sample topographically distinct beds and to maximize section height.

3.4. Bed thickness measurement error

We consider error in bed thickness measurements from three sources: imprecise bed identification, uncertainty in bed orientation, and errors in the DEM (Table 2). To estimate the error in bed ledge identification, an independent investigator delineated bed ledges in previously measured locations at two sites (sites NP2 and SP1), which contained 30 beds with measured thicknesses from 1-12 meters (Fig. S6). Bed thickness measurements by different investigators using the plane differencing technique show no consistent trend in measurement error as a function of stratigraphic position. Although most beds less than 5 meters thick at site SP1 possess higher relative error than those at site NP2, this trend is inconsistent and may not be significant given the limited number of SP1 beds in that thickness scale range. We also conducted point measurements of true (dip-corrected) bed thickness over more than a kilometer laterally at these sites to characterize lateral bed thickness variability at the scale of stratigraphic horizon averaging. Both methods suggest a median relative uncertainty in bed thickness of about 10 percent owing to differences in where a bed ledge is sampled.

Surface roughness and bed ledge deviation from planarity contribute to uncertainty in a fitted plane's orientation. We estimate the uncertainty in bed thickness arising from the planar fit using a Monte Carlo technique. For each group of beds assumed to share the same orientation, bed thickness is calculated using the subset of well-constrained orientation measurements. The average of the planar regression coefficients and their 1-σ confidence intervals are used to generate a population of 1000 normally distributed values of dip azimuth and magnitude (mean and standard deviation listed in Table 1). For each set of orientation angles, the bed thickness is calculated from the difference of stratigraphic

heights (c in equation 1) for each ledge. We calculate the error as the standard deviation in thickness for each individual bed, as measured from the calculated population of orientations for the suite of beds. Our measurements show this relative magnitude of this error source to be ≤1% of bed thickness at all measured beds (Table 2).

An additional contribution to error in stratigraphic height results from errors in the DEM. The theoretical DEM vertical precision is a function of spacecraft position, image resolution, and pixel correlation error [see further *Kirk et al*., 2008; *Fishbaugh et al*., 2010a; *Okubo*, 2010], and is listed in Table 2 for each site. Although vertical precision at the study sites ranges from 0.4-0.9 m, we reduce the standard error by averaging stratigraphic height determined from equation 1 over at least 100 locations along a bed ledge, which reduces the error in ledge stratigraphic height by a factor of at least 10. Since bed thickness is determined using the difference of the upper and lower bed boundaries, the absolute error in thickness of each bed is determined using the following equation

$$E_{t,i} = \sqrt{e_{a,UL}^2 + e_{a,LL}^2 + \left(e_{r,s}t_i\right)^2 + \left(e_{r,o}t_i\right)^2}, \quad (3)$$

where $E_{t,i}$ is the absolute error in thickness in bed i with thickness t_i, $e_{a,UL}$ is the absolute in error upper bed ledge stratigraphic height, $e_{a,LL}$ is the absolute error in lower bed ledge stratigraphic height, $e_{r,s}$ is the relative error due to subjectivity in bed delineation, and $e_{r,o}$ is the relative error due to uncertainty in bed orientation.

4. Stratigraphy and bed thickness within the PLD

4.1.1 Site NP2

Site NP2 (Fig. 1 and S1) occupies a trough wall with a rounded exposure of NPLD and relief in excess of 1 km. The exposed section lies within the Planum Boreum 1 unit

[*Tanaka et al*., 2008], which comprises most of the NPLD, and is near its periphery. Bright frost, perhaps seasonal, obscures the highest beds at the site. An angular unconformity is present, and is extrapolated to a paraconformity within the measured section (Fig. 3); this may represent a period of erosion.

Three distinct sets of fine beds exist within the measured stratigraphic column. Structural measurements taken from the middle and upper fine-bedded sections indicate a consistent dip with an average magnitude of 0.6°. The lowermost thin bed set begins beneath the starting point of the column, and possesses a stratigraphic thickness greater than 45 m. Some beds of the lower thin bed set exhibit local slumping, but most remain intact; however, contacts between fine beds at the top of the set are gradational. Immediately above the lower fine bed set is a dark, topographically prominent marker bed, with some surface erosion. Undifferentiated sections bracket the middle fine bed set, which has a thickness of ~25 m. Following another undifferentiated section with partially obscured fine beds at the top, the top thin bed set proceeds upward for ~10 m before terminating in another undifferentiated section. As observed by *Fishbaugh et al*. [2010b] for site NP1, the bed types at site NP2 are sets of fine beds that alternate with thicker, darker marker beds, and undifferentiated sections. In places the undifferentiated sections show traces of smoothed fine beds [*Fishbaugh et al*., 2010a], while some sections bereft of apparent bedding might have been deposited as massive units. Bed thicknesses were directly measured where attainable, and compared to relative stratigraphic height within the measured section (Fig. 5a). All of the beds measured belong to fine bed sets, because of ambiguous marker bed boundaries. The directly measured beds all possess thicknesses

between 1 and 2 m, and are similar in thickness to the fine beds measured at site NP1 [*Fishbaugh et al*., 2010b]. The uppermost beds thin with depth, while the lowermost beds thicken with depth; however neither group contains enough beds for these trends to be statistically significant.

4.1.2. Site NP3

Site NP3 (Fig. 1 and S2) occupies a topographically complex region between two local highs. Thickness measurements and bed types were noted along the transect shown in Fig. S2. Structure measurements from beds in the lower and middle part of the transect, indicate a consistent dip with an average magnitude of 0.7°. As with sites NP1 and NP2, site NP3 lies within the Planum Boreum 1 unit [*Tanaka et al*., 2008]; the distance from site NP3 to the NPLD periphery is intermediate between the equivalent distances for NP1 and NP2 (Fig. 1). Small amounts of frost highlight particular beds, but other mantling deposits partially drape bed exposures. Some unit contacts are gradational, but many of the fine beds remain topographically well defined.

The stratigraphic column (Fig. 4) shows that four sets of fine beds are present, the lower two of which are each less than 10 m thick. The lower two fine bed sets are separated by an undifferentiated unit, which nonetheless contains a few faint, continuous horizons that appear to represent mantled fine beds. The upper two sets of fine beds possess similar collective thicknesses (~62 m for the lower, ~58 m for the higher). Except for the bottom fine bed set, all fine bed sets are overlain by an undifferentiated unit and then a marker bed above. Notably, the fine beds again cluster between 1 and 2 m thickness (Fig. 5b), whereas the marker beds form a distinct thickness population with thickness 3.0-3.6 m. Fine bed

thickness shows no trend with depth in the section. Measured bed thicknesses are comparable in magnitude to those at sites NP1 and NP2. The separation distances observed between marker beds (~74 m, ~67 m) are much greater than the 24-36 m separation distance which would correspond to the peak in spectral power at that wavelength noted by *Milkovich and Head* [2005] in many sections of the NPLD. *Fishbaugh et al*. [2010b] note that the 24-36 m separation distance corresponds to only half of the marker beds at site NP1.

4.2.1. Site SP1

Site SP1 (Fig. 1 and S3) occupies a trough in the interior of the SPLD [*Tanaka and Scott*, 1987]. The highest surface has a morphology similar to the broad, pitted surfaces of the Bench-Forming Layers (BFL) [*Byrne and Ivanov*, 2004] and exists within their mapped planview extent [*Milkovich and Plaut*, 2008], but all measurements at this site are made below the potential BFL horizon. The site contains over 20 beds exposed along the measured transect, and no angular unconformities are apparent. Structure measurements indicate a mean dip of 2.7°. We extracted measurements from two sets of locations along the transect, which are separated by a section where bedding is present but indistinct. The bed thickness distribution (Fig. 6a) shows a larger spread in bed thickness than observed for the NPLD sites, and a larger mean thickness. Bed thickness decreases non-monotonically with depth.

4.2.2. Site SP2

Site SP2 (Fig. 1 and S4) exhibits an outcrop with concentrically exposed beds, in the Ultimi Lobe near the margin of the SPLD [*Tanaka and Scott*, 1987]. This region, which

includes site SP3, is the principal zone of brittle deformation within the SPLD [*Kolb and Tanaka*, 2001; *Murray et al*., 2001; *Milkovich and Plaut*, 2008]; however no faults are observed at either of the study sites. Based on their planview location, the beds at these two sites belong exclusively to the PLL interpreted by *Milkovich and Plaut* [2008]. At site SP2, nine structure measurements show dip magnitudes ≤ 1.3° with widely varying azimuths; the well-constrained and small dip magnitude leads to a relatively small uncertainty in bed thickness measurements. The scatter in bed orientations results, at least in part, from the hummocky bed surfaces from which they are derived. A prominent angular unconformity intersect the study section near the transect area and likely transitions to a paraconformity within the measured section (Fig. S4). The thickness measurements show a similar spread in bed thickness compared to site SP1, but also include several beds with thickness greater than 20 m. As at site SP1, bed thickness decreases non-monotonically with depth (Fig. 6b); given the caveat of a small sample size, regression analysis indicates a significant association between depth and thickness at both sites SP1 (n=18, p=0.02) and SP2 (n=23, p=0.04).

4.2.3. Site SP3

Site SP3 (Fig. 1 and S5) also lies near the SPLD margin [*Tanaka and Scott*, 1987]. The site possesses substantial relief (>500 m) and generally well-exposed beds. Bed orientation measurements reveal structure not immediately obvious based on the image alone. The measured section possesses three groups of beds with different orientations. While dip magnitude ranges from 2.2-5.2° within the transect, dip direction varies markedly between, but not within, the three sections (Table 1). Although bed truncations

that would separate these sections are difficult to isolate in the image, we tentatively interpret each of these sections to be separated by angular unconformities based on the three distinct structural zones. We also note two more prominent angular unconformities, including one near the upper portion of the middle section (Fig. S5). The lower and upper sections show measured bed thicknesses ranging from 1 to 5 m, while the upper section ranges in bed thickness from roughly 5 to 27 m (Fig. 7). Bed thickness decreases with depth in the middle section, but increases with depth in the lower 50 meters. No robust trend in thickness is observed leading up to either unconformity.

5. Spectral estimates of PLD periodicity

5.1. Methods

In contrast to the direct measurements of bed thickness and the stratigraphic succession of bed types presented in the previous section, spectral analysis can be used to objectively infer the characteristic spatial scales associated with a stratigraphic section as a whole and can reveal scales of organization beyond the thickness of individual beds (e.g., *Lewis et al*. [2008]). We have performed spectral analysis of image brightness and slope profiles from each of the five study sites, using the multitaper method (Thomson, 1982), which limits leakage of spectral power into sideband frequencies. Brightness and slope are retrieved from the locations of the measured stratigraphic section at each site (Fig. S1-S5). Because multiple factors can influence surface brightness, we concurrently analyze slope derived solely from the DEM in order to determine if slope and brightness yield consistent results.

Climate time series commonly show enhanced power at low frequencies [*Mann and Lees*, 1996], a behavior mirrored by power spectra of PLD image brightness [*Perron and Huybers*, 2009]. Consequently, we evaluate the significance of spectral peaks with respect to a modeled red noise background, using the robust estimation technique of *Mann and Lees* [1996]. Red noise is modeled as a first-order autoregressive process

$$r_n = \rho r_{n-1} + w_n \quad (4)$$

where r_n is red noise, ρ is the lag-one autocorrelation coefficient, and w_n is Gaussian white noise. The algorithm generates a modeled red noise spectrum from input data by (1) identifying and removing narrow-band peaks from the multi-taper power spectrum; (2) smoothing the power spectrum by replacing the power estimate at each frequency with the median of a window centered on that frequency; and (3) optimizing a red noise model, in the least-squares sense, for the remaining spectrum, for the lag-one autocorrelation coefficient and the average value of the spectrum. Confidence levels are computed assuming a χ^2-distribution of spectral power with six degrees of freedom, where the degrees of freedom are proportional to the number of data tapers [*Mann and Lees*, 1996]. The brightness and slope data are corrected for topography and bed orientation, and sampled at 0.1 m^{-1} frequency in the local stratigraphic reference frame. A linear trend is removed from the data and the derived spectra utilize three Slepian data tapers and a smoothing interval of 0.2 m^{-1}; derived spectra and confidence levels vary slightly using a reasonable range of these parameters, but remain qualitatively similar.

5.2. NPLD spectra

Power spectra from site NP3 show several peaks exceeding the 99% confidence level in both image brightness and slope (Fig. 8). Some peaks fall within the 1-σ range of measured bed thickness at the site, while others occupy shorter wavelengths. Power spectra at site NP2 show similar characteristics, with the brightness spectrum showing one peak at slightly longer wavelength than the 1-σ range of bed thickness at that site. When the sampling is restricted to portions of the stratigraphy which contain only fine beds, the most power is associated with beds that fall within the 1-σ range of measured bed thickness at both sites NP2 and NP3, and the spectral peaks are significant at the 99% confidence level (Fig. 9). This directly demonstrates the correspondence between a significant peak in spectral power and a direct thickness measurement in the PLD, a relationship suggested in previous studies [*Perron and Huybers*, 2009; *Fishbaugh et al*., 2010b]. Notably, the peak in spectral power associated with the repeating thickness of fine beds is much less conspicuous in a typical stratigraphic section that contains fine beds, marker beds, and undifferentiated sections. No repeating scale of bed organization greater than the 1-σ range of measured bed thicknesses is observed.

5.3. SPLD spectra

Power spectra of slope and brightness in the SPLD reflect the broad range of measured bed thicknesses. Figure 10 shows a representative power spectrum of slope for the measured stratigraphic section at site SP1. Only one peak exceeds the 99% confidence level. The direct bed thickness measurements do not show clustering around this peak, but rather span a range of greater thicknesses. This may result from difficulty in identifying bed boundaries in limited portions of the section. Power spectra of slope and brightness at sites

SP2 and SP3 (middle section) likewise show no dominant spectral peak; several peaks exceed the 99% confidence level, but show little correspondence to the measured 1-σ range of bed thicknesses at those sites. The SPLD power spectra confirm direct thickness measurements, which imply that the SPLD sites lack a repeating bed thickness.

Several derived power spectra contain peaks at long wavelengths from 30-250 m. These features could arise from large-scale changes in composition or surficial modification. However, the stratigraphic length-scales of the measured transects, at a few hundred meters, are too short to assert the periodicity of long-wavelength features. Therefore, although long-wavelength features do contribute to the spectral signatures of slope and brightness, they do not represent repeating stratigraphic features at the scales of probed by this study. In the specific context of identifying periodic signals in the stratigraphy, it is important to look for signals at similar wavelengths in different records because even a random signal will occasionally exceed the background. However, long-wavelength peaks are not observed to occur at the same wavelengths in either slope or brightness at any of the study sites, and do not correlate between sites. In contrast, the spectral signal of fine beds is observed in slope and brightness records at both NPLD sites, and the wavelength of the fine bed signal is much shorter than all stratigraphic record lengths.

6. Discussion

The stratigraphic columns and bed thickness measurements presented herein and in *Fishbaugh et al*. [2010b] suggest that beds of 1-2 m thickness are common within the Planum Boreum 1 unit of the NPLD. Taken together, the thickness of fine beds at sites NP2

and NP3 is consistent with a normal distribution at a 95% confidence level via the Kolmogorov-Smirnov test, comparing the observed distribution (n = 39) to a theoretical one with the same mean and variance [*Lilliefors*, 1967]. While fine bed thickness is tightly distributed, the fine bed package thickness varies considerably. The moderate side slopes of the PLD troughs strongly enhance stratigraphic resolution to a typical sample interval of ~10 cm, in principle allowing our analysis to detect periodic signals with a stratigraphic wavelength as short as ~20 cm. The reduced spectral power at these short wavelengths implies that any beds thinner than the thinnest measured here—1.0 m for the NPLD, 1.4 m for the SPLD—must be several times thinner [*Herkenhoff et al*., 2007].

Marker bed thickness, fine bed set thickness, and the separation distance between marker beds are less consistent than fine bed thickness, also in agreement with the findings of Fishbaugh et al. [2010b] for site NP1. Wavelet analysis of MOC images of the upper NPLD commonly indicates thinning with depth [*Perron and Huybers*, 2009], and *Fishbaugh et al*. [2010b] suggested that beds at site NP1 show a weak marker-bed thinning trend with depth. Among NPLD bed thickness measurements presented here, the only observed trend is a weak thinning with depth of the fine beds at site NP3. All of the SPLD sites show non-monotonically decreasing bed thickness with depth. The large magnitude of the thickness difference (a factor of several) between beds near the top of these sections versus beds near the bottom, as well as the trend's reversal in the middle section of site SP3, argues against compaction serving as the dominant thinning mechanism. Rather, we speculate that the trends in thickness in the SPLD sections result from changes in deposition rates or bed preservation potential.

The beds of 1-2 m have been confirmed to correspond to the rise in spectral power above a modeled red noise background at ~1.6 m wavelength in several MOC images of the NPLD [*Perron and Huybers*, 2009], as suggested by *Fishbaugh et al*. [2010b]. The consistent thickness of individual fine beds across several columns is suggestive of a quasi-periodic control on fine bed thickness for the NPLD. Whether the consistent thickness of fine beds is related to self-organization within the Mars climate system, or to external forcing on orbital or sub-orbital [*Weedon*, 2003] timescales, represents an important and unresolved question. Numerous terrestrial sedimentary environments show high-frequency cycles in stratigraphy that may result from intrinsic organization [*Einsele et al*., 1991]. Alternatively, *Levrard et al*. [2007] suggested that several beds could form during one orbital cycle, particularly if ice and dust are sourced from multiple reservoirs. The meter-scale beds are considerably finer than those produced by the climate model of *Levrard et al*. [2007], in which beds are emplaced in response to orbital cycles and range in thickness from 10 to 80 meters. However, influences on bed characteristics from local topography, seasonal effects, dust cycles [*Levrard et al*., 2007], and the distribution and evolution of shallow subsurface ice at lower latitudes [*Boynton et al*., 2002; *Schorghofer*, 2007] remain to be considered in future models.

SPLD bed thickness measurements show much greater variability than corresponding measurements for the NPLD (Fig. 11), and the SPLD beds lack the morphologic and albedo differences that distinguish fine beds from marker beds in the NPLD. The large variance in bed thickness either argues against periodic forcing for generating the stratigraphy at the SPLD sites, or alternatively suggests that processes

inherent to bed generation overwhelmed any orbital forcing of ice and dust cycles. The large difference in stratigraphic exposure age implied by surface exposure ages [*Herkenhoff and Plaut*, 2000; *Koutnik et al*., 2002; *Tanaka et al*., 2008] likely has some influence on exposed stratigraphy, and could render fine beds relatively more susceptible to being obscured in the SPLD compared to the NPLD. However, partially obscured fine bed sets are uncommon in the measured SPLD sections, and the overall SPLD bed thickness distribution (Fig. 11) does include beds as fine as 1.8 m. Therefore, while we cannot rule out such processes, the observed stratigraphy does not obviously imply obscuring or amalgamation of fine beds.

Additional sites within the SPLD may yet reveal a class of beds similar to the fine beds at sites NP1, NP2, and NP3; sites SP2 and SP3 are located close to the margin of the SPLD and represent basal exposures. However, no evidence is found to suggest a change in the character of stratigraphy with depth or geographic location within the SPLD comparable to the difference between the NPLD and the Planum Boreum Cavi [*Tanaka and Kolb*, 2001].

Spectral analysis confirms the quasi-periodicity of fine beds in the NPLD. Several factors influence the brightness of the polar layered deposits, including roughness, outcrop-scale slope, and surficial modification [*Fishbaugh et al*., 2010a]. It would be surprising if brightness were independent of bed properties, including ice grain size and dust fraction. The extrinsic influences on brightness may thus complement, rather than completely overprint, compositional signals recorded in the remotely observable stratigraphy. If repeating patterns in brightness do occur and can be linked to independent measurements of

bed or unit thickness, as has been done in this study, then it seems likely that the signals in image brightness reveal bed properties. The brightness variations most likely reflect (1) slope variations dictated by the stratigraphy itself, or (2) intrinsic variations in bed albedo. Measurements of bed thickness, coupled with spectral analysis of brightness and slope, demonstrate that quasi-periodic bed sequences occur at multiple locations in the NPLD, and that in these areas brightness variations are unlikely to be an artifact of roughness, frost, or outcrop-scale slope. This suggests that fine bed sets within the PLDs are recording repeating events that have similar outcomes for the accumulation of ice and dust. In contrast, power spectra of slope and brightness show no consistent wavelength of stratigraphic organization at three SPLD sites, an observation that is also consistent with direct bed thickness measurements.

With a dataset expanded to include bed thickness measurements for three sites within the NPLD and three additional sites within the SPLD, the emerging picture indicates that the only discernable periodicity within the PLD is the consistency for fine bed thickness within the NPLD, a result consistent with previous analyses of the NPLD [*Perron and Huybers*, 2009] that is confirmed here with higher-resolution data. This interpretation is consistent with the SPLD sites analyzed here, which contain no bed-controlled, quasi-periodic signals, but other SPLD sites imaged by HiRISE do occasionally possess adjacent beds which appear fine and of potentially similar thickness (e.g., images PSP_004707_0990 and ESP_014360_0985). These locations also include basal exposures of the SPLD, as at sites SP2 and SP3. Such locations warrant further investigation with high-resolution topographic data, as apparent bed thickness can be deceptive without

detailed analysis to account for bed orientation and topographic exposure. If fine bed sequences are major components of the stratigraphy at other SPLD sites, this would suggest lateral variability in SPLD fine bed accumulation, as such sequences are not observed at the sites studied here. Such a result would contrast with the NPLD stratigraphy, in which thickness of individual stratigraphic horizons varies longitudinally [*Fishbaugh and Hvidberg*, 2006] but the facies types appear consistent across large distances; however, a spotty distribution of fine beds in the SPLD would be consistent with the finding that the large-scale stratigraphy of the SPLD reflects regional variation in net accumulation [*Milkovich and Plaut*, 2008]. If, as suggested by sites SP1-SP3, fine bed sequences are generally rare in the SPLD, it may represent a fundamental difference between the accumulation history of the NPLD and SPLD.

Future observations extending beyond the spatial scale of this study may alter or lend support to this trend. PLD stratigraphy has been shown to correlate laterally within portions of the NPLD [*Fishbaugh and Hvidberg*, 2006], but not yet at the scale of fine bed sets [*Fishbaugh et al*., 2010b]. Moreover, controls on the slope of PLD surfaces remain largely unexplored. Estimates from radar, gravity, and topography data indicate a dustier bulk composition for the SPLD than for the NPLD. We speculate that the difference in bed prominence may owe in part to dust content. If so, the departure of trough topography from a stair-stepped profile could be used to constrain bed composition [*Byrne et al*., 2011].

7. Conclusions

This study presents two quantitative stratigraphic columns of the NPLD, the first three bed thickness profiles of the SPLD using HiRISE data, and refined spectral estimates

of PLD brightness and slope using high-resolution digital elevation models. Observations at three sites—separated from each other by hundreds of kilometers—suggest consistent stratigraphic characteristics of the NPLD at 1-meter horizontal resolution. Direct measurements of bed thickness show that beds 1-2 m thick are common at all three NPLD sites. Marker beds, distinguished by their topographic prominence and low albedo, exhibit thicknesses with greater mean and comparable variance. Neither the thickness of fine bed sets nor the separation distance of marker beds within the NPLD have characteristic values. Using the criteria of topographic prominence and albedo, the SPLD sites show only one type of bed, and the bed thickness shows greater mean and variance than observed for the NPLD fine beds. Data show little evidence for bed compaction at any site, nor waning bed thickness near unconformities. The consistent thickness of fine beds within the NPLD currently represents the only evidence for a quasi-periodic component of PLD stratigraphy.

Acknowledgments

This work was supported by the van Wingen Fellowship, the W. M. Keck Institute for Space Studies, and the NASA Mars Data Analysis Program, award 65P-1089493. Kevin Lewis provided valuable consultation, and Terry-Ann Suer and Michael Lauria contributed to stereogrammetry processing. We gratefully acknowledge the HiRISE Team for the image data, and thank Sarah Milkovich and an anonymous reviewer for comments that greatly improved this manuscript.

Tables

Site	Location	Figures	Bed thicknesses measured	Mean bed thickness and std. dev. (m)	Mean dip azimuth and error (°)	Mean dip magnitude and error (°)
NP2	85.1°N, 143.1°E	3, 5a, 9ab, S1	12	1.7 (0.3)	79.6 (0.7)	0.6 (0.1)
NP3	84.4°N, 253.1°E	4, 5b, 8, 9cd, S2	30	1.8 (0.6)	40.5 (0.3)	0.8 (0.1)
SP1	86.1°S, 172.0°E	6a, S3	18	5.7 (3.1)	73.2 (1.3)	2.7 (0.3)
SP2	76.2°S, 134.5°E	6b, S4	23	1.8-46.3 (range)	14.5-354.5 (range)	0.2-1.3 (range)
SP3	73.1°S, 133.5°E	2, 7, S5	25	12.2 (7.8)	36.9 (1.6) 226 (0.4) 4.0 (0.5)	4.7 (0.5) 3.8 (0.4) 2.5 (0.3)

Table 1. Summary of bed thickness and orientation data.

Site	DEM vertical precision (m)	Bed profile standard error from DEM (100 meas.) (m)	Bed thickness standard error from DEM (m)	Median relative error due to bed orientation (%)		Estimated relative error in bed ledge identification (%)
NP2	0.5	0.05	0.07	0.2		10
NP3	0.4	0.04	0.06	0.1		10
SP1	0.7	0.07	0.09	0.7		10
SP2	0.4	0.04	0.05	0.3		10
SP3	0.5	0.05	0.08	Sect. 1	1.0	10
				Sect. 2	0.2	
				Sect. 3	1.0	

Table 2. Contributions to bed thickness measurement error at each site.

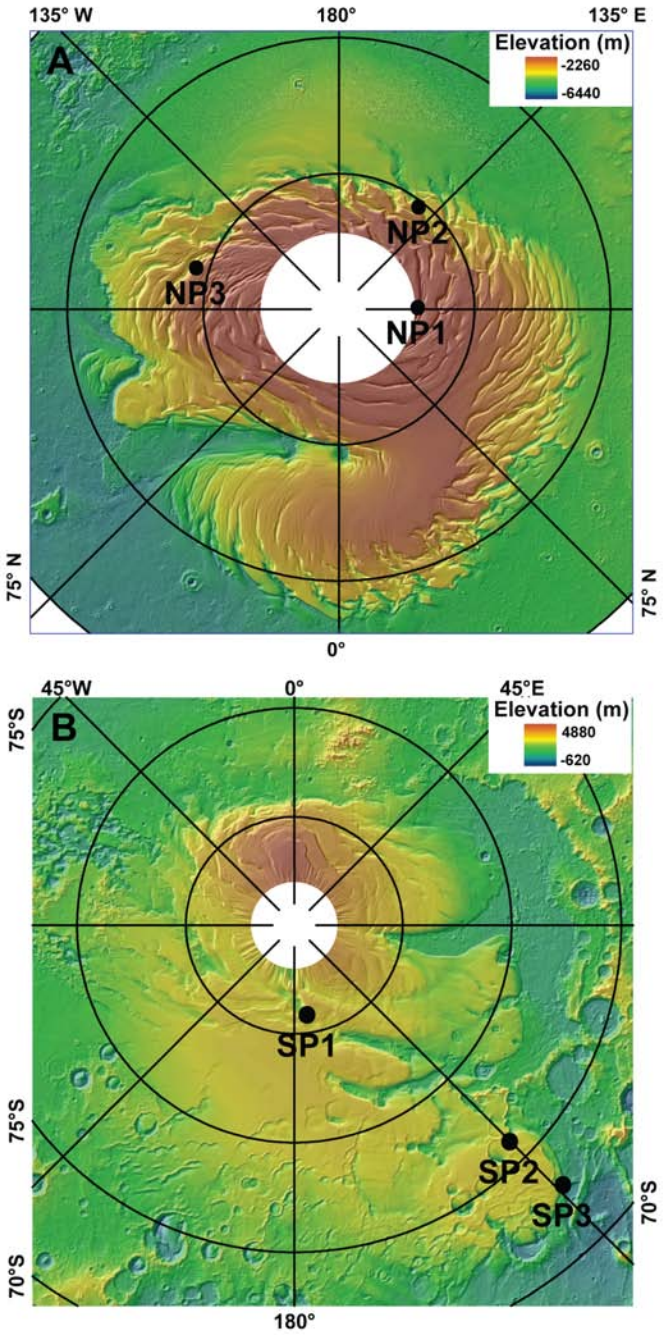

Figure 1. Locations of study sites in the polar regions of Mars. Base image is color-coded, shaded relief of Mars Orbiter Laser Altimeter (MOLA) topography. **(A)** NPLD sites. NP1 has been analyzed by Fishbaugh et al. (2010b). Sites NP2 and NP3 are analyzed herein. **(B)** SPLD sites SP1, SP2, and SP3.

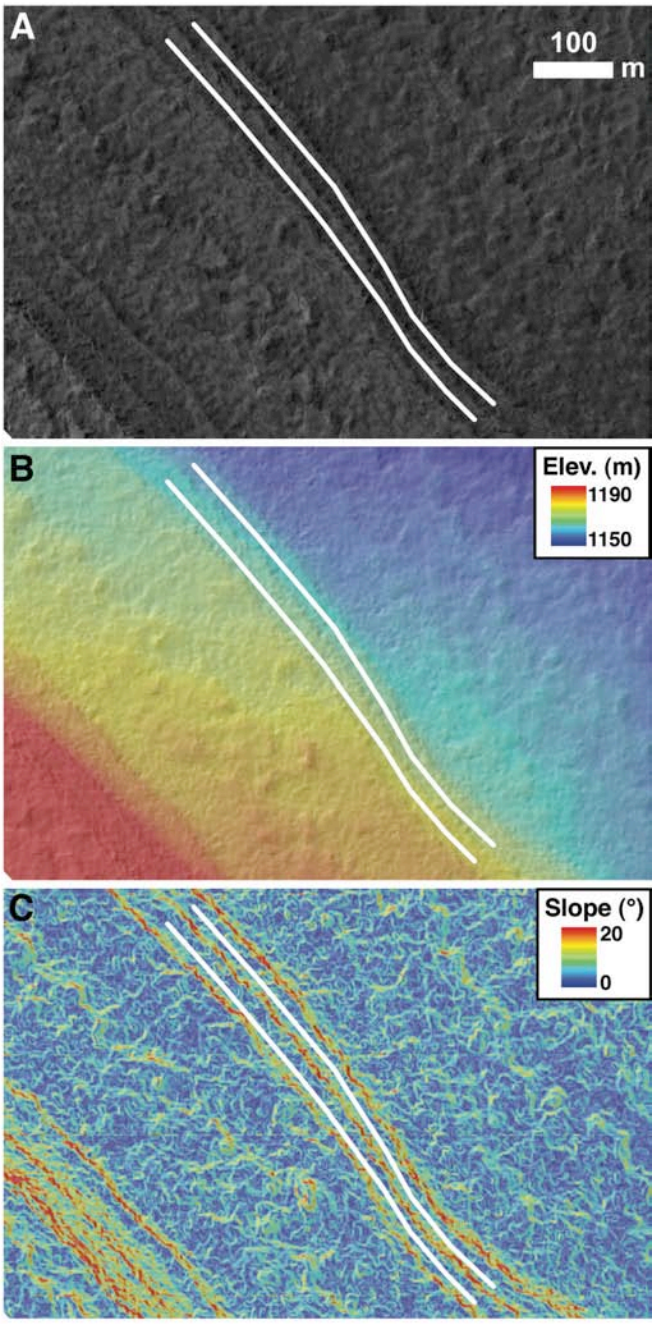

Figure 2. Illustration of bed thickness measurement technique, using a single bed at site SP3. Pixel values are extracted along white profile lines, which delineate bed ledge surfaces. **(A)** Orthophoto produced using HiRISE image ESP_013277_1070. **(B)** Digital elevation model, which shows that right profile samples the lower bounding surface, and left profile samples the upper bounding surface. **(C)** Slope map. Bed risers possess relatively high slopes (red-orange), while bed ledges possess relatively lower slopes (blue-green).

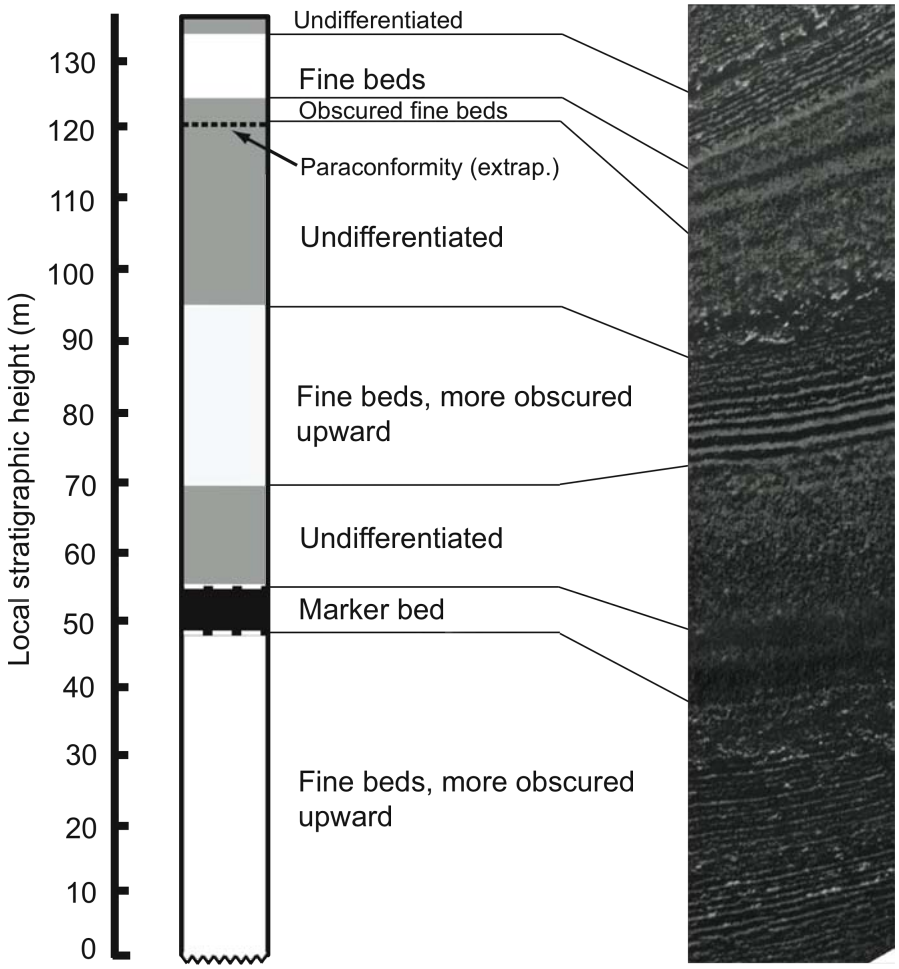

Figure 3. Stratigraphic section of site NP2. Fine bed sequences are shaded white, undifferentiated units gray, and marker beds black. At right, the corresponding portion of orthorectified image PSP_010014_2650. Black lines demarcate unit contacts. White dashed line demarcates tentative marker bed contact. Sawtooth lower boundary on stratigraphic column indicates that fine beds continue below the lower edge of the image. Black dashed line shows extrapolated location of paraconformity (see Fig. S1). Maximum horizontal scale of image is approximately 500 m.

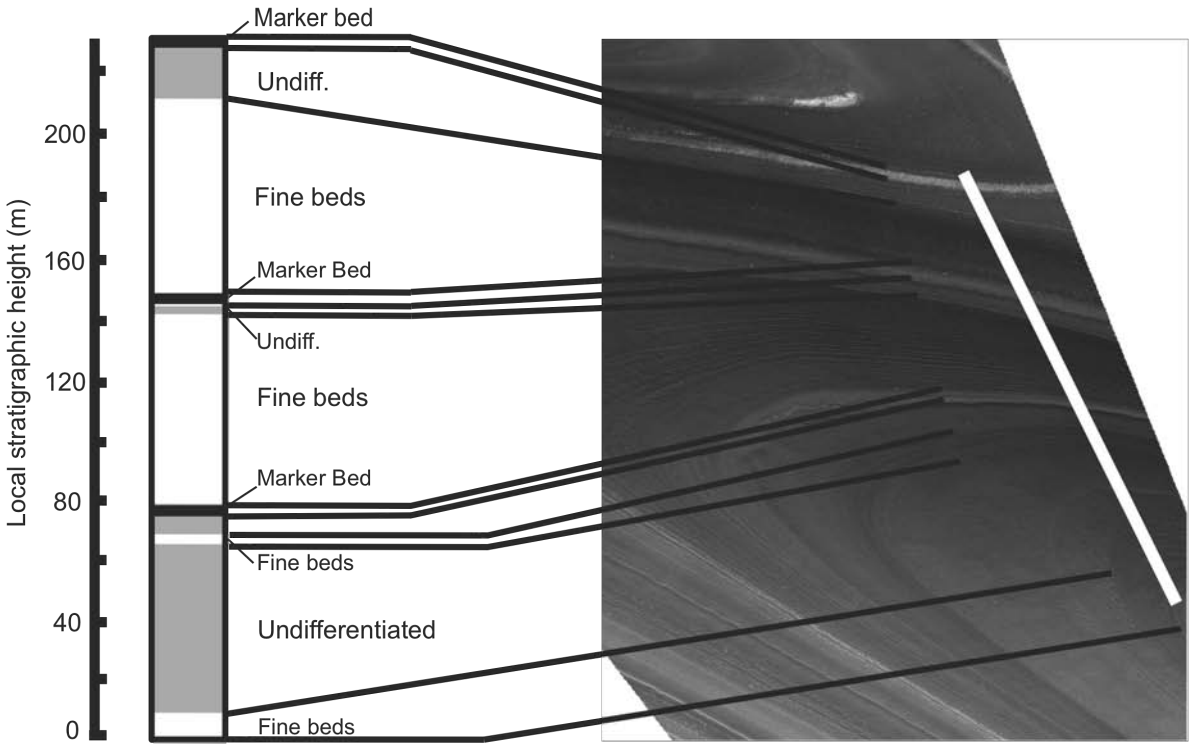

Figure 4. Stratigraphic section of site NP3. Column shading matches that in Fig. 3. At right, the corresponding portion of orthorectified image PSP_010004_2650. Black lines demarcate contacts. White line indicates measurement transect. Maximum distance across image is approximately 5.5 km.

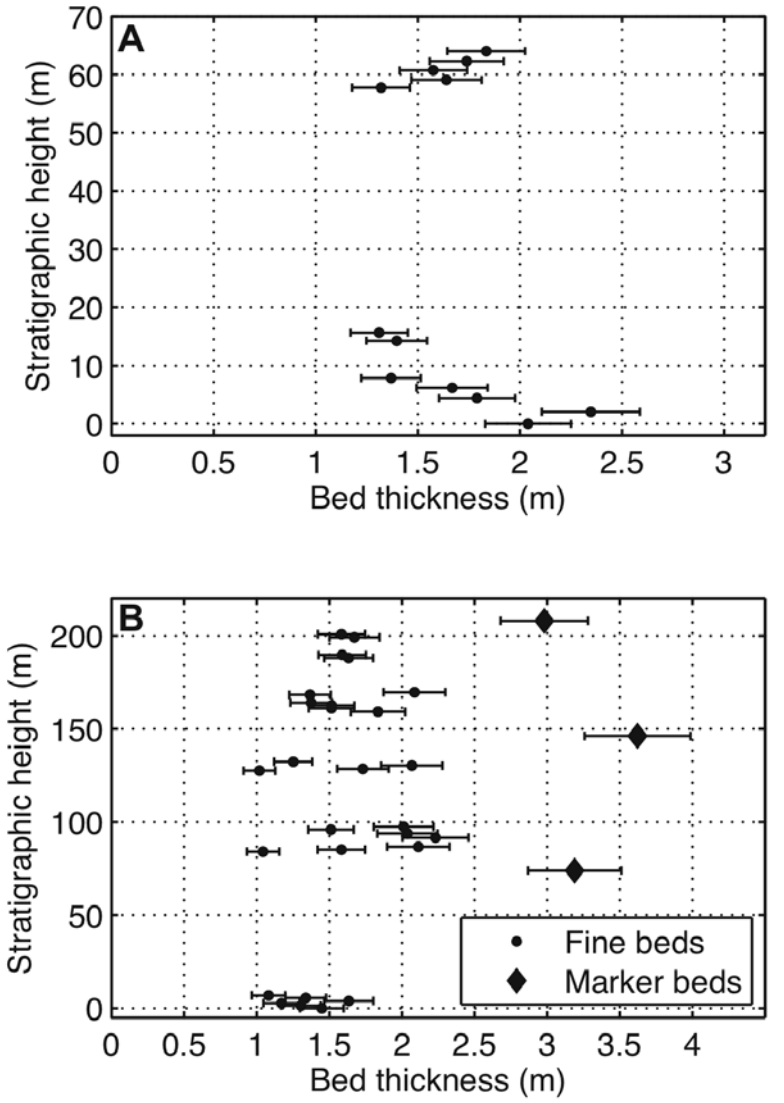

Figure 5. Relative stratigraphic height versus bed thickness for NPLD stratigraphic sections. **(A)** Site NP2. The number of thickness measurements represents the number of directly measured beds; many other beds are present, but are more poorly exposed or more highly eroded. **(B)** Site NP3. The three beds with thickness greater than 2 m are all marker beds; the rest belong to fine bed units.

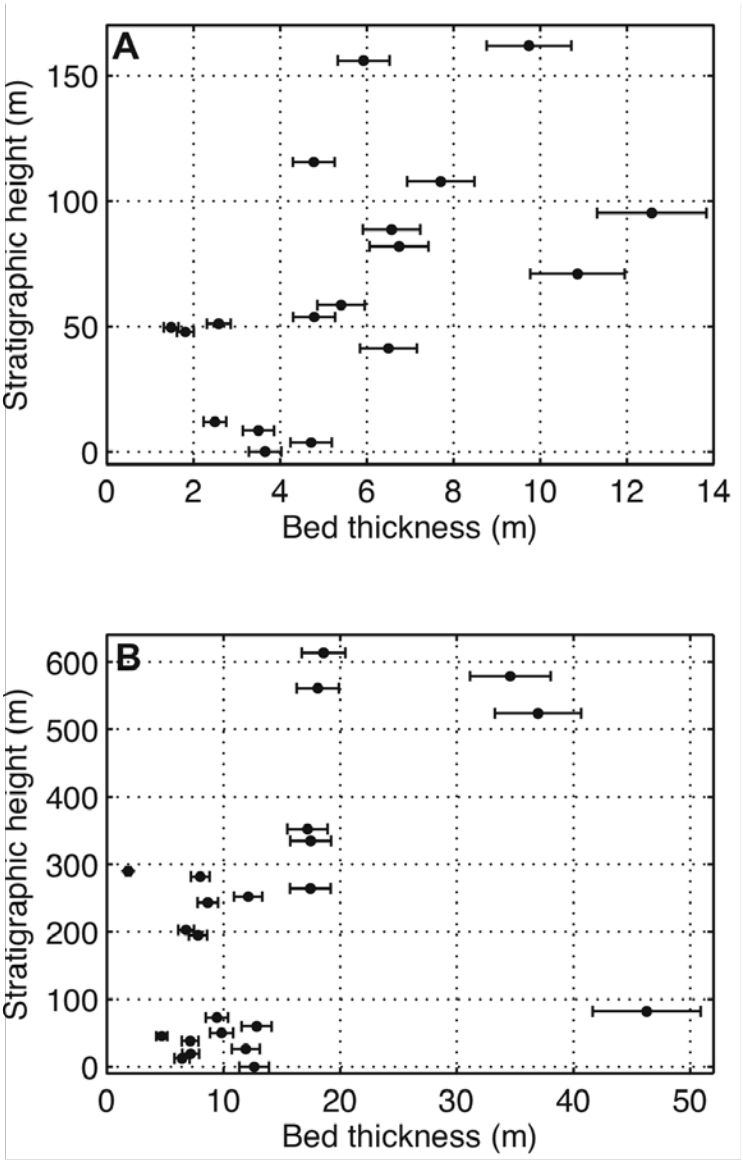

Figure 6. Relative stratigraphic height versus bed thickness for **(A)** site SP1, and **(B)** site SP2.

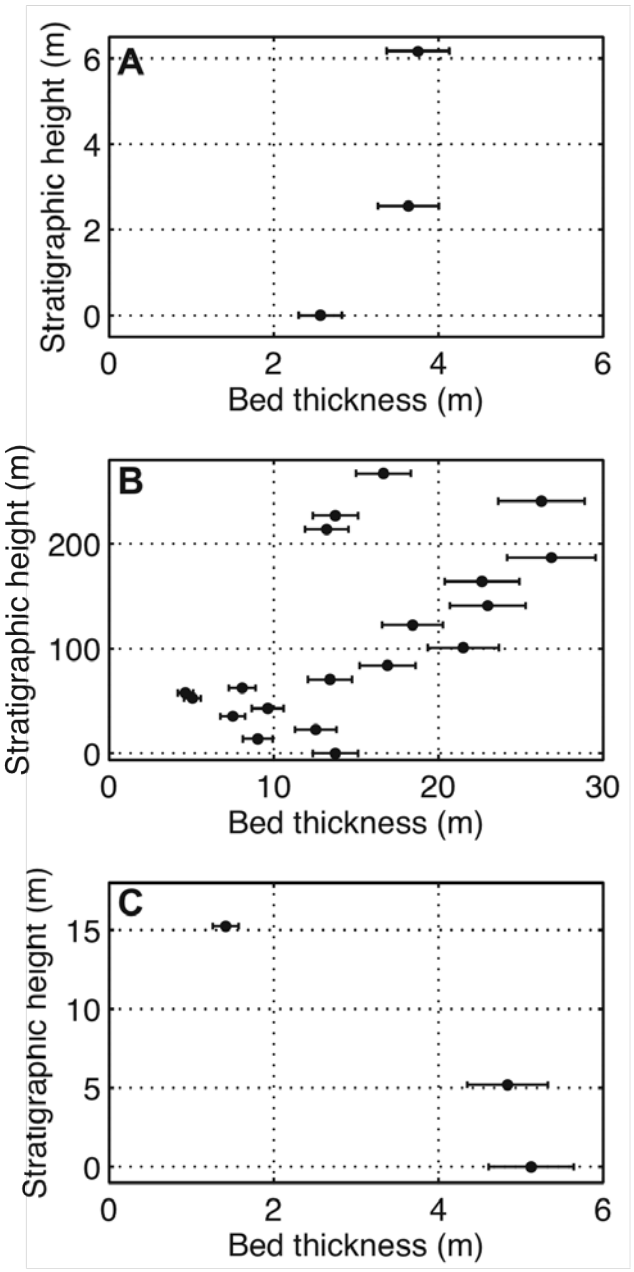

Figure 7. Relative stratigraphic height versus bed thickness for site SP3. **(A)** Upper section; **(B)** middle section; **(C)** lower section. Sections are grouped by bed orientation.

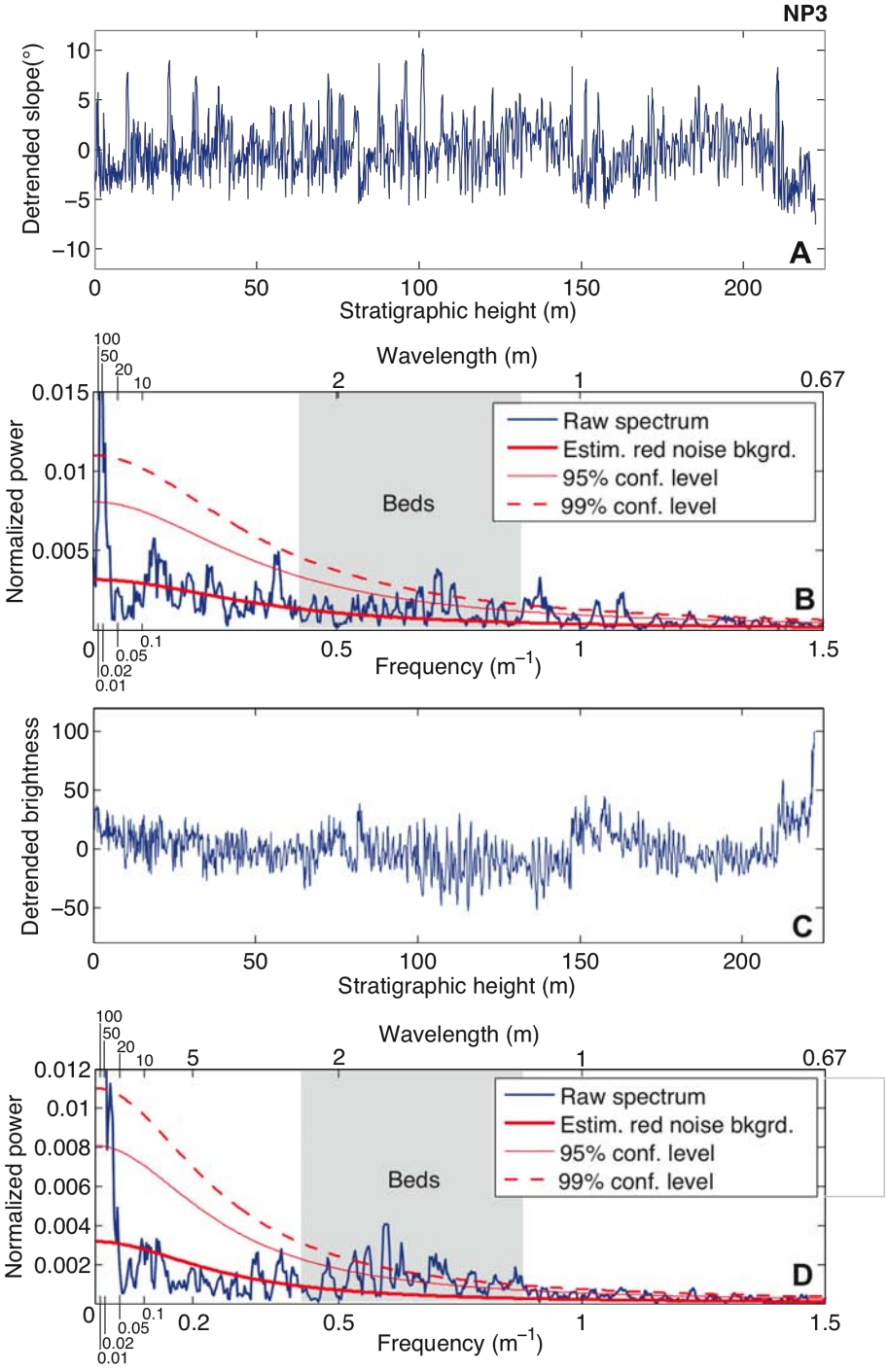

Figure 8. (A) Detrended image grayscale values for the stratigraphic transect at site NP3. **(B)** Power spectrum of data in (A). Shaded portion corresponds to 1-σ range of bed thickness measurements at same site. **(C)** Detrended slope, same location and reference frame as (a). **(D)** Power spectrum of data in (C). Shaded portion corresponds to 1-σ range of bed thickness measurements at the same site.

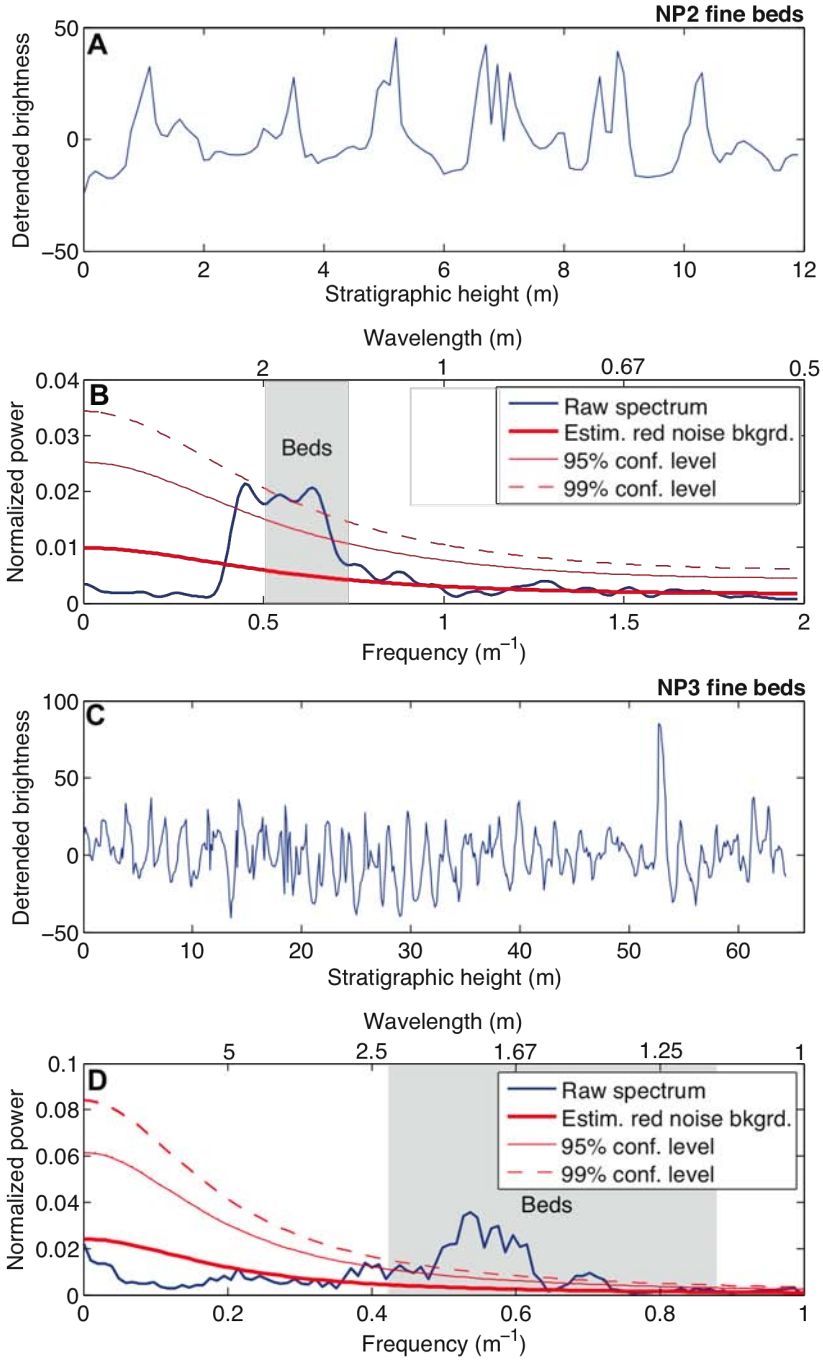

Figure 9. (A) Detrended image grayscale values for a section of fine beds at site NP2, in a stratigraphic reference frame corrected for topography and bed orientation. **(B)** Power spectrum of data in (A). Shaded portion corresponds to 1-σ range of bed thickness measurements at site NP2. **(C)** Detrended image grayscale values for a section of fine beds at site NP3, in stratigraphic reference frame. **(D)** Power spectrum of data in (C). Shaded portion corresponds to 1-σ range of bed thickness measurements at site NP3, including fine beds and marker beds.

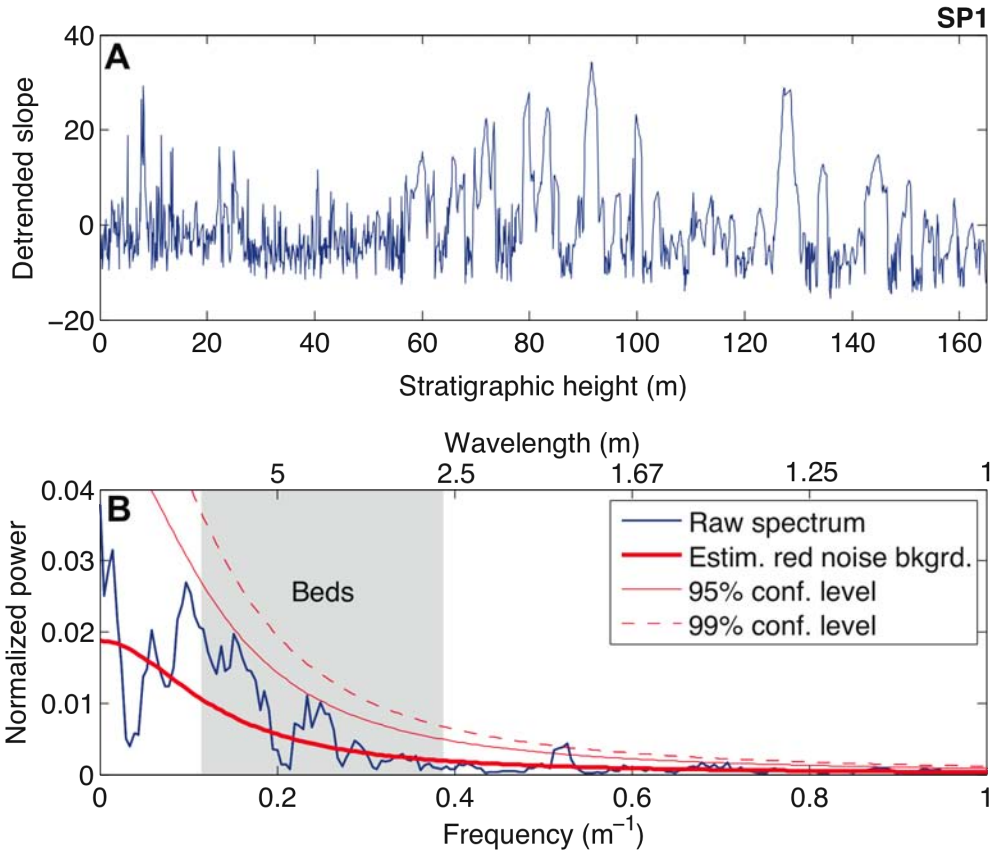

Figure 10. (A) Detrended slope for the stratigraphic transect at site SP1. **(B)** Power spectrum of data in (A). Shaded portion corresponds to 1-σ range of bed thickness measurements at same site.

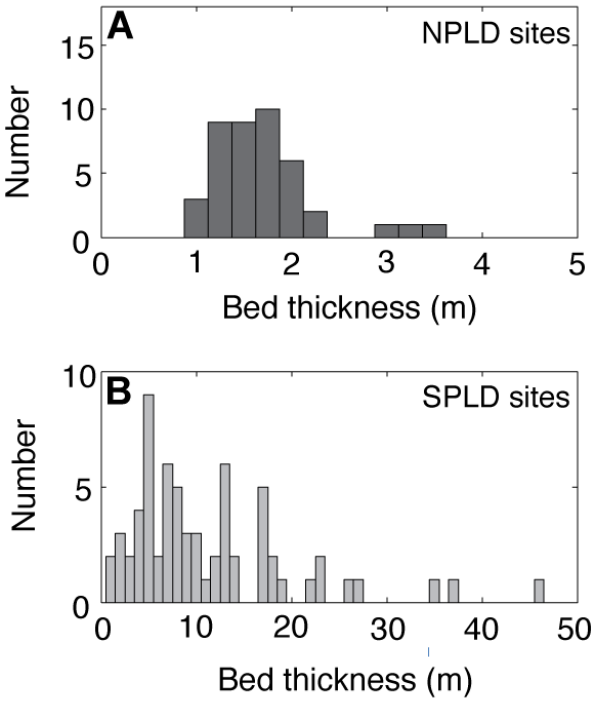

Figure 11. Summary of bed thickness measurements for sites within **(A)** the NPLD, binned at 0.25 m intervals, and **(B)** the SPLD, binned at 1 m intervals.

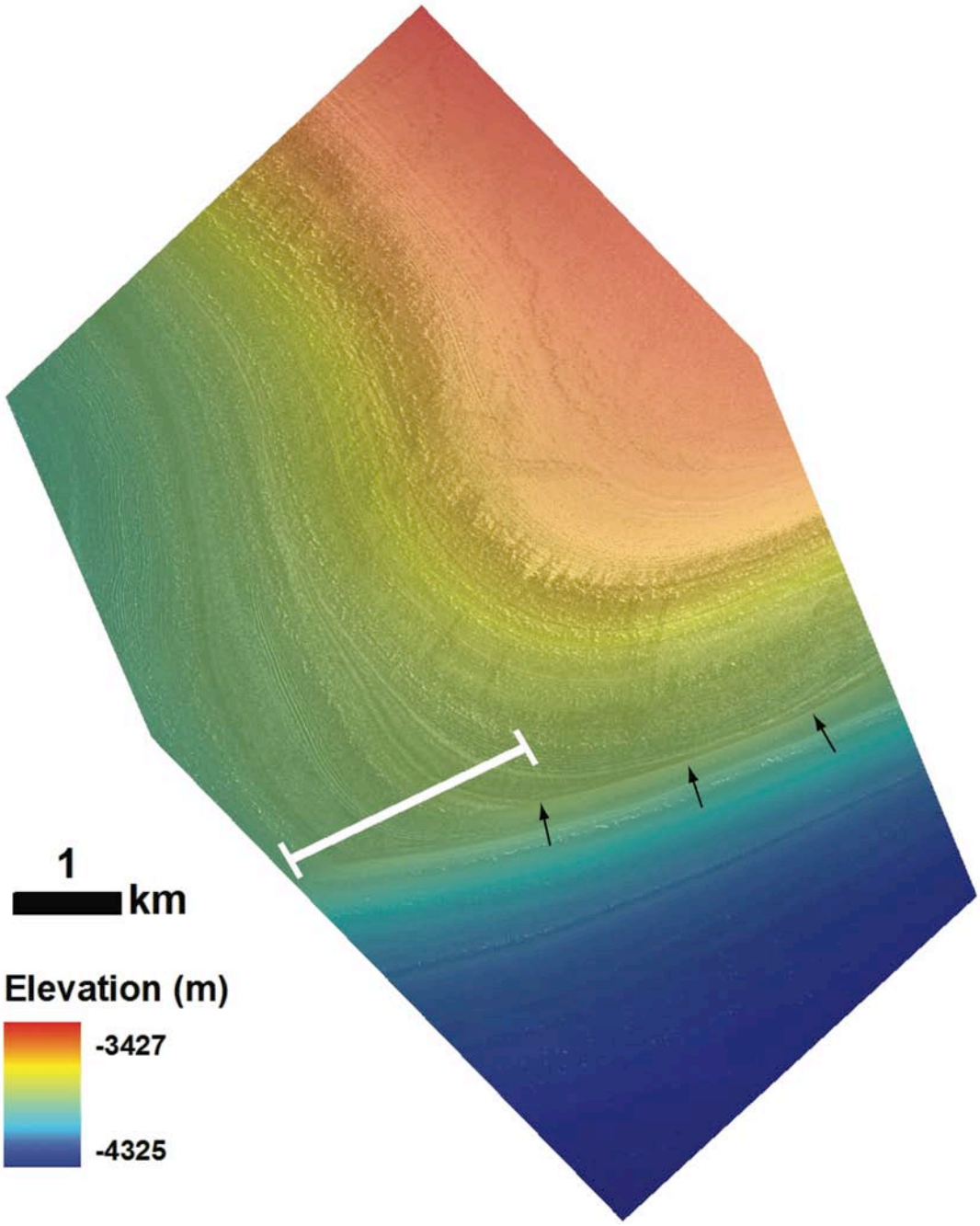

Figure S1. Site NP2. A 1 m-resolution digital elevation model is superimposed on orthorectified HiRISE image PSP_010004_2650 (stereo pair: image PSP_010374_2650). White line denotes location of stratigraphic transect. Arrows denote an angular unconformity, which is extrapolated to a paraconformity within the transect (see Fig. 3).

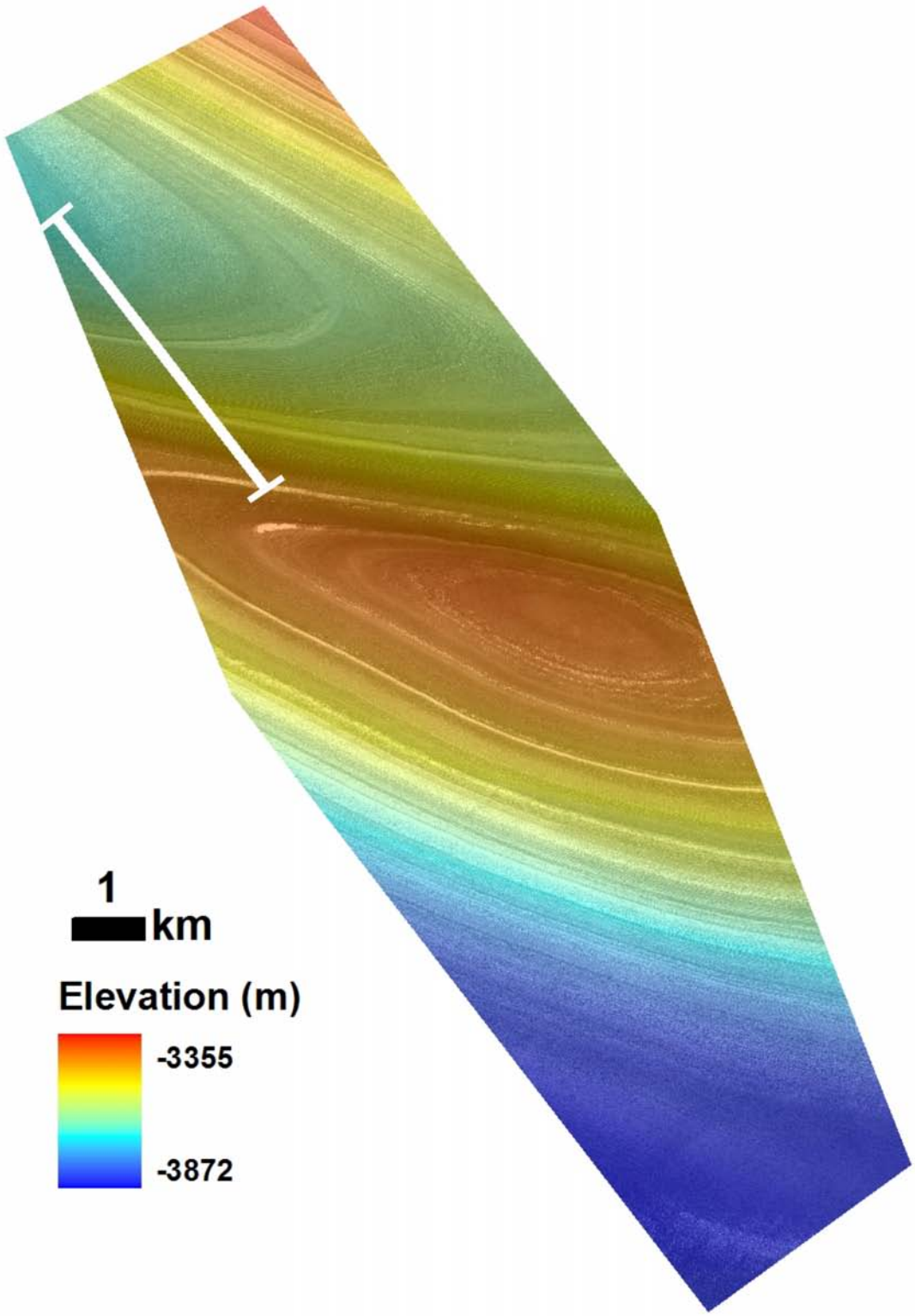

Figure S2. Site NP3. A 1 m-resolution digital elevation model is superimposed on HiRISE orthorectified HiRISE image PSP_010014_2645 (stereo pair: image PSP_010198_2645). White line denotes location of stratigraphic transect.

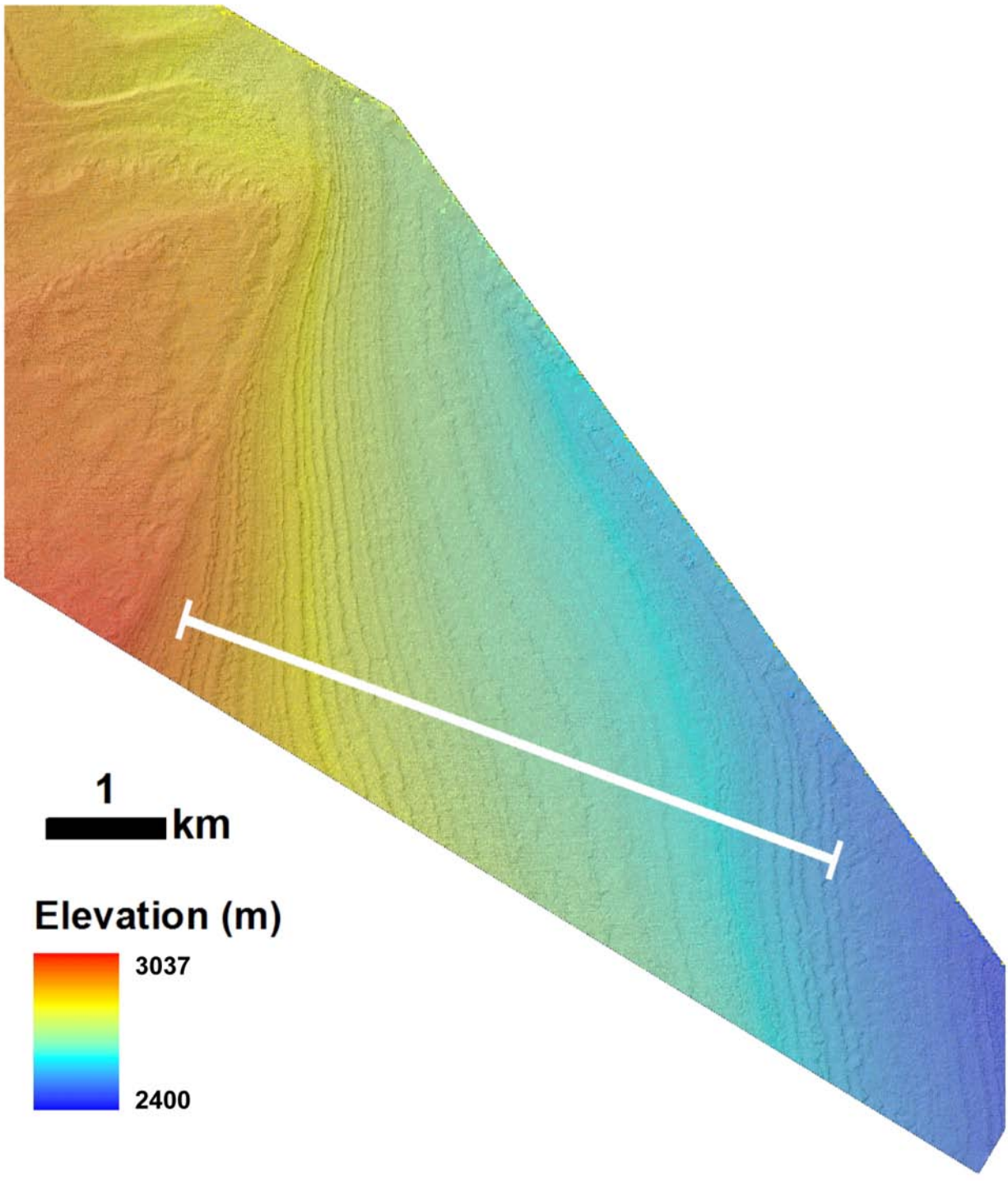

Figure S3. Site SP1. A 1 m-resolution digital elevation model is superimposed on orthorectified HiRISE image PSP_005076_0940 (stereo pair: image PSP_005207_0940). White line denotes location of stratigraphic transect.

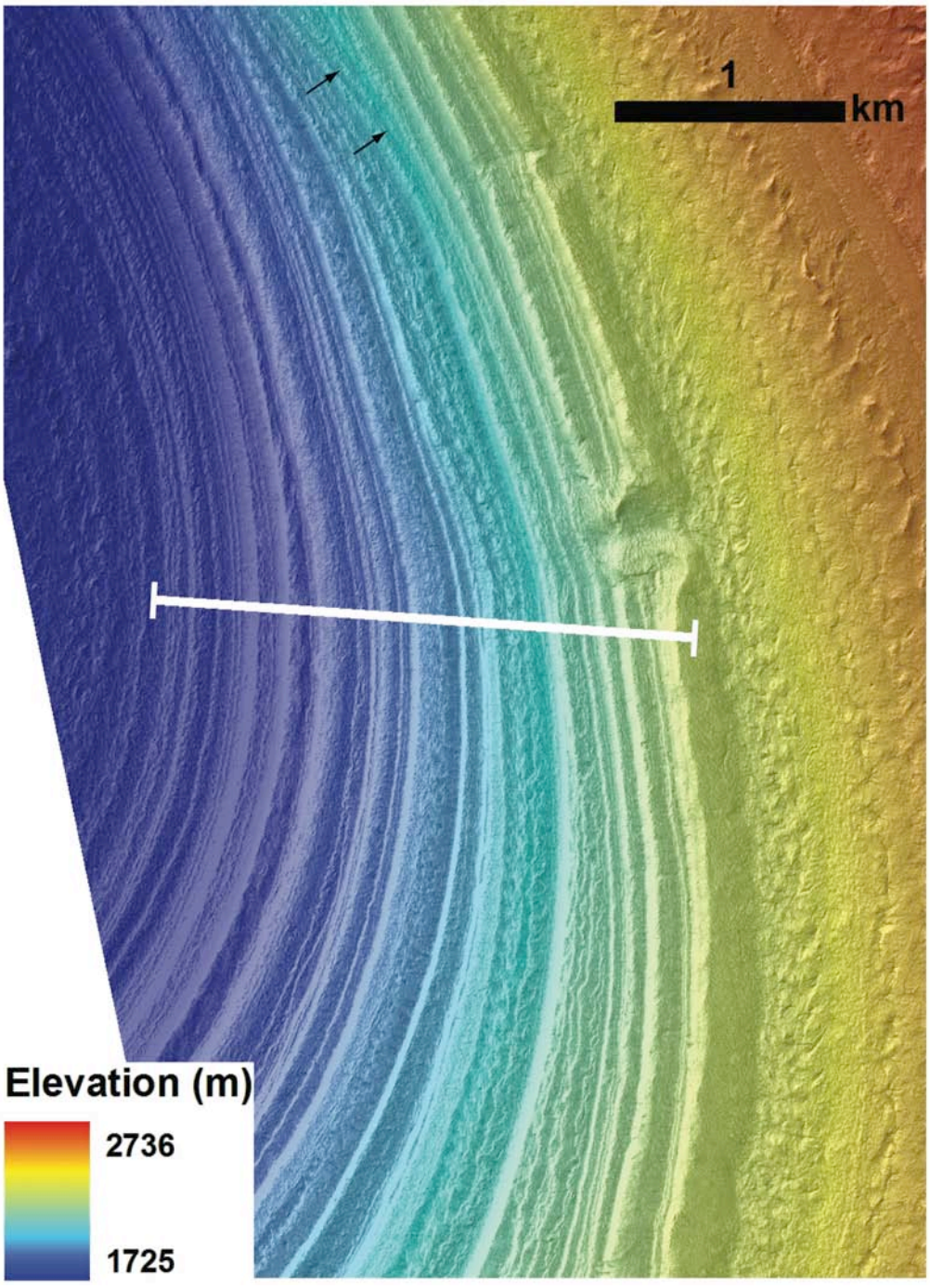

Figure S4. Site SP2. A 1 m-resolution digital elevation model is superimposed on orthorectified HiRISE image PSP_005458_1035 (stereo pair: image PSP_005682_1035). White line denotes location of stratigraphic transect. Arrows denote an angular unconformity.

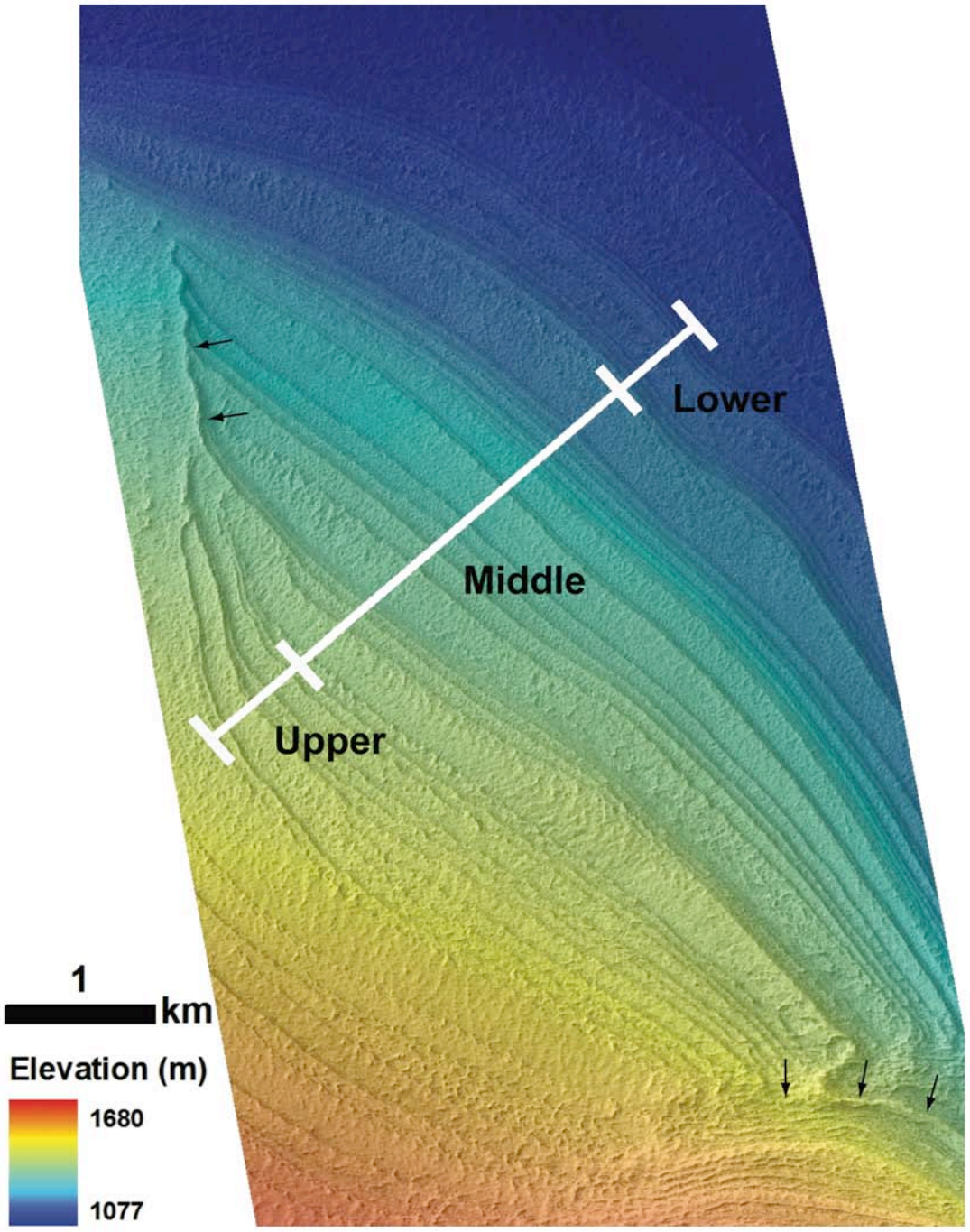

Figure S5. Site SP3. A 1 m-resolution digital elevation model is superimposed on HiRISE image ESP_013277_1070 (stereo pair: image ESP_013145_1070). White line denotes location of stratigraphic transect. Tick marks separate the lower, middle, and upper sections, in which beds are grouped by orientation. We tentatively interpret these three sections to be separated by low-angle two angular unconformities. Arrows denote two other prominent unconformities.

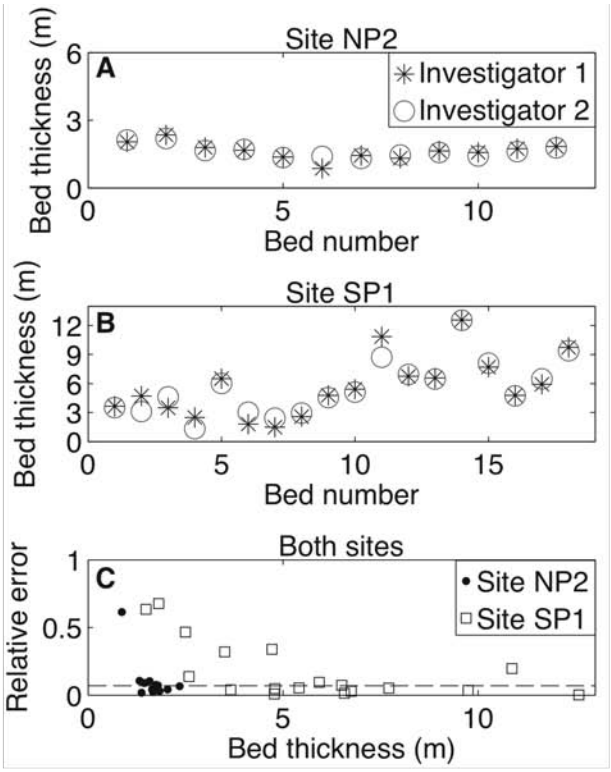

Figure S6. (A-B) Bed thickness data at sites NP2 and SP1, as measured by two different investigators. (C) The relative error for the combined set of measurements. Median relative error shown with dashed line.

Chapter 6: Conclusion

Meandering rivers exhibit a rich suite of interactions between flow, sediment transport, and topography that continues to motivate a large body of empirical and theoretical work [*Seminara*, 2006]. Yet apart from the processes occurring within meandering channels, the complex boundary geometry of evolving river meanders and their surrounding environment represents a key issue for predicting landscape evolution and stratigraphic development. As understanding of the underlying physical controls on meander evolution continues to develop, a robust framework also is needed to explore long-term model implications. Chapter 2 illustrates how interactions between meandering channels and their surrounding bank materials exert a fundamental control on landscape and stratigraphic evolution—and that numerical model predictions of this evolution can be highly sensitive to underlying numerical methods for tracking channel evolution.

Gradients in river properties such as flow velocity and bed topography are often relatively small in the along-stream direction, but the corresponding gradients in channel and valley properties in the transverse direction an be much stronger. This disparity, combined with the evolving river bank geometry, underlies the difficulty of tracking bank-material properties—even utilizing a relatively simple, geometrically based model for channel evolution [*Howard and Knutson*, 1984]. The methods for tracking bank-material properties developed and employed in this thesis offer new insights into the geologic timescale implications of longstanding conceptual models of valley evolution [e.g., *Davis*, 1909]. In particular, Chapters 3 and 4 offer new, quantitative predictions for how meandering rivers generate large-scale valley topography and develop terraces as a

function of river kinematics, channel geometry, and bank-material properties. By delineating the conditions under which particular valley and terrace types are likely to form by meandering under constant external forcing, these studies offer a framework for targeting field investigations to valleys where climate and tectonic signals are less likely to be confounded by intrinsic patterns of landscape evolution.

In order to isolate the fundamental behavior of a migrating and vertically incising meandering river—and most importantly, to treat the planform dynamics over geologic timescales—the model that underlies the numerical experiments in Chapters 2-4 is highly simplified. Several possibilities exist to incorporate additional complexity—for example, by explicitly tracking sediment fluxes and by employing dynamic models for vertical incision. Advances in understanding hydraulics, sediment transport, and erosion in alluvial and bedrock rivers may yield improved models for of short-term channel planform dynamics. Relating these short-timescale dynamics to long-term valley evolution will help to fingerprint how rivers translate, preserve, and destroy external signals [*Jerolmack and Paola*, 2010].

Bibliography

Abreu, V., M. Sullivan, C. Pirmez, and D. Mohrig (2003), Lateral accretion packages (LAPs): an important reservoir element in deep water sinuous channels, *Marine and Petroleum Geology*, *20*(6–8), 631–648, doi:10.1016/j.marpetgeo.2003.08.003.

Alford, J. J., and J. C. Holmes (1985), Meander scars as evidence of major climate change in southwest Louisiana, *Annals of the Association of American Geographers*, *75*(3), 395–403, doi:10.1111/j.1467-8306.1985.tb00074.x.

Allen, J. R. (1982), Free meandering channels and lateral deposits, in *Sedimentary structures, their character and physical basis*, vol. 2, pp. 53–100, Elsevier Science and Technology, New York.

Amos, C. B., and D. W. Burbank (2007), Channel width response to differential uplift, *Journal of Geophysical Research: Earth Surface*, *112*(F2), doi:10.1029/2006JF000672.

Baker, V. R. (1977), Stream-channel response to floods, with examples from central Texas, *Geological Society of America Bulletin*, *88*(8), 1057–1071, doi:10.1130/0016-7606(1977)88<1057:SRTFWE>2.0.CO;2.

Baker, V. R. (2001), Water and the martian landscape, *Nature*, *412*(6843), 228–236, doi:10.1038/35084172.

Baker, V. R., and M. M. Penteado-Orellana (1977), Adjustment to Quaternary climatic change by the Colorado River in central Texas, *The Journal of Geology*, *85*(4), 395–422.

Banks, M. E., S. Byrne, K. Galla, A. S. McEwen, V. J. Bray, C. M. Dundas, K. E. Fishbaugh, K. E. Herkenhoff, and B. C. Murray (2010), Crater population and resurfacing of the Martian north polar layered deposits, *Journal of Geophysical Research: Planets (1991–2012)*, *115*(E8).

Barbour, J. R. (2008), The origin and significance of sinuosity along incising bedrock rivers, Columbia University, New York, New York.

Barnes, V. E. et al. (1974a), Austin sheet, 1:250,000 scale, Bureau of Economic Geology Geologic Atlas of Texas, Austin, Texas.

Barnes, V. E. et al. (1974b), Seguin sheet, 1:250,000 scale, Bureau of Economic Geology Geologic Atlas of Texas, Austin, Texas.

Ben Moshe, L., I. Haviv, Y. Enzel, E. Zilberman, and A. Matmon (2008), Incision of alluvial channels in response to a continuous base level fall: Field characterization, modeling, and validation along the Dead Sea, *Geomorphology*, *93*(3–4), 524–536, doi:10.1016/j.geomorph.2007.03.014.

Beyer, R. P., and R. J. LeVeque (1992), Analysis of a one-dimensional model for the immersed boundary method, *SIAM Journal on Numerical Analysis*, *29*(2), 332–364.

Bibring, J.-P., Y. Langevin, F. Poulet, A. Gendrin, B. Gondet, M. Berthé, A. Soufflot, P. Drossart, M. Combes, and G. Bellucci (2004), Perennial water ice identified in the south polar cap of Mars, *Nature*, *428*(6983), 627–630.

Blondeaux, P., and G. Seminara (1985), A unified bar-bend theory of river meanders, *Journal of Fluid Mechanics*, *157*, 449–470.

Blum, M. D. (1992), Modern depositional environments and recent alluvial history of the lower Colorado River, Gulf coastal plain of Texas, Ph. D. thesis, Univ. Texas at Austin, Austin, Texas.

Blum, M. D., and A. Aslan (2006), Signatures of climate vs. sea-level change within incised valley-fill successions: Quaternary examples from the Texas Gulf coast, *Sedimentary Geology*, *190*(1-4), 177–211, doi:10.1016/j.sedgeo.2006.05.024.

Blum, M. D., and T. E. Tornqvist (2000), Fluvial responses to climate and sea-level change: A review and look forward, *Sedimentology*, *47*, 2–48, doi:10.1046/j.1365-3091.2000.00008.x.

Blum, M. D., and S. Valastro (1994), Late Quaternary sedimentation, lower Colorado River, Gulf coastal-plain, *Geological Society of America Bulletin*, *106*(8), 1002–1016, doi:10.1130/0016-7606(1994)106<1002:LQSLCR>2.3.CO;2.

Bogaart, P. W., R. T. V. Balen, C. Kasse, and J. Vandenberghe (2003), Process-based modelling of fluvial system response to rapid climate change II. Application to the River Maas (The Netherlands) during the Last Glacial–Interglacial Transition, *Quaternary Science Reviews*, *22*(20), 2097–2110, doi:10.1016/S0277-3791(03)00144-6.

Born, S. M., and D. F. Ritter (1970), Modern terrace development near Pyramid Lake, Nevada, and its geologic implications, *Geological Society of America Bulletin*, *81*(4), 1233–1242, doi:10.1130/0016-7606(1970)81[1233:MTDNPL]2.0.CO;2.

Boynton, W. V., W. C. Feldman, S. W. Squyres, T. H. Prettyman, J. Brückner, L. G. Evans, R. C. Reedy, R. Starr, J. R. Arnold, and D. M. Drake (2002), Distribution of hydrogen in the near surface of Mars: Evidence for subsurface ice deposits, *Science*, *297*(5578), 81–85.

Bradley, D. N., and G. E. Tucker (2013), The storage time, age, and erosion hazard of laterally accreted sediment on the floodplain of a simulated meandering river, *Journal of Geophysical Research: Earth Surface*, *118*(3), 1308–1319, doi:10.1002/jgrf.20083.

Braudrick, C. A., W. E. Dietrich, G. T. Leverich, and L. S. Sklar (2009), Experimental evidence for the conditions necessary to sustain meandering in coarse-bedded rivers, *Proceedings of the National Academy of Sciences*, *106*(40), 16936–16941, doi:10.1073/pnas.0909417106.

Braun, J., and M. Sambridge (1997), Modelling landscape evolution on geological time scales: A new method based on irregular spatial discretization, *Basin Research*, *9*(1), 27–52, doi:10.1046/j.1365-2117.1997.00030.x.

Brice, J. (1974), Evolution of meander loops, *Geological Society of America Bulletin*, *85*(4), 581–586, doi:10.1130/0016-7606(1974)85<581:EOML>2.0.CO;2.

Bridge, J. S. (2003), *Rivers and floodplains: Forms, processes, and sedimentary record*, Wiley-Blackwell, Malden, Massachusetts.

Bridgland, D., and R. Westaway (2008), Climatically controlled river terrace staircases: A worldwide Quaternary phenomenon, *Geomorphology*, *98*(3-4), 285–315, doi:10.1016/j.geomorph.2006.12.032.

Bucher, W. H. (1932), "Strath" as a geomorphic term, *Science*, *75*(1935), 130–131, doi:10.1126/science.75.1935.130-a.

Bull, W. B. (1991), *Geomorphic responses to climatic change*, Oxford University Press, New York.

Burr, D. M., J. T. Perron, M. P. Lamb, R. P. Irwin, G. C. Collins, A. D. Howard, L. S. Sklar, J. M. Moore, M. Ádámkovics, and V. R. Baker (2013), Fluvial features on Titan: Insights from morphology and modeling, *Geological Society of America Bulletin*, *125*(3-4), 299–321.

Byrne, S. (2009), The polar deposits of Mars, *Annual Review of Earth and Planetary Sciences*, *37*(1), 535–560, doi:10.1146/annurev.earth.031208.100101.

Byrne, S., and A. B. Ivanov (2004), Internal structure of the Martian south polar layered deposits, *Journal of Geophysical Research*, *109*(E11), doi:10.1029/2004JE002267.

Byrne, S. et al. (2011), Exposure analysis of polar stratigraphy from HiRISE topography, *LPI Contributions*, *1623*, 6012.

Camporeale, C., P. Perona, A. Porporato, and L. Ridolfi (2005), On the long-term behavior of meandering rivers, *Water Resources Research*, *41*(12), W12403, doi:10.1029/2005WR004109.

Carson, M. A., and M. F. Lapointe (1983), The inherent asymmetry of river meander planform, *The Journal of Geology*, *91*(1), 41–55.

Case, J. C., C. S. Arneson, and L. L. Hallberg (1998), Surficial geology map of Wyoming,

Castelltort, S., L. Goren, S. D. Willett, J.-D. Champagnac, F. Herman, and J. Braun (2012), River drainage patterns in the New Zealand Alps primarily controlled by plate tectonic strain, *Nature Geoscience*, *5*(10), 744–748, doi:10.1038/ngeo1582.

Challinor, J. (1932), River terraces as normal features of valley development, *Geography*, *17*(2), 141–147.

Claessens, L., A. Veldkamp, E. M. ten Broeke, and H. Vloemans (2009), A Quaternary uplift record for the Auckland region, North Island, New Zealand, based on marine and fluvial terraces, *Global and Planetary Change*, *68*(4), 383–394, doi:10.1016/j.gloplacha.2009.03.001.

Clevis, Q., G. E. Tucker, G. Lock, S. T. Lancaster, N. Gasparini, A. Desitter, and R. L. Bras (2006), Geoarchaeological simulation of meandering river deposits and settlement distributions: A three-dimensional approach, *Geoarchaeology*, *21*(8), 843–874, doi:10.1002/gea.20142.

Constantine, J. A., and T. Dunne (2008), Meander cutoff and the controls on the production of oxbow lakes, *Geology*, *36*(1), 23–26.

Cook, K. L., K. X. Whipple, A. M. Heimsath, and T. C. Hanks (2009), Rapid incision of the Colorado River in Glen Canyon - insights from channel profiles, local incision rates, and modeling of lithologic controls, *Earth Surface Processes and Landforms*, 994–1010, doi:10.1002/esp.1790.

Coulthard, T. J., and M. J. Van De Wiel (2006), A cellular model of river meandering, *Earth Surface Processes and Landforms*, *31*(1), 123–132, doi:10.1002/esp.1315.

Crosato, A. (2007), Effects of smoothing and regridding in numerical meander migration models, *Water Resources Research*, *43*(1), W01401, doi:10.1029/2006WR005087.

Cutts, J., and B. Lewis (1982), Models of climate cycles recorded in Martian polar layered deposits, *Icarus*, *50*(2-3), 216–244, doi:10.1016/0019-1035(82)90124-5.

Darby, S. E. (2002), Numerical simulation of bank erosion and channel migration in meandering rivers, *Water Resources Research*, *38*(9), 1163, doi:10.1029/2001WR000602.

Davies, N. S., and M. R. Gibling (2010), Paleozoic vegetation and the Siluro-Devonian rise of fluvial lateral accretion sets, *Geology*, *38*(1), 51–54, doi:10.1130/G30443.1.

Davis, W. M. (1893), The topographic maps of the United States Geological Survey, *Science*, *21*(534), 225–227.

Davis, W. M. (1909), *Geographical essays*, Ginn and Company, Boston.

Demir, T., A. Seyrek, H. Guillou, S. Scaillet, R. Westaway, and D. Bridgland (2009), Preservation by basalt of a staircase of latest Pliocene terraces of the River Murat in eastern Turkey: Evidence for rapid uplift of the eastern Anatolian Plateau, *Global and Planetary Change*, *68*(4), 254–269, doi:10.1016/j.gloplacha.2009.02.008.

Dibblee, T. W., and J. A. Minch (2008), Geologic map of the Point Delgada & Garberville 15 minute quadrangles, Humboldt and Mendocino Counties, California,

DiBiase, R. A., K. X. Whipple, M. P. Lamb, and A. M. Heimsath (in press), The role of waterfalls and knickzones in controlling the style and pace of landscape adjustment in the western San Gabriel Mountains, CA, *Geological Society of America Bulletin*.

Dietrich, W. E., and J. T. Perron (2006), The search for a topographic signature of life, *Nature*, *439*(7075), 411–418, doi:10.1038/nature04452.

Dietrich, W. E., D. G. Bellugi, L. S. Sklar, J. D. Stock, A. M. Heimsath, and J. J. Roering (2003), Geomorphic transport laws for predicting landscape form and dynamics, in *Geophysical Monograph Series*, vol. 135, edited by P. R. Wilcock and R. M. Iverson, pp. 103–132, American Geophysical Union, Washington, D. C.

Doğan, U. (2011), Climate-controlled river terrace formation in the Kızılırmak Valley, Cappadocia section, Turkey: Inferred from Ar–Ar dating of Quaternary basalts and terraces stratigraphy, *Geomorphology*, *126*(1–2), 66–81, doi:10.1016/j.geomorph.2010.10.028.

Duan, J. G., and P. Y. Julien (2010), Numerical simulation of meandering evolution, *Journal of Hydrology*, *391*(1–2), 34–46, doi:10.1016/j.jhydrol.2010.07.005.

Dury, G. (1985), Attainable Standards of Accuracy in the Retrodiction of Paleodischarge from Channel Dimensions, *Earth Surf. Process. Landf.*, *10*(3), 205–213, doi:10.1002/esp.3290100303.

Dury, G. H. (1964), *Principles of underfit streams*, Professional Paper, US Geological Survey.

Einsele, G., W. Ricken, and A. Seilacher (1991), Cycles and events in stratigraphy—basic concepts and terms, edited by G. Einsele, W. Ricken, and A. Seilacher, pp. 1–19, Springer-Verlag, Berlin.

Einstein, A. (1926), The cause of the formation of meanders in the courses of rivers and of the so-called Baer's law, in *Ideas and Opinions*, pp. 249–253, Crown Publishers Inc., New York.

Erkens, G., R. Dambeck, K. P. Volleberg, M. T. I. J. Bouman, J. A. A. Bos, K. M. Cohen, J. Wallinga, and W. Z. Hoek (2009), Fluvial terrace formation in the northern Upper Rhine Graben during the last 20000 years as a result of allogenic controls and autogenic evolution, *Geomorphology*, *103*(3), 476–495, doi:10.1016/j.geomorph.2008.07.021.

Fagherazzi, S., A. Bortoluzzi, W. E. Dietrich, A. Adami, S. Lanzoni, M. Marani, and A. Rinaldo (1999), Tidal networks 1. Automatic network extraction and preliminary scaling features from digital terrain maps, *Water Resources Research*, *35*(12), 3891–3904.

Fenton, L. K., and K. E. Herkenhoff (2000), Topography and stratigraphy of the northern Martian polar layered deposits using photoclinometry, stereogrammetry, and MOLA altimetry, *Icarus*, *147*(2), 433–443.

Ferguson, R. I. (1973), Channel pattern and sediment type, *Area*, *5*, 38–41.

Finnegan, N. J. (2013), Interpretation and downstream correlation of bedrock river terrace treads created from propagating knickpoints, *Journal of Geophysical Research: Earth Surface*, *118*(1), 54–64, doi:10.1029/2012JF002534.

Finnegan, N. J., and G. Balco (2013), Sediment supply, base level, braiding, and bedrock river terrace formation: Arroyo Seco, California, USA, *Geological Society of America Bulletin*, *125*(7-8), 1114–1124, doi:10.1130/B30727.1.

Finnegan, N. J., and W. E. Dietrich (2011), Episodic bedrock strath terrace formation due to meander migration and cutoff, *Geology*, *39*(2), 143–146, doi:10.1130/G31716.1.

Finnegan, N. J., G. Roe, D. R. Montgomery, and B. Hallet (2005), Controls on the channel width of rivers: Implications for modeling fluvial incision of bedrock, *Geology*, *33*(3), 229–232, doi:10.1130/G21171.1.

Finnegan, N. J., R. Schumer, and S. Finnegan (2014), A signature of transience in bedrock river incision rates over timescales of 10^4-10^7 years, *Nature*, *505*(7483), 391–394, doi:10.1038/nature12913.

Fishbaugh, K. E., and C. S. Hvidberg (2006), Martian north polar layered deposits stratigraphy: Implications for accumulation rates and flow, *Journal of Geophysical Research*, *111*(E6), doi:10.1029/2005JE002571.

Fishbaugh, K. E., S. Byrne, K. E. Herkenhoff, R. L. Kirk, C. Fortezzo, P. S. Russell, and A. McEwen (2010a), Evaluating the meaning of "layer" in the Martian north polar layered deposits and the impact on the climate connection, *Icarus*, *205*(1), 269–282, doi:10.1016/j.icarus.2009.04.011.

Fishbaugh, K. E., C. S. Hvidberg, S. Byrne, P. S. Russell, K. E. Herkenhoff, M. Winstrup, and R. Kirk (2010b), First high-resolution stratigraphic column of the Martian north polar layered deposits, *Geophysical Research Letters*, *37*(7), doi:10.1029/2009GL041642.

Fisk, H. N. (1944), *Geological investigation of the alluvial valley of the lower Mississippi River*, Mississippi River Commission, Vicksburg.

Fisk, H. N. (1947), *Fine-grained alluvial deposits and their effect on Mississippi River activity*, Waterways Experiment Station, US Army Corps of Engineers, Vicksburg.

Forget, F., R. M. Haberle, F. Montmessin, B. Levrard, and J. W. Head (2006), Formation of glaciers on Mars by atmospheric precipitation at high obliquity, *Science*, *311*(5759), 368–371.

Frankel, K. L., F. J. Pazzaglia, and J. D. Vaughn (2007), Knickpoint evolution in a vertically bedded substrate, upstream-dipping terraces, and Atlantic slope bedrock channels, *Geological Society of America Bulletin*, *119*(3-4), 476–486.

Frascati, A., and S. Lanzoni (2010), Long-term river meandering as a part of chaotic dynamics? A contribution from mathematical modelling, *Earth Surface Processes and Landforms*, *35*(7), 791–802, doi:10.1002/esp.1974.

Fuller, T. K., L. A. Perg, J. K. Willenbring, and K. Lepper (2009a), Field evidence for climate-driven changes in sediment supply leading to strath terrace formation, *Geology*, *37*(5), 467–470.

Fuller, T. K., L. A. Perg, J. K. Willenbring, and K. Lepper (2009b), Field evidence for climate-driven changes in sediment supply leading to strath terrace formation, *Geology*, *37*(5), 467–470, doi:10.1130/G25487A.1.

Ganti, V., C. Paola, and E. Foufoula-Georgiou (2013), Kinematic controls on the geometry of the preserved cross sets, *Journal of Geophysical Research: Earth Surface*, *118*(3), 1296–1307, doi:10.1002/jgrf.20094.

Ganti, V., M. P. Lamb, and B. McElroy (2014), Quantitative bounds on morphodynamics and implications for reading the sedimentary record, *Nature Communications*, *5*, doi:10.1038/ncomms4298.

Gilbert, G. K. (1877), *Report on the geology of the Henry Mountains*, US Government Printing Office, Washington, D. C.

Gran, K. B., N. Finnegan, A. L. Johnson, P. Belmont, C. Wittkop, and T. Rittenour (2013), Landscape evolution, valley excavation, and terrace development following abrupt postglacial base-level fall, *Geological Society of America Bulletin*, *125*(11/12), 1851–1864, doi:10.1130/B30772.1.

Greeley, R., S. A. Fagents, R. S. Harris, S. D. Kadel, D. A. Williams, and J. E. Guest (1998), Erosion by flowing lava: Field evidence, *Journal of Geophysical Research: Solid Earth*, *103*(B11), 27325–27345, doi:10.1029/97JB03543.

Griffiths, G. A. (1982), Stochastic prediction in geomorphology using Bayesian inference models, *Mathematical Geology*, *14*(1), 65–75, doi:10.1007/BF01037448.

Güneralp, İ., and B. L. Rhoads (2011), Influence of floodplain erosional heterogeneity on planform complexity of meandering rivers: MEANDERING IN HETEROGENEOUS FLOODPLAINS, *Geophysical Research Letters*, *38*(14), n/a–n/a, doi:10.1029/2011GL048134.

Hack, J. T. (1955), *Geology of the Brandywine area and origin of the upland of southern Maryland*, Professional Paper 267-A, US Geological Survey, Washington.

Hajek, E. A., P. L. Heller, and B. A. Sheets (2010), Significance of channel-belt clustering in alluvial basins, *Geology*, *38*(6), 535–538.

Hancock, G. S., and R. S. Anderson (2002), Numerical modeling of fluvial strath-terrace formation in response to oscillating climate, *Geological Society of America Bulletin*, *114*(9), 1131–1142.

Hancock, G. S., R. S. Anderson, O. A. Chadwick, and R. C. Finkel (1999), Dating fluvial terraces with 10Be and 26Al profiles: Application to the Wind River, Wyoming, *Geomorphology*, *27*(1), 41–60.

Hanks, T. C., and R. C. Finkel (2005), Early Pleistocene incision of the San Juan River, Utah, dated with 26Al and 10Be: Comment and Reply COMMENT, *Geology*, *33*(1), e78–e79, doi:10.1130/0091-7613-33.1.e78.

Harden, D. (1990), Controlling factors in the distribution and development of incised meanders in the central Colorado Plateau, *Geological Society of America Bulletin*, *102*(2), 233–242, doi:10.1130/0016-7606(1990)102<0233:CFITDA>2.3.CO;2.

Hartshorn, K., N. Hovius, W. B. Dade, and R. L. Slingerland (2002), Climate-driven bedrock incision in an active mountain belt, *Science*, *297*(5589), 2036–2038, doi:10.1126/science.1075078.

Hays, J. D., J. Imbrie, and N. J. Shackleton (1976), Variations in the Earth's orbit: Pacemaker of the ice ages, American Association for the Advancement of Science.

Head, J. W., J. F. Mustard, M. A. Kreslavsky, R. E. Milliken, and D. R. Marchant (2003), Recent ice ages on Mars, *Nature*, *426*(6968), 797–802.

Head, J. W. et al. (2005), Tropical to mid-latitude snow and ice accumulation, flow and glaciation on Mars, *Nature*, *434*(7031), 346–351, doi:10.1038/nature03359.

Henriquez, A., K. Tyler, and A. Hurst (1990), Characterization of fluvial sedimentology for reservoir simulation modeling, *SPE Formation Evaluation*, *5*(3), 211–216, doi:10.2118/18323-PA.

Herkenhoff, K. E., and R. L. Kirk (2001), MOC photoclinometry of the polar layered deposits on Mars, in *Lunar and Planetary Institute Science Conference Abstracts*, vol. 32, p. 1129.

Herkenhoff, K. E., and J. J. Plaut (2000), Surface ages and resurfacing rates of the polar layered deposits on Mars, *Icarus*, *144*(2), 243–253.

Herkenhoff, K. E., S. Byrne, P. S. Russell, K. E. Fishbaugh, and A. S. McEwen (2007), Meter-scale morphology of the north polar region of Mars, *Science*, *317*(5845), 1711–1715.

Hess, S., J. Ryan, J. Tillman, R. Henry, and C. Leovy (1980), The annual cycle of pressure on Mars measured by Viking Lander 1 and Viking Lander 2, *Geophys. Res. Lett.*, *7*(3), 197–200, doi:10.1029/GL007i003p00197.

Hickin, E. J., and G. C. Nanson (1975), The character of channel migration on the Beatton River, northeast British Columbia, Canada, *Geological Society of America Bulletin*, *86*(4), 487–494, doi:10.1130/0016-7606(1975)86<487:TCOCMO>2.0.CO;2.

Hirst, J. P. P., C. R. Blackstock, and S. Tyson (1993), Stochastic modelling of fluvial sandstone bodies, edited by S. S. Flint and I. D. Bryant, *The Geological Modelling of Hydrocarbon Reservoirs and Outcrop Analogues: International Association of Sedimentologists, Special Publication 15*, 237–252.

Howard, A., and A. Hemberger (1991), Multivariate characterization of meandering, *Geomorphology*, *4*(3-4), 161–186, doi:10.1016/0169-555X(91)90002-R.

Howard, A. D. (1984), Simulation model of meandering, in *River meandering*, edited by C. Elliot, pp. 952–963, ASCE, New York.

Howard, A. D. (1992), Modeling channel migration and floodplain sedimentation in meandering streams, in *Lowland floodplain rivers: Geomorphological perspectives*, edited by P. A. Carling and G. E. Petts, pp. 1–41, John Wiley and Sons, Ltd., Chichester.

Howard, A. D. (1996), Modelling channel evolution and floodplain morphology, in *Floodplain processes*, edited by M. G. Anderson, D. E. Walling, and P. E. Bates, pp. 15–62, John Wiley and Sons, Ltd., Chichester.

Howard, A. D. (2009), How to make a meandering river, *PNAS*, *106*(41), 17245–17246, doi:10.1073/pnas.0910005106.

Howard, A. D., and G. Kerby (1983), Channel changes in badlands, *Geological Society of America Bulletin*, *94*(6), 739–752.

Howard, A. D., and T. R. Knutson (1984), Sufficient conditions for river meandering—a simulation approach, *Water Resources Research*, *20*(11), 1659–1667, doi:10.1029/WR020i011p01659.

Howard, A. D., J. A. Cutts, and K. R. Blasius (1982), Stratigraphic relationships within Martian polar cap deposits, *Icarus*, *50*(2), 161–215.

Howard, A. D., W. E. Dietrich, and M. A. Seidl (1994), Modeling fluvial erosion on regional to continental scales, *Journal of Geophysical Research: Solid Earth*, *99*(B7), 13971–13986, doi:10.1029/94JB00744.

Hudson, P. F., and R. H. Kesel (2000), Channel migration and meander-bend curvature in the lower Mississippi River prior to major human modification, *Geology*, *28*(6), 531–534, doi:10.1130/0091-7613(2000)28<531:CMAMCI>2.0.CO;2.

Ikeda, H. (1989), Sedimentary controls on channel migration and origin of point bars in sand-bedded meandering rivers, *Water Resources Monograph*, *12*, 51–68, doi:10.1029/WM012p0051.

Ikeda, S., and G. Parker (1989), in *River Meandering*, pp. i–ix, American Geophysical Union.

Ikeda, S., G. Parker, and K. Sawai (1981), Bend theory of river meanders. Part 1. Linear development, *Journal of Fluid Mechanics*, *112*(11), 363–377.

Jakosky, B., B. Henderson, and M. Mellon (1995), Chaotic obliquity and the nature of the Martian climate, *J. Geophys. Res.-Planets*, *100*(E1), 1579–1584, doi:10.1029/94JE02801.

Jakosky, B. M., B. G. Henderson, and M. T. Mellon (1993), The Mars water cycle at other epochs: Recent history of the polar caps and layered terrain, *Icarus*, *102*(2), 286–297.

Jerolmack, D. J., and C. Paola (2010), Shredding of environmental signals by sediment transport, *Geophysical Research Letters*, *37*(L19401), doi:10.1029/2010GL044638.

Johannesson, H., and G. Parker (1989), Linear theory of river meanders, *Water Resources Monograph*, *12*, 181–213, doi:10.1029/WM012p0181.

Karlstrom, L., P. Gajjar, and M. Manga (2013), Meander formation in supraglacial streams, *Journal of Geophysical Research: Earth Surface*, *118*, 1897–1907, doi:10.1002/jgrf.20135.

Karssenberg, D., and J. S. Bridge (2008), A three-dimensional numerical model of sediment transport, erosion and deposition within a network of channel belts, floodplain and hill slope: Extrinsic and intrinsic controls on floodplain dynamics and alluvial architecture, *Sedimentology*, *55*(6), 1717–1745.

Katsikadelis, J. T. (2002), *Boundary elements: Theory and applications*, Elsevier, Kidlington, Oxford.

Kerr, R. C. (2001), Thermal erosion by laminar lava flows, *Journal of Geophysical Research*, *106*(B11), 26453–26465.

Kirk, R. L. et al. (2008), Ultrahigh resolution topographic mapping of Mars with MRO HiRISE stereo images: Meter-scale slopes of candidate Phoenix landing sites, *Journal of Geophysical Research*, *113*, doi:10.1029/2007JE003000.

Knighton, D. (1998), *Fluvial forms and processes: A new perspective*, Arnold, London.

Kolb, E. J., and K. L. Tanaka (2001), Geologic history of the polar regions of Mars based on Mars Global Surveyor data: II. Amazonian Period, *Icarus*, *154*(1), 22–39.

Kolb, E. J., and K. L. Tanaka (2006), Accumulation and erosion of south polar layered deposits in the Promethei Lingula region, Planum Australe, Mars, *Mars*, doi:10.1555/mars.2006.0001.

Komatsu, G., and V. R. Baker (1996), Channels in the solar system, *Planetary and Space Science*, *44*(8), 801–815, doi:10.1016/0032-0633(96)00010-4.

Kondolf, G. M. (2006), River restoration and meanders, *Ecology and Society*, *11*(2), 42.

Koutnik, M. (2002), South polar layered deposits of Mars: The cratering record, *Journal of Geophysical Research*, *107*(E11), doi:10.1029/2001JE001805.

Lague, D. (2010), Reduction of long-term bedrock incision efficiency by short-term alluvial cover intermittency, *Journal of Geophysical Research: Earth Surface*, *115*(F2), doi:10.1029/2008JF001210.

Lancaster, S. T. (1998), A nonlinear river meandering model and its incorporation in a landscape evolution model, Ph. D. thesis, Massachusetts Institute of Technology, Cambridge, Massachusetts.

Lancaster, S. T., and R. L. Bras (2002), A simple model of river meandering and its comparison to natural channels, *Hydrological Processes*, *16*(1), 1–26, doi:10.1002/hyp.273.

Langbein, W. B., and L. B. Leopold (1966), *River meanders: Theory of minimum variance*, US Government Printing Office.

Langevin, Y. (2005), Summer evolution of the north polar cap of Mars as observed by OMEGA/Mars Express, *Science*, *307*(5715), 1581–1584, doi:10.1126/science.1109438.

Laskar, J., B. Levrard, and J. F. Mustard (2002), Orbital forcing of the Martian polar layered deposits, *Nature*, *419*(6905), 375–377, doi:10.1038/nature01066.

Laskar, J., A. C. M. Correia, M. Gastineau, F. Joutel, B. Levrard, and P. Robutel (2004), Long term evolution and chaotic diffusion of the insolation quantities of Mars, *Icarus*, *170*(2), 343–364.

Lavé, J., and J. P. Avouac (2000), Active folding of fluvial terraces across the Siwaliks Hills, Himalayas of central Nepal, *Journal of Geophysical Research*, *105*(B3), 5735–5770, doi:10.1029/1999JB900292.

Lavé, J., and J. P. Avouac (2001), Fluvial incision and tectonic uplift across the Himalayas of central Nepal, *Journal of Geophysical Research*, *106*(B11), 26561–26,591, doi:10.1029/2001JB000359.

Leigh, D. S., and T. P. Feeney (1995), Paleochannels indicating wet climate and lack of response to lower sea level, southeast Georgia, *Geology*, *23*(8), 687–690, doi:10.1130/0091-7613(1995)023<0687:PIWCAL>2.3.CO;2.

Leopold, L. B., and M. G. Wolman (1957), *River channel patterns: braided, meandering, and straight*, U.S. Govt. Printing Office, Washington, D. C.

Leopold, L. B., and M. G. Wolman (1960), River meanders, *Geological Society of America Bulletin*, *71*(6), 769–794, doi:10.1130/0016-7606(1960)71[769:RM]2.0.CO;2.

Levrard, B., F. Forget, F. Montmessin, and J. Laskar (2007), Recent formation and evolution of northern Martian polar layered deposits as inferred from a Global Climate Model, *Journal of Geophysical Research*, *112*(E6), doi:10.1029/2006JE002772.

Lewin, J. (1976), Initiation of bed forms and meanders in coarse-grained sediment, *Geological Society of America Bulletin*, *87*(2), 281–285, doi:10.1130/0016-7606(1976)87<281:IOBFAM>2.0.CO;2.

Lewin, J., and B. J. Brindle (1977), Confined meanders, in *River channel changes*, edited by K. J. Gregory, pp. 221–233, John Wiley and Sons, Ltd., Chichester.

Lewin, J., and M. G. Macklin (2003), Preservation potential for late Quaternary river alluvium, *Journal of Quaternary Science*, *18*(2), 107–120, doi:10.1002/jqs.738.

Lewis, K. W., O. Aharonson, J. P. Grotzinger, R. L. Kirk, A. S. McEwen, and T.-A. Suer (2008), Quasi-periodic bedding in the sedimentary rock record of Mars, *Science*, *322*(5907), 1532–1535.

Lilliefors, H. W. (1967), On the Kolmogorov-Smirnov test for normality with mean and variance unknown, *Journal of the American Statistical Association*, *62*(318), 399–402.

Limaye, A. B. S., and M. P. Lamb (2013a), A vector-based method for bank-material tracking in coupled models of meandering and landscape evolution, *Journal of Geophysical Research Earth Surface*, *118*, 2421–2437, doi:10.1002/2013JF002854.

Limaye, A. B. S., and M. P. Lamb (2013b), A vector-based method for bank-material tracking in coupled models of meandering and landscape evolution, *Journal of Geophysical Research: Earth Surface*, *118*(4), 2421–2437, doi:10.1002/2013JF002854.

Limaye, A. B. S., and M. P. Lamb (2014), Numerical simulations of bedrock valley evolution by meandering rivers with variable bank material, *J. Geophys. Res. Earth Surf.*, *119*(4), 927–950, doi:10.1002/2013JF002997.

Li, S., and W. K. Liu (2002), Meshfree and particle methods and their applications, *Applied Mechanics Reviews*, *55*(1), 1–34.

Liu, G. R. (2010), *Meshfree methods: Moving beyond the finite element method*, CRC Press, Washington, D. C.

Malin, M. C., and K. S. Edgett (2001), Mars global surveyor Mars orbiter camera: interplanetary cruise through primary mission, *Journal of Geophysical Research: Planets (1991–2012)*, *106*(E10), 23429–23570.

Mann, M. E., and J. M. Lees (1996), Robust estimation of background noise and signal detection in climatic time series, *Climatic Change*, *33*(3), 409 – 445.

Matoshko, A., P. Gozhik, and V. Semenenko (2009), Late Cenozoic fluvial development within the Sea of Azov and Black Sea coastal plains, *Global and Planetary Change*, *68*(4), 270–287, doi:10.1016/j.gloplacha.2009.03.003.

McEwen, A. S. et al. (2007), Mars Reconnaissance Orbiter's High Resolution Imaging Science Experiment (HiRISE), *Journal of Geophysical Research*, *112*(E5), doi:10.1029/2005JE002605.

Mellon, M. T. (1996), Limits on the CO2 content of the Martian polar deposits, *Icarus*, *124*(1), 268–279.

Merritts, D. J., K. R. Vincent, and E. E. Wohl (1994), Long river profiles, tectonism, and eustasy: A guide to interpreting fluvial terraces, *Journal of Geophysical Research: Solid Earth*, *99*(B7), 14031–14050, doi:10.1029/94JB00857.

Meyer, G. A., S. G. Wells, and A. T. Jull (1995), Fire and alluvial chronology in Yellowstone National Park: climatic and intrinsic controls on Holocene geomorphic processes, *Geological Society of America Bulletin*, *107*(10), 1211–1230.

Milkovich, S. M., and J. W. Head (2005), North polar cap of Mars: Polar layered deposit characterization and identification of a fundamental climate signal, *Journal of Geophysical Research: Planets (1991–2012)*, *110*(E1).

Milkovich, S. M., and J. J. Plaut (2008), Martian south polar layered deposit stratigraphy and implications for accumulation history, *Journal of Geophysical Research*, *113*(E6), doi:10.1029/2007JE002987.

Milkovich, S. M., J. W. Head, and Gerhard Neukum (2008), Stratigraphic analysis of the northern polar layered deposits of Mars: Implications for recent climate history, *Planetary and Space Science*, *56*(2), 266–288, doi:10.1016/j.pss.2007.08.004.

Milkovich, S. M., J. J. Plaut, A. Safaeinili, G. Picardi, R. Seu, and R. J. Phillips (2009), Stratigraphy of Promethei Lingula, south polar layered deposits, Mars, in radar and imaging data sets, *Journal of Geophysical Research*, *114*(E3), doi:10.1029/2008JE003162.

Mizutani, T. (1998), Laboratory experiment and digital simulation of multiple fill-cut terrace formation, *Geomorphology*, *24*(4), 353–361, doi:10.1016/S0169-555X(98)00027-0.

Molnar, P., E. T. Brown, B. C. Burchfiel, Q. Deng, X. Feng, J. Li, G. M. Raisbeck, J. Shi, W. Zhangming, and F. Yiou (1994), Quaternary climate change and the formation of river terraces across growing anticlines on the north flank of the Tien Shan, China, *The Journal of Geology*, *102*(5), 583–602.

Montgomery, D. R. (2004), Observations on the role of lithology in strath terrace formation and bedrock channel width, *American Journal of Science*, *304*(5), 454–476, doi:10.2475/ajs.304.5.454.

Motta, D., J. D. Abad, E. J. Langendoen, and M. H. Garcia (2012a), A simplified 2D model for meander migration with physically-based bank evolution, *Geomorphology*, *163*, 10–25.

Motta, D., J. D. Abad, E. J. Langendoen, and M. H. García (2012b), The effects of floodplain soil heterogeneity on meander planform shape, *Water Resources Research*, *48*(9), doi:10.1029/2011WR011601.

Murray, A. B., and C. Paola (1994), A cellular model of braided rivers, *Nature*, *371*, 54–57.

Murray, B., M. Koutnik, S. Byrne, L. Soderblom, K. Herkenhoff, and K. L. Tanaka (2001), Preliminary geological assessment of the northern edge of Ultimi Lobe, Mars south polar layered deposits, *Icarus*, *154*(1), 80–97.

Murray, B. C., W. R. Ward, and S. C. Yeung (1973), Periodic insolation variations on Mars, *Science*, *180*(4086), 638–640.

Nagata, N., T. Hosoda, and Y. Muramoto (2000), Numerical Analysis of River Channel Processes with Bank Erosion, *Journal of Hydraulic Engineering*, *126*(4), 243–252, doi:10.1061/(ASCE)0733-9429(2000)126:4(243).

Nakagawa, T., and J. C. Scott (1984), Stream meanders on a smooth hydrophobic surface, *Journal of Fluid Mechanics*, *149*, 89–99.

Nanson, G. C., and E. J. Hickin (1983), Channel migration and incision on the Beatton River, *Journal of Hydraulic Engineering*, *109*(3), 327–337.

Nanson, G. C., and E. J. Hickin (1986), A statistical analysis of bank erosion and channel migration in western Canada, *Geological Society of America Bulletin*, *97*(4), 497–504, doi:10.1130/0016-7606(1986)97<497:ASAOBE>2.0.CO;2.

Nicholas, A. P., and T. A. Quine (2010), Quantitative assessment of landform equifinality and palaeoenvironmental reconstruction using geomorphic models, *Geomorphology*, *121*(3–4), 167–183, doi:10.1016/j.geomorph.2010.04.004.

Nicoll, T. J., and E. J. Hickin (2010), Planform geometry and channel migration of confined meandering rivers on the Canadian prairies, *Geomorphology*, *116*(1-2), 37–47, doi:10.1016/j.geomorph.2009.10.005.

Niviere, B., and G. Marquis (2000), Evolution of terrace risers along the upper Rhine graben inferred from morphologic dating methods: Evidence of climatic and tectonic forcing, *Geophys. J. Int.*, *141*(3), 577–594, doi:10.1046/j.1365-246x.2000.00123.x.

Nye, J. F., W. B. Durham, P. M. Schenk, and J. M. Moore (2000), The instability of a south polar cap on Mars composed of carbon dioxide, *Icarus*, *144*(2), 449–455.

Okubo, C. H. (2010), Structural geology of Amazonian-aged layered sedimentary deposits in southwest Candor Chasma, Mars, *Icarus*, *207*(1), 210–225, doi:10.1016/j.icarus.2009.11.012.

Osman, A., and C. Thorne (1988), Riverbank stability analysis. I: Theory, *Journal of Hydraulic Engineering*, *114*(2), 134–150, doi:10.1061/(ASCE)0733-9429(1988)114:2(134).

Panagiotopoulos, I., G. Voulgaris, and M. B. Collins (1997), The influence of clay on the threshold of movement of fine sandy beds, *Coastal Engineering*, *32*(1), 19–43, doi:10.1016/S0378-3839(97)00013-6.

Pan, B., D. Burbank, Y. Wang, G. Wu, J. Li, and Q. Guan (2003), A 900 k.y. record of strath terrace formation during glacial-interglacial transitions in northwest China, *Geology*, *31*(11), 957–960, doi:10.1130/G19685.1.

Parker, G. (1975), Meandering of supraglacial melt streams, *Water Resources Research*, *11*(4), 551–552, doi:10.1029/WR011i004p00551.

Parker, G. (1976), On the cause and characteristic scales of meandering and braiding in rivers, *Journal of Fluid Mechanics*, *76*(3), 457–480, doi:10.1017/S0022112076000748.

Parker, G., P. Diplas, and J. Akiyama (1983), Meander bends of high amplitude, *Journal of Hydraulic Engineering*, *109*(10), 1323–1337, doi:10.1061/(ASCE)0733-9429(1983)109:10(1323).

Parker, G., Y. Shimizu, G. V. Wilkerson, E. C. Eke, J. D. Abad, J. W. Lauer, C. Paola, W. E. Dietrich, and V. R. Voller (2011a), A new framework for modeling the migration of meandering rivers, *Earth Surface Processes and Landforms*, *36*(1), 70–86, doi:10.1002/esp.2113.

Parker, G., Y. Shimizu, G. V. Wilkerson, E. C. Eke, J. D. Abad, J. W. Lauer, C. Paola, W. E. Dietrich, and V. R. Voller (2011b), A new framework for modeling the migration of meandering rivers, *Earth Surface Processes and Landforms*, *36*(1), 70–86, doi:10.1002/esp.2113.

Pathare, A. V., D. A. Paige, and E. Turtle (2005), Viscous relaxation of craters within the Martian south polar layered deposits, *Icarus*, *174*(2), 396–418.

Pazzaglia, F. J. (2013), Fluvial terraces, in *Treatise on Geomorphology*, vol. 9, edited by E. Wohl, pp. 379–412, Academic Press, San Diego.

Pazzaglia, F. J., and T. W. Gardner (1993), Fluvial terraces of the lower Susquehanna River, *Geomorphology*, *8*(2), 83–113.

Pazzaglia, F. J., T. W. Gardner, and D. J. Merritts (1998), Bedrock fluvial incision and longitudinal profile development over geologic time scales determined by fluvial terraces, in *Rivers over rock: fluvial processes in bedrock channels*, vol. 107, edited by K. J. Tinkler and E. E. Wohl, pp. 207–235, American Geophysical Union, Washington, D. C.

Pederson, J., K. Karlstrom, W. Sharp, and W. McIntosh (2002), Differential incision of the Grand Canyon related to Quaternary faulting—Constraints from U-series and Ar/Ar dating, *Geology*, *30*(8), 739–742.

Perron, J. T., and S. Fagherazzi (2012), The legacy of initial conditions in landscape evolution, *Earth Surface Processes and Landforms*, *37*(1), 52–63, doi:10.1002/esp.2205.

Perron, J. T., and P. Huybers (2009), Is there an orbital signal in the polar layered deposits on Mars?, *Geology*, *37*(2), 155–158, doi:10.1130/G25143A.1.

Personius, S. (1995), Late Quaternary stream incision and uplift in the forearc of the Cascadia subduction zone, western Oregon, *Journal of Geophysical Research*, *100*(B10), 20193–20210.

Peters, G., and R. T. van Balen (2007), Pleistocene tectonics inferred from fluvial terraces of the northern Upper Rhine Graben, Germany, *Tectonophysics*, *430*(1–4), 41–65, doi:10.1016/j.tecto.2006.10.008.

Phillips, J. D., and M. C. Slattery (2006), Sediment storage, sea level, and sediment delivery to the ocean by coastal plain rivers, *Progress in Physical Geography*, *30*(4), 513–530, doi:10.1191/0309133306pp494ra.

Phillips, R. J. et al. (2008), Mars north polar deposits: Stratigraphy, age, and geodynamical response, *Science*, *320*(5880), 1182–1185, doi:10.1126/science.1157546.

Phillips, R. J. et al. (2011), Massive CO2 ice deposits sequestered in the south polar layered deposits of Mars, *Science*, *332*(6031), 838–841, doi:10.1126/science.1203091.

Picardi, G., J. J. Plaut, D. Biccari, O. Bombaci, D. Calabrese, M. Cartacci, A. Cicchetti, S. M. Clifford, P. Edenhofer, and W. M. Farrell (2005), Radar soundings of the subsurface of Mars, *Science*, *310*(5756), 1925–1928.

Picotti, V., and F. J. Pazzaglia (2008), A new active tectonic model for the construction of the Northern Apennines mountain front near Bologna (Italy), *Journal of Geophysical Research*, *113*(B8), doi:10.1029/2007JB005307.

Piqueux, S., C. S. Edwards, and P. R. Christensen (2008), Distribution of the ices exposed near the south pole of Mars using Thermal Emission Imaging System (THEMIS) temperature measurements, *Journal of Geophysical Research: Planets (1991–2012)*, *113*(E8).

Plaut, J. J., G. Picardi, A. Safaeinili, A. B. Ivanov, S. M. Milkovich, A. Cicchetti, W. Kofman, J. Mouginot, W. M. Farrell, and R. J. Phillips (2007), Subsurface radar sounding of the south polar layered deposits of Mars, *Science*, *316*(5821), 92–95.

Posner, A. J., and J. G. Duan (2012), Simulating river meandering processes using stochastic bank erosion coefficient, *Geomorphology*, *163–164*, 26–36, doi:10.1016/j.geomorph.2011.05.025.

Pyrcz, M. J., and C. V. Deutsch (2005), Conditioning event-based fluvial models, *Geostatistics Banff 2004*, 135–144.

Pyrcz, M. J., J. B. Boisvert, and C. V. Deutsch (2009), ALLUVSIM: A program for event-based stochastic modeling of fluvial depositional systems, *Computers & Geosciences*, *35*(8), 1671–1685, doi:10.1016/j.cageo.2008.09.012.

Repka, J. L., R. S. Anderson, and R. C. Finkel (1997), Cosmogenic dating of fluvial terraces, Fremont River, Utah, *Earth and Planetary Science Letters*, *152*(1), 59–73.

Rockwell, T. K., E. A. Keller, M. N. Clark, and D. L. Johnson (1984), Chronology and rates of faulting of Ventura River terraces, California, *Geological Society of America Bulletin*, *95*(12), 1466–1474, doi:10.1130/0016-7606(1984)95<1466:CAROFO>2.0.CO;2.

Schorghofer, N. (2007), Dynamics of ice ages on Mars, *Nature*, *449*(7159), 192–194.

Schumm, S. A. (1977), *The fluvial system*, Wiley, New York.

Sear, D. A. (1994), River restoration and geomorphology, *Aquatic Conservation: Marine and Freshwater Ecosystems*, *4*(2), 169–177.

Seidl, M. A., and W. E. Dietrich (1992), The problem of channel erosion into bedrock, *Catena Supplement*, *23*, 101–124.

Seminara, G. (2006), Meanders, *Journal of Fluid Mechanics*, *554*(1), 271–297, doi:10.1017/S0022112006008925.

Shimizu, Y. (2002), A method for simultaneous computation of bed and bank deformation of a river, in *River Flow 2002*, vol. 2, edited by D. Bousmar and Y. Zech, pp. 793–801, Taylor and Francis, London.

Shiono, K., Y. Muto, D. W. Knight, and A. F. L. Hyde (1999), Energy losses due to secondary flow and turbulence in meandering channels with overbank flows, *Journal of Hydraulic Research*, *37*(5), 641–664, doi:10.1080/00221689909498521.

Shyu, J. B. H., K. Sieh, J.-P. Avouac, W.-S. Chen, and Y.-G. Chen (2006), Millennial slip rate of the Longitudinal Valley fault from river terraces: Implications for convergence across the active suture of eastern Taiwan, *Journal of Geophysical Research*, *111*(B8), doi:10.1029/2005JB003971.

Sklar, L. S., and W. E. Dietrich (2001), Sediment and rock strength controls on river incision into bedrock, *Geology*, *29*(12), 1087–1090, doi:10.1130/0091-7613(2001)029<1087:SARSCO>2.0.CO;2.

Smalley, M. L., W. W. Emmett, and A. M. Wacker (1994), *Annual replenishment of bed material by sediment transport in the Wind River near Riverton, Wyoming*, US Department of the Interior, US Geological Survey.

Smith, C. D. (1978), Effect of channel meanders on flood stage in valley, *Journal of the Hydraulics Division*, *104*(1), 49–58.

Sori, M. M., J. T. Perron, P. Huybers, and O. Aharonson (2011), Preservation of orbital signals in the Martian polar layered deposits: A statistical approach, *LPI Contributions*, *1623*, 6063.

Stark, C. P. (2006), A self-regulating model of bedrock river channel geometry, *Geophysical Research Letters*, *33*(4), doi:10.1029/2005GL023193.

Stark, C. P., J. R. Barbour, Y. S. Hayakawa, T. Hattanji, N. Hovius, H. Chen, C.-W. Lin, M.-J. Horng, K.-Q. Xu, and Y. Fukahata (2010), The climatic signature of incised river meanders, *Science*, *327*(5972), 1497–1501, doi:10.1126/science.1184406.

Stølum, H.-H. (1996), River meandering as a self-organization process, *Science*, *271*(5256), 1710–1713, doi:10.1126/science.271.5256.1710.

Stout, J. C., and P. Belmont (2013), TerEx Toolbox for semi-automated selection of fluvial terrace and floodplain features from lidar, *Earth Surface Processes and Landforms*, *39*(5), 569–580, doi:10.1002/esp.3464.

Stricklin, F. L. (1961), Degradational stream deposits of the Brazos River, central Texas, *Geological Society of America Bulletin*, *72*(1), 19–36.

Sun, T., P. Meakin, T. Jossang, and K. Schwarz (1996), A simulation model for meandering rivers, *Water Resources Research*, *32*(9), 2937–2954, doi:10.1029/96WR00998.

Sun, T., P. Meakin, and T. Jøssang (2001), A computer model for meandering rivers with multiple bed load sediment sizes: 2. Computer simulations, *Water Resources Research*, *37*(8), 2243–2258, doi:10.1029/2000WR900397.

Sylvester, Z., C. Pirmez, and A. Cantelli (2011), A model of submarine channel-levee evolution based on channel trajectories: Implications for stratigraphic architecture, *Marine and Petroleum Geology*, *28*(3), 716–727, doi:10.1016/j.marpetgeo.2010.05.012.

Tanaka, K. L., and E. J. Kolb (2005), *Geologic mapping of the polar regions of Mars: Preliminary results and climate implications*, USGS Open File Report.

Tanaka, K. L., and D. H. Scott (1987), Geologic map of the polar regions of Mars,

Tanaka, K. L., J. A. P. Rodriguez, J. A. Skinner Jr, M. C. Bourke, C. M. Fortezzo, K. E. Herkenhoff, E. J. Kolb, and C. H. Okubo (2008), North polar region of Mars: Advances in stratigraphy, structure, and erosional modification, *Icarus*, *196*(2), 318–358.

Thomas, P., S. Squyres, K. Herkenhoff, A. Howard, B. Murray, H. H. Kieffer, B. Jakosky, C. W. Snyder, and M. S. Matthews (1992), Polar deposits of Mars, in *Mars*, pp. 767–795, University of Arizona Press, Tucson, AZ.

Thomson, J. (1876), On the origin of windings of rivers in alluvial plains, with remarks on the flow of water round bends in pipes, in *Proceedings of the Royal Society*.

Thorne, C. R. (1992), Bend scour and bank erosion on the meandering Red River, Louisiana, in *Lowland floodplain rivers: geomorphological perspectives*, pp. 95–115, John Wiley and Sons, Ltd., Chichester.

Tinkler, J., and E. Wohl (1998), *Rivers over rock: Fluvial processes in bedrock channels*, Geophysical Monograph Series, American Geophysical Union, Washington, D. C.

Toon, O. B., J. B. Pollack, W. Ward, J. A. Burns, and K. Bilski (1980), The astronomical theory of climatic change on Mars, *Icarus*, *44*(3), 552–607.

Trush, W. J., S. M. McBain, and L. B. Leopold (2000), Attributes of an alluvial river and their relation to water policy and management, *Proceedings of the National Academy of Sciences*, *97*(22), 11858–11863, doi:10.1073/pnas.97.22.11858.

Tucker, G. E., and G. R. Hancock (2010), Modelling landscape evolution, *Earth Surface Processes and Landforms*, *35*(1), 28–50, doi:10.1002/esp.1952.

Tucker, G. E., and R. Slingerland (1997), Drainage basin responses to climate change, *Water Resour. Res.*, *33*(8), 2031–2047, doi:10.1029/97WR00409.

Tucker, G. E., S. T. Lancaster, N. M. Gasparini, and R. L. Bras (2001), The channel-hillslope integrated landscape development model (CHILD), in *Landscape erosion and evolution modeling*, edited by R. S. Harmon and W. W. Doe III, pp. 349–388, Kluwer Academic/Plenum Publishers, New York.

Turowski, J. M., N. Hovius, H. Meng-Long, D. Lague, and C. Men-Chiang (2008), Distribution of erosion across bedrock channels, *Earth Surface Processes and Landforms*, *33*(3), 353–363, doi:10.1002/esp.1559.

Tyráček, J., R. Westaway, and D. Bridgland (2004), River terraces of the Vltava and Labe (Elbe) system, Czech Republic, and their implications for the uplift history of the Bohemian Massif, *Proceedings of the Geologists' Association*, *115*(2), 101–124, doi:10.1016/S0016-7878(04)80022-1.

Udaykumar, H. S., and W. Shyy (1995), Simulation of interfacial instabilities during solidification—I. Conduction and capillarity effects, *International Journal of Heat and Mass Transfer*, *38*(11), 2057–2073, doi:10.1016/0017-9310(94)00315-M.

Udaykumar, H. S., W. Shyy, and M. M. Rao (1996), Elafint: A mixed Eulerian–Lagrangian method for fluid flows with complex and moving boundaries, *International Journal for Numerical Methods in Fluids*, *22*(8), 691–712, doi:10.1002/(SICI)1097-0363(19960430)22:8<691::AID-FLD371>3.0.CO;2-U.

Udaykumar, H. S., R. Mittal, and W. Shyy (1999), Computation of solid–liquid phase fronts in the sharp interface limit on fixed grids, *Journal of Computational Physics*, *153*(2), 535–574, doi:10.1006/jcph.1999.6294.

Van De Wiel, M. J., T. J. Coulthard, M. G. Macklin, and J. Lewin (2011), Modelling the response of river systems to environmental change: Progress, problems and prospects for palaeo-environmental reconstructions, *Earth-Science Reviews*, *104*(1-3), 167–185, doi:10.1016/j.earscirev.2010.10.004.

Van den Berg, M. W. (1996), Fluvial sequences of the Maas: A 10 Ma record of neotectonics and climatic change at various time-scales, Ph. D. thesis, Wageningen Agricultural University, The Netherlands.

Van den Berg, M. W., and T. van Hoof (2001), The Maas terrace sequence at Maastricht, SE Netherlands: Evidence for 200 m of late Neogene and Quaternary surface uplift, in *River Basin Sediment Systems: Archives of Environmental Change*, pp. 45–86, Abingdon, England.

Vandenberghe, J. (2003), Climate forcing of fluvial system development: An evolution of ideas, *Quaternary Science Reviews*, *22*(20), 2053–2060.

Veldkamp, A., and J. J. van Dijke (2000), Simulating internal and external controls on fluvial terrace stratigraphy: A qualitative comparison with the Maas record, *Geomorphology*, *33*(3-4), 225–236, doi:10.1016/S0169-555X(99)00125-7.

Ward, W. R. (1973), Large-scale variations in the obliquity of Mars, *Science*, *181*(4096), 260–262.

Weedon, G. P. (2003), *Time-series analysis and cyclostratigraphy: Examining stratigraphic records of environmental cycles*, Cambridge University Press.

Weertman, J. (1972), General theory of water flow at the base of a glacier or ice sheet, *Reviews of Geophysics*, *10*(1), 287–333, doi:10.1029/RG010i001p00287.

Wegmann, K. W., and F. J. Pazzaglia (2002a), Holocene strath terraces, climate change, and active tectonics: The Clearwater River basin, Olympic Peninsula,

Washington State, *Geol. Soc. Am. Bull.*, *114*(6), 731–744, doi:10.1130/0016-7606(2002)114<0731:HSTCCA>2.0.CO;2.

Wegmann, K. W., and F. J. Pazzaglia (2002b), Holocene strath terraces, climate change, and active tectonics: The Clearwater River basin, Olympic Peninsula, Washington State, *Geological Society of America Bulletin*, *114*(6), 731–744.

Wegmann, K. W., and F. J. Pazzaglia (2009), Late Quaternary fluvial terraces of the Romagna and Marche Apennines, Italy: Climatic, lithologic, and tectonic controls on terrace genesis in an active orogen, *Quaternary Science Reviews*, *28*(1-2), 137–165, doi:10.1016/j.quascirev.2008.10.006.

Weldon, R. J. (1986), The late Cenozoic geology of Cajon Pass: Implications for tectonics and sedimentation along the San Andreas fault, Ph. D. thesis, California Institute of Technology, Pasadena, California.

Wellmeyer, J. L., M. C. Slattery, and J. D. Phillips (2005), Quantifying downstream impacts of impoundment on flow regime and channel planform, lower Trinity River, Texas, *Geomorphology*, *69*(1), 1–13.

Westaway, R., D. R. Bridgland, R. Sinha, and T. Demir (2009), Fluvial sequences as evidence for landscape and climatic evolution in the Late Cenozoic: A synthesis of data from IGCP 518, *Global and Planetary Change*, *68*(4), 237–253, doi:10.1016/j.gloplacha.2009.02.009.

Whipple, K. X. (2004), Bedrock rivers and the geomorphology of active orogens, *Annual Review of Earth and Planetary Sciences*, *32*(1), 151–185, doi:10.1146/annurev.earth.32.101802.120356.

Whipple, K. X., and G. E. Tucker (1999), Dynamics of the stream-power river incision model: Implications for height limits of mountain ranges, landscape response timescales, and research needs, *Journal of Geophysical Research*, *104*(B8), 17661–17647, doi:199910.1029/1999JB900120.

Wieczorek, M. A. (2008), Constraints on the composition of the Martian south polar cap from gravity and topography, *Icarus*, *196*(2), 506–517.

Williams, G. P. (1986), River meanders and channel size, *Journal of Hydrology*, *88*(1–2), 147–164, doi:10.1016/0022-1694(86)90202-7.

Wobus, C. W., B. T. Crosby, and K. X. Whipple (2006a), Hanging valleys in fluvial systems: Controls on occurrence and implications for landscape evolution, *Journal of Geophysical Research*, *111*(F2), F02017, doi:10.1029/2005JF000406.

Wobus, C. W., G. E. Tucker, and R. S. Anderson (2006b), Self-formed bedrock channels, *Geophysical Research Letters*, *33*(18), L18408, doi:10.1029/2006GL027182.

Wohl, E., P. L. Angermeier, B. Bledsoe, G. M. Kondolf, L. MacDonnell, D. M. Merritt, M. A. Palmer, N. L. Poff, and D. Tarboton (2005), River restoration, *Water Resources Research*, *41*(10), doi:10.1029/2005WR003985.

Wolkowinsky, A. J., and D. E. Granger (2004), Early Pleistocene incision of the San Juan River, Utah, dated with 26Al and 10Be, *Geology*, *32*(9), 749–752, doi:10.1130/G20541.1.

Yanites, B. J., and G. E. Tucker (2010), Controls and limits on bedrock channel geometry, *Journal of Geophysical Research: Earth Surface*, *115*(F4), F04019, doi:10.1029/2009JF001601.

Yanites, B. J., G. E. Tucker, K. J. Mueller, and Y.-G. Chen (2010), How rivers react to large earthquakes: Evidence from central Taiwan, *Geology*, *38*(7), 639–642, doi:10.1130/G30883.1.

Zaprowski, B. J., E. B. Evenson, F. J. Pazzaglia, and J. B. Epstein (2001), Knickzone propagation in the Black Hills and northern High Plains: A different perspective on the late Cenozoic exhumation of the Laramide Rocky Mountains, *Geology*, *29*(6), 547–550.

Zolezzi, G., and G. Seminara (2001), Downstream and upstream influence in river meandering. Part 1. General theory and application to overdeepening, *Journal of Fluid Mechanics*, *438*, 183–211.

Zuber, M. T., R. J. Phillips, J. C. Andrews-Hanna, S. W. Asmar, A. S. Konopliv, F. G. Lemoine, J. J. Plaut, D. E. Smith, and S. E. Smrekar (2007), Density of Mars' south polar layered deposits, *Science*, *317*(5845), 1718–1719.